INTERNATIONAL CENTRE FOR NUMERICAL METHODS IN ENGINEERING

A fully Lagrangian formulation for fluid-structure interaction between free-surface flows and multi-fracturing solids and structures

Alejandro Cornejo
Eugenio Oñate
Francisco Zárate

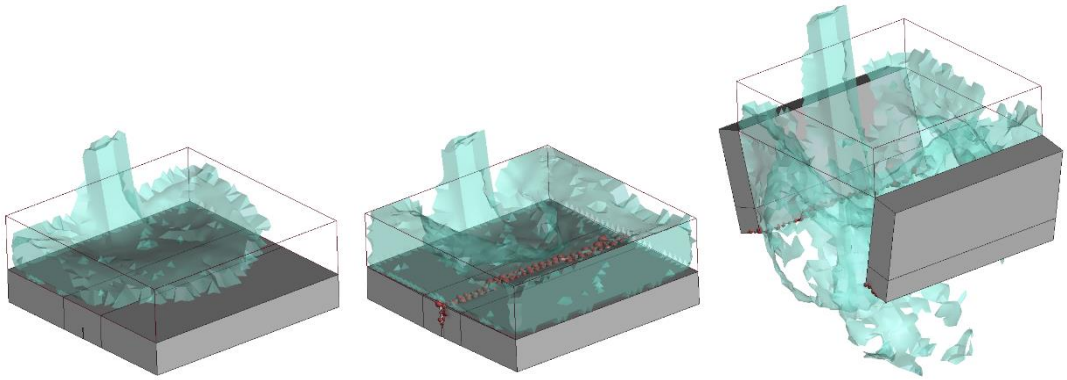

Monograph CIMNE Nº-192, January 2021

A fully Lagrangian formulation for fluid-structure interaction between free-surface flows and multi-fracturing solids and structures

Alejandro Cornejo
Eugenio Oñate
Francisco Zárate

Monograph CIMNE Nº-192, January 2021

International Center for Numerical Methods in Engineering
Gran Capitán s/n, 08034 Barcelona, Spain

INTERNATIONAL CENTER FOR NUMERICAL METHODS IN ENGINEERING
Edificio C1, Campus Norte UPC
Gran Capitán s/n
08034 Barcelona, Spain
www.cimne.com

First edition: January 2021

A FULLY LAGRANGIAN FORMULATION FOR FLUID-STRUCTURE INTERACTION BETWEEN FREE-SURFACE FLOWS AND MULTI-FRACTURING SOLIDS AND STRUCTURES
Monograph CIMNE M192

“We are what we repeatedly do. Excellence, then, is not an act, but a habit”
Aristotle 384-322 BC

“He who has a why to live for can bear almost any how”
rism, *Friedrich Nietzsche*

Abstract

It is well known that in civil engineering structures are designed so that they remain, whenever possible, in an elastic regime and with their mechanical properties intact. The truth is that in reality there are uncertainties either in the execution of the work (geometric errors or material quality) or during its subsequent use (loads not contemplated or its value has been estimated incorrectly) that can lead to the collapse of the structure. This is why the study of the failure of structures is inherently interesting and, once is known, its design can be improved to be the less catastrophic as possible or to dissipate the maximum energy before collapsing. Another area of application of fracture mechanics is that of processes of which interest lies in the breakage or cracking of a medium. Within the mining engineering we can enumerate several processes of this nature, namely: hydraulic fracture processes or *fracking*, blasting for tunnels, explosion of slopes in open pit mines, among others. Equally relevant is the analysis of structural failures due to natural disasters, such as large avenues or even tsunamis impacting protection structures such as walls or dikes. In this work numerous implementations and studies have been made in relation to the mentioned processes.

That said, the objective of this work is to develop an advanced numerical method capable of simulating multi-fracture processes in materials and structures. The general approach of the proposed method can be seen in various publications made by the author and directors of this work. This methodology is meant to cover the maximum spectrum of engineering applications possible. For this purpose, a coupled formulation of the Finite Element Method (FEM) and the Discrete Element Method (DEM) is used, which employs an isotropic damage constitutive model to simulate the initial degradation of the material and, once the strength of the material has been completely exhausted, those Finite Element (FE) are removed from the FEM mesh and a set of Discrete Element (DE) are generated at its nodes. In addition to ensure the conservation of the mass of the system, these DE prevent the indentation between the fissure planes thanks to the frictional repulsive forces calculated by the DEM, if any.

Additionally, in this work it has been studied how the proposed coupled method named FEM-DEM together with the smoothing of stresses

based on the *super-convergent patch* is able to obtain reasonably mesh-independent results but, as one can imagine, the crack width is directly related to the size of the elements that have been removed. This favours the inclusion of an adaptive remeshing technique that will refine the mesh where it is required (according to the Hessian of a nodal indicator of interest) thus improving the discretization quality of the crack obtained and thereby optimizing the simulation cost. In this sense, the procedures for mapping nodal and internal variables as well as the calculation of the nodal variable of interest will be discussed.

As far as the studies of natural disasters are concerned, especially those related to free-surface water flows such as tsunamis, one more level of coupling between the aforementioned method FEM-DEM and one Computational Fluid Dynamics (CFD) formulation commonly referred to as Particle Finite Element Method (PFEM) has been implemented. With this strong coupled formulation, many cases of wave impacts and fluid flows have been simulated against solid structures such as walls and dikes, among others.

Resumen

Es bien sabido que en ingeniería civil las estructuras se diseñan para que permanezcan, siempre que sea posible, en régimen elástico y con sus propiedades mecánicas intactas. Lo cierto es que en realidad existen incertidumbres tanto en la ejecución de la obra (errores geométricos o de calidad de los materiales) como en su posterior utilización (cargas no contempladas o cuyo valor y/o punto de aplicación se ha estimado incorrectamente) que pueden conllevar al colapso de la estructura. Por ello, el estudio del fallo de las estructuras es inherentemente interesante y, una vez conocido, se puede mejorar el diseño de la misma para que sea lo menos catastrófico posible o para que disipe la máxima energía antes del colapso y aumentar así su ductilidad y seguridad.

Otra área de aplicación de la mecánica de la fractura es la de los procesos cuyo interés radica en la rotura o la fisuración de un medio. Dentro de la ingeniería de minas podemos enumerar varios procesos de esta naturaleza, a saber: procesos de fractura hidráulica o *fracking*, voladuras para excavación de túneles, explosión de taludes en minas a cielo abierto, entre otros. Igualmente relevante es el análisis de los fallos estructurales debidos a desastres naturales, como grandes avenidas o incluso tsunamis que impactan en estructuras de protección como muros o diques. En este ámbito se han realizado numerosas implementaciones y estudios en relación con los procesos mencionados.

Dicho esto, el objetivo de este trabajo es desarrollar un método numérico avanzado, cuyo enfoque general puede verse en diversas publicaciones realizadas por el autor y los directores de este trabajo, capaz de simular procesos de multifractura en materiales y estructuras cubriendo así el máximo espectro de aplicaciones de ingeniería posible. Para ello se emplea una formulación acoplada del Método de los Elementos Finitos (FEM) y del Método de los Elementos Discretos (DEM), que internamente incluye un modelo constitutivo de daño isótropo para simular la degradación irrecuperable del material. Una vez agotada la energía de deformación disponible de algunos elementos finitos (FE), se eliminan de la malla FEM y se genera un conjunto de elementos discretos (DE) en los nodos del mismo. Los DE generados, además de asegurar la conservación de la masa del sistema, evitan la indentación entre los planos de

la fisura gracias a las fuerzas friccionales de repulsión calculadas por el DEM, si las hubiere.

En este trabajo se ha estudiado cómo el método acoplado propuesto denominado FEM-DEM junto con el suavizado de tensiones basado en el *super-convergent patch* es capaz de obtener resultados razonablemente independientes de la malla pero, como se puede imaginar, el ancho de la fisura está directamente relacionado con el tamaño de los elementos finitos que se han eliminado. Esto propicia la inclusión de una técnica de remallado adaptativo que refinará la malla donde se requiera (según la matriz Hessiana de un indicador nodal) mejorando así la calidad de discretización de la fisura obtenida y optimizando el coste computacional de la simulación. En este sentido, se discutirán los procedimientos de mapeo de las variables nodales e internas, así como el cálculo de la variable nodal de interés.

En lo que respecta al estudio de los desastres naturales, especialmente los relacionados con flujos de agua de superficie libre como los tsunamis, se ha implementado un nivel más de acoplamiento entre el mencionado método FEM-DEM y una formulación de Dinámica de Fluidos Computacional (CFD) comúnmente conocida como Método de Elementos Finitos y Partículas (PFEM). Con esta formulación fuertemente acoplada, se han simulado diversos casos de impactos de olas contra estructuras sólidas como muros y diques, entre otros.

Contents

Acknowledgements

El proceso de creación de este documento y de todo el trabajo que ello conlleva ha sido uno de los retos personales más ambiciosos y enriquecedores que haya tenido en estos 28 años. Esta aventura ha sido una montaña rusa de emociones, desde días en los que nada funciona y crees que 5 años no serán suficiente para terminar hasta otros en los que uno entra en un estado de iluminación ingenieril y resuelve varios problemas en un día. Lo cierto es que cada una de estas experiencias son necesarias y te transmiten valores que, tanto dentro como fuera del trabajo, tienen un valor incalculable: esfuerzo, perseverancia, paciencia y humildad.

Pese a que hacer un doctorado es un trabajo eminentemente en solitario la mayor parte del tiempo, donde los criterios de calidad, consistencia y plazos se los marca uno mismo, es cierto que sin la ayuda o apoyo de ciertas personas no hubiera podido realizar este trabajo tal y como aquí se presenta.

Primeramente, querría agradecer a mis padres, a mi hermano y familiares todo su apoyo y cariño, siempre animándome a aspirar a más y, aunque ellos quizás no lo sepan, siempre han sido un referente de esfuerzo y superación para mi y espero haberlos hecho sentir orgullosos, os quiero.

Si los anteriores son los integrantes de mi casa propia, debo decir que CIMNE ha sido mi segundo hogar y me ha dado la oportunidad de llevar a buen término todo lo que me he propuesto, sean temas relacionados con la tesis o transversales. Por esto quiero agradecer a los profesores Eugenio Oñate y Francisco Zárate, mis directores, el haber confiado en mi y haberme supervisado y apoyado en este proceso, desde que empecé siendo un estudiante de máster fascinado por los elementos finitos.

De CIMNE también quiero acordarme de todos mis compañeros y amigos con los que hemos compartido estrés y risas por igual. Quiero agradecer a Lucia Barbu su valiosa amistad la cual nos ha permitido compartir infinidad de momentos que llevaré siempre conmigo y espero seguir sumando más a día de hoy. Quiero acordarme también de la ayuda inestimable de Miguel Ángel Celigueta con el que, especialmente al inicio, y cuando las cosas me superaban un poco, conseguía siempre desatascarme y seguir adelante. Es especial para mí también todos los momentos distendidos que tenemos el grupo ANAV (Sergio Jiménez, Lucia y yo) en las horas de café y comidas y que, de un modo u otro, me alegran un poco más el día a día. No quiero dejar de agradecer a Vicente Mataix su ayuda en muchas de las implementaciones llevadas a cabo en este trabajo así como ser mi referente en todo lo que a programación se refiere.

Gracias también a Rubén Zorrilla, Alessandro Franci, Riccardo Rossi y Carlos Roig por vuestra ayuda en diversos momentos durante el transcurso de mi tesis.

Es también muy valiosa para mí la amistad (ya se cumple casi una década prácticamente) que tenemos Mar, Víctor y yo, con los que he ido a la otra punta del globo y siempre hemos tenido anécdotas de las que reír durante semanas.

Por último quiero destacar la excelente influencia académica y docente que han tenido los profesores Sergio Oller, Miguel Cervera y Álex Barbat que, sin duda alguna, queda reflejada en el trabajo que aquí expongo, gracias por vuestro tiempo, pasión y paciencia.

A todos, gracias

Alejandro, 12 de noviembre de 2020.

Part I

Introduction

Chapter 1

Motivation

The modelling and simulation of the mechanical process of fracturing of materials and structures is one of the most challenging topics in computational mechanics. The laboratory predictions of the ultimate strength of materials and the detection/propagation of fractures is also a complex research topic due to their typical prompt or abrupt behaviour of crack, which difficulties the experimental analysis.

Indeed, natural hazards is one of the most dangerous and costly events in economical and human-lifes terms. This natural hazards are physical phenomena caused either by rapid or slow onset events which can be geophysical (earthquakes, landslides, tsunamis and volcanic activity), hydrological (avalanches and floods), climatological (extreme temperatures, drought and wildfires), meteorological (cyclones and storms/wave surges) or biological (disease epidemics and insect/animal plagues). This is why it is of vital importance to develop a tool that is capable of assessing the risks and predicting the damages induced by this phenomena in order to design infrastructures in the most efficient and safe way possible.

In addition to being able to prevent structural damage caused by natural disasters, it is also of vital importance to study the industrial applicability of such a numerical tool. In this regard, it is clear that a methodology capable of simulating multi-fracture processes in continuous mediums can be highly useful in engineering fields such as: the mining industry, tunnel excavation, hydraulic fracturing, and structural design, among others. Bearing this in mind, the increase in efficiency that can be induced (and the consequent reduction in industrial costs) by the use of a prediction tool such

as the one proposed in this work justifies further study in this field, which is one of the objectives of this work.

In the last decades, the use of computer methods and numerical algorithms for simulating many multidisciplinary science and engineering problems has increased dramatically in terms of complexity and generality. Said that, the fracture mechanics field is not an exception and some different numerical approaches are competing each other in order to obtain a (qualitatively and quantitatively) realistic fracture paths with the less computational cost possible. One of the most used methodologies is the Finite Element Method (FEM), which is able to deal with a wide set of problems of different physics and geometries. In addition, due to its proven thermodynamic consistence, a solid mathematical formulation is available. Nonetheless, simulating the onset and propagation of fractures in Mode I (opening), Mode II (sliding) or Mode III (tearing) (see Fig. 1.1) or any combination of them is still a challenging field in Computational Solid Mechanics (CSM).

Recently, numerous numerical strategies have been developed that attempt to capture the phenomena described in the previous paragraphs but, thus far, no sufficiently robust and consistent formulation has been developed that is generalizable to any cracking problem. Indeed, some of the methods try to capture the creation of fracture surfaces by mathematically generate a jump in the displacement/strain field over the domain, which increases the complexity of the numerical resolution and require the use of crack-tracking (also known as tracing) procedures in order to predict the crack localization. The development of new advanced computational methods (FE based) such as B-bar elements, XFEM, phase field (PF) formulations, $u-p$ and $u-\varepsilon$ mixed formulations, remeshing techniques, etc. (see Part II for a more detailed description), applied on fracture mechanics denote the research and industrial interest of this field.

If one moves on from the methods based on the FEM to the Discrete Element Method (DEM) [CS79; LO09], the kind of problematic is intrinsically different. There are several approaches that discretize the continuum as a set of discrete elements (DE) (hereafter termed particles) attached by a bonding between them ruled by local or non-local constitutive laws [WO99; Oña+15]. However, the calibration of the local material parameters of the bonds between the particles is complex [Cel+17] and only under certain conditions behaves as a continuum. In addition, the large number of particles needed to solve practical problems discourages its use.

Bearing all this information in mind and trying to combine the best features of

the FEM and the DEM, the FEM-DEM methodology was developed [ZO15; ZCO18]. The continuum is initially represented with FE of which non-linear material behaviour is represented by an isotropic damage model. A smoothing procedure is used by computing the stresses at the element edges. When the damage in a certain element achieves a maximum threshold, it is removed from the mesh and a set of DE are placed at its nodes. The new DE avoid the indentation between the crack faces by computing the frictional contact forces resulting from the indentation of the DE inside the FE edge. Then, these forces are transferred to the FE nodes as equivalent nodal forces in the next time step.

The FEM-DEM algorithm has been designed to deal with multi-fracturing processes in solids and structures as can be seen in Fig. 1.2. This implies that the method should perform accurately for strength of materials benchmark tests, blast excavation processes, hydraulic fracturing or *fracking* procedures, generic structures demolitions and natural hazards phenomena such as tsunamis impacts over walls or landslides, among others.

In order to be capable of simulating natural hazards involving free-flows and fracturing structures, a coupled Fluid Structure Interaction (FSI) formulation between the PFEM and the already mentioned FEM-DEM methodology has been studied and validated.

Considering the above, the main challenge of this work is to develop a robust and fast numerical tool that can reproduce a wide spectrum of multi-fracture processes in solids, such as impacts or blasting of structures. In addition, such a formulation should also be coupled with a fluid dynamics methodology in order to predict cracking or failure of structures due to wave impacts and other natural events. In order to achieve this, a multi-coupled formulation has been developed that is capable of dealing simultaneously with:

1. Multi-fracturing processes of solids: onset, bifurcation and merging of fractures: Damage mechanics and FE erosion.

2. Fluid-structure interaction: staggered scheme with Aitken relaxation technique.

3. Frictional contact between solids: DEM contact search and estimation.

4. Fully detachment and separation of solids due to cracking.

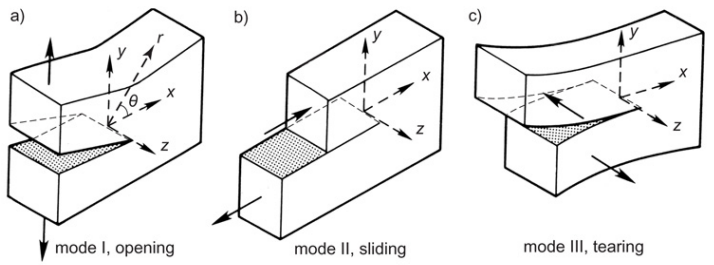

Figure 1.1: Fracture modes [KP85].

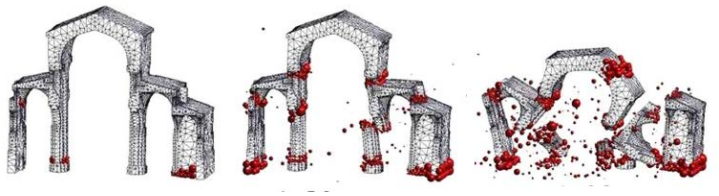

Figure 1.2: Cistercian church at the monastery of Poblet submitted to an earthquake. Source: Zárate et al. [ZCO18].

5. Large displacements and rotations in solids: Total Lagrangian (TL) formulation for the FEM kinematics.

6. Generation and simulation of solid debris by means of discrete particles: Automatic generation of particles and use of explicit time schemes.

Chapter 2

Research objectives and outline

2.1 Research objectives

The methodology developed in this work has been specially designed to be capable of simulating a broad spectrum of applications regarding multi-fractures in solids and structures, fluid-structure interaction problems and blast loading mining processes. In this way, a polivalent, consistent and robust formulation for multi-fractures has been developed combining the following characteristics:

- **Must be reliable.** This is why a wide selection of standard benchmarks are included in this document. The proposed methodologies have been compared with analytical results when possible or with other numerical simulations available in the literature in order to ensure its correctness and accuracy.

- **Must be fast.** The analytical linearisation of the problem is not possible due to the phenomenological operations that the FEM-DEM performs. Nevertheless, some utilities have been implemented in order to obtain a numerical approximation of the tangent constitutive tensor (see appendix C). Additionally, the methodology is totally compatible with the use of iterative linear solvers such as the AMGCL [Dem19] solver available in Kratos.

- **The indentation between the crack faces is not admissible**. This is achieved by creating a layer of DE at the crack nodes of which frictional repulsive forces are computed (if an indentation of the DE inside the FE face occurs) and transferred to the FEM calculations (at each time step if one-way coupling or at each iteration if two-way coupling) as a set of nodal forces. This avoids the use of conventional contact formulations (Penalty method, Lagrange Multipliers (LM), Augmented Lagrange Multipliers (ALM)) which are computationally more expensive and, regarding multi-fracturing, present several difficulties when dealing with multi-body contact surfaces especially if they are not predefined (complex master-slave surface definition).

- **The formulation must overcome the size-objectivity issue and diminish the mesh-dependency.** The size-objectivity issue has been dealt with the inclusion of the *characteristic length* normalisation when computing the dissipated energy. The mesh-dependency is controlled by the quality of the strain/stress field in the continuum. Regarding this, an smoothing of the stress field based on the work of Zienkiewicz and Zhu [ZZ92] is proposed (see appendix A). In this regard, an adaptive remeshing technique has been developed in order to circumvent the mesh-dependency issue.

- **An adaptive remeshing technique must be added in order to overcome the mesh-dependency.** As will be explained, the FEM-DEM methodology has been improved with the inclusion of an adaptive remeshing technique which objective is to improve the quality of the mesh according to a certain nodal criterion (the Hessian of a nodal variable of interest). This improves the discretization quality of the crack where necessary whereas optimizing the computational cost.

- **The formulation must be coupled with a CFD strategy.** In order to be capable of simulating fluid impacts over structures a coupled PFEM-FEM-DEM algorithm has been developed. This is why a strong coupling (two-way coupling) between the PFEM and the FEM-DEM has been studied. The proposed methodology is able to simulate the interaction between solids and free-surface flows even when the *added-mass effect* occurs.

- **The formulation must allow fully detachments and large displacements and rotations of solids.** Indeed, the FEM-DEM methodology has been implemented in a Total Lagrangian (TL) approach with small strains and finite strains (Neo-Hookean hyper-elasticity [Bel+14]). This is of great importance in blast

loading problems where the rock blocks can be detached from the body and suffer large displacements and rotations in addition with contacts.

- **The inclusion of steel rebars must be possible.** In this regard, a classical rule of mixtures has been included within the FEM-DEM framework including the eventual plastification of the steel rebars in an homogenized phenomenological constitutive way [Cor+18; Cor+15; Bar+19; JBO18] within the FEM-DEM methodology.

- **The methodology has to be generalized to deal with orthotropic materials in non-linear regime.** Indeed, a general definition of an implicit orthotropic criterion has been implemented as well as the required rotation operations.

Summing up, the developments proposed in this work bring together existing ideas in the fields of CSM, particle mechanics, CFD and remeshing procedures in a proper way and combine/extend them towards a treatment of multi physics-coupled problems in engineering.

All the methods and models used are implemented in the open source finite element code Kratos-Multiphysics framework [DRO10] (see appendix E) developed at International Centre for Numerical Methods in Engineering (CIMNE) that has been especially designed for helping the development of multidisciplinary finite element programs and even particle methods like the DEM, Material Point Method (MPM), Smoothed Particle Hydrodynamics (SPH), etc.

2.2 Outline

The document is composed by seven parts. In **Part II**, a review of the state of the art in fracture mechanics is conducted. This part is relevant because it defines the current state of the technology as well as the limitations of the available formulations. This part provides an overview of common numerical techniques which have been used for modelling solid fracture mechanics.

In **Part III** the basic FEM-DEM methodology is described, starting from the governing equations used in solid mechanics and its finite element discretization. Next, DEM is reviewed as well as its coupling with the FEM. Finally, some numerical examples that show the FEM-DEM correctness and consistency are shown.

Part IV extends the aforementioned FEM-DEM methodology and introduces the hessian based adaptive remeshing technique accompanied by several numerical examples that denote the correctness and usefulness of the nodal indicator to the fracture mechanics problem.

The coupling between the FEM-DEM and the free-surface flow strategy (PFEM) is documented in **Part V**. In this part all the governing equations of the free-surface computational fluid dynamics are stated in addition to the fluid-structure interaction implementation details.

Part VI details all the implementations and results obtained regarding mining processes and blast excavations. The required pressure load extrapolation through the crack and its value decay due to the volume change is explained.

Part VII includes the discussion of the pros and cons of the proposed FEM-DEM methodology in addition to the future research lines and alternative fields of application of the implemented algorithm. Further successful applications of the FEM-DEM formulation are outlined in the same part.

Part I bibliography

[Bar+19] LG. Barbu et al. “Methodology for the analysis of post-tensioned structures using a constitutive serial-parallel rule of mixtures: large scale non-linear analysis”. *Composite Structures*. Vol. 216, pp. 315–330 , 2019.

[Bel+14] T. Belytschko et al. *Nonlinear Finite Elements for Continua and Structure*. Wiley. 2nd ed. 2014.

[Cel+17] MA. Celigueta et al. “Accurate modelling of the elastic behavior of a continuum with the Discrete Element Method”. *Computational Mechanics*. Vol. 60, pp. 997–1010 , 2017.

[Cor+15] A. Cornejo et al. “High-cycle fatigue constitutive model and a load-advance strategy for the analysis of unidirectional fiber reinforced composites subjected to longitudinal loads”. *Composite Structures*. Vol. 220, pp. 622–641 , 2015.

[Cor+18] A. Cornejo et al. “Methodology for the analysis of post-tensioned structures using a constitutive serial-parallel rule of mixtures”. *Composite Structures*. Vol. 200, pp. 480–497 , 2018.

[CS79] P.A. Cundall and O.D.L. Strack. “A discrete numerical model for granular assemblies”. *Geotechnique*. Vol. 29, pp. 47–65 , 1979.

[Dem19] D. Demidov. “AMGCL: An Efficient, Flexible, and Extensible Algebraic Multigrid Implementation”. *Lobachevskii Journal of Mathematics*. No. 5, Vol. 40, pp. 535–546 , 2019. DOI: 10.1134/S1995080219050056.

[DRO10] P. Dadvand, R. Rossi, and E. Oñate. “An Object-oriented Environment for Developing Finite Element Codes for Multi-disciplinary Applications”. *Computational Methods in Engineering*. Vol. 17, pp. 253–297 , 2010.

[JBO18] S. Jiménez, LG. Barbu, and S. Oller. *Analysis of post-tensioned structures by means of a constitutive serial-parallel rule of mixtures*. CIMNE. 2018.

[KP85] Melvin F. Kanninen and Carl H. Popelar. *Advanced Fracture Mechanics*. Oxford University Press. 1st. 1985.

[LO09] C. Labra and E. Oñate. “High-density sphere packing for discrete element method simulations”. *Commun Numer Meth Eng*. Vol. 25, pp. 837–849 , 2009.

[Oña+15] E. Oñate et al. “A local constitutive model for the discrete element method. Application to geomaterials and concrete”. *Computational Particle Mechanics*. No. 2, Vol. 2, pp. 139–160 , 2015.

[WO99] J. Williams and R. OConnor. “Discrete element simulation and contact problem”. *Arch Comput Methods Eng*. Vol. 6, pp. 279–304 , 1999.

[ZCO18] F. Zárate, A. Cornejo, and E. Oñate. “A three-dimensional FEMDEM technique for predicting the evolution of fracture in geomaterials and concrete”. *Comput Methods Appl Mech Eng*. Vol. 5, pp. 411–420 , 2018.

[ZO15] F. Zárate and E. Oñate. “A simple FEMDEM technique for fracture prediction in materials and structures”. *Computational Particle Mechanics*. Vol. 2, pp. 301–314 , 2015.

[ZZ92] O.C. Zienkiewicz and JZ. Zhu. “The superconvergent patch recovery (SPR) and adaptive finite element refinement”. *Comput Methods Appl Mech Eng*. Vol. 101, pp. 207–224 , 1992.

Part II

State of the art

Chapter 3

Introduction

Fracture mechanics is one of the most common and dangerous phenomena within the material engineering and structural analysis fields. The correct engineering design and the prevention of cracking and the eventual collapse of the structure are its major concerns. Like many other physical phenomena, computational fracture modelling is an indispensable tool not only for assessing the safety of cracked structures, for which large-scale experiments are not affordable, but also for shedding light on the understanding of the fracture processes of many materials such as concrete, rock, ceramics, metals, etc.

Failure of solids and structures can be seen in two distinct ways. There are cases in which the structure can fail even when the material remains elastic, which is the case of elastic buckling. However, the material degradation or the generation of plastic deformation at certain zones of the structures will lead to the failure of the whole structure.

In the early stages, the prediction of material strength in solids was generally based on phenomenological approaches before the emergence of fracture mechanics. Indeed, a wide range of phenomenological failure criteria were developed (in terms of stresses or strains) in order to reproduce experimental data. In general, the classical approaches could predict accurately the material failure as long as the stress field was relatively uniform. This is why, when there is a high-stress gradient in the material, the solution obtained with these simplified methodologies were unreliable and lead to many unexpected structural failures.

One of the most known examples is the structural brittle failure of Liberty cargo ships, which were build during World War II [Ros97]. More than 100 over the 2700 ships suffered some fracturing and about 10 were totally fractured in half. After several studies, was demonstrated that the cracks were initiated at certain regions were some stress concentration was located. Once initiated, the crack propagated in the hull, resulting in a prompt and sudden failure (see Fig. 3.1). Another example include the failures of the fuselage in Comet jet air-planes between the years 1953 and 1955 [Wel55] (see Fig. 3.2). As a civil engineering example, it is remarkable the catastrophic effects that the failure of a dam can cause. In 1802, in Murcia (Spain), a dam that was holding the Puentes swamp failed due to a flood and provoked 608 casualties (see Fig. 3.3).

The above examples serve to illustrate the severity that a bad design can have in terms of the ultimate capacity estimation of the structure. If the models used are not capable of predicting correctly the failure of an structure, its security and safety could be compromised. With the objective of predicting more accurately the failure of structures the Fracture Mechanics and the Computational Failure Mechanics (CFM) disciplines emerged. Since the Griffiths pioneering work on brittle failure of glass in 1920s [Gri20] until now, much research has been conducted with the objective of developing a robust tool to predict the onset and evolution of cracks in materials and structures.

In the next chapter (see Chapter 4) a detailed description of the most used methodologies applied to fracture mechanics is performed: Starting from the early stages of the fracture mechanics discipline to the modern finite elements and numerical methods applied to cracking.

3.1 Research dissemination

The work done in this work and some complementary research has been published in several articles that are cited below.

1. Zárate F., Cornejo A. and Oñate E., "A three-dimensional FEMDEM technique for predicting the evolution of fracture in geomaterials and concrete". *Computational Particle Mechanics*, 5(3), 411-420 (2018). [ZCO18]

2. Cornejo A., Barbu L.G., Escudero C., Martínez X., Oller S. and Barbat A.H., "Methodology for the analysis of post-tensioned structures using a constitutive

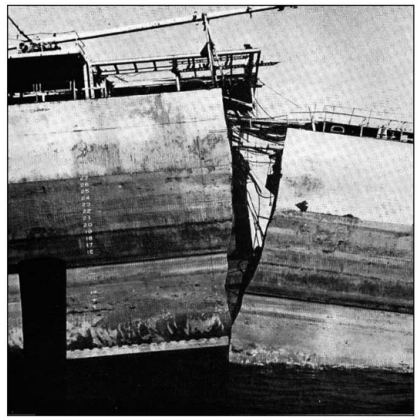

Figure 3.1: Fracture path in the Liberty cargo ships. Image from https://metallurgyandmaterials.wordpress.com.

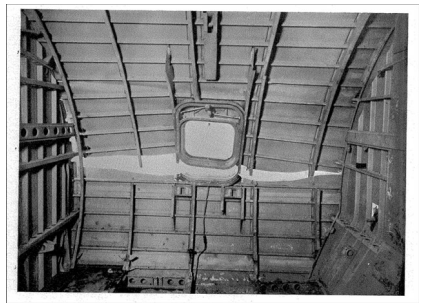

Figure 3.2: Crack occurred in the Comet air-plane. Image from http://aerossurance.com.

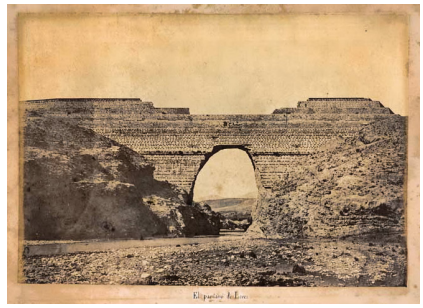

Figure 3.3: Puentes dam after destruction, Lorca. Image from Confederación Hidrográfica del Segura.

serial-parallel rule of mixtures". *Composite Structures*, 200, 480-497 (2018). [Cor+18]

3. Barbu L.G., Cornejo A., Martínez X., Oller S. and Barbat A.H., "Methodology for the analysis of post-tensioned structures using a constitutive serial-parallel rule of mixtures: Large scale non-linear analysis". *Composite Structures*, 216, 315-330 (2019). [Bar+19]

4. Cornejo A., Zárate F. and Oñate E., "Combination of an adaptive remeshing technique with a coupled FEMDEM approach for analysis of crack propagation problems". *Computational Particle Mechanics* , 1-18 (2019). [Cor+19]

5. Jiménez S., Cornejo A., Barbu L.G., Oller S. and Barbat A.H., "Analysis of the mock-up of a reactor containment building: comparison with experimental results". *Nuclear Engineering and Design* ,359, 110454 (2020). [Jim+20]

6. Cornejo A., Franci A., Zárate F. and Oñate E., "A fully Lagrangian formulation for fluid-structure interaction problems with free-surface fluids and fracturing solids". *Computers and Structures* , Under revision.

7. Jiménez S., Cornejo A., Barbu L.G., Barbat AH. and Oller S., "Failure pressure analysis of a nuclear reactor prestressed concrete containment building". *Engineering Structures* , Under revision.

Chapter 4

Literature review

In this chapter a compilation of the different methodologies used for the simulation of fractures in solids and structures is described. At first, a brief historical perspective of the fracture mechanics field is exposed, which serves as an introduction to the more modern numerical methods. Following that, an overview of the different numerical methodologies applied to cracking simulation in solids is performed. In the last section, some conclusions are drawn regarding the pros and cons of the described methods and how the proposed methodology can contribute to improve the existing technology.

4.1 Early research in Fracture Mechanics

This section describes briefly the historical background of fracture mechanics, starting from the Griffiths works in the 1920s, to the Irwins stress factor theoretical concept and fracture criterion in the 1950s. Subsequently, the elastic-plastic fracture mechanics developments in the 1960s-1970s. Additionally, an historical introduction of the most used failure mechanisms and yield criteria is given.

Previously to the emergence of numerical methods, the theory of Linear Elastic Fracture Mechanics (LEFM) was the most used when assessing the ultimate strength of materials. LEFM is based on the analysis of cracks in isotropic linear elastic materials. Based on these assumptions, the stress field near the crack tip is calculated using the theory of elasticity. When the stresses near the crack front exceed the

material fracture toughness, the crack will propagate. The main limitation of this approach is that analytical expressions are only available in basic/simple geometries and the hypothesis that the inelastic deformation is small compared to the size of the crack, the so-called *small-scale yielding*.

The first contributions to the analysis of stress concentrations were made by Ernst Gustav Kirsch [Kir98] in 1898 with the development of a linear elastic solution for stresses around a hole in an infinite plate. The Kirsch's solution provided an estimation of the maximum stress along the plate that was compared with the yield stress in order to predict the failure of the sample. Since the linear elasticity assumption was used, different loading conditions were solved by applying superposition principles.

A major improvement of the Kirsch's was performed by Charles E. Inglis in 1913 by generalizing the stress distribution surrounding an ellipse [Ing13]. This new solution allowed to estimate the stress distribution to an infinite number of crack geometries according to ellipses with different aspect ratios. In the limit, this solution could overcome the calculation of an ellipse flattened to form a crack. Despite its great importance, the Inglis's solution was not immediately accepted since the stresses at the tip of the crack were infinite. Inglis's solution was correct and consistent with linear elasticity and with the assumption of the Hooke's law and no stress limitation. However, this singularity of stresses was a serious drawback since they could not be directly compared with the maximum stress of the material, which was the main interest of the industry at that time.

Alan Arnold Griffith's energy-based analysis of cracks in 1920 [Gri20] was a revolutionary development and solved the stress singularity of the Inglis's solution. This paper was basically his PhD work work at Cambridge University under the guidance of G. I. Taylor. It had been known before Griffiths work that the theoretical fracture strength of glass determined based on the breaking of atomic bonds exceeds the strength of laboratory specimens by one to two orders of magnitude. Griffith believed that this huge discrepancy could be due to microcracks in the glass and that these cracks could propagate under a load level that is much smaller than the theoretical strength [SJ12]. Unlike its predecessors, Griffith based its solution on an energy balance to determine the remaining strength of a cracked solid, which implied that the work done by an advancing crack surface must be equal to the energy stored in the newly created crack planes.

Despite its agreement with the experimental results in brittle materials, the Griffith theory failed to predict the maximum strength of metals, in which plastic deformations

develop around the crack tip. The limitation described was overcome by Orowan [Oro45] and Irwin [Irw57b]. Orowan and Irwin suggested to add an extra term regarding the plastic work due to the plastic deformation near the crack tip for ductile materials and in this way obtaining more realistic results.

Meanwhile, in 1939, Harold M. Westergaard [Wes39] developed a solution of stress distribution surrounding a sharp crack. Subsequently, Irwin improved the Westergaard approach and demonstrated that the displacements and stresses along the crack are related to the rate of crack growth. This relation is the so-called *stress intensity factor* [Irw57a] and it is one of the most useful and fundamental parameters in fracture mechanics. A few years later, Irwin [Irw58] introduced the well-known fracture modes that are used today: the Mode I (opening mode), Mode II (shear) and Mode III (tearing) and their corresponding stress intensity factor.

Simultaneously, Williams [Wil57] developed the asymptotic stress field near a crack tip. The Williams solution, with both symmetric and asymmetric terms, gives a universal expression for the crack tip stress field independent of external loads and crack geometries.

In the 1960s and 1970s much efforts were made with the objective of obtaining stress intensity factors for a wide variety of loading conditions and geometries. A complete compilation of this solutions are given in Tada et al. [TPI00] and Sih et al. [Sih73; KS75; Sih77]. However, the LEFM failed when the metal reaches a large-scale yielding conditions. In those cases a failure criteria based on plasticity of the cracked solid should be used. Irwin [Irw60] introduced a new effective stress intensity factor that took into account the crack tip plasticity effect. This new effective stress intensity factor is derived by adding to the original crack length the half of the plastic zone size.

With a different perspective of the problem with respect to the LEFM, the plasticity, damage, and combined plasticity-damage models emerged as a very powerful tool for predicting the onset and evolution of fracture in solids. In 1773, Charles-Augustin de Coulomb published an essay entitled *"Essai sur une application des règles des maximis et minimis à quelques problèmes de statique relatifs à l'architecture* [Cou73] in which introduced the first yield condition of solids, in this case applied to soils. Later, in the 19th century, Christian Otto Mohr generalized the Coulomb's work and the well-known Mohr-Coulomb yield surface was derived.

One century after the Coulomb's development, Henri Tresca [Tre68] formulated

the so-called Tresca yield surface after the detection of plastification in extruded metal samples submitted to shear stresses. At the same time, William John Macquorn Rankine published his work regarding the stress field solution that predicts active and passive earth pressures [Ran57] as well as in strength and equilibrium of solids [Ran68].

The first attempt of formulating a relationship between the stresses and plastic deformation was made by Saint-Venant in 1870. Saint-Venant work was based on plane strain conditions, Tresca yield surface and assumed that the work hardening was null. Additionally, Saint-Venant stated for the first time that the principal axes of the strain increment coincided with the principal stresses axes. At that time, the elastic strain was neglected son the plastic strain was equal to the total strain. in 1870, Lévy [Lév70] extrapolated the ideas of Saint-Venant to the 3D case. In 1913, independently from Lévy (the work of Lévy remained unknown outside his country at that time), Mises [Mis13] confirmed the isochoric formula from Lévy and the *Lévy-Mises theory of plasticity* was mathematically stated. This plasticity theory assumed that the elastic strain was very small and negligible. In addition, it assumed that the strain increment is coaxial with the stresses.

The Lévy equations were widely applied to metallic materials, where the elastic strain is negligible in comparison with the plastic strains. When the magnitude of the elastic strain is comparable to the plastic strain, the Lévy assumption of negligible elastic strain can result in significant error. This issue was overcome in the following years with the work of Ludwig Prandtl [Pra20], Heinrich Hencky [Hen23] and A. Reuss [Reu30]. In these cases, plastic strain was assumed as isochoric and the elastic deformation caused volume change.

With a similar mathematical foundation as plasticity, Kachanov [Kac58] established the basis of the damage models by identifying the reduction of the stiffness of the materials as a potential failure mechanism of structures. These damage models differentiate the behaviour of the effective undamaged material and the real damaged state. The principal assumption implies that the strain in the real and the effective space are equal whereas the stresses of the real space are dependend on the stresses in the undamaged or effective space (see Mazars and Lemaitre [ML85], Lemaitre [Lem85] and Chaboche [Cha88a; Cha88b]. Conversely, Simo and Ju [SJ87b; SJ87a] assumed that the stresses in the real and the fictitious space were equal and introduced the concept of effective strains. Later some plastic-damage combined models were developed like in Lubliner et al. [Lub+89].

In the 1960s, the plasticity, damage and the LEFM methodologies were a well established and mathematically consistent models when applied to cracking in solids. However, for general geometries and material properties, no analytical solutions were available. This limitation was overcome with the development of numerical methods like the finite element method, whose literature review is performed in the next sections.

4.2 Literature review

In the 1960s, an alternative to classical fracture mechanics appeared for the study of this discontinuous phenomenon. Thus, the *continuum mechanics* begins its development incorporating some concepts that had already been established in classical fracture mechanics. At the beginning, there was a lot of controversy since it was intended to represent an eminently discontinuous phenomenon using techniques based on the mechanics of continuous media. It was in 1967 when Scordelis and Ngo [NS67] opened this line of research. Thus, classical mechanics supported by numerical methods, such as the FEM (see Zienkiewicz, Zhu and Taylor [ZZT13]), have given way to one of the most consistent methodologies for the treatment of the fracture phenomenon. This formulation has made it possible to incorporate more sophisticated material behaviour models than those previously used. These models allow the treatment of complex stress states and the incorporation of coexisting phenomena such as fracture, plasticity, damage, time-dependent viscous phenomena, thermal problems, etc. All these advances are almost impossible to contain in a classical formulation of fracture mechanics and this is one of the reasons that have promoted the use of formulations within continuum mechanics.

Currently the problem is not completely solved but it can be said that, after several decades of the birth of the idea of approximating a discontinuous phenomenon using continuous numerically regularized techniques, a sufficient maturity has been reached that allows the subject of fracture to be treated using different numerical methodologies.

In this chapter, a review of the numerical methods used in fracture mechanics is performed. Generally, computational mechanics can be approached in two different categories: the *Continuum-based* and the *Discontinuum-based* methods. The *Continuum-based* methods discretize the computational domain into elements (finite elements in general cases) and the domain is treated as a single continuous entity

whose behaviour is controlled by a certain governing equation, material constitutive law, boundary and initial conditions.The most used Continuum-based numerical methods are the FEM, FD method, mesh-less methods, etc.

Conversely, the Discontinuum-based methods, which are relatively recent, model the continuum as a collection of discrete bodies (or elements) that can move, rotate and interact between them. In this case, the mathematical formulation of the balance principles and the law between particles must be defined. Distinct element method, lattice model and Bonded particle method are the most common Discontinuum-based methods. Finally, with the objective of taking advantage of the best features of the Continuum and Discontinuum base methods, combined methods and multi-scale methods emerged.

4.2.1 Continuum methods applied to cracking

Within the continuum methods, the FEM is one of the most popular and widely used methodology when treating with Partial Differential Equation (PDE). Depending on how the crack is treated, one can divide the continuum-based methods in Discrete Crack Approach (DCA) and the Smeared Crack Approach (SCA). In the DCA, the displacement field presents a discontinuity (strong discontinuity, see Fig. 4.1.a) along the crack. In this case, the fracture is represented by a line (in 2D) or a surface (in 3D) where the displacements exhibit a discontinuity and the strains are unbounded. This can be formulated by enriching the displacement field in the elements affected with discontinuous functions. Conversely, in the SCA the displacement and strain discontinuity is smeared over a transition region usually called localization-band (see Fig. 4.1.b). Note that the limit case of an Smeared approach where the localization-band width tends to be zero recovers the Discrete crack approach.

4.2.1.1 Discrete crack approach

One of the simplest methods to represents discrete cracks over the continuum is the Element Erosion Method (EEM) (Beissel and Popelar [BJP98], Rabczuk [Rab13] and Song [Son12]). This methods represented the topology of cracks by a set of deactivated/erased elements (Fig. 4.4). This element erosion can be performed through two approaches: (1) complete element erasion technique, in which the deleted elements are replaced by rigid masses and (2) setting the stresses of those elements to zero (Rabczuk [Rab13] and Song [Son12]).

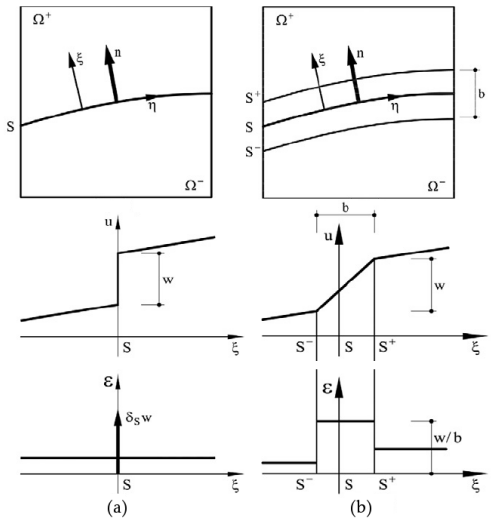

Figure 4.1: Discontinuities in a continuum (a) strong discontinuity (b) continuum smeared approach. Image from Cervera [Cer08b].

Another alternative was to create the cracks by separating elements that fulfilled a certain condition [Clo62; Nil68; NS67]. The crack, in this methodology, is represented by the element edges and an auxiliary set of nodes were added in order to obtain a discontinuous displacement field. This procedure is commonly known as the *nodal relaxation technique*. Another approach was the use of discrete interface elements to represent the crack path [GTB68; HMP76; Sch75]. This procedure has become very popular when analysing masonry structural failures.

The main drawback of these presented methodologies is the disability to prevent the indentation between the crack faces (except the interface elements method) of the erased elements and the intrinsic mesh dependency of the crack path. In order to overcome this problematic, several solutions were proposed. One of them was to use a mesh aligned with the expected crack path [Cen+00; Gál+02], which took advantage of the correct behaviour of the irreducible Galerkin discretization when the mesh is aligned with the crack. A second choice is to adapt the mesh to the topology of the crack when necessary (see Fig. 4.2.b). This procedure was introduced by Shepard et al. [She+85] and Wawrzynek and Ingraffea [WI89] and later improved by Bittencourt

et al. [Bit+96], Trädegård et al. [TNÖ98] and Bouchard et al. [Bou+00]. With this technique, the mesh is regenerated in the vicinity of the crack in order to better adapt the fracture path. The remeshing can lead to an increment of the computational cost due to the generation of the new mesh and the mapping of the nodal and integration points variables from the old mesh to the new one. Additionally, the re-meshing introduces a error when mapping the information between meshes and in terms of equilibrium. Indeed, previously to the remeshing the structure was in equilibrium but, after the mapping of the kinematics to the new mesh, the structure may not be in equilibrium according to the new element configuration.

For this reason, in order to avoid the use of remeshing techniques, a new way of describing the cracks within the elements (see Fig. 4.2.f) in an embedded approach was developed i.e. the Embedded Finite Element Method (EFEM). The first works in this direction were made by Johnson et al. [JS81]. In the following years, Dvorkin et al. [DCG90] introduced the crack discontinuities embedded within the elements. Many different modifications of the method were developed afterwards [AG96; KRS91; LRO93; OCM98], among others.

In the late 1990s, a new formulation known as the eXtended Finite Element Method (XFEM) was developed (Fig. 4.2.c). Belytschko and Black [BB99], Dolbow and Belytschko [DB99], Sukumar et al. [Suk+00; Suk+01] and Moës and Belytschko [MB02] introduced the idea of including a set of enhanced/enriched shape functions in the elements affected by the crack. This method requires the use of additional degrees of freedom at each affected nodes which are needed for the computation of the stresses near the crack front. This methodology was widely accepted since it does not require the use of a remeshing technique and, subsequently, many similar approaches were studied like the Partition of Unit Finite Element Method (PUFEM) [MB96; GS00] and the Generalized Finite Element Method (GFEM) [SBC00; Dua+01]. An extensive review of the different variations of the XFEM can be found in [AH08; BGV09; FB10; KX03].

Although this method was extensively used, had major limitations regarding the constitutive model at the discontinuity (traction-split law) which are not trivial to estimate. Additionally, an additional set of integration rules were necessary to consider the enriched element. Finally, the reliability of the XFEM depends on the correct prediction of the crack path and, subsequently, on the propagation direction criterion adopted. Thus, an additional *tracking technique* is necessary in order to know the elements to be enriched (see Fig. 4.3). This is why the XFEM formulation becomes more complex

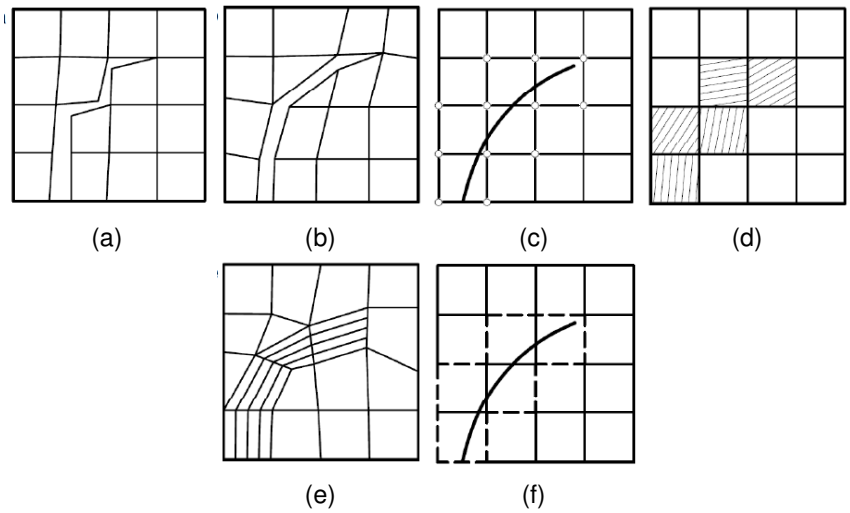

Figure 4.2: Different crack modelling in discrete approaches. a) Discrete strong discontinuity b) Remeshed strong discontinuity c) Embedded strong discontinuity d) Discrete weak discontinuity e) Remeshed weak discontinuity and f) Embedded weak discontinuity. Image from Cervera et al. [CC06a].

and computationally expensive with multiple crack initiation and evolution. In addition, the crack branching/merging cannot be followed consistently in order to model the geometry separation and fragmentation.

4.2.1.2 Smeared crack approach

An alternative to the DCA is the so-called smeared crack approach. This model was initially proposed by Rashid [Ras68] and it describes the crack path by a band of elements whose displacements field is continuous and its strain field discontinuous but bounded. Fig. 4.2.d shows the finite elements band affected by the weak discontinuities. This approach is based on the definition of a constitutive law that states a relationship between the stresses and strains and the localization is induced by a stress softening. An advantage of this methodology is that the mesh topology is never changed and the crack is intrinsically taken into account in a constitutive way. Therefore, a numerous variety of constitutive models were developed as in Bazant and Cedolin [BC79], Lubliner et al. [Lub+89], Rots et al. [Rot+85], Cervera et al. [Cer+90; COF95], Oliver et al. [Oli+90], etc.

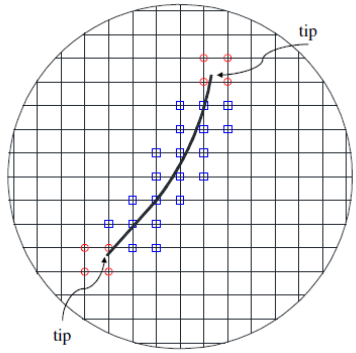

Figure 4.3: Crack growth in XFEM. Red nodes are front enriched and the blue nodes are Heaviside enrichment. Image from Mohammadnejad et al. [Moh+18].

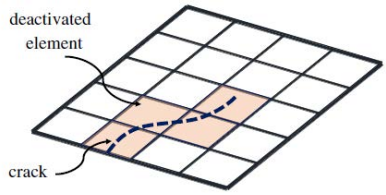

Figure 4.4: Element Erosion Method, schematic illustration. Image from Mohammadnejad et al. [Moh+18].

The SCA was very popular but after some years of its adoption Pietruszczak and Mroz [PM81] and Bazant and Oh [BO83] noticed that the fracture process is not only dependant on the fracture energy, but also on the characteristic length of the mesh analysed. This issue provokes that the finer the mesh is, the more brittle the behaviour is, which was an unacceptable inconsistency.

In order to overcome this limitation, the stress-strain relationships were reformulated into a *characteristic-length* regularized models. In this way, the mesh-objectivity problem was solved. Hereinafter, the mesh-bias dependency of the method became an important issue. One of the solutions was to use again remeshing techniques (see Zienkiewicz et al. [ZH90; ZHP95]) in order to improve the quality and orientation of the mesh (Fig. 4.2.e).

Another approach consists in the enrichment of the strain field in order to capture the kinematic singularities near the cracks. The Enhanced Assumed Strain Method (EASM) was initially developed by Ortiz et al. [OLN87] and Belytschko et al. [BFE88] and proposed to enrich the strain field by means of including an additional incompatible deformation modes to the cracked elements. More recent approaches based the strain enrichment on splitting the strains into elastic and inelastic strains, like the Mesh Corrected Crack Model (MCCM) formulated by Cervera et al. [Cer08b; Cer08a]. Must be said that this kind of strain enhancements, when extrapolated to 2D and 3D geometries, it is complex to regularise the displacement jump over the affected elements and, in some cases, numerical instabilities and ill-conditioning arise.

As has been exposed for the DCA (Section 4.2.1.1), tracking algorithms can improve the mesh-independence and efficiently improve the crack propagation analysis. This methodology was introduced into the SCA by Cervera and Chiumenti [CC06a; CC06b] with the objective is preselecting the elements that are damaged by means of a certain criterion.

After analysing the previous approaches used in fracture mechanics, it is clear that the standard irreducible Galerkin formulations are unable to ensure the local convergence of stresses, especially at singular points. This is why methodologies like the EFEM and the XFEM needs the support of tracking techniques, which are not variationally consistent, in order to perform correctly.

These inconvenients encouraged, in the mid 1960s, the use of mixed formulations whose aim was to mitigate the mesh-dependency and the discretization error. These approaches consist in solving the Initial Boundary Value Problem (IBVP) with an addi-

tional set of nodal unknowns (pressure, strain, stress, etc.). Mixed formulations are commonly used in fluid dynamics, especially in incompressible conditions. However, in solids, were only used in strain localization problems like in Zienkiewicz et al. [ZHP95] and Pastor et al. [Pas+99]. More recently, several mixed formulations have been proposed like the mixed pressure-displacement formulations [Cer03; CCS04; Chi+02; Chi+04; SSH07], stress-displacement [CCC10; CC10] and strain-displacement formulations [BCC15; BCC16; Cer+15; CCC10; CBC17; CCC11].

Despite its greater accuracy, there are some concerns regarding the mixed formulations: since it is required to solve multiple unknowns, they are considerably more expensive than the standard formulations; Additionally, in the monolytical schemes, since the matrix can be ill-conditioned, only direct linear solvers can be employed. This can be solved by implementing an staggered scheme as has been done in [Don+82; Cod11; FOC15]. Besides that, the finite strain kinematics in mixed formulations have not yet been completely explored, which is an important limitation, especially for the kind of practical problems simulated in this work.

4.2.1.3 Regularized smeared crack approach

In the recent years, a powerful alternative to the aforementioned methods has been developed: the variational Phase Field (PF) approach [Li+17; Sar+17; Kli+15; KSM15; KM15; UHM13]. This methodology is mathematically based on the thermodynamics equations and evaluates the fracture problem using the energy minimization principles. The phase field method does not represent the crack as a geometrical discontinuity. Instead, it represents the cracked material in an smooth way, controlled by a order parameter termed phase-field variable. This approach can recover the Griffith's theory as a limit case but requires the definition of an internal length (different from the characteristic length from the element) in which the degradation is located as an highly refined mesh within this zone to properly capture the degradation gradient. The PF approach can easily deal with complex crack patterns with no remeshing nor tracking technique but, conversely, requires a very fine mesh in the localization zone (can be seen in Fig. 4.5) and suffers from the inability to model detachment and separation of the domain. Therefore, the PF method is currently limited to crack initiation and propagation.

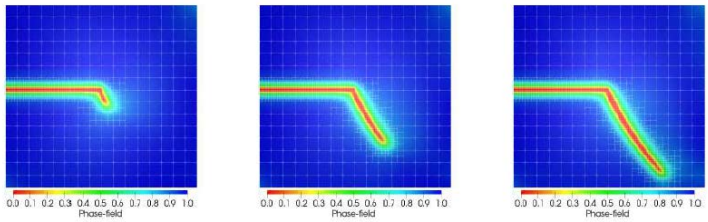

Figure 4.5: PF crack evolution. Image from Nagaraja et al. [Nag+19].

4.2.2 Mesh-Free methods

With the objective of avoiding the limitations of the continuum-based methods, a new mesh-free methodologies arised. These mesh-free approaches employ a system of nodes and a different sets of external and internal boundaries in order to model the solid. Due to its mesh-less approach, it is notably advantageous when simulating large deformations, free-surface flows and FSI.

Mesh-free methods can be classified in two main categories: the methods based on the definition of a global weak form, which requires a background mesh; and the methods based on a local weak form and requiring the predefinition of a set of particles acting as mass. One of the most popular mesh-free methods is the so-called Smoothed Particle Hydrodynamics (SPH) [GM77; Luc77], which belong to the second group. In these methodologies (see more recent developments in [Bui+08; Pas+09; Non+15]), the domain is discretized by a set of interpolating points (or particles) with constant material coordinates. The SPH particles carry the information of the mass of the continuum and the physical properties information of the problem. In this way, the PDE is discretized employing a collocation technique which not only leads to an smoothly discretized PDE, but also defines an interpolation scheme between the SPH particles.

Even though the SPH has been extensively used in computational mechanics, this method suffers from inconsistency and, in practical problems, high computational cost. Indeed, SPH presents tensile instability, lack of consistency when interpolating, boundary conditions difficulties, among other problems.

A powerful alternative to the SPH, is the Material Point Method (MPM) [Har64; SZS95; SCS94]. The MPM represents the solid domain as a set of Lagrangian

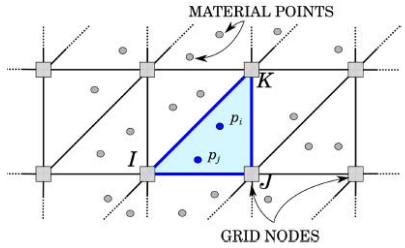

Figure 4.6: MPM schematic illustration. The interpolation functions on the material/-particle point p_i are evaluated using the FE shape function of the I-J-K element. Image from Iaconeta et al. [Iac19].

particles, called *material points*, with the complementary use of a mesh, commonly named *background grid*, as can be seen in Fig. 4.6. Unlike in the SPH, standard boundary conditions can be applied easily and it does not suffer from tensile instability. This methodology allows to model the deformation of the domain and track the historical information at each time step without mapping errors, typically committed when using remeshing techniques. This encourages the use of the MPM for the simulation of large deformations in solids and the use of complex constitutive laws. However, the MPM is not free of numerical flaws. Indeed, since the shape functions used are linear, the gradients are discontinuous. This generates a cell-crossing error when a material point on the cell boundary is not represented by the local shape functions of the neighbouring cells.

4.2.3 Discontinuum methods

The Discontinuum methods discretize the solid domain as a set of particles that interact and can move and rotate according to the Newton's law. The most used Discontinuum methods are the Distinct Element Method and the Bonded Particle Method (BPM), all of them based on the prior work of Cundall and Strack [CS79].

The Distinct Element Method divides the discontinuous medium in rigid discrete elements that move, rotate, contact and separate based on a contact constitutive law [Bob+09; JS07]. With this method, crack is created and grow along the edges of blocks when a certain stress threshold is reached.

Another option is the BPM [Cel+17; Cel+19]. In this approaches, the discrete

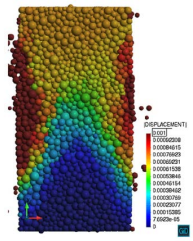

Figure 4.7: Uniaxial compression test simulated with the BPM. Image from Celigueta et al. [Cel+19].

elements can be understood as a discretization method. Indeed, the BPM divides the domain into circular (2D) and spherical (3D) elements (see Fig. 4.7) that are bonded by a cohesive force, according to Newton's second law. The inherent ability of the BPM to reproduce multi-cracking, branching and merging and large displacements encourages its use. However, the difficulty of calibrating the material properties of the discrete elements in order to obtain a macro Young modulus and Poisson ratio (simulate continuum elasticity) reduces its generality for practical problems (Celigueta et al. [Cel+19; Cel+17] works diminished the effect of this limitation). Additionally, since the BPM uses an explicit time scheme, the required time step must be very small in comparison with the implicit schemes (4 o 5 order of magnitude larger), which increases the computational cost.

Part II bibliography

[AG96] F. Armero and K. Garikipati. “An analysis of strong discontinuities in multiplicative finite strain plasticity and their relation with the numerical simulation of strain localization in solids”. *International Journal of Solids and Structures 33*. Vol. 22-23, pp. 2863–2885 , 1996.

[AH08] Y. Abdelaziz and A. Hamouine. “A survey of the extended finite element”. *Computers and Structures 86*. Vol. 11-12, pp. 1141–1151 , 2008.

[Bar+19] LG. Barbu et al. “Methodology for the analysis of post-tensioned structures using a constitutive serial-parallel rule of mixtures: large scale non-linear analysis”. *Composite Structures*. Vol. 216, pp. 315–330 , 2019.

[BB99] T. Belytschko and T. Black. “Elastic crack growth in finite elements with minimal remeshing”. *International journal for numerical methods in engineering*. Vol. 45(5), pp. 601–620 , 1999.

[BC79] Z.P. Bazant and L. Cedolin. “Blunt crack band propagation in finite element analysis”. *Journal of the Engineering Mechanics Division*. Vol. 105(2), pp. 297–315 , 1979.

[BCC15] L. Benedetti, M. Cervera, and M. Chiumenti. “Stress-accurate Mixed FEM for soil failure under shallow foundations involving strain localization in plasticity”. *Computers and Geotechnics*. Vol. 64, pp. 32–47 , 2015.

[BCC16] L. Benedetti, M. Cervera, and M. Chiumenti. “High-fidelity prediction of crack formation in 2D and 3D pullout tests”. *Computers & Structures*. Vol. 172, pp. 93–109 , 2016.

[BFE88] T. Belytschko, J. Fish, and B. E. Engelmann. “A finite element with embedded localization zones”. *Computer Methods in Applied Mechanics and Engineering 70*. Vol. 1, pp. 59–89 , 1988.

[BGV09] T. Belytschko, R. Gracie, and G. Ventura. “A review of extended/generalized finite element methods for material modeling”. *Modelling and Simulation in Materials Science and Engineering 17*. P. 043001 , 2009.

[Bit+96] T. N. Bittencourt et al. “Quasi-automatic simulation of crack propagation for 2D lefm problems”. *Engineering Fracture Mechanics*. Vol. 55, pp. 321–334 , 1996.

[BJP98] S. R. Beissel, G. R. Johnson, and C.H. Popelar. “An element-failure algorithm for dynamic crack propagation in general directions”. *Engineering Fracture Mechanics*. Vol. 61, pp. 407–425 , 1998.

[BO83] Z.P. Baant and B.H. Oh. “Crack band theory for fracture of concrete”. *Matériaux et construction*. Vol. 16, pp. 155–177 , 1983.

[Bob+09] A. Bobet et al. “Numerical models in discontinuous media: Review of advances for rock mechanics applications”. *Journal of Geotechnical and Geoenvironmental Engineering*. Vol. 135(11), pp. 1547–1561 , 2009.

[Bou+00] P.O. Bouchard et al. “Crack propagation modelling using an advanced remeshing technique”. *Computer methods in applied mechanics and engineering*. Vol. 189, pp. 723–742 , 2000.

[Bui+08] H. H. Bui et al. “Lagrangian meshfree particles method (sph) for large deformation and failure flows of geomaterial using elasticplastic soil constitutive model”. *International Journal for Numerical and Analytical Methods in Geomechanics*. Vol. 32(12), pp. 1537–1570 , 2008.

[CBC17] M. Cervera, G.B. Barbat, and M. Chiumenti. “Finite element modelling of quasi-brittle cracks in 2D and 3D with enhanced strain accuracy”. *Computational Mechanics*. Vol. 60, pp. 767–796 , 2017.

[CC06a] M. Cervera and M. Chiumenti. “Mesh objective tensile cracking via a local continuum damage model and a crack tracking technique”. *Computer Methods in Applied Mechanics and Engineering*. Vol. 196(1), pp. 304–320 , 2006.

[CC06b] M. Cervera and M. Chiumenti. “Smeared crack approach: back to the original track”. *International journal for numerical methods in engineering*. Vol. 12, pp. 1173–1199 , 2006.

[CC10] M. Cervera M. Chiumenti and R. Codina. “Mixed stabilized finite element methods in nonlinear solid mechanics. Part II: Strain localization”. *Computer Methods in Applied Mechanics and Engineering*. Vol. 37-40, pp. 2571–2589 , 2010.

[CCC10] M. Cervera, M. Chiumenti, and R. Codina. “Mixed stabilized finite element methods in nonlinear solid mechanics. Part I: Formulation”. *Computer Methods in Applied Mechanics and Engineering*. Vol. 37-40, pp. 2559–2570 , 2010.

[CCC11] M. Cervera, M. Chiumenti, and R. Codina. “Mesh objective modeling of cracks using continuous linear strain and displacement interpolations”. *Int. J. Numer. Meth. Engng*. Vol. 87, pp. 962–987 , 2011.

[CCS04] M. Cervera, M. Chiumenti, and C. Agelet de Saracibar. “Shear band localization via local J2 continuum damage mechanics”. *Computer Methods in Applied Mechanics and Engineering*. Vol. 9-11, pp. 849–880 , 2004.

[Cel+17] MA. Celigueta et al. “Accurate modelling of the elastic behavior of a continuum with the Discrete Element Method”. *Computational Mechanics*. Vol. 60, pp. 997–1010 , 2017.

[Cel+19] MA. Celigueta et al. “An accurate nonlocal bonded discrete element-method for nonlinear analysis of solids: application to concrete fracture tests”. *Comp. Part. Mech.* , 2019.

[Cen+00] D. A. Cendón et al. “Modelling the fracture of concrete under mixed loading”. *International journal of fracture*. Vol. 103, pp. 293–310 , 2000.

[Cer+15] M. Cervera et al. “Mixed stabilized finite element methods in nonlinear solid mechanics. Part III: Compressible and incompressible plasticity”. *Computer Methods in Applied Mechanics and Engineering*. Vol. 285, pp. 752–775 , 2015.

[Cer+90] M. Cervera et al. “A computational model for progressive cracking in large dams due to the swelling of concrete”. *Engineering Fracture Mechanics*. Vol. 35(1), pp. 573–585 , 1990.

[Cer03] M. Cervera. *Viscoelasticity and Rate-dependent Continuum Damage Models*. Monography N-79.CIMNE, Barcelona. 2003.

[Cer08a] M. Cervera. “A smeared-embedded mesh-corrected damage model for tensile cracking”. *International journal for numerical methods in engineering*. Vol. 76(12), pp. 1930–1954 , 2008.

[Cer08b] M. Cervera. “An orthotropic mesh corrected crack model”. *Computer Methods in Applied Mechanics and Engineering*. Vol. 197, pp. 1603–1619 , 2008.

[Cha88a] J.L. Chaboche. “Continuum Damage Mechanics: Part I General Concepts”. *Journal of Applied Mechanics*. Vol. 55(1), pp. 59–64 , 1988.

[Cha88b] J.L. Chaboche. “Continuum damage mechanics: Part II Damage growth, crack initiation, and crack growth”. *Journal of Applied Mechanics*. Vol. 55(1), pp. 65–72 , 1988.

[Chi+02] M. Chiumenti et al. “A stabilized formulation for incompressible elasticity using linear displacement and pressure interpolations”. *Computer Methods in Applied Mechanics and Engineering*. Vol. 46, pp. 5253–5264 , 2002.

[Chi+04] M. Chiumenti et al. “A stabilized formulation for incompressible plasticity using linear triangles and tetrahedra”. *International Journal of Plasticity*. Vol. 8-9, pp. 1487–1504 , 2004.

[Clo62] R. Clough. “The stress distribution of Norfork Dam”. *Structures and Materials Research*. Vol. 100, pp. 1–108 , 1962.

[Cod11] R. Codina. “Pressure stability in fractional step finite element methods for incompressible flows”. *Journal of Computational Physics*. Vol. 170(1), pp. 112–140 , 2011.

[COF95] M. Cervera, J. Oliver, and R. Faria. “Seismic evaluation of concrete dams via continuum damage models”. *Earthquake Engineering and Structural Dynamics*. Vol. 24(9), pp. 1225–1246 , 1995.

[Cor+18] A. Cornejo et al. “Methodology for the analysis of post-tensioned structures using a constitutive serial-parallel rule of mixtures”. *Composite Structures*. Vol. 200, pp. 480–497 , 2018.

[Cor+19] A. Cornejo et al. “Combination of an adaptive remeshing technique with a coupled FEM-DEM approach for analysis of crack propagation problems”. *Computational Particle Mechanics*. Pp. 1–18 , 2019.

[Cou73] C.A. Coulomb. “Essai sur une application des règles de maximis et de minimis à quelques problèmes de Statique relatifs à lArchitecture”. . , 1773.

[CS79] P.A. Cundall and O.D.L. Strack. “A discrete numerical model for granular assemblies”. *Geotechnique*. Vol. 29, pp. 47–65 , 1979.

[DB99] J. Dolbow and T. Belytschko. “A finite element method for crack growth without remeshing”. *International journal for numerical methods in engineering*. Vol. 46(1), pp. 131–150 , 1999.

[DCG90] E. N. Dvorkin, A. M. Cuitiño, and G. Gioia. “Finite elements with displacement interpolated embedded localization lines insensitive to mesh size and distortions”. *Numerical Methods in Engineering 30*. Vol. 3, pp. 541–564 , 1990.

[Don+82] J. Donea et al. “Finite element solution of the unsteady Navier-Stokes equations by a fractional step method”. *Computer Methods in Applied Mechanics and Engineering*. Vol. 30(1), pp. 53–73 , 1982.

[Dua+01] C. A. Duarte et al. “Generalized finite element method for the simulation of three-dimensional dynamic crack propagation”. *Computer Methods in Applied Mechanics and Engineering*. Vol. 190(15), pp. 2227–2262 , 2001.

[FB10] T.P. Fries and T. Belytschko. “The extended/generalized finite element method: An overview of the method and its applications”. *International Journal for Numerical Methods in Engineering 84*. Vol. 3, pp. 253–304 , 2010.

[FOC15] A. Franci, E. Oñate, and J.M. Carbonell. *Unified Lagrangian formulation for fluid and solid mechanics, fluid-structure interaction and coupled thermal problems using the PFEM*. 2015.

[Gál+02] J. C. Gálvez et al. “A discrete crack approach to normal/shear cracking of concrete”. *Cement and Concrete Research 32*. Vol. 10, pp. 1567–1585 , 2002.

[GM77] R.A. Gingold and J.J. Monaghan. “Smoothed particle hydrodynamics-theory and application to non-spherical stars”. *Monthly Notices of the Royal Astronomical Society*. Vol. 181, pp. 375–389 , 1977.

[Gri20] A.A. Griffith. “The phenomena of rupture and flow in solids”. *Philos Trans R Soc Lond*. Pp. 163–198 , 1920.

[GS00] M. Griebel and M. A. Schweitzer. “A particle-partition of unity method for the solution of elliptic, parabolic, and hyperbolic pdes”. *SIAM Journal on Scientific Computing*. Vol. 22(3), pp. 853–890 , 2000.

[GTB68] R. Goodman, R. Taylor, and T. Brekke. “A model for the mechanics of jointed rock”. *Journal of Soil Mechanics & Foundations Div 94*. Vol. 3, pp. 637–659 , 1968.

[Har64] FH. Harlow. “The particle-in-cell computing method for fluid dynamics”. *Methods for Computational Physics*. Vol. 3, pp. 319–343 , 1964.

[Hen23] H. Hencky. “Über einige statisch bestimmte fälle des gleichgewichts in plastischen körpern”. *ZAMM-Journal of Applied Mathematics and Mechanics/Zeitschrift für Angewandte Mathematik und Mechanik*. Vol. 3(4), pp. 241–251 , 1923.

[HMP76] A. Hillerborg, M. Modéer, and P.E. Petersson. “Analysis of crack formation and crack growth in concrete by means of fracture mechanics and finite elements”. *Cement and Concrete Research*. Vol. 6, pp. 773–781 , 1976.

[Iac19] I. Iaconeta. *Discrete-continuum hybrid modelling of flowing and static regimes*. Universitat Politècnica de Catalunya, PhD Thesis. 2019.

[Ing13] C.E. Inglis. “Stresses in Plates Due to the Presence of Cracks and Sharp Corners”. *Transactions of the Institute of Naval Architects*. Vol. 55, pp. 219–241 , 1913.

[Irw57a] G.R. Irwin. “Analysis of Stresses and Strains Near the End of a Crack Traversing a Plate”. *Journal of Applied Mechanics*. Vol. 24, pp. 361–364 , 1957.

[Irw57b] G.R. Irwin. “Fracture dynamics”. *Fracture of Metals, ASM, Cleveland, OH*. Pp. 147–166 , 1957.

[Irw58] G.R. Irwin. “Fracture”. *Handbook der Physik 6*. Pp. 551–590 , 1958.

[Irw60] G.R. Irwin. “Plastic zone near a crack and fracture toughness”. *Proceedings of the 7th Sagamore Ordnance Materials Conference, Syracuse University,*. Pp. IV-63-IV–78 , 1960.

[Jim+20] S. Jimenez et al. “Analysis of the mock-up of a reactor containment building: comparison with experimental results”. *Nuclear Engineering and Design*. Vol. 359, p. 110454 , 2020.

[JS07] L. Jing and O. Stephansson. *Numerical models in discontinuous media: Review of advances for rock mechanics applications*. Amsterdam: Elsevier. 2007.

[JS81] C. Johnson and R. Scott. “A Finite Element Method for Problems in Perfect Plasticity Using Discontinuous Trial Functions”. *Nonlinear Finite Element Analysis in Structural Mechanics*. Pp. 307–324 , 1981.

[Kac58] L.M. Kachanov. “Time of the rupture process under creep conditions”. *Isv. Akad. Nauk. SSR. Otd Tekh. Nauk*. Vol. 8, pp. 26–31 , 1958.

[Kir98] E.G. Kirsch. “Die Theorie der Elastizität und die Bedürfnisse der Festigkeitslehre”. *Zeitschrift des Vereines deutscher Ingenieure*. Vol. 42, pp. 797–807 , 1898.

[Kli+15] M. Klinsmann et al. “An assessment of the phase field formulation for crack growth”. *Computer Methods in Applied Mechanics and Engineering*. Vol. 294, pp. 313–330 , 2015.

[KM15] C. Kuhn and R. Müller. “A phase field model for fracture”. *PAMM*. Vol. 8(1), pp. 10223–10224 , 2015.

[KRS91] M. Klisinski, K. Runesson, and S. Sture. “Finite element with inner softening band”. *Journal of engineering mechanics 117*. Vol. 23, p. 575 , 1991.

[KS75] M.K. Kassir and G.C. Sih. *Mechanics of Fracture Vol. 2: Three-Dimensional Crack Problems*. Leyden, Noordhoff International Pub. 1975.

[KSM15] C. Kuhn, A. Schlüter, and R. Müller. “On degradation functions in phase field fracture models”. *Computational Materials Science*. Vol. 108, pp. 374–384 , 2015.

[KX03] B. L. Karihaloo and Q. Z. Xiao. “Modelling of stationary and growing cracks in FE framework without remeshing: A state-of-the-art review”. *Computers and Structures 81*. Pp. 119–129 , 2003.

[Lem85] J. Lemaitre. “A continuous damage mechanics model for ductile fracture”. *Journal of engineering materials and technology*. Vol. 107(1), pp. 83–89 , 1985.

[Lév70] M. Lévy. *Mémoire sur les équations générales des mouvements intérieurs des corps solides ductiles au delà des limites où lélasticité pourrait les ramener à leur premier état*. Comptes Rendus de lAcadémie des Sciences. 1870.

[Li+17] Y. Li et al. “Applications of the phase field method in predicting microstructure and property evolution of irradiated nuclear materials”. *Computational Materials*. Vol. 3(1), p. 11 , 2017.

[LRO93] R. Larsson, K. Runesson, and N. S. Ottosen. “Discontinuous displacement approximation for capturing plastic localization”. *International Journal for Numerical Methods in Engineering 36*. Vol. 12, pp. 2087–2105 , 1993.

[Lub+89] J. Lubliner et al. “A plastic-damage model for concrete”. *International Journal of solids and structures*. Vol. 25(3), pp. 299–326 , 1989.

[Luc77] L. B. Lucy. “A numerical approach to the testing of the fission hypothesis”. *The Astronomical Journal*. Vol. 82, pp. 1013–1024 , 1977.

[MB02] N. Moës and T. Belytschko. “Extended finite element method for cohesive crack growth”. *Engineering fracture mechanics*. Vol. 69(7), pp. 813–833 , 2002.

[MB96] J. M. Melenk and I. Babuka. “The partition of unity finite element method: basic theory and applications”. *Computer methods in applied mechanics and engineering*. Vol. 139(1-4), pp. 289–314 , 1996.

[Mis13] R. Von Mises. “Mechanik der festen Körper im plastisch-deformablen Zustand”. *Nachrichten von der Gesellschaft der Wissenschaften zu Göttingen, Mathematisch-Physikalische Klasse*. 1913:582–592 , 1913.

[ML85] J. Mazars and J. Lemaitre. “Application of continuous damage mechanics to strain and fracture behavior of concrete”. *Application of Fracture Mechanics to Cementitious Composites*. Pp. 507–520 , 1985.

[Moh+18] M. Mohammadnejad et al. “An overview on advances in computational fracture mechanics of rock”. *Geosystem Engineering*. Pp. 1–24 , 2018.

[Nag+19] S. Nagaraja et al. “Phase-Field modelling of brittle fracture with multi-level hp-FEM and the finite cell method”. *Computational Mechanics*. Vol. 63, pp. 1283–1300 , 2019.

[Nil68] A.H. Nilson. “Nonlinear Analysis of Reinforced Concrete by the Finite Element Method”. *ACI Journal 65*. Vol. 9, pp. 757–766 , 1968.

[Non+15] H. Nonoyama et al. “Slope stability analysis using smoothed particle hydrodynamics (sph) method”. *Soils and foundations*. Vol. 55(2), pp. 458–470 , 2015.

[NS67] D. Ngo and A. Scordelis. “Finite element analysis of reinforced concrete beams”. *Journal of the American Concrete Institute*. Vol. 64(14), pp. 152–163 , 1967.

[OCM98] J. Oliver, M. Cervera, and O. Manzoli. “The Use of Strain-Softening models for the Simulation of Strong Discontinuities in Solids”. *Material Instabilities in Solids*. Pp. 104–123 , 1998.

[Oli+90] J. Oliver et al. “Isotropic damage models and smeared crack analysis of concrete”. *Second international conference on Computer Aided Analysis and Design of Concrete Structures*. , 1990.

[OLN87] M. Ortiz, Y. Leroy, and A. Needleman. “A finite element method for localized failure analysis”. *Computer Methods in Applied Mechanics and Engineering 61*. Vol. 2, pp. 189–214 , 1987.

[Oro45] E. Orowan. “Notch brittleness and strength of metals”. *Trans. Inst. Engrs Shipbuilders in Scotland*. Vol. 89, pp. 165–215 , 1945.

[Pas+09] M. Pastor et al. “A depth-integrated, coupled sph model for flow-like landslides and related phenomena”. *International Journal for numerical and analytical methods in geomechanics*. Vol. 33(2), pp. 143–172 , 2009.

[Pas+99] M. Pastor et al. “Stabilized low-order finite elements for failure and localization problems in undrained soils and foundations”. *Computer Methods in Applied Mechanics and Engineering*. Vol. 1-2, pp. 219–234 , 1999.

[PM81] S.T. Pietruszczak and Z. Mroz. “Finite element analysis of deformation of strain-softening materials”. *International Journal for Numerical Methods in Engineering*. Vol. 17, pp. 327–334 , 1981.

[Pra20] L. Prandtl. “Über die härte plastischer körper”. *Nachrichten von der Gesellschaft der Wissenschaften zu Göttingen, Mathematisch-Physikalische Klasse*. Pp. 74–85 , 1920.

[Rab13] T. Rabczuk. “Computational methods for fracture in brittle and quasi-brittle solids: State-of-the-art review and future perspectives”. *Applied Mathematics*. P. 38 , 2013.

[Ran57] W.J.M. Rankine. *On the stability of loose earth*. 1857.

[Ran68] W.J.M. Rankine. *Manual of Applied Mechanics*. Griffin, London. 1868.

[Ras68] Y.R. Rashid. “Ultimate strength analysis of prestressed concrete pressure vessels”. *Nuclear Engineering and Design*. Vol. 7, pp. 334–344 , 1968.

[Reu30] A. Reuss. “Berücksichtigung der elastischen Formänderung in der Plastizitätstheorie”. *ZAMM-Journal of Applied Mathematics and Mechanics/Zeitschrift für Angewandte Mathematik und Mechanik*. Vol. 10(3), pp. 266–274 , 1930.

[Ros97] H.P. Rossmanith. “The struggle for recognition of engineering fracture mechanics”. *Fracture Research in Retrospect*. Pp. 37–94 , 1997.

[Rot+85] J. G. Rots et al. “Smeared crack approach and fracture localization in concrete”. *HERON, 30*. Vol. 10, , 1985.

[Sar+17] J. M. L. Sargado et al. “High-accuracy phase-field models for brittle fracture based on a new family of degradation functions”. *Journal of the Mechanics and Physics of Solids*. Vol. 111, pp. 458–489 , 2017.

[SBC00] T. Strouboulis, I. Babuka, and K. Copps. “The design and analysis of the generalized finite element method”. *Computer methods in applied mechanics and engineering*. Vol. 181(1), pp. 43–69 , 2000.

[Sch75] H. Schäfer. “A contribution to the solution of contact problems with the aid of bond elements”. *Computer Methods in Applied Mechanics and Engineering*. Vol. 6, pp. 335–353 , 1975.

[SCS94] D. Sulsk, Z. Chen, and H.L. Schreyer. “A particle method for history-dependent materials”. *Computer Methods in Applied Mechanics and Engineering*. Vol. 118(1-2), pp. 179–196 , 1994.

[She+85] M. S. Shephard et al. “Automatic crack propagation tracking”. *Computers and Structures*. Vol. 20, pp. 211–223 , 1985.

[Sih73] G.C. Sih. *Mechanics of Fracture Vol. 1: Methods of Analysis and Solutions of Crack Problems*. Leyden, Noordhoff International Pub. 1973.

[Sih77] G.C. Sih. *Mechanics of Fracture Vol. 3: Plates and Shells with Cracks*. Leyden, Noordhoff International Pub. 1977.

[SJ12] C.T. Sun and Z.H. Jin. *Fracture Mechanics*. Elsevier. 2012.

[SJ87a] J. C. Simo and Ju. “Strain-and stress-based continuum damage models II. Computational aspects”. *International journal of solids and structures*. Vol. 23(7), pp. 841–869 , 1987.

[SJ87b] J.C. Simo and Ju. “Strain-and stress-based continuum damage models I. Formulation”. *International journal of solids and structures*. Vol. 23(7), pp. 821–840 , 1987.

[Son12] J.H. Song. *Computations of the dynamic fracture of quasi-brittle plane and shell structures by the extended finite element method. Evanston*. Northwestern University. 2012.

[SSH07] P. J. Sánchez, V. E. Sonzogni, and A. E. Huespe. “Study of a stabilized mixed finite element with emphasis on its numerical performance for strain localization problems”. *Communications in Numerical Methods in Engineering 24*. Vol. 4, pp. 297–320 , 2007.

[Suk+00] N. Sukumar et al. “Extended finite element method for three-dimensional crack modelling”. *International journal for numerical methods in engineering*. Vol. 48(11), pp. 1549–1570 , 2000.

[Suk+01] N. Sukumar et al. “Modeling holes and inclusions by level sets in the extended finite-element method”. *Computer methods in applied mechanics and engineering*. Vol. 190(46), pp. 6183–6200 , 2001.

[SZS95] D. Sulsky, S.J. Zhou, and H. L. Schreyer. “Application of a particle-in-cell method to solid mechanics”. *Computer Physics Communications*. Vol. 87(1-2), pp. 236–252 , 1995.

[TNÖ98] A. Trädegård, F. Nilsson, and S. Östlund. “Fem-remeshing technique applied to crack growth problems”. *Computer Methods in Applied Mechanics and Engineering*. Vol. 160, pp. 115–131 , 1998.

[TPI00] H. Tada, P.C. Paris, and G.R. Irwin. *The Stress Analysis of Cracks Handbook*. ASME Press. 2000.

[Tre68] H. Tresca. *Mémoire sur lecoulement des corps solides*. volume 18 of Mémoires présentés par divers savants á lInstitut impérial de France. 1868.

[UHM13] H. Ulmer, M. Hofacker, and C. Miehe. “Phase field modeling of brittle and ductile fracture”. *PAMM*. Vol. 13(1), pp. 533–536 , 2013.

[Wel55] A.A. Wells. “The condition of fast fracture in aluminum alloys with particularly reference to Comet failures”. *British Welding Research Association Report*. , 1955.

[Wes39] H.M. Westergaard. “Bearing Pressures and Cracks”. *Journal of Applied Mechanics*. Vol. 6, pp. 49–53 , 1939.

[WI89] P. A. Wawrzynek and A. R. Ingraffea. “An interactive approach to local remeshing around a propagating crack”. *Finite Elements in Analysis and Design*. Vol. 5, pp. 87–96 , 1989.

[Wil57] M.L. Williams. “On the stress distribution at the base of a stationary crack”. *J. Appl. Mech*. Vol. 24, pp. 109–114 , 1957.

[ZCO18] F. Zárate, A. Cornejo, and E. Oñate. “A three-dimensional FEMDEM technique for predicting the evolution of fracture in geomaterials and concrete”. *Comput Methods Appl Mech Eng*. Vol. 5, pp. 411–420 , 2018.

[ZH90] O. C. Zienkiewicz and G. C. Huang. “A note on localization phenomena and adaptive finite element analysis in forming processes”. *Communications in Applied Numerical Methods*. Vol. 2, pp. 71–76 , 1990.

[ZHP95] O. C. Zienkiewicz, M. Huang, and M. Pastor. “Localization problems in plasticity using finite elements with adaptive remeshing”. *Journal for Numerical and Analytical Methods in Geomechanics*. Vol. 19(2), pp. 127–148 , 1995.

[ZZT13] O. C. Zienkiewicz, J.Z. Zhu, and Robert L. Taylor. *The Finite Element Method: its Basis and Fundamentals*. Butterworth-Heinemann. 7th ed. 2013.

Part III

FEM-DEM formulation

Chapter 5

Introduction to the FEM-DEM formulation

The coupled FEM-DEM formulation was initially developed by Zárate and Oñate [ZO15] as an effective procedure for predicting the onset and propagation of cracks in concrete and rocks. Zárate et al. [ZCO18] extended the formulation to 3D problems and in Cornejo et al. [Cor+19] an adaptive remeshing technique was included.

The FEM-DEM coupled formulation initially employs the FEM to model the continuum, whose mechanical degradation is simulated by an isotropic damage model evaluated at the edges of the FE. Once a FE has exhausted all its energy, this element is removed from the FEM mesh and a set of DE is created at its nodes. Those DE will prevent the indentation of the crack faces by computing the frictional contact forces between the DE and the FE faces and transferring these forces as nodal forces to the FEM mesh.

The continuum is modelled with simplex FE (3-noded triangles in 2D and 4-noded tetrahedra in 3D). The FE solution is obtained by reaching the dynamic equilibrium via an implicit transient dynamic solution scheme. An isotropic damage constitutive law is chosen in order to verify failure at the edges of the FE (using the Super convergent Patch Recovery (SPR) technique developed by Zienkiewicz and Zhu [ZZ92c]). This smoothing of the stress field efficiently improves the stability of the problem (in terms of numerical convergence) and to a lesser degree improves the quality of the crack path obtained. Some important aspects inherent to the FEM-DEM formulation guarantee

the good results obtained, such as a smoothed stress field, mass conservation and the use of a simple algorithm to ensure the post-fracture contact between the fractured edge and the adjacent FE and DE in the mesh [ZO15; ZCO18].

In addition, The fact that the fracture is effectively created in the continuum (the FEM-DEM erases the fully damaged FE) implies that the separated bodies resulting from the fracturing process can fully detach and collide between each other and exhibit large displacements and rotations (Fig. 1.2 and Fig. 5.1), which is not straight forward with other existing formulations.

Since the DEM requires an explicit time integration scheme, several strategies for coupling the two methods are discussed. One approach is to perform a sub-stepping of the DEM in which after an implicit step of the FEM, n sub-steps of the DEM are computed. This procedure stabilizes the DEM solution and is capable of capturing properly the kinematics of the free DE. Another option is to compute the contact forces in the DEM with the time step corresponding to the implicit FEM scheme. This is the cheapest version but could be unstable if the implicit time step is too large (particles can cross each other without computing any contact force). More information about this sub-stepping procedure is given in Chapter 11 and in Zárate et al. [ZO15] and Cornejo et al. [Cor+19].

One of the major advantages of the method presented in this work is its great versatility and applicability. In fact, given that the methodology implemented is capable of dealing with multi-fracture processes (initiation, branching and merging of cracks), large displacements and rotations, mutual frictional contact and material crushing (thanks to the sub-stepping procedure applied to the discrete particles), the spectrum of engineering problems to be potentially solved is very diverse.

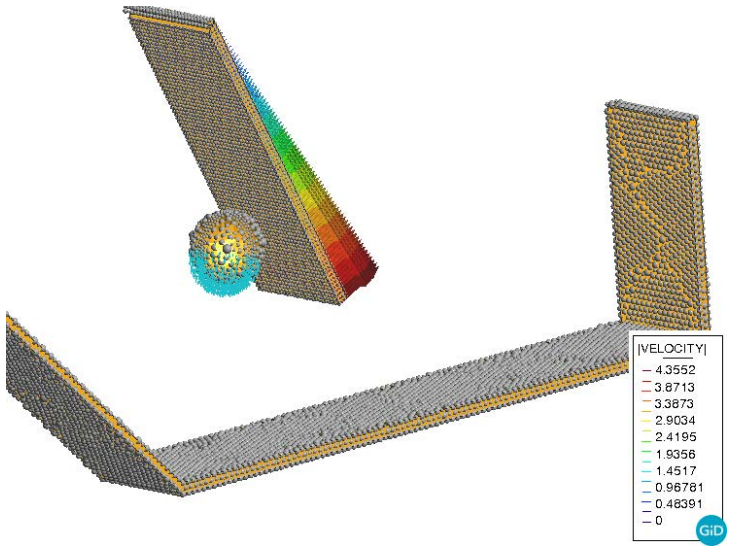

Figure 5.1: FEM-DEM numerical simulation of a ball impacting a vertical wall.

Chapter 6

Solid mechanics governing equations and FE formulation

In this chapter, the basics concepts of non-linear continuum mechanics are reviewed with a focus on the governing equations for solid dynamics. Additionally, a description of the isotropic damage constitutive law is conducted. Next, en overview of discretization techniques and especially FEM formulations along with the typical numerical solutions is given.

A brief introduction to non-linear solid dynamics serves as starting point for all further investigations. These remarks are not intended to give an exhaustive overview of the topic, but are rather geared towards outlining the necessary basics for contact, non-linear constitutive modelling and FSI mechanics. Since the FEM-DEM is based on 2D or 3D solid elements, all the structural mechanics models derived from special kinematic assumptions, such as beams, plates or shells, are not considered. For more extensive reviews in the field of solid and structural dynamics, the reader is referred to the corresponding literature, e.g., Bonet and Wood [BW97], Gurtin [Gur81], Holzapfel [Hol00], Marsden and Hughes [MH94], Ogden [Ogd97] and Simo and Hughes [SH98].

6.1 Kinematics

In this section, the kinematic relationships that describe the motion and deformations of bodies are presented (see Fig. 6.1). The classical continuum model in a three-dimensional Euclidean space description is assumed. However, the derived concepts hold similarly in two dimensions. A common Cartesian coordinate system is considered here for all configurations, also if several bodies are involved, while the concept of curvilinear coordinates only becomes important for local surface descriptions within the FE discretization. In Fig. 6.1 one can identify the body in its reference configuration $\Omega_0 \subset \mathbb{R}^3$, which symbolizes the domain occupied by all the material points $\mathbf{X}$ at time $t = 0$. Additionally, at a certain time t, the body has moved and/or deformed. This deformed geometry is called the current configuration $\Omega_t \subset \mathbb{R}^3$ which describes the changed positions $\mathbf{x}$ at a certain time t. The motion and deformation from the reference configuration to the current configuration is done by means of a bijective non-linear deformation map

$$\Phi_t = \left\{ \begin{matrix} \Omega_0 \rightarrow \Omega_t \\ \mathbf{X} \rightarrow \mathbf{x} \end{matrix} \right\} \tag{6.1}$$

that allows us to write $\mathbf{x} = \Phi_t(\mathbf{X}, t)$ and $\mathbf{X} = \Phi_t^{-1}(\mathbf{x}, t)$. The absolute displacement of a material point (vector $\mathbf{u}$ in Fig. 6.1) is expressed as

$$\mathbf{u}(\mathbf{X}, t) = \mathbf{x}(\mathbf{X}, t) - \mathbf{X}. \tag{6.2}$$

In the Total Lagrangian (TL) approach employed in this work, the kinematic relations and equilibrium equations are stated with respect to the material points in the reference configuration Ω_0 (Lagrangian framework). Thus, the material point position $\mathbf{X}$ is the main independent variable for the problem formulation while the primary unknown to be computed is the displacement vector $\mathbf{u}(\mathbf{X}, t)$.

The main measure for deformation and strain in finite deformation solid mechanics is represented by the deformation gradient tensor $\mathbf{F}$, which can be obtained as the partial derivative of the current configuration with respect to the reference configuration, as:

$$\mathbf{F} = \frac{\partial \mathbf{x}(\mathbf{X}, t)}{\partial \mathbf{X}} = \mathbf{I} + \frac{\partial \mathbf{u}(\mathbf{X}, t)}{\partial \mathbf{X}} \tag{6.3}$$

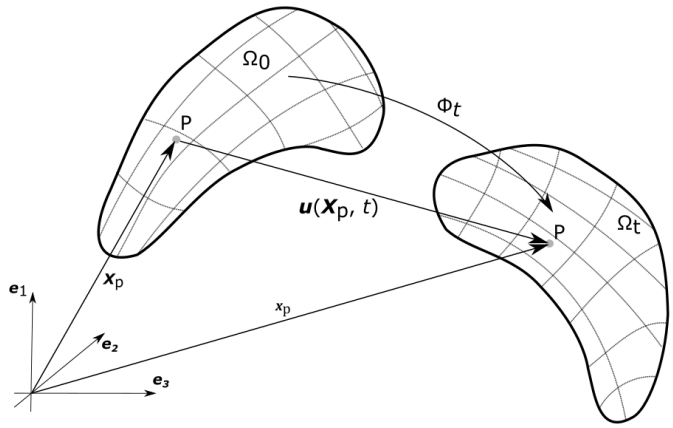

Figure 6.1: Cartesian coordinate system, reference and current deformed configuration for a total Lagrangian formulation.

being **I** the second order identity tensor. It is important to note that the deformation gradient tensor **F** has one basis in the reference configuration and the other in the current configuration. This is why the deformation gradient is a so-called two-point tensor. Geometrically, **F** represents the mapping of an infinitesimal line d**X** in the reference configuration to its corresponding line element d**x** in the current configuration, usually called as *push-forward* operation, i.e.

$$\mathrm{d}\mathbf{x} = \mathbf{F} \cdot \mathrm{d}\mathbf{X} \tag{6.4}$$

Assuming bijectivity of Φ_t, the inverse of the deformation gradient tensor $\mathbf{F}^{-1} = \partial\mathbf{X}/\partial\mathbf{x}$ and the associated *pull-back* operation $\mathrm{d}\mathbf{X} = \mathbf{F}^{-1} \cdot \mathrm{d}\mathbf{x}$ are well defined so it guarantees a positive determinant $\mathrm{J} = \det(\mathbf{F}) > 0$. This quantity J represents the transformation of an infinitesimal volume between the two configurations:

$$\mathrm{d}V = \det(\mathbf{F}) \cdot \mathrm{d}V_0 \tag{6.5}$$

According to the polar decomposition theorem, any deformation characterized by the deformation gradient **F** can be split into a volume-preserving rigid body motion

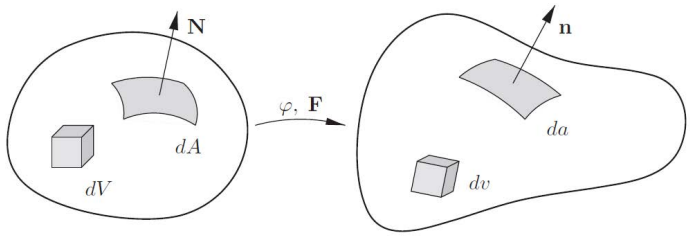

Figure 6.2: Transformation between area and volume elements, image from Wriggers [Wri06].

part and a volume changing stretch part, i.e.

$$\mathbf{F} = \mathbf{R} \cdot \mathbf{U} = \mathbf{V} \cdot \mathbf{R} \tag{6.6}$$

being **R** a two-field tensor which connects both configurations, **U** is the right stretch tensor with a basis in the reference configuration and **V** is the left stretch tensor which is an object in the current configuration. Once the deformation gradient **F** is known, transformations of area and volume elements between Ω_0 and Ω_t can be derived. The transformation between the area elements in the reference configuration and in the current configuration is given by:

$$\mathrm{d}\mathbf{a} = \mathbf{n}\mathrm{d}a = \mathrm{J}\,\mathbf{F}^{-T}\mathrm{N}\,\mathrm{d}A = \mathrm{J}\,\mathbf{F}^{-T}\mathrm{d}\mathbf{A} \tag{6.7}$$

In Eq. (6.7), the vector *n* is the normal direction of a surface from Ω_t (see Fig. 6.2). J is the Jacobian defined in Eq. (6.5) and N denotes the normal vector in the reference configuration Ω_0. For the transformation of volumes between the two configurations we have:

$$\mathrm{d}v = \mathrm{J}\,\mathrm{d}V \tag{6.8}$$

6.2 Strain measures

Once the kinematics of general solids have been exposed, one can analyse the different strain measures which will be applied later. One of the most used strain measures is the so-called right Cauchy-Green tensor **C** which is referred to the reference configuration Ω_0.

$$\mathbf{C} = \mathbf{F}^T\mathbf{F} \tag{6.9}$$

Since this strain measure is not zero in the initial stage ($\mathbf{F} = \mathbf{I} \Rightarrow \mathbf{C} = \mathbf{I}$) it is more usual to use the Green-Lagrange strain tensor **E** which is based on the reference configuration Ω_0.

$$\mathbf{E} = \frac{1}{2}\left(\mathbf{F}^T\mathbf{F} - \mathbf{I}\right) \tag{6.10}$$

Although strain measures are never unique, the Green-Lagrange strain tensor is a very common choice in non-linear solid mechanics, and can be considered particularly convenient if large deformations occur but only a moderate amount of stretch and compression. Another used strain measures in solid mechanics is the so-called Euler-Almansi strain tensor, which is the spatial counterpart of the Green-Lagrange strain tensor, and the logarithmic strain tensor, which is the most used in large strain inelasticity.

6.3 Time derivatives

The time dependency of the deformation Φ_t must be considered in non-linear problems when either the constitutive equations are time/history dependent, or if the considered problem is inherently time-dependent, like impact problems.

The velocity of a material point can be computed as the material time-derivative

$$\mathbf{V}(\mathbf{X}, t) = \frac{\partial \Phi_t}{\partial t}(\mathbf{X}, t) = \dot{\Phi}_t(\mathbf{X}, t) \tag{6.11}$$

In the current configuration, one can write for the velocity **v** of a particle, which is a point **x** at a time t in Ω_t

$$\mathbf{v}(\mathbf{x}, t) = \mathbf{v}(\Phi_t(\mathbf{X}, t), t) \tag{6.12}$$

Analogously, one can obtain the acceleration in the reference configuration by differentiation of the velocity

$$\mathbf{A}(\mathbf{X}, t) = \ddot{\Phi}_t(\mathbf{X}, t) \tag{6.13}$$

Using this definition, the acceleration with respect to the current configuration yields, using Eq. (6.12) and the chain rule,

$$\mathbf{a} = \dot{\mathbf{v}} = \frac{\partial \mathbf{v}}{\partial t} + \text{grad}(\mathbf{v})\,\mathbf{v} \tag{6.14}$$

The first term is usually known as *local derivative* and the second term is the *convective part* of the time derivative. The time derivative defined in Eq. (6.14) must be applied to Eulerian descriptions of motion, which is very common in fluid mechanics. Note that the grad($\mathbf{v}$) is the gradient with respect the current coordinates $\mathbf{x}$ which can be transformed as $\text{Grad}(G) = \mathbf{F}^T\text{grad}(g)$, being Grad the gradient with respect the reference coordinates.

The time derivative of the deformation gradient tensor $\mathbf{F}$ yields

$$\dot{\mathbf{F}} = \text{Grad}\dot{\Phi}_t(\mathbf{X}, t) = \text{Grad}(\mathbf{V}) = \text{grad}(\mathbf{v})\,\mathbf{F} \tag{6.15}$$

Eq. (6.15) can be applied to compute the time derivative of the Green-Lagrange strain tensor $\dot{\mathbf{E}}$ (defined in Eq. (6.10)):

$$\dot{\mathbf{E}} = \frac{1}{2}(\dot{\mathbf{F}}^T\mathbf{F} + \mathbf{F}^T\dot{\mathbf{F}}) \tag{6.16}$$

6.4 Stress measures and constitutive laws

The described motion and deformation in solids induces internal stresses within the continuum. This effect can be described by a traction vector $\mathbf{t}$ in the current configuration:

$$\mathbf{t}(\mathbf{n}, \mathbf{x}, t) = \lim_{\Delta A \to 0} \frac{\Delta \mathbf{f}}{\Delta A} \tag{6.17}$$

which is the limit value of a resulting force $\mathbf{f}$ over an arbitrary surface area ΔA whose normal is defined by $\mathbf{n}$. The Cauchy's theorem, usually derived from equilibrium considerations using a tetrahedral volume element, correlates tractions and stresses by

$$\mathbf{t} = \boldsymbol{\sigma} \cdot \mathbf{n} \tag{6.18}$$

The Cauchy stress tensor $\boldsymbol{\sigma}$ is symmetric and describes the true internal stress in the deformed current configuration. With diagonal and off-diagonal components components being interpretable as normal stresses and shear stresses, respectively. As has been seen regarding the multiple strain measures, one can extrapolate the same idea to the different stress measures. Exemplarily, the first Piola-Kirchoff stress tensor $\mathbf{P}$, a two-point tensor, maps the material surface element $\mathrm{d}\mathbf{A}_0 = \mathrm{d}A_0\mathbf{N}$ (see Fig. 6.2) onto the spatial resulting force $\mathbf{f}$. Its definition can be obtained from the Cauchy stress tensor by applying Eq. (6.7):

$$\mathbf{P} = \mathrm{J}\,\boldsymbol{\sigma}\,\mathbf{F}^{-T}. \tag{6.19}$$

In the same way we can define an stress measure in the reference configuration. The second Piola-Kirchoff stress tensor $\mathbf{S}$ can be defined as

$$\mathbf{S} = \mathbf{F}^{-1} \cdot \mathbf{P} = \mathrm{J}\,\mathbf{F}^{-1} \cdot \boldsymbol{\sigma} \cdot \mathbf{F}^{-T}. \tag{6.20}$$

Unlike the Cauchy or "true" stress tensor $\boldsymbol{\sigma}$, the first and second Piola-Kirchoff stresses do not have a clear physical interpretation. It is important to note that strain and stress definitions cannot be combined arbitrarily, but there exist some natural connections based on the notion of energy conjugate pairs (see Bonet and Wood [BW97]). Using the relations derived in the previous equations, the following equivalent internal power $\mathcal{P}_{int}$ are available:

$$\mathcal{P}_{int} = \int_{\Omega_t} \boldsymbol{\sigma} : (\mathbf{F}^{-T} \cdot \dot{\mathbf{E}} \cdot \mathbf{F}^{-1})\,\mathrm{d}\Omega_t = \int_{\Omega_0} \mathbf{P} : \dot{\mathbf{F}}\,\mathrm{d}\Omega_0 = \int_{\Omega_0} \mathbf{S} : \dot{\mathbf{E}}\,\mathrm{d}\Omega_0 \tag{6.21}$$

Once the most used strains and stress measures have been defined, one can overcome the constitutive relations or material models that relate the strains and the stresses in the solid. In this regard, the existence of a so-called *strain energy function* $\Psi(\mathbf{F})$ is assumed (can be divided in an elastic and plastic parts in non-linear constitutive laws). The requirement of objectivity of Ψ implies that the energy function must be independent of the rotation component $\mathbf{R}$ of the deformation gradient, i.e.

$$\Psi(\mathbf{F}) = \Psi(\mathbf{F}) = \Psi(\mathbf{U}) = \Psi(\mathbf{C}) = \Psi(\mathbf{E}) \tag{6.22}$$

For example, in the case of a linear elastic law assuming small strains, the strain energy function can be expressed as [Oll02]:

$$\Psi(\varepsilon) = \frac{1}{2}(\varepsilon : \mathcal{C}_0 : \varepsilon) \tag{6.23}$$

Being $\mathcal{C}_0$ the linear elastic constitutive matrix (see Oñate [Oña92; Cor17]) and ε the infinitesimal strain tensor. In the case of an isotropic damage model (see Oliver et al. [Oli+90]), the strain energy function could be written as [Oll02] $\Psi(\varepsilon) = \frac{1-\mathrm{d}}{2}(\varepsilon : \mathcal{C}_0 : \varepsilon)$, where d is the damage internal variable whose expression is given in Chapter 7. In the finite strain framework, a common formulation of hyperelastic materials in the reference configuration can be expressed as:

$$\mathbf{S} = \frac{\partial \Psi}{\partial \mathbf{E}} \tag{6.24}$$

This relation is, in general cases, non-linear. Thus, in order to compute the fourth-order material elasticity tensor $\mathcal{C}$ we can perform repeated derivation, yielding

$$\mathcal{C} = \frac{\partial \mathbf{S}}{\partial \mathbf{E}} = \frac{\partial^2 \Psi}{\partial \mathbf{E}\, \partial \mathbf{E}} \tag{6.25}$$

As an example of hyperelastic model (which has been implemented and used in the FEM-DEM methodology), one can analyse the compressible Neo-Hookean model with the strain energy function

$$\Psi_{NH} = \frac{\mu}{2}\left(\mathrm{tr}(\mathbf{C}) - 3\right) - \mu \ln(\mathrm{J}) + \frac{\lambda}{2}(\ln(\mathrm{J}))^2) \tag{6.26}$$

Being λ and μ the so-called Lamé parameters, which are related with the Young modulus E and Poisson's ratio ν via

$$\lambda = \frac{\mathrm{E}\,\nu}{(1+\nu)(1-2\nu)} \quad ; \quad \mu = \frac{\mathrm{E}}{2(1+\nu)} \tag{6.27}$$

For more information about hyper-elasticity, visco-elasticity or elasto-plasticity, the reader is referred to Holzapfel [Hol00], Ogden [Ogd97] and Simo and Hugues [SH98].

6.5 Balance equations

Besides the kinematic relations, strain and stress measures and constitutive laws, the solid deformation and motion are characterized by a set of governing equations for mass, momentum and energy that define the kind of physical problem to face. There also exist associated conservation laws for these mechanical quantities, which are all valid under certain conditions.

6.5.1 Conservation of mass

The global expression for mass conservation in the current configuration is

$$\frac{\mathrm{d}m}{\mathrm{d}t} = \frac{\mathrm{d}}{\mathrm{d}t}\int_{\Omega_t} \rho\,\mathrm{d}V = \int_{\Omega_t} (\dot{\rho} + \rho\,\mathrm{div}(\dot{\mathbf{u}}))\mathrm{d}V = 0 \tag{6.28}$$

where ρ is the spatial mass density of the spatial volume element $\mathrm{d}V$. By using the Reynold's transport theorem and the spatial divergence operator $\mathrm{div}(\cdot)$ one can rewrite in material form the mass conservation:

$$\frac{\mathrm{d}m}{\mathrm{d}t} = \frac{\mathrm{d}}{\mathrm{d}t}\int_{\Omega_0} \rho_0 \mathrm{d}V_0 = \int_{\Omega_0} \dot{\rho}_0\,\mathrm{d}V_0 \tag{6.29}$$

Where the reference mass density $\rho_0 = \mathrm{J}\rho$ of the material volume $\mathrm{d}V_0$ is correlated with the spatial mass density ρ by means of the Jacobian determinant J. Obtaining the local formulations of mass conservation from Eqs. (6.28) and (6.29) is straightforward since they must hold at any materials point, i.e.

$$\dot{\rho} + \rho \operatorname{div}(\dot{\mathbf{u}}) = 0 \tag{6.30}$$

$$\dot{\rho}_0 = 0 \tag{6.31}$$

6.5.2 Balance of linear momentum

By stating that the sum of the external forces must be equal to the time-derivative of the linear momentum acting on a body one can write:

$$\frac{\mathrm{d}}{\mathrm{d}t} \int_{\Omega_t} \rho \, \dot{\mathbf{u}} \, \mathrm{d}V = \int_{\Omega_t} \hat{\mathbf{b}} \, \mathrm{d}V + \int_{\partial\Omega_t} \hat{\mathbf{t}} \, \mathrm{d}A \tag{6.32}$$

Being $\hat{\mathbf{t}}$ the external tractions on the boundary $\partial\Omega_t$ of the body in the current configuration, and $\hat{\mathbf{b}}$ represents the external body force per current unit volume. After the application of the Reynold's transport theorem and the local mass conservation (Eq. (6.30)) to the left-hand side and Gauss divergence theorem to the right-hand side of Eq. (6.32), a more useful expression of the global linear momentum is obtained:

$$\int_{\Omega_t} \rho \, \ddot{\mathbf{u}} \mathrm{d}V = \int_{\Omega_t} (\operatorname{div}\boldsymbol{\sigma} + \hat{\mathbf{b}}) \mathrm{d}V \tag{6.33}$$

In the same way, the global form in the current configuration is initially given by:

$$\frac{\mathrm{d}}{\mathrm{d}t} \int_{\Omega_0} \rho_0 \, \dot{\mathbf{u}} \, \mathrm{d}V_0 = \int_{\Omega_0} \hat{\mathbf{b}}_0 \, \mathrm{d}V_0 + \int_{\partial\Omega_0} \hat{\mathbf{t}}_0 \, \mathrm{d}A_0 \tag{6.34}$$

And, analogously, one can obtain the global linear momentum balance in material description:

$$\int_{\Omega_t} \rho_0 \, \ddot{\mathbf{u}} \mathrm{d}V_0 = \int_{\Omega_0} (\operatorname{Div}\mathbf{P} + \hat{\mathbf{b}}_0) \mathrm{d}V_0, \tag{6.35}$$

where the material divergence operator Div(·) is used. The external volume and surface forces $\hat{\mathbf{b}}_0$ and $\hat{\mathbf{t}}_0$ are defined in the undeformed geometry. Finally, the local formulations in spatial and material configurations can be defined as

$$\rho\,\ddot{\mathbf{u}} = \mathrm{div}(\boldsymbol{\sigma}) + \hat{\mathbf{b}}, \tag{6.36}$$

$$\rho_0\,\ddot{\mathbf{u}} = \mathrm{Div}(\mathbf{P}) + \hat{\mathbf{b}}_0, \tag{6.37}$$

which is usually known as Cauchy's first equation of motion. This equation is crucial when formulating the Initial Boundary Value Problem (IBVP) of solid mechanics, as will be explained in section 6.6.

6.5.3 Balance of angular momentum

Similarly to the balance of linear momentum, the balance of angular momentum can be derived from the requirement that the time derivative of the angular momentum from a fixed point equals the sum of all external moments acting on a body.

$$\frac{\mathrm{d}}{\mathrm{d}t}\int_{\Omega_t} \rho\,\mathbf{x}\times\dot{\mathbf{u}}\,\mathrm{d}V = \int_{\Omega_t}\mathbf{x}\times\hat{\mathbf{b}}\,\mathrm{d}V + \int_{\partial\Omega_t}\mathbf{x}\times\hat{\mathbf{t}}\,\mathrm{d}A \tag{6.38}$$

Mapping all the information from Eq. (6.38) to the reference geometry in material description:

$$\frac{\mathrm{d}}{\mathrm{d}t}\int_{\Omega_0} \rho_0\,\mathbf{x}\times\dot{\mathbf{u}}\,\mathrm{d}V_0 = \int_{\Omega_0}\mathbf{x}\times\hat{\mathbf{b}}_0\,\mathrm{d}V_0 + \int_{\partial\Omega_0}\mathbf{x}\times\hat{\mathbf{t}}_0\,\mathrm{d}A_0 \tag{6.39}$$

By applying the Gauss divergence theorem to the boundary integral in Eqs. (6.38)-(6.39) one can state the interesting observation that the Cauchy stress tensor $\boldsymbol{\sigma}$ and the second Piola-Kirchoff stress tensor $\mathbf{S}$ are symmetric, i.e.

$$\boldsymbol{\sigma} = \boldsymbol{\sigma}^T \quad , \quad \mathbf{S} = \mathbf{S}^T \tag{6.40}$$

This result is also known as Cauchy's second equation of motion. However, the balance of angular momentum does not affect the IBVP but implicitly demands symmetry of $\boldsymbol{\sigma}$ and $\mathbf{S}$.

6.5.4 Balance of mechanical energy

The balance of energy can be obtained by stating that the change in total energy equals the introduced by the external power (only mechanical energy is taken into account), i.e

$$\overbrace{\frac{\mathrm{d}}{\mathrm{d}t}\int_{\Omega_t}\frac{1}{2}\rho\,\dot{\mathbf{u}}\cdot\dot{\mathbf{u}}\,\mathrm{d}V}^{\mathcal{P}_{kin}}+\overbrace{\int_{\Omega_t}\boldsymbol{\sigma}:(\mathbf{F}^{-T}\cdot\dot{\mathbf{E}}\cdot\mathbf{F}^{-1})\mathrm{d}V}^{\mathcal{P}_{int}}=\overbrace{\int_{\Omega_t}\hat{\mathbf{b}}\cdot\dot{\mathbf{u}}\,\mathrm{d}V+\int_{\partial\Omega_t}\hat{\mathbf{t}}\cdot\dot{\mathbf{u}}\,\mathrm{d}A}^{\mathcal{P}_{ext}}\quad(6.41)$$

In the previous equation, $\mathcal{P}_{kin}$ represents the kinetic energy whereas the second term $\mathcal{P}_{int}$ is the internal mechanical power. The right-hand side comprises the external power $\mathcal{P}_{ext}$ generated by the volume and surface forces. The material version of the global energy balance is given here too:

$$\overbrace{\frac{\mathrm{d}}{\mathrm{d}t}\int_{\Omega_0}\frac{1}{2}\rho_0\,\dot{\mathbf{u}}\cdot\dot{\mathbf{u}}\,\mathrm{d}V_0}^{\mathcal{P}_{kin}}+\overbrace{\int_{\Omega_0}\mathbf{S}:\dot{\mathbf{E}}\,\mathrm{d}V_0}^{\mathcal{P}_{int}}=\overbrace{\int_{\Omega_0}\hat{\mathbf{b}}\cdot\dot{\mathbf{u}}\,\mathrm{d}V+\int_{\partial\Omega_0}\hat{\mathbf{t}}_0\cdot\dot{\mathbf{u}}\,\mathrm{d}A_0}^{\mathcal{P}_{ext}}\quad(6.42)$$

it can easily be shown to reduce to a mere consequence of the balance of linear momentum in the case of purely mechanical systems considered here, see e.g. the lecture notes in Wall and Cyron [WC11].

6.6 Initial Boundary Value Problem

Taking into account the three previous sections, one can state a set of coupled second-order partial differential equations that must satisfy an initial set of conditions as well as boundary conditions. This is commonly known as defining the Initial Boundary Value Problem (IBVP), in the case of this work, the non-linear solid mechanics IBVP. Since the FEM-DEM has been implemented in a TL framework, the IBVP will be presented in the reference configuration. For the definition of the boundary conditions, the contour of the domain $\partial\Omega_0$ has to be decomposed into two complementary sets: Γ_σ representing the Neumann boundary, where the tractions $\hat{\mathbf{t}}_0$ are known, and Γ_u, denoted as Dirichlet boundary, where the prescribed displacements are applied. Neumann and Dirichlet boundaries are disjoint sets, i.e.

$$\Gamma_\sigma \cup \Gamma_u = \partial\Omega_0 \ , \ \Gamma_\sigma \cap \Gamma_u = \emptyset \tag{6.43}$$

Now, the initial boundary value problem can be formulated as (in material form):

$$\text{Div}\mathbf{P} + \hat{\mathbf{b}}_0 = \rho_0 \ddot{\mathbf{u}} \ \text{ in } \ \Omega_0 \times [0, T] \tag{6.44}$$

$$\mathbf{u} = \hat{\mathbf{u}} \ \text{ in } \ \Gamma_u \times [0, T] \tag{6.45}$$

$$\mathbf{P} \cdot \mathbf{N} = \hat{\mathbf{t}}_0 \ \text{ in } \ \Gamma_\sigma \times [0, T] \tag{6.46}$$

Where T is the end of the considered time interval of the problem. Since the balance of linear momentum equation (6.44) involves the second derivatives with respect to time t, a suitable set of initial conditions specifying the displacements $\hat{\mathbf{u}}_0$ and velocities $\hat{\mathbf{v}}_0$ at time $t = 0$ is needed:

$$\mathbf{u}(\mathbf{X}, 0) = \hat{\mathbf{u}}_0(\mathbf{X}) \text{ in } \Omega_0 \tag{6.47}$$

$$\mathbf{v}(\mathbf{X}, 0) = \hat{\mathbf{v}}_0(\mathbf{X}) \text{ in } \Omega_0 \tag{6.48}$$

Next, the definition of a certain material model (constitutive law) such as the ones in section 6.4 will finalize the definition of the IBVP for finite deformation solid mechanics. The exposed IBVP is also known as *strong formulation* of non-linear solid mechanics, as eqs. (6.44)-(6.48) are enforced at each individual point within the domain Ω_0. There is no analytical solution for this system of equations for general cases, only exists in some special cases with simple geometries and under simplifying a assumptions. However, as will be seen in section 6.7, its definition as *weak formulation* is the basis for numerical discretization techniques such as the FEM.

6.7 FE formulations and solution schemes

This chapter introduces the general methodology when solving non-linear solid mechanics problems by using the FEM. First, one must obtain the *weak* form of the IBVP and, by using the FEM for the space discretization as well as the definition of a typical implicit time stepping schemes for the time discretization, one can proceed to perform the calculation. All these necessary items will be reviewed in this section.

6.7.1 Weak formulation

In general, many of the numerical methods that solve partial differential equations (FEM is not an exception) require a transformation of the IBVP (see section 6.6) within the so-called weak or variational formulation. In this work, only the Principle of Virtual Work (PVW) is used. However, other approaches (variational principles) are available. If one states a weighted residual notation of the balance equation (6.44) and the traction condition (6.46) results in:

$$\int_{\Omega_0} (\rho_0 \, \ddot{\mathbf{u}} - \mathrm{Div}(\mathbf{P}) - \hat{\mathbf{b}}_0) \cdot \boldsymbol{\eta} \, \mathrm{d}V_0 + \int_{\Gamma_\sigma} (\mathbf{P} \cdot \mathbf{N} - \hat{\mathbf{t}}_0) \cdot \boldsymbol{\eta} \, \mathrm{d}A_0 = 0 \tag{6.49}$$

where the weighting functions or test functions $\boldsymbol{\eta}$ are arbitrary and can be treated as virtual displacements $\delta\mathbf{u}$. In addition, one must verify the already known values of the displacements in the Dirichlet boundary Γ_u, which means:

$$\boldsymbol{\eta} = \mathbf{0} \;\text{ on }\; \Gamma_u \times [0, T]. \tag{6.50}$$

If one applies the Gauss divergence theorem and inserting eqs. (6.50) and (6.20):

$$\int_{\Omega_0} (\rho_0 \, \ddot{\mathbf{u}} - \hat{\mathbf{b}}_0) \cdot \delta\mathbf{u} \, \mathrm{d}V_0 + \int_{\Omega_0} (\mathrm{Grad}(\delta\mathbf{u}))^T : (\mathbf{F} \cdot \mathbf{S}) \, \mathrm{d}V_0 - \int_{\Gamma_\sigma} \hat{\mathbf{t}}_0 \cdot \delta\mathbf{u} \, \mathrm{d}A_0 = 0, \tag{6.51}$$

in which the material gradient $\mathrm{Grad}(\cdot)$ has been employed. Since the variation of the Green-Lagrange strain tensor can be rewritten as $\delta\mathbf{E} = \frac{1}{2}((\mathbf{F}^T \cdot \mathrm{Grad}(\delta\mathbf{u}))^T + \mathbf{F}^T \cdot \mathrm{Grad}(\delta\mathbf{u}))$ and $\mathbf{S}$ is symmetric, the PVW in material description can be expressed as:

$$\delta\mathcal{W} := \underbrace{\int_{\Omega_0} \rho_0 \, \ddot{\mathbf{u}} \cdot \delta\mathbf{u} \, \mathrm{d}V_0}_{-\delta\mathcal{W}_{kin}} + \underbrace{\int_{\Omega_0} \mathbf{S} : \delta\mathbf{E} \, \mathrm{d}V_0}_{-\delta\mathcal{W}_{int}} - \underbrace{\int_{\Omega_0} \hat{\mathbf{b}}_0 \cdot \delta\mathbf{u} \, \mathrm{d}V_0 - \int_{\Gamma_\sigma} \hat{\mathbf{t}}_0 \cdot \delta\mathbf{u} \, \mathrm{d}A_0}_{-\delta\mathcal{W}_{ext}} = 0 \tag{6.52}$$

As can be analysed in the previous equation, the first term corresponds to the virtual work of the kinetic terms $\delta\mathcal{W}_{kin}$, the second term denotes the internal virtual work $\delta\mathcal{W}_{int}$ and the third and fourth are the contributions of the external loads $\delta\mathcal{W}_{ext}$. Since there are no previous hypothesis performed in order to define the PVW, it is valid and applicable for problems such as elastoplasticity, damage, non-conservative loading, etc. This is why the PVW is the most used variational principles for solid mechanics. It has been demonstrated that the solution of the IBVP (strong formulation) must also satisfy the weak formulation (6.52). Since the weighting functions $\boldsymbol{\eta} \equiv \delta\mathbf{u}$ used in (6.49) are arbitrary, the two formulations are formally equivalent, see Hughes [Hug00].

6.7.2 Space discretization

The discrete equations for a FE model are obtained from the principle of virtual work by using finite element interpolations for the test and trial functions. The problem domain is subdivided into elements $e = 1$ to $e = n_e$ with n_n nodes. The aim of this discretization is to find a numerical solution to (6.52) at a set of discrete points, named nodes. These nodes conform elements, which allow the partitioning of the domain Ω_0 into n_e finite subdomains (see Oñate [Oña92], Hughes [Hug00] and Zienkiewicz et al. [ZZT13; ZT13]):

$$\Omega_0 \approx \bigcup_{e=1}^{n_e} \Omega_0^{(e)} \tag{6.53}$$

The displacement $\mathbf{u}^{(e)}$ (which is the independent variable usually) on the e element is typically estimated by local interpolation via the shape functions $N_k(\mathbf{X})$, yielding

$$\mathbf{u}^{(e)}(\mathbf{X}, t) \approx \mathbf{u}_h^{(e)}(\mathbf{X}, t) = \sum_{k=1}^{n_n^{(e)}} N_k(\mathbf{X})\, \mathbf{d}_k(t), \tag{6.54}$$

where the nodal values of the displacement $\mathbf{d}_k(t)$ have been presented. Formally, the subscript $(\cdot)_h$ represents the spatially discretized values over the FE mesh and $n_n^{(e)}$ represents the number of nodes associated to an element e. In general, the interpolation or shape functions $N_k(\mathbf{X}$ are low-order polynomials that must ensure

the differentiability requirements of the weak formulation. Additionally, if the element implementation is based on the iso-parametric space, the element geometry in the reference configuration $\mathbf{X}^{(e)}$ and current configuration $\mathbf{x}^{(e)}$ can be approximated using the same set of shape functions. In general, the element domain $\Omega_0^{(e)}$ is referred to a new space $\boldsymbol{\xi} = (\xi, \eta, \zeta)$ which is usually a simple geometry like the cube $[-1, 1] \times [-1, 1] \times [-1, 1]$. This basis change has its own Jacobian matrix $\mathbf{J}^{(e)} = \partial \mathbf{X}^{(e)} / \partial \boldsymbol{\xi}$. In conclusion, the displacement, current geometry and reference geometry interpolations inside the elements can be expressed in terms of the new iso-parametric space as:

$$\mathbf{u}_h^{(e)}(\boldsymbol{\xi}, t) = \sum_{k=1}^{n_n^{(e)}} N_k(\boldsymbol{\xi})\, \mathbf{d}_k(t), \tag{6.55}$$

$$\mathbf{x}_h^{(e)}(\boldsymbol{\xi}, t) = \sum_{k=1}^{n_n^{(e)}} N_k(\boldsymbol{\xi})\, \mathbf{x}_k(t), \tag{6.56}$$

$$\mathbf{X}_h^{(e)}(\boldsymbol{\xi}, t) = \sum_{k=1}^{n_n^{(e)}} N_k(\boldsymbol{\xi})\, \mathbf{X}_k(t), \tag{6.57}$$

Being the $\mathbf{X}_k$ and $\mathbf{x}_k$ the nodal values of the positions in the reference and current configuration, respectively. Finally, the interpolations of the derivatives of the displacements are also interpolated with the same functions (if using the Bubnov-Galerking approach). It is important to note that, as can be studied in the Eq. (6.55), the FEM introduces a restriction or an approximation of the solution. Indeed, the weak formulation introduced in Eq. (6.52) can be rewritten in a discrete form, which is not equivalent to the weak/strong form, but represents an approximation of the solution.

The contributions of each FE are integrated element-wise by using a Gauss quadrature and then assembled into a global vector. This assembling of the contributions is carried out by an assembly-operator $\mathbb{A}$, i.e.

$$\int_{\Omega_0} (\cdot)\, \mathrm{d}V_0 = \mathbb{A}_{e=1}^{n_e} \int_{\Omega_{0,h}^{(e)}} (\cdot)\, \mathrm{d}V_0^{(e)}. \tag{6.58}$$

After applying the approximations defined in Eq. (6.55) into the weak formulation (6.52) one can derive the discretized formulation as

$$\delta \mathbf{d}^T (\mathbf{M}\ddot{\mathbf{d}} + \mathbf{f}_{\text{int}}(\mathbf{d}) - \mathbf{f}_{\text{ext}}) = 0, \tag{6.59}$$

Being $\mathbf{M}$ the global mass matrix, $\mathbf{f}_{\text{int}}$ the global vector of non-linear internal forces and $\mathbf{f}_{\text{ext}}$ the global vector of external forces. Additionally, the vectors $\delta \mathbf{d}^T$, $\ddot{\mathbf{d}}$ and $\mathbf{d}$ are the global vectors of all the nodal values of the virtual displacements, accelerations and displacements. The vector of nodal displacements $\mathbf{d}$ (independent unknown) are also called the degrees of freedom of the problem. Due to the approximation in Eq. (6.55), the size of the vectors are $n_{DoF} = Dim \cdot n_{nodes}$, being Dim the dimension of the problem (2D or 3D). Since Eq. (6.59) must be verified for any virtual displacement $\delta \mathbf{d}$, it is equivalent to write:

$$\mathbf{M}\ddot{\mathbf{d}} + \mathbf{f}_{\text{int}}(\mathbf{d}) - \mathbf{f}_{\text{ext}} = \mathbf{0}. \tag{6.60}$$

The Eq. (6.60) states a system of n_{DoF} ordinary differential equations (ODE). It is very usual to add some damping to this semi-discrete equations of motion (6.60) via the so-called Rayleigh model, i.e.

$$\mathbf{M}\ddot{\mathbf{d}} + \mathbb{C}\,\dot{\mathbf{d}} + \mathbf{f}_{\text{int}}(\mathbf{d}) - \mathbf{f}_{\text{ext}} = \mathbf{0}, \tag{6.61}$$

where $\dot{\mathbf{d}}$ is the global vector of nodal velocities and $\mathbb{C}$ represents the damping matrix which, in general, is computed as a linear combination of the mass matrix $\mathbf{M}$ and the initial stiffness matrix $\mathbf{K}_0$ (whose expression will be presented in the next paragraphs) as:

$$\mathbb{C} = \alpha \mathbf{M} + \beta \mathbf{K}_0 \tag{6.62}$$

Within the framework of this work, when damping is required in the simulation, a set of non-zero parameters are used: $\alpha = 0.5$ and $\beta = 0.02$.

6.7.3 Time discretization

In this chapter the time resolution of the motion equation in its semi-discrete form (6.61) is studied. As have been said before, the Eq. (6.61) defines a system of

Ordinary Differential Equation (ODE) containing the polynomial approximation (spatial discretization) of the displacements, velocities and accelerations, $\mathbf{d}$, $\dot{\mathbf{d}}$ and $\ddot{\mathbf{d}}$, respectively.

The main philosophy for the solution of this classical problem in structural dynamics is based on the *concept of separation of variables* that assumes that spatial and temporal problems are independent from one another. Thus, the finite element method is adopted for the solution of the spatial problem, while the finite differences is used for temporal problems. In conclusion, the semi-discrete equation defined in Eq. (6.61) is solved at each time t, which means that the spatial equilibrium is reached.

6.7.3.1 Explicit-Implicit solution

The time solution of Eq. (6.61) can be obtained either through an implicit or explicit strategy. If the response of the current time ($t + \Delta t$) only depends on the solution of the previous step t, then the solution is explicit. On the other hand, if the current solution depends on the velocity and the accelerations of the current step ($t + \Delta t$), then the solution is implicit. In general, the main characteristics of the explicit/implicit schemes can be summarized as:

Explicit time integration:

- The solution algorithm is simple and it allows carrying out a simple treatment of the different non-linearities.
- It requires less memory storage.
- It does not need expensive tangent operators like in implicit algorithms.
- The explicit methods lead to reliable algorithms.
- The solution time increment Δt is bounded and it is usually very small.

Implicit time integration:

- The time increments can be much larger than in explicit methods, preserving the solution stability.
- They allow more precise solutions, with lower error tolerances.

- A relative drawback is the linearisation of the solution through Newton-Raphson which requires tangent operators that are usually very difficult or expensive to obtain.
- Another drawback is the large storage demand when using direct solution methods for the system of equations.

In this work, due to the more interesting properties of the implicit solutions, all the implementations have been conducted in implicit schemes (excepting the DEM , which will be discussed in Chapter 10).

6.7.3.2 Generalized-α implicit scheme

In this chapter, the well-known Generalized-α method developed by Chung and Hulbert [CH93], which is the one used for the calculations in this work, is described. This one-step scheme is based on the Newmark's method [New59], which allows the expression of the discrete velocities $\mathbf{v}_{n+1} \approx \dot{\mathbf{d}}(t_{n+1})$ and accelerations $\mathbf{a}_{n+1} \approx \ddot{\mathbf{d}}(t_{n+1})$ only in terms of the already known values at time t_n and the unknown displacements of the current step $\mathbf{d}_{n+1}$, i.e.

$$\mathbf{v}_{n+1}(\mathbf{d}_{n+1}) = \frac{\gamma}{\beta\,\Delta t}(\mathbf{d}_{n+1} - \mathbf{d}_n) - \frac{\gamma-\beta}{\beta}\mathbf{v}_n - \frac{\gamma-2\beta}{2\beta}\,\Delta t\,\mathbf{a}_n, \tag{6.63}$$

$$\mathbf{a}_{n+1}(\mathbf{d}_{n+1}) = \frac{1}{\beta\Delta t^2}(\mathbf{d}_{n+1} - \mathbf{d}_n) - \frac{1}{\beta\Delta t}\mathbf{v}_n - \frac{1-2\beta}{2\beta}\,\Delta t\,\mathbf{a}_n, \tag{6.64}$$

being $\beta \in [0, 1/2]$ and $\gamma \in [0, 1]$ the two main parameters that define the behaviour of the method. This generalized-*alpha* method defines two mid-point times $t_{n+1-\alpha_m}$ and $t_{n+1-\alpha_f}$ and evaluates the equilibrium of Eq. (6.61) at these mid-points instead of the current time t_{n+1}. In this way, the generalized-α method defines:

$$\mathbf{d}_{n+1-\alpha_f} = (1-\alpha_f)\,\mathbf{d}_{n+1} + \alpha_f\,\mathbf{d}_n, \tag{6.65a}$$
$$\mathbf{v}_{n+1-\alpha_f} = (1-\alpha_f)\,\mathbf{v}_{n+1} + \alpha_f\,\mathbf{v}_n, \tag{6.65b}$$
$$\mathbf{a}_{n+1-\alpha_f} = (1-\alpha_m)\,\mathbf{a}_{n+1} + \alpha_m\,\mathbf{a}_n, \tag{6.65c}$$
$$\mathbf{f}_{\text{ext},n+1-\alpha_f} = (1-\alpha_f)\,\mathbf{f}_{\text{ext},n+1} + \alpha_f\,\mathbf{f}_{\text{ext},n}. \tag{6.65d}$$

Finally, the space-time discretized FE formulation of non-linear solid mechanics can be written as:

$$\mathbf{M}\,\mathbf{a}_{n+1-\alpha_f} + \mathbb{C}\,\mathbf{v}_{n+1-\alpha_f} + \mathbf{f}_{\text{int}}(\mathbf{d}_{n+1-\alpha_f}) - \mathbf{f}_{\text{ext},n+1-\alpha_f} = \mathbf{0}. \tag{6.66}$$

The powerful characteristic of this generalized-α method is that allows to control numerically the dissipation of the considered system and, at the same time, maintaining the unconditional stability and second order accuracy. By modifying the values of the parameters β, γ, α_f and α_m one can ensure that the desired damping effect is only achieved in the spurious high frequency modes, while in the low frequency modes is kept at a minimum. It is important to note that, if $\alpha_m = \alpha_f = 0$, the Newmark method is recovered.

6.7.3.3 Newmark time scheme

As stated in the previous section, if $\alpha_m = \alpha_f = 0$ one can formulate the Newmark scheme [New59] that reads:

$$(c_3\mathbf{M} + c_2\mathbf{C} + c_1\mathbf{K})\,\mathbf{d}_{n+1} + \mathbf{f}_{n+1} = \mathbf{0} \tag{6.67}$$

and

$$\mathbf{d}_{n+1} = \mathbf{d}_n + \Delta t\dot{\mathbf{d}}_n + \left(\frac{1}{2} - \beta\right)\Delta t^2\ddot{\mathbf{d}}_n + \beta\Delta t^2\ddot{\mathbf{d}}_{n+1} \tag{6.68a}$$

$$\dot{\mathbf{d}}_{n+1} = \dot{\mathbf{d}}_n + (1-\gamma)\Delta t\ddot{\mathbf{d}}_n + \gamma\Delta t\ddot{\mathbf{d}}_{n+1} \tag{6.68b}$$

where c_1, c_2 and c_3 are the Newmark parameters whose expression is: $c_1 = 1$, $c_2 = \frac{\gamma}{\beta\Delta t}$ and $c_3 = \frac{1}{\beta\Delta t^2}$.

6.7.3.4 Linearisation and solution techniques for non-linear system of equations

At each time step, the mentioned system of semi-discrete equations (6.61) has to be solved numerically, which means obtaining a solution for the displacements of that

step $\mathbf{d}_{n+1}$ that verifies the equilibrium of the equation of motion. In this regard, the most used iterative non-linear numerical technique is the well-known Newton-Raphson method. At each i iteration of the discrete momentum balance equation, the residual $\mathbf{r}_{\text{eff,dyn}}$ can be defined as:

$$\mathbf{r}_{\text{eff,dyn}}(\mathbf{d}^i_{n+1}) = \mathbf{M}\,\mathbf{a}^i_{n+1-\alpha_f} + \mathbb{C}\,\mathbf{v}^i_{n+1-\alpha_f} + \mathbf{f}_{\text{int}}(\mathbf{d}^i_{n+1-\alpha_f}) - \mathbf{f}_{\text{ext},n+1-\alpha_f}. \tag{6.69}$$

Then, the Newton-Raphson method linearises the residual $\mathbf{r}_{\text{eff,dyn}}$ and updates the value of the unknowns until a certain convergence criteria are verified. The linearisation of the residual is done from the truncated Taylor expansion [TFR96] of Eq. (6.69) as:

$$\text{Lin}\,\mathbf{r}_{\text{eff,dyn}}(\mathbf{d}^i_{n+1}) = \mathbf{r}_{\text{eff,dyn}}(\mathbf{d}^i_{n+1}) + \underbrace{\frac{\partial \mathbf{r}_{\text{eff,dyn}}(\mathbf{d}^i_{n+1})}{\partial \mathbf{d}^i_{n+1}}}_{\mathbf{K}_{eff,dyn}(\mathbf{d}^i_{n+1})} \cdot \Delta \mathbf{d}^{\boldsymbol{i+1}}_{\boldsymbol{n+1}}, \tag{6.70}$$

where the partial derivative of the residual $\mathbf{r}_{\text{eff,dyn}}(\mathbf{d}^i_{n+1})$ is the so-called dynamic effective tangential stiffness matrix $\mathbf{K}_{eff,dyn}(\mathbf{d}^i_{n+1})$ whose size is $n_{DoF} \times n_{DoF}$. In the case od the generalized-α method, the $\mathbf{K}_{eff,dyn}(\mathbf{d}^i_{n+1})$ can be computed (in terms of the mid-points defined in Eq. (6.65)) as:

$$\mathbf{K}_{\text{eff,dyn}}(\mathbf{d}^i_{n+1}) = \left[\frac{1-\alpha_m}{\beta \Delta t^2}\mathbf{M} + \frac{(1-\alpha_f)\gamma}{\beta \Delta t}\mathbb{C} + (1-\alpha_f)\mathbf{K}_T(\mathbf{d}^i_{n+1-\alpha_f})\right]^i, \tag{6.71}$$

where $\mathbf{K}_T(\mathbf{d}^i_{n+1-\alpha_f})$ is the tangential stiffness matrix, whose relationship with the internal forces $\mathbf{f}_{\text{int}}$ is

$$\mathbf{K}_T(\mathbf{d}^i_{n+1-\alpha_f}) = \frac{\partial \mathbf{f}_{\text{int}}(\mathbf{d}^i_{n+1-\alpha_f})}{\partial(\mathbf{d}^i_{n+1-\alpha_f})}. \tag{6.72}$$

the computation of the tangential stiffness matrix $\mathbf{K}_{\text{T}}(\mathbf{d}^i_{n+1-\alpha_f})$ is done numerically via perturbation method [Cor+19]. A comparison between different numerical estimations of the tangent stiffness matrix is done in Appendix C.

In conclusion, the Newton-Raphson method iteratively updates the independent variable $\mathbf{d}^i_{n+1}$ until the residual $\mathbf{r}_{\text{eff,dyn}}(\mathbf{d}^i_{n+1})$ of the system of equations is lower than a certain tolerance. this means that, at each iteration, it is required that

$$\text{Lin}\, \mathbf{r}_{\text{eff,dyn}}(\mathbf{d}^i_{n+1}) \stackrel{?}{=} \mathbf{0}. \tag{6.73}$$

This leads to the resolution of this system of equations:

$$\mathbf{K}_{\text{eff,dyn}}(\mathbf{d}^i_{n+1}) \cdot \Delta\mathbf{d}^{i+1}_{n+1} = -\mathbf{r}_{\text{eff,dyn}}(\mathbf{d}^i_{n+1}). \tag{6.74}$$

And, after computing the new displacements increment $\Delta\mathbf{d}^{i+1}_{n+1}$, one can update the displacements of this iteration $\mathbf{d}^{i+1}_{n+1}$ as:

$$\mathbf{d}^{i+1}_{n+1} = \mathbf{d}^i_{n+1} + \Delta\mathbf{d}^{i+1}_{n+1}, \tag{6.75}$$

And then the iteration counter $i = i + 1$ increases and the algorithm checks whether the residual of the new solution $\mathbf{d}^{i+1}_{n+1}$ is sufficiently low. One of the most important advantage of the Newton-Raphson methodology is the local quadratic convergence rate when the iteration $\mathbf{d}^0_{n+1}$ is close to the solution $\mathbf{d}_{n+1}$. In order to take advantage of this quadratic convergence rate one must use the exact tangent stiffness matrix $\mathbf{K}_T(\mathbf{d}^i_{n+1-\alpha_f})$, whose calculation is, in general, not trivial or rather expensive. In the case of this work, the constitutive tangent tensor $\mathcal{C}$ (see definition in Eq. (6.25)) is obtained via numerical derivation [Cor+19]. The different approaches for computing the secant or tangent constitutive tensor used in this work are discussed in the Appendix C. In general, the operations described in Eqs. (6.74) and (6.75) are repeated until a certain convergence criteria is fulfilled. Normally, the convergence criteria used are defined in terms of the L^2-norm of the residual $\mathbf{r}_{\text{eff,dyn}}$.

Chapter 7

FEM-DEM constitutive law: isotropic damage mechanics

Since the constitutive model of the FEM-DEM formulation is based on the widely known isotropic damage model [Oli+90], it is convenient to first expose its details and, subsequently, to detail the smoothing procedures, fracture modes and damage calculations performed within the FEM-DEM methodology.

7.1 Constitutive model background: isotropic damage model

In order to model the material degradation of the material (non-linear constitutive behaviour) an isotropic damage model have been used, originally developed by Oliver et al. [Oli+90] despite is not the only one [SJ87a; SJ87b; BPP], which were especially developed for crack analysis in concrete and frictional materials. The general behaviour of the model is depicted in Fig. 7.1. In this constitutive model, an internal damage variable d describes the material degradation. This scalar variable ranges from 0 (intact material) to 1 (fully damaged material). The constitutive relation between the strains and stresses is (assuming small strains: $\det(\mathbf{F}) \approx 1$):

$$\boldsymbol{\sigma} = \mathcal{C}_s\, \varepsilon = (1 - d)\, \mathcal{C}_0\, \varepsilon = (1 - d)\, \bar{\boldsymbol{\sigma}}, \tag{7.1}$$

where the effective stress tensor $\bar{\boldsymbol{\sigma}} = \mathcal{C}_0\, \varepsilon$, the elastic constitutive tensor $\mathcal{C}_0$ and

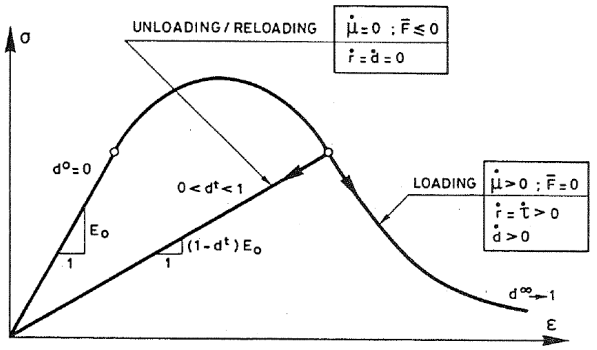

Figure 7.1: General behaviour of the isotropic damage model. Source: Oliver et al. [Oli+90].

the secant constitutive tensor $\mathcal{C}_s = (1 - d)\,\mathcal{C}_0$ have been introduced. Since in this work we are interested in model large displacements and rotations but strain are never large (the FEM-DEM methodology is used for simulating frictional materials and concrete) one can reformulate the same constitutive relation Eq. (7.1) in large displacements as

$$\mathbf{S} = \mathcal{C}_s\,\mathbf{E} = (1 - d)\,\mathcal{C}_0\,\mathbf{E} = (1 - d)\,\bar{\mathbf{S}}, \tag{7.2}$$

where **E** is the Green-Lagrange strain tensor defined in Eq. (6.10) and **S** is the second Piola-Kirchoff stress tensor. It is important to note that the isotropic damage model can also be derived from an associated strain energy potential whose definition is [Oll02]

$$\Psi(\varepsilon) = \frac{1 - \mathrm{d}}{2}(\varepsilon : \mathcal{C}_0 : \varepsilon). \tag{7.3}$$

In order to know whether the material is in elastic or plastic regime, one must define a yield surface and stablish a damage criterion such as:

$$\Phi = f(\bar{\mathbf{S}}) - \kappa \leq 0 \tag{7.4}$$

where $f(\mathbf{S})$ is the so-called equivalent effective stress whose definition depends on the yield surface of interest (Rankine, Mohr-Coulomb, Simo-Ju, Drucker-Prager, etc.), and κ is the stress threshold (related to the material strength), which each yield surface will define and updated afterwards. In order to see the expressions of $f(\mathbf{S})$ and κ of the yield surfaces used in this work the reader is referred to the Appendix B. The stress threshold κ has to be updated during calculation as:

$$\kappa = \max(\kappa_0, \max(f(\bar{\mathbf{S}})_t)) \; t \in [0, T], \tag{7.5}$$

which means that the material threshold is the maximum historical equivalent stress achieved if has ever been damaged. This ensures the irreversibility of the damaging process. Once the damage occurs, the internal damage variable d has to be computed. There are several expressions available for softening and hardening (usual in directional damage in compression [CT17]) but only the first option has been implemented in the scope of this work. In this regard, an exponential softening law for the damage has been considered as [Oli+90]:

$$d(\bar{\mathbf{S}}) = 1 - \frac{\kappa_0}{f(\bar{\mathbf{S}})} \exp\left(A\left(1 - \frac{f(\bar{\mathbf{S}})}{\kappa_0}\right)\right) \tag{7.6}$$

in which the A parameter is determined from the energy dissipated in an uniaxial tension test as [Oli+90]

$$A = \left(\frac{G_f E}{\hat{l} f_t^2} - \frac{1}{2}\right)^{-1} \geq 0 \tag{7.7}$$

being f_t is the tensile strength, G_f is the specific fracture energy per unit area (taken as a material property) and $\hat{l}$ is the characteristic length of the element. By using this normalization, the size-effect problem is overcome (see also Appendix A).

7.2 FEM-DEM smoothed isotropic damage model

In this section the main characteristics of the smoothed isotropic damage model are presented. The main difference of the FEM-DEM methodology with respect to the

standard isotropic damage model described previously is the fact that the damage d and the effective stress tensor $\tilde{\mathbf{S}}$ are evaluated at the FE edges. This smoothing procedure improves the effective stresses field quality and the stability of the solution (see appendix A). The smoothing presented follows the work developed by Zienkiewicz and Zhu [ZZ92c] in which they proved that this procedure can reduce the error when recovering stresses (gradients of nodal values) and efficiently improves the quality of the solution. Indeed, It has been demonstrated (see Chen [Chu80] and Levine [Lev82]) that evaluating the derivatives of the nodal values at the mid-sides of the adjacent elements is *super convergent*. This means that the error of the computed values at these *super-convergent* points decreases with a higher order of convergence than elsewhere.

7.2.1 Super-convergent patch recovery theoretical concept and application

Irreducible displacement based FE formulations like the one used in this work result in piece-wise continuous strains and stresses fields. This is an obvious approximation since the actual stresses may be continuous through all the domain. Super-convergence at one point means that the rate of convergence of the derivatives of a nodal variable (stress field in this case) is higher that in other points. In other words, the solution at those super-convergent points is more accurate.

Stress recovery procedures were developed initially to overcome the limitation of having piece-wise continuous strains and stresses fields , starting from the simplest form of averaging the stresses at each node from the shared adjacent IP. Indeed, it was proved that the difference between the results obtained with the Finite Element Analysis (FEA) and the ones computed via the recovered procedures were a good measure of the error committed with the simulation [ZZ92b; ZBZ99].

This motivated the development of several stress recovery procedures during the last decades like in [ZZ92c; ZZ92a; ZZ92b; ZZ95; ZBZ99; KGN00; GK00; GZH04]. The Super convergent Patch Recovery (SPR) developed by Zienkiewicz and Zhu [ZZ92c; ZZ92a; ZZ92b; ZZ95; ZBZ99] is one of the most used and effective recovery procedures for recovering stress fields.

According to Khoei and Gharehbaghi [KG07], the robustness and stability of the SPR is based on the super-convergence properties if structured meshes are used. Even with unstructured meshes, if some kind of remeshing is used, a certain level of

structure is given locally to the adapted zones of the FE mesh. The super-convergence properties of the SPR have been studied and demonstrated in Zhang [Zha00] for rectangular meshes and in Li and Zhang [LZ99] for linear triangular elements, which is the case of this work.

7.2.1.1 One-dimensional example

For the sake of simplicity, a one dimensional second-order equation example is used in order to describe all these concepts. The proposed equation can be seen as the displacement field u of an elastic bar with a variable cross-section. This equation reads [ZZT13]:

$$\frac{d}{dx}\left(k\frac{du}{dx}\right) + \beta u + Q = 0 \tag{7.8}$$

in addition to the necessary boundary conditions of the displacement or its gradients at the contour of the domain ($\partial\Omega$). Fig. 7.2 depicts the expected analytical solution for u and its gradient du/dx in addition to the approximate solution that would result from the FE calculation using linear elements. As can be seen, the exact solution of u is reached at the nodes of the elements[1] whereas for the gradients one can observe severe discrepancies at the nodes but, somewhere inside the element, the results are in agreement. Barlow [Bar76] experimentally observed that these interior points were in fact the Gauss IP of the element. In conclusion, the order of convergence of the main function and its gradient can be higher than the expected from its polynomial approximation and thus such locations are known to be *super-convergent*. The mathematical demonstration of this *super-convergence* can be studied in Hermann [Her72].

7.2.1.2 Super-convergent patch recovery

In the previous section it has been shown that the stresses evaluated at the IP of the element have the quality of super-convergence. However, could be interesting to have similar accurate quantities elsewhere within the element for general purposes. Since in previous sections we have seen that very large errors can exist beyond the super-convergent points, many attempts have been proposed to obtain a more

[1] This happens only if $\beta = 0$, k is constant at each element and polynomial shape functions are employed.

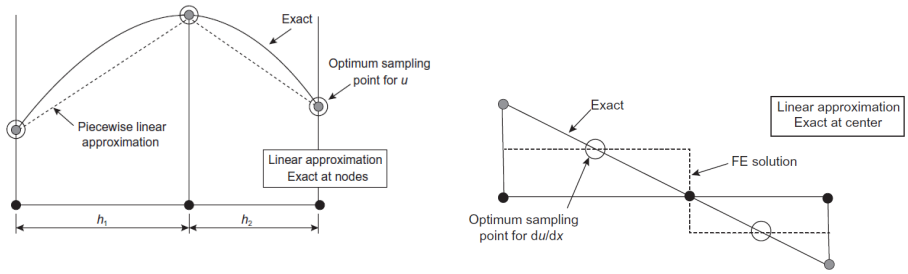

(a) (b)

Figure 7.2: Most accurate sample points for the main variable (a) and for its gradient (b). One dimensional linear elements. Image from Zienkiewicz et al. [ZZT13].

general picture of the stresses field which are more accurate overall [Kri94; QR89; Kri89; GW89]. An intuitive option could be to perform a smoothing of the sampling points within a *patch of elements* . Fig. 7.3 shows the geometrical interpretation o such patches for different kind of elements and order of approximation proposed by Zienkiewicz [ZZ92c; ZZ92a; ZZ92b; ZZ95; ZBZ99]. For simplex linear elements (triangles and tetrahedra), it has been demonstrated that the average values of the gradient (stresses) at mid sides of adjacent elements is super-convergent [Lev82; Chu80; GW89; Mat20]. This solution can be seen as an enrichment of the stress field thanks to obtaining information from the elements that share the patch.

7.2.2 Inclusion of the SPR to the isotropic damage model

As can be seen in Fig. 7.4, the effective stress tensor $\bar{\mathbf{S}}$ at the edges of the FE as the average of the two Integration Points (IP) that share its edge. In the case of 2D geometries, the effective stress tensor at the edge $\bar{\mathbf{S}}_{\text{edge}}$ i.e.

Besides, in the 3D version, the effective stress tensor is computed as the average of all the IP stresses (in this work only linear triangle/tetrahedra with 1 integration points are used) that share that edge (see Fig. 7.4.b and Eq. (7.9)):

$$\bar{\mathbf{S}}_{\text{edge}} = \frac{1}{n_{elem}} \sum_{i=1}^{n_{elem}} \bar{\mathbf{S}}_{\text{i,neighbour}} \tag{7.9}$$

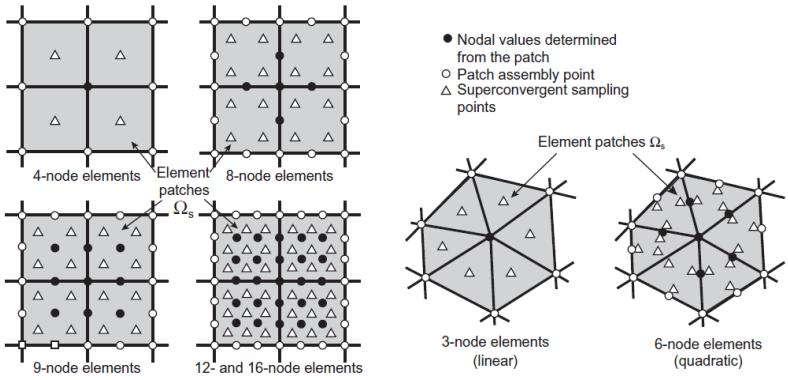

Figure 7.3: Interior super-convergent patches for quadrilateral and triangular elements of different order. Source: Zienkiewicz et al. [ZZT13].

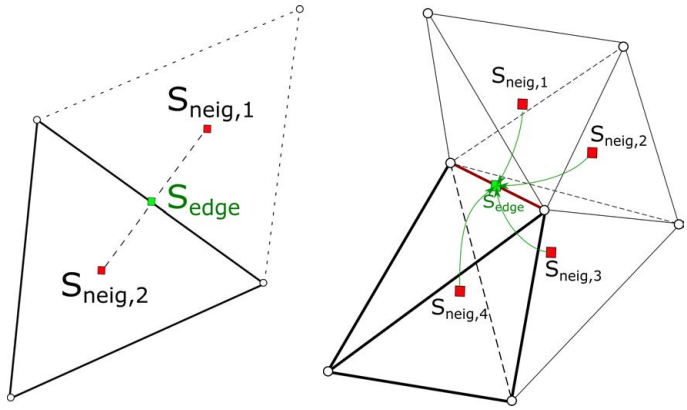

(a) 2D (b) 3D

Figure 7.4: *Super-convergent* points, "neigh" stands for neighbour.

Once the effective stress tensor is computed at the edge of the FE $\bar{\boldsymbol{\sigma}}_{edge}$, one must proceed in the same way that the standard isotropic damage model. This means that the damage criterion must be checked (Eq. (7.4)) and the damage value is computed at each edge (via Eq. (7.6)). Next, one must evaluate the elemental damage d_e that depends on the already computed damages at the edges $d_{i,edge}$. By analysing all the fracture modes that can occur, the damage of the element d_e is the one corresponding with the less energy mode (Fig. 7.5). In the 2D problem one can use the average of the two maximum damages at the element edges, as:

$$d_e = \frac{1}{2}\left(d_{\text{edge,max}} + d_{\text{edge,max}-1}\right) \tag{7.10}$$

Whereas in 3D the elemental damage d_e is computed as the maximum of the seven fracture modes d_i:

$$d_1 = \tfrac{1}{3}(d_{edge,1} + d_{edge,2} + d_{edge,3}) \tag{7.11a}$$
$$d_2 = \tfrac{1}{3}(d_{edge,1} + d_{edge,4} + d_{edge,5}) \tag{7.11b}$$
$$d_3 = \tfrac{1}{3}(d_{edge,2} + d_{edge,4} + d_{edge,6}) \tag{7.11c}$$
$$d_4 = \tfrac{1}{3}(d_{edge,3} + d_{edge,5} + d_{edge,6}) \tag{7.11d}$$
$$d_5 = \tfrac{1}{4}(d_{edge,2} + d_{edge,3} + d_{edge,4} + d_{edge,5}) \tag{7.11e}$$
$$d_6 = \tfrac{1}{4}(d_{edge,1} + d_{edge,2} + d_{edge,5} + d_{edge,6}) \tag{7.11f}$$
$$d_7 = \tfrac{1}{4}(d_{edge,1} + d_{edge,3} + d_{edge,4} + d_{edge,6}). \tag{7.11g}$$

This heuristic way of computing the elemental damage d_e ensures that if one fracture mode exhausts the material strength, that element is erased from the mesh (see Chapter 11).

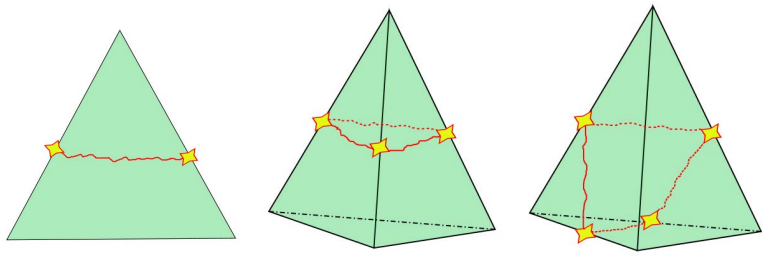

(a) 2D version (b) 3 Edged mode (c) 4 Edged mode

Figure 7.5: Different fracture modes in 2D and 3D element geometries. Source: Cornejo et al. [Cor+19].

Chapter 8

General orthotropy: non-linear constitutive modelling and orientation rotations

8.1 Introduction

In nature there are many materials of which mechanical properties vary according to the direction in which they are exerted. Specifically, in argillaceous or anisotropic rocks (slates, shales, phyllites, schists, gneisses, etc.) [SG11], the strength and stiffness of the rock material depends upon the orientation of the plane of weakness (Fig. 8.1). In order to be able to perform calculations involving anisotropic materials or rocks within the FEM-DEM formulation, the general *space mapping theory* [Oll+93; Oll+95; Oll03] has been implemented and adapted to the FEM-DEM.

Historically, the formulations used in anisotropic materials that exhibit non-linear behaviour are based on formulating anisotropic plastic potential and yield criteria, which likewise forces a reformulation of the constitutive law in its entirety [Hil71; Bas77; BLB91], which can be very difficult or even unfeasible for some cases.

By means of the *space mapping theory* it is possible to use the conventional isotropic non-linear constitutive models (damage, plasticity, viscoelasticity, etc.) to materials which elastic properties (Young modulus and Poisson ratio) and strengths (elas-

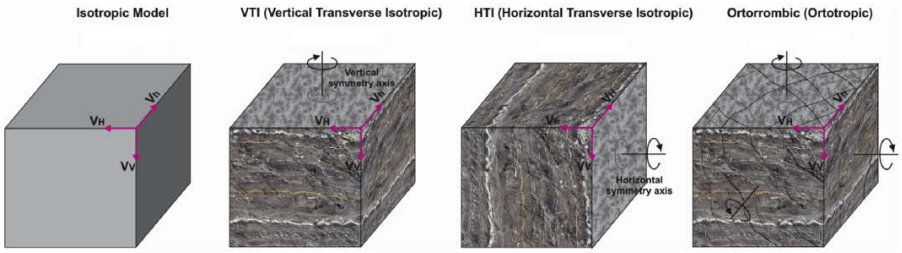

Figure 8.1: Different anisotropic rock configurations found in Vaca Muerta Formation, Argentina. Source: Sosa et al. [Sos+17].

tic limits) depend on the spatial direction without the need of formulating anisotropic yield functions and constitutive laws. In this sense, the mentioned formulation is based on transforming all the constitutive parameters of the material as well as its stress-strain state from a *real anisotropic space* to another *fictitious isotropic space*. Once there, an isotropic constitutive model can be used to integrate the material equation as is done conventionally in isotropic materials.

Additionally, in the case that the local axes of orthotropy are not aligned with the global axes of the problem, a set of rotations must be performed in order to take that misalignment into account. All these features and its adaption to the FEM-DEM are detailed in the following section.

8.2 General definition of an implicit orthotropic criterion

As introduced in the previous section, the traditional procedures that allow obtaining constitutive equations for non-linear anisotropic materials are based on reformulating the yield and plastic potential surfaces according to the anisotropic properties of the material. In this case, satisfying the invariance conditions can be difficult and, in some cases, impossible. Indeed, the mathematical formulation of constitutive laws for orthotropic non-proportional[1] solids is a complex problem. The mechanical behaviour of anisotropic materials in elasticity has been solved by a generalization of the Hooke's law (Matthews and Rawlings [MR94]) but the inelastic behaviour still has some limitations. The first attempts to formulate yield functions applicable to non-

[1] A non-proportional solid is characterized by showing a non constant ratio between the elastic modulus and yield strengths at each different direction.

proportional orthotropic materials are owed to Hill [Hil48] who in 1948 extended the isotropic Von Mises criterion to the orthotropic case and improving it in several posterior publications [Hil48; Hil65; Hil79; Hil90]. The main limitation of the formulations developed by Hill lies in their inability to represent the behaviour of pressure-sensitive materials, such as geo-materials or composites. In the following years, several authors have proposed different yield surfaces for anisotropic materials like in Bassani [Bas77] and Barlat et al. [BLB91]. In [BLB91] a linear transformation of the stress state of the anisotropic material by multiplying its components by different constants is performed.

Dvorak and Bahei-El-Din [DB82] involved tensorial operators together with the Von Mises criterion for the analysis of composite materials. Similarly, several authors have used fourth order tensors for formulating yield criteria for anisotropic materials like Shih and Lee [SL78], Eisemberg and Yen [EY84] and Voyiadjis and Foroozesh [VF90], to mention a few.

Conversely, the *implicit general definition* developed by Oller et al. [Oll+93; Oll+95; Oll03] employs a bijective transformation between two spaces, namely *real anisotropic space* (Ω_0) and *fictitious isotropic space* ($\check{\Omega}_0$)[2]. This implies that it is not necessary to mathematically formulate an anisotropic criterion, but that this is defined in a conventional way in an isotropic space and to admit the existence of a numerical transformation that allows the exchange of information between both spaces. In this sense, the symmetric operators that allow the mapping of stresses ($\mathbf{A}^S$), deformations ($\mathbf{A}^E$) and internal variables from one space to another must be defined in detail, always guaranteeing the invariance conditions.

8.2.1 Stress mapping operator $\mathbf{A}^S$

The transformation of the second Piola-Kirchoff stress vector (voigt notation) between the fictitious isotropic space $\check{\mathbf{S}}$ and the real anisotropic space[3] $\mathbf{S}$ is done via [Oll+95]:

$$\check{\mathbf{S}} := \mathbf{A}^S \cdot \mathbf{S} \tag{8.1}$$

[2] From now on, all the variables denoted by $[\check{\cdot}]$ means that are defined in the fictitious isotropic space

[3] Up to now, we assume that the local axes of orthotropy are aligned with the global axes. It is important to note that the mapping between the isotropic and the anisotropic space must be done in local axes.

where $\mathbf{A}^S$ is a matrix defined in the reference configuration and remains constant in that configuration. The simplified expression of $\mathbf{A}^S$ is [Oll+95]:

$$\mathbf{A}^S = \begin{bmatrix} \frac{f_t}{f_{t,xx}} & 0 & 0 & 0 & 0 & 0 \\ 0 & \frac{f_t}{f_{t,yy}} & 0 & 0 & 0 & 0 \\ 0 & 0 & \frac{f_t}{f_{t,zz}} & 0 & 0 & 0 \\ 0 & 0 & 0 & \frac{f_t}{f_{t,xy}} & 0 & 0 \\ 0 & 0 & 0 & 0 & \frac{f_t}{f_{t,yz}} & 0 \\ 0 & 0 & 0 & 0 & 0 & \frac{f_t}{f_{t,xz}} \end{bmatrix} \tag{8.2}$$

where f_t represents the yield stress in the isotropic space (reference value) and $f_{t,ij}$ is the yield stress in a certain geometrical direction.

8.2.2 Strain mapping operator $\mathbf{A}^E$

Analogously, the Green-Lagrange strain vector can be transformed from the real space to the isotropic space as:

$$\check{\mathbf{E}} := \mathbf{A}^E \cdot \mathbf{E} \tag{8.3}$$

where the strain mapper $\mathbf{A}^E$ is defined as:

$$\mathbf{A}^E = \left(\check{\mathcal{C}}_0\right)^{-1} \cdot \mathbf{A}^S \cdot \mathcal{C}_0 \tag{8.4}$$

being $\mathcal{C}_0$ the elastic constitutive tensor in the anisotropic space and $\check{\mathcal{C}}_0$ is the isotropic elastic constitutive tensor in the fictitious space[4].

It is important to note that Eq. (8.4) can be derived from Eq. (8.1) as:

$$\check{\mathbf{S}} = \mathbf{A}^S \cdot \mathbf{S} \tag{8.5a}$$

[4]The elastic properties used for the computation of this tensor can be arbitrary since its effect is cancelled when returning the results to the real space afterwards.

$$\Rightarrow \check{\mathcal{C}} \cdot \check{\mathbf{E}}^e = \mathbf{A}^S \cdot \mathcal{C} \cdot \mathbf{E}^e \tag{8.5b}$$

$$\Rightarrow \check{\mathcal{C}} \cdot \mathbf{A}^E = \mathbf{A}^S \cdot \mathcal{C} \tag{8.5c}$$

$$\Rightarrow \mathbf{A}^E = \left(\check{\mathcal{C}}\right)^{-1} \mathbf{A}^S \cdot \mathcal{C} \tag{8.5d}$$

8.2.3 Tangent tensor mapping

After a mathematical demonstration performed in Oller et al. [Oll+93; Oll+95; Oll03], the elastoplastic tangent constitutive tensor in the real anisotropic space ($\mathcal{C}$) can be computed from the one obtained in the isotropic space $\check{\mathcal{C}}$ as:

$$\mathcal{C} = \left(\mathbf{A}^S\right)^{-1} \cdot \check{\mathcal{C}} \cdot \mathbf{A}^E \tag{8.6}$$

8.2.4 Coordinate transformation of strains, stresses and constitutive tensors

In a general case, the orthotropic properties of the material are not aligned with the global axes of the problem but are arbitrarily oriented according to a set of Euler angles (ϕ, θ, ψ) (see Fig. 8.2). In that case, since the space mapping defined in the previous section between the real and the fictitious space are performed in local axes, one must orient the strains, stresses and constitutive matrices before conducting those operations.

An arbitrary vector $\mathbf{x}$ defined in global axes can be transformed to local axes (denoted by $\mathbf{x}'$) as [ZZT13]:

$$\mathbf{x}' = \mathbf{\Lambda} \cdot \mathbf{x} \;\text{ where }\; \mathbf{\Lambda} = \begin{bmatrix} l_1 & m_1 & n_1 \\ l_2 & m_2 & n_2 \\ l_3 & m_3 & n_3 \end{bmatrix}. \tag{8.7}$$

Matrix $\mathbf{\Lambda}$ is usually called a *rotation matrix*, which is an orthogonal matrix i.e. $\mathbf{\Lambda}^T = \mathbf{\Lambda}^{-1}$. The relation between the $\mathbf{\Lambda}$ coefficients ans the Euler angles is:

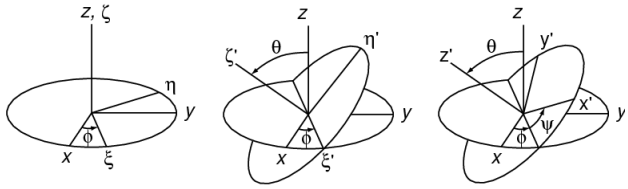

Figure 8.2: Graphical representation of Euler angles. Source: https://mathworld.wolfram.com/EulerAngles.html

$$
\begin{aligned}
l_1 &= \cos\psi\cos\phi - \cos\theta\sin\phi\sin\psi \\
m_1 &= \cos\psi\sin\phi + \cos\theta\cos\phi\sin\psi \\
n_1 &= \sin\psi\sin\theta \\
l_2 &= -\sin\psi\cos\phi - \cos\theta\sin\phi\cos\psi \\
m_2 &= -\sin\psi\sin\phi + \cos\theta\cos\phi\cos\psi \\
n_2 &= \cos\psi\sin\theta \\
l_3 &= \sin\theta\sin\phi \\
m_3 &= -\sin\theta\cos\phi \\
n_3 &= \cos\theta
\end{aligned}
\tag{8.8}
$$

In order to transform the Green-Lagrange strain vector $\mathbf{E}$ according to a set of Euler angles, an expansion and gathering of terms must be performed, obtaining [ZZT13]:

$$
\mathbf{E}' = \mathbf{T}_\varepsilon \cdot \mathbf{E} \tag{8.9}
$$

where $\mathbf{E} = \left\{\varepsilon_x \quad \varepsilon_y \quad \varepsilon_z \quad \gamma_{xy} \quad \gamma_{yz} \quad \gamma_{xz}\right\}^T$ and the strain transformation matrix is:

$$\mathbf{T}_{\varepsilon} = \begin{bmatrix} l_1^2 & m_1^2 & n_1^2 & l_1 m_1 & m_1 n_1 & n_1 l_1 \\ l_2^2 & m_2^2 & n_2^2 & l_2 m_2 & m_2 n_2 & n_2 l_2 \\ l_1^3 & m_3^2 & n_3^2 & l_3 m_3 & m_3 n_3 & n_3 l_3 \\ 2l_1 l_2 & 2m_1 m_2 & 2n_1 n_2 & l_1 m_2 + l_2 m_1 & m_1 n_2 + m_2 n_1 & n_1 l_2 + n_2 l_1 \\ 2l_2 l_3 & 2m_2 m_3 & 2n_2 n_3 & l_2 m_3 + l_3 m_2 & m_2 n_3 + m_3 n_2 & n_2 l_3 + n_3 l_2 \\ 2l_3 l_1 & 2m_3 m_1 & 2n_3 n_1 & l_3 m_1 + l_1 m_3 & m_3 n_1 + m_1 n_3 & n_3 l_1 + n_1 l_3 \end{bmatrix} \tag{8.10}$$

Operating one can find the relationship between the local and global stress vectors:

$$\mathbf{S} = \mathbf{T}_{\varepsilon}^{T} \cdot \mathbf{S}' \tag{8.11}$$

Finally, the relation between the global and the local constitutive tensor is

$$\mathcal{C} = \mathbf{T}_{\varepsilon}^{T} \cdot \mathcal{C}' \cdot \mathbf{T}_{\varepsilon}. \tag{8.12}$$

8.3 General non-linear orthotropic oriented algorithm

Now that all the operations required to perform a non-linear anisotropic calculation whose axes are rotated with respect to the global axes have been detailed, it is convenient to show the sequence of these operations using by describing an algorithm within an IP. In the case of the FEM-DEM, the damage is always computed in the fictitious isotropic space whereas the effective stress smoothing is conducted in the real anisotropic space and then mapped to the isotropic space.

8.4 Application example

In order to demonstrate the capabilities of the non-linear anisotropic formulation presented, a 3D holed shell is studied (see Fig. 8.3). The left end is clamped whereas

Algorithm 1 General non-linear orthotropic oriented algorithm

Time t and iteration k. Rotation matrices $\mathbf{\Lambda}$ and $\mathbf{T}_\varepsilon$ already computed

- Obtain the real global Green-Lagrange strain vector $\mathbf{E}$ from the element kinematics
- Rotate $\mathbf{E}$ to local axes via Eq. (8.9): $\mathbf{E}' = \mathbf{T}_\varepsilon \cdot \mathbf{E}$
- Map the local strain vector to the fictitious isotropic space via Eq. (8.3): $\check{\mathbf{E}} = \mathbf{A}^E \cdot \mathbf{E}'$
- Integrate the constitutive law in the isotropic space. If damage, Eq. (7.2) can be used: $\check{\mathbf{S}} = (1-d)\check{\mathcal{C}}_0 \cdot \check{\mathbf{E}}$
- Return the stress vector to the real local space via Eq. (8.1): $\mathbf{S}' = \left(\mathbf{A}^S\right)^{-1} \cdot \check{\mathbf{S}}$
- Return the tangent constitutive tensor to the real local space via Eq. (8.6): $\mathcal{C}' = \left(\mathbf{A}^S\right)^{-1} \cdot \check{\mathcal{C}} \cdot \mathbf{A}^E$
- Transform the stress vector to the global axes via Eq. (8.11): $\mathbf{S} = \mathbf{T}_\varepsilon^T \cdot \mathbf{S}'$
- Transform the tangent constitutive tensor to the global axes via Eq. (8.12): $\mathcal{C} = \mathbf{T}_\varepsilon^T \cdot \mathcal{C}' \cdot \mathbf{T}_\varepsilon$

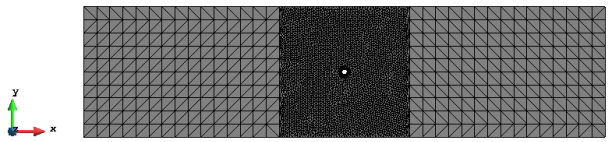

Figure 8.3: FE mesh used in the orthotropic non-linear case (6856 nodes).

only a horizontal displacement is imposed on the right end of the sample. The material used is orthotropic being E_x = 40 GPa and $E_y = E_z$ = 10 GPa. The Poisson ratios (ν = 0.2) and the yield strengths (f_t = 8 MPa) are assumed to be equal in all directions. The sample has a dimension of 2x0.5x0.02 m. Fig. 8.4 depicts the results obtained for different local axes orientations (rotation along z axis) in elastic regime. As can be seen, the orthotropy and orientation of the material induces a displacement along the y axis.

Additionally, a non-linear case has been studied. The material properties have been defined in the previous paragraph with the inclusion of an isotropic damage model in the fictitious space. The results obtained for different orientation can be seen in Fig. 8.5. As expected, the damage field rotates according to the Euler angle applied in each case.

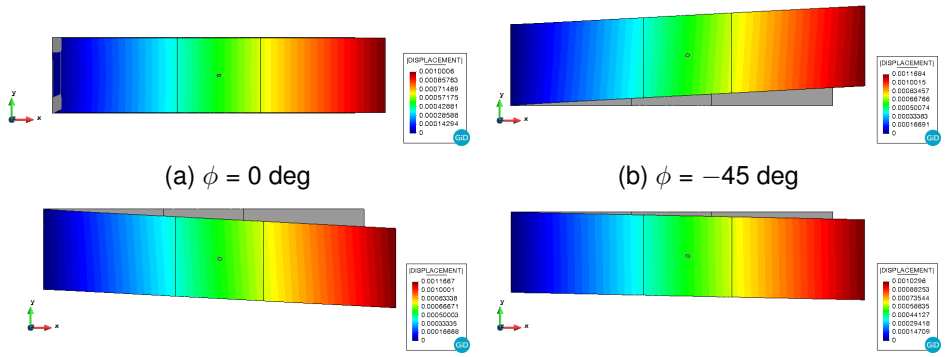

(a) ϕ = 0 deg (b) ϕ = -45 deg

(c) ϕ = 45 deg (d) ϕ = 70 deg

Figure 8.4: Numerical results in elastic regime for different orientations of the local axes. The angle ϕ rotates the local axes along the z axis. Deformation amplified x200 times.

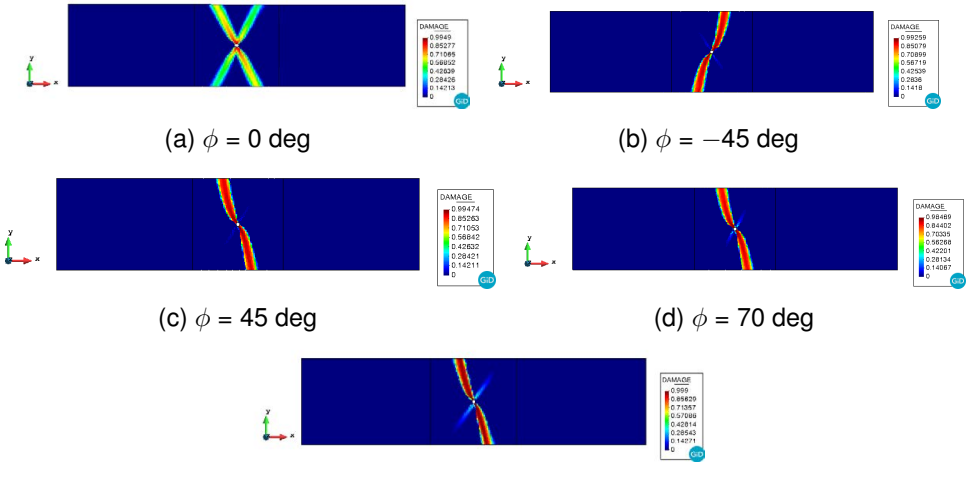

(a) ϕ = 0 deg (b) ϕ = -45 deg

(c) ϕ = 45 deg (d) ϕ = 70 deg

(e) ϕ = 15 deg

Figure 8.5: Numerical results in non-linear regime for different orientations of the local axes. The angle ϕ rotates the local axes along the z axis.

Chapter 9

Composite materials: rule of mixtures and plasticity

So far, the formulations developed in this work have been oriented to a single simple material, either isotropic or anisotropic. This is a major limitation, especially within the engineering field where, for example, in air plane fuselages, boat hulls, reinforced concrete structures, are formed by one or more layers of composite materials. Within the civil engineering field, in addition to the use of materials composed of concrete and steel -pre-stressed and/or reinforced concrete-, the reinforcement of structures through composite materials such as carbon fibre and epoxy resin laminates is particularly important. These types of reinforcements have experienced a great increase in use thanks to their excellent mechanical properties, good corrosion resistance and low weight compared to conventional simple materials.

Another use of reinforced composites is to replace steel bars in reinforced concrete with fibres. This application is especially recommended in areas of high corrosion or magnetism. In summary, the main characteristics of composite materials are:

- Low cost.
- Good structural behaviour, it dissipates a high quantity of energy before collapsing since the microcracking of the interface between the simple materials releases a remarkable amount of energy.

- Low weight.
- Massive industrial production is possible.
- Good thermal and acoustic isolation properties.
- Chemical resistance and thermal isolation.

However, composite materials are not exempt from a number of disadvantages. Among the shortcomings, it is important to mention:

- The composite materials exhibit non-linear behaviours even for low stress states.
- The manufacturing process of composite materials induces residual stresses very difficult to quantify and asses its effects.
- The reinforcement laminates usually change its mechanical properties due to its interaction with the environment.

For the use of these composite materials in structural parts, it is necessary to carry out a specific design of the material (number of layers, orientation of the layers, volumetric participation of matrix and fibre, etc.) that adapts to the solicitations to which it will be submitted. This design is of vital importance as composite materials are characterised by a high level of anisotropy. This requires the development of advanced constitutive models that are capable of capturing non-linear phenomena in some of the component materials as well as differentiated behaviour depending on the direction of the fibres and/or their anisotropy. An extensive description of the different composite materials usually used in industry, the reader is referred to Car (2000) [Car00].

In the framework of this work, the classical mixture theories -parallel Rule of Mixtures (RoM)- as well as the generalized Serial Parallel Rule of Mixtures (SPRoM) [Cor+18; Bar+19; Cor+15; Jim+20; JBO18] theory for long fibres have been implemented and adapted to the FEM-DEM. As far as the material components of the composite, within the scope of this work, the composite material will be composed by concrete -isotropic damage constitutive law- and steel rebars -isotropic plasticity with linear hardening- whose combined behaviour will be taken into account by the rule of mixtures. This is why the following section is a brief description of the constitutive model used for steel: isotropic plasticity. Subsequently, the different RoM implemented and its algorithmic details are exposed.

9.1 Isotropic plasticity for steel rebars

The theory of plasticity provides a framework for the constitutive simulation of materials that, after being subjected to loads beyond their elastic limit, maintain a residual deformation, also called plastic deformation. This phenomenological constitutive model has been effectively applied to a wide number of materials, such as metals, concrete, clays, soils, etc. [Hil71; Hil48; Mau92].

In order to simulate the material plastification of the steel rebars i.e. the development of inelastic deformations, an isotropic plasticity model based on the Von Mises yield surface (see Section B.7) has been considered. Additionally, only linear hardening of perfect plasticity has been contemplated in this work. An extensive description of the different phenomenological plasticity models can be studied in Souza et al. [SPO08] which has served as a basis of the implementation performed.

An idealized one-dimensional graphical description of the stress-strain evolution of the mathematical theory of plasticity can be seen in Fig. 9.1. In the first stage, under monotonic loading, the material exhibit elastic behaviour along the $O_0 - Y_0$ path. If the stress exceeds the yield stress of the virgin material (Y_0), a non-smooth change of stiffness -slope of the curve- is performed meaning that the material is developing plastic non-recoverable strains. This behaviour is depicted in Fig. 9.1 along the path $Y_0 - Z_1$. Eventually, the load can reduce its value and the stresses will reduce accordingly. In that case, the behaviour is assumed to be linear elastic with a constant plastic strain ε^p and a new yield limit σ_0. In this case, within the path $O_1 - Y_1$, the relationship between the uniaxial stress σ and the total strain ε is given by [SPO08]:

$$\sigma = E(\varepsilon - \varepsilon^p), \tag{9.1}$$

where E is the Young's modulus of the material of the sample. It is important to note that even though the plastic strain ε_p is no recoverable, the current elastic strain $\varepsilon^e = \varepsilon - \varepsilon^p$ is fully reversible, which encourages the additive decomposition of the strains in the mathematical theory of plasticity.

9.1.1 Integration algorithm for the isotropic hardening Von Mises model

One of the main hypothesis of the small strain theory of plasticity is the additive decomposition of the total strain ε as the sum of an elastic -recoverable- strain ε^e, and a plastic -permanent- strain ε^p:

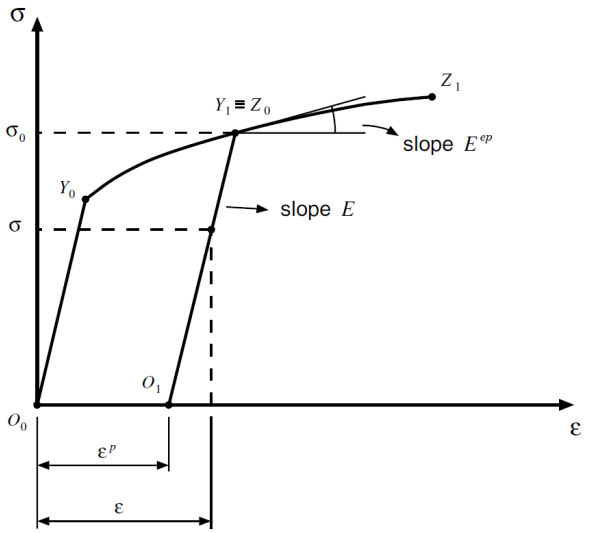

Figure 9.1: Stress-strain behaviour of an steel sample submitted to an uniaxial tension experiment. Source: Souza et al. [SPO08].

$$\varepsilon = \varepsilon^e + \varepsilon^p \tag{9.2}$$

where the elastic strain has been stated as

$$\varepsilon^e = \varepsilon - \varepsilon^p. \tag{9.3}$$

The isotropic plasticity constitutive law in small strains framework is defined as

$$\boldsymbol{\sigma} = \mathcal{C}_0 \varepsilon^e = \mathcal{C}_0(\varepsilon - \varepsilon^p). \tag{9.4}$$

being $\mathcal{C}_0$ the isotropic elastic constitutive tensor. Note that once a certain quantity of plastic deformation has been developed, its effect is non-recoverable, which is reflected in the constitutive law. Then, in order to delimit the elastic regime for a given stress state, that is, to know the moment when a stress state exceeds a critical value that makes it enter a non-linear regime, a yield criterion $\Phi(\boldsymbol{\sigma}, \sigma_y)$ must be defined.

Usually, yield criteria are mathematically defined as a real function of tensor variable[1] whose value is negative when the material is in an elastic regime and is identical to zero when plastification is imminent. In other words, plastic flow will develop only when

$$\Phi(\boldsymbol{\sigma}, \sigma_y) = \overbrace{\sqrt{3J_2(\mathbf{s}(\boldsymbol{\sigma}))}}^{\text{Von Mises criterion}} - \sigma_y = 0, \tag{9.5}$$

where $\boldsymbol{\sigma}$ is the stress tensor, $\mathbf{s}$ corresponds to the deviatoric part of the stress tensor and σ_y is the uniaxial yield stress. Must be said that the uniaxial yield stress depends on an internal variable as $\sigma_y = \sigma_y(\bar{\varepsilon}^p)$, which is the accumulated plastic strain $\bar{\varepsilon}^p$. For linear isotropic hardening, the evolution equation for the uniaxial yield stress is:

$$\sigma_y = \sigma_0 + H \cdot \bar{\varepsilon}^p \tag{9.6}$$

where σ_0 is the virgin material yield stress and H is the constant *hardening modulus*. Note that if the *hardening modulus* is null, perfect plasticity model is recovered. This equation implies that the yield surface (defined in Eq. (9.9)) will change its shape, expanding or contracting according to this hardening modulus.

In this regard, the yield criterion defines an *elastic domain* as

$$\mathcal{E} = \{\boldsymbol{\sigma} | \Phi(\boldsymbol{\sigma}, \sigma_y) < 0\} \tag{9.7}$$

in which the plastification is not possible. This means that any stress state lying inside the elastic domain is said to be plastically admissible. Now one can define the *set of plastically admissible stresses* as [SPO08]

$$\bar{\mathcal{E}} = \{\boldsymbol{\sigma} | \Phi(\boldsymbol{\sigma}, \sigma_y) \leq 0\} \tag{9.8}$$

As stated before, the boundary of the yield criterion, i.e. when $\Phi(\boldsymbol{\sigma}, \sigma_y) = 0$, can be represented by a hyper-surface in the stress space usually named as *yield surface*. This yield surface is mathematically defined as:

[1] This kind of functions take as an input a tensor, in this case the stress tensor, and returns a 1-D representation of this stress state.

$$\mathcal{Y} = \{\boldsymbol{\sigma} | \Phi(\boldsymbol{\sigma}, \sigma_y) = 0\} \tag{9.9}$$

To finalize the mathematical formulation of the isotropic plasticity models, it is necessary to introduce the concepts of *plastic flow rule* and *hardening law*. This two entities define the evolution of the internal variables of the problem, which are the variables associated to the plastic dissipation phenomena. For a general case, one can state a plastic flow rule and the evolution equation for the hardening internal variable by

$$\dot{\boldsymbol{\varepsilon}}^p = \dot{\gamma}\mathbf{N} = \overbrace{\dot{\gamma}\sqrt{\frac{3}{2}}\frac{\mathbf{s}}{\|\mathbf{s}\|}}^{\text{only for Von Mises criterion}} , \tag{9.10}$$

$$\dot{\varepsilon}^p = \sqrt{\frac{2}{3}}\,\|\dot{\boldsymbol{\varepsilon}}^p\| = \dot{\gamma} \tag{9.11}$$

where the tensor $\mathbf{N}$ is the so-called *flow vector*, $\dot{\boldsymbol{\varepsilon}}^p$ corresponds to the plastic strain increment and $\dot{\gamma}$ is the plastic multiplier. The aforementioned equations (9.10)-(9.11) must be complemented by the loading/unloading conditions[2], i.e.

$$\Phi \leq 0, \quad \dot{\gamma} \geq 0, \quad \Phi\dot{\gamma} = 0, \tag{9.12}$$

that stablish when the plastification occurs ($\dot{\gamma} > 0$).

When formulating plasticity models in a general tensorial approach, it is very common and useful to define the flow rule in terms of a *plastic potential* Ψ. Obviously, one must assume the existence or the possibility to be formulated a plastic potential as

$$\Psi = \Psi(\boldsymbol{\sigma}, \sigma_y) \tag{9.13}$$

whose partial derivative with respect the stresses define the flow vector $\mathbf{N}$:

[2] Also called Kuhn-Tucker conditions [Mau92], which is an alternative representation of the maximum dissipation axiom.

$$\mathbf{N} \equiv \frac{\partial \Psi}{\partial \boldsymbol{\sigma}}. \tag{9.14}$$

In the framework of this work, since the material whose constitutive model is represented by the isotropic plasticity is steel, it is a good choice to assume that the plasticity is *associative*[3] [SPO08]. This means that the yield function and the plastic potential are the same entities, i.e.

$$\Phi \equiv \Psi. \tag{9.15}$$

In order to obtain the value of the plastic multiplier $\dot{\gamma}$, after a mathematical elaboration (see Souza et al. [SPO08]) that takes as starting point an additional consistency condition $\dot{\Phi}\dot{\gamma} = 0 \implies \dot{\Phi} = 0$ one can obtain, for the case of linear hardening -which has a closed form in the case of associative Von Mises isotropic hardening-:

$$\dot{\gamma} = \frac{\Phi(\boldsymbol{\sigma}, \sigma_y)}{3G + H} \tag{9.16}$$

being $G = \dfrac{E}{2(1+\nu)}$ the shear modulus and H the aforementioned hardening modulus.

9.1.2 Implicit return mapping algorithm

The *return mapping* procedure can be seen as a set of operations whose aim is to correct a plastically inadmissible stress prediction i.e. $\Phi(\boldsymbol{\sigma}_{n+1}^{trial}, \sigma_{y,n}) > 0$ iteratively until the stress state lies on the yield surface, which means that the stress state becomes plastically admissible. This correction is performed via an iterative calculation of plastic strain increments (see Eq. (9.10)) until the yield criterion is fulfilled i.e. $\Phi(\boldsymbol{\sigma}_{n+1}, \sigma_{y,n+1}) = 0$. This idea is depicted in Fig. 9.2 in which the stress predictor $\boldsymbol{\sigma}_{n+1}^{trial}$ is located outside the yield surface and, after a plastic correction inwards, the admissible stress state $\boldsymbol{\sigma}_{n+1}$ lies on the updated yield surface. Fig. 9.2 also shows the concept of hardening. Indeed, for the case of linear hardening, one can see how

[3] Another interesting property of the *associative* plasticity models is that the plastic strain rate is always normal to the yield surface in the stress space.

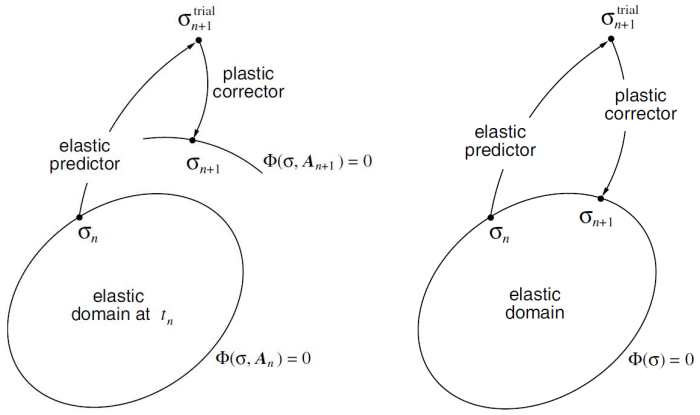

(a) Hardening (b) Perfect plasticity

Figure 9.2: Different return mapping schemes. Source: Souza et al. [SPO08].

the updated yield surface has expanded according to a certain level of plastification whereas in the perfect plasticity case it remains constant.

The return mapping methodology described has been summarized in the following algorithm. For the sake of simplicity, the equations and operations have been simplified to the associative isotropic plasticity based on the Von Mises yield surface and linear hardening, which is the scope of the implementation.

9.2 Reinforced concrete modelization within the FEM-DEM: rule of mixtures

The reinforced concrete material can be seen as a composite material composed by two main simple materials: concrete and steel rebars. Now that the constitutive models of each material component (isotropic damage for the concrete and isotropic plasticity for steel) have been described, it is convenient to study how this two constitutive models interact between in each other when are combined in a composite material. This integration of the different constitutive models adopted for each simple material is conducted by the definition of a Rule of Mixtures (RoM).

There are various theories that have enabled to simulate the constitutive behaviour

Algorithm 2 Implicit return mapping algorithm

- Initialization of the step $n+1$. $\varepsilon_{n+1} = \varepsilon_n + \boldsymbol{\Delta}\varepsilon$.
- Calculation of the stress predictor via Eq. (9.4): $\boldsymbol{\sigma}^{trial}_{n+1} = \boldsymbol{\mathcal{C}}_0(\varepsilon_{n+1} - \varepsilon^p_n)$

Check the yield criterion:

- **if** $\Phi(\boldsymbol{\sigma}^{trial}_{n+1}, \sigma_{y,n}) < 0$ **then**

  Elastic behaviour, update stresses and internal variables:

  - Update stresses $\boldsymbol{\sigma}_{n+1} = \boldsymbol{\sigma}^{trial}_{n+1}$
  - Update plastic strain vector $\varepsilon^p_{n+1} = \varepsilon^p_n$
  - Update accumulated plastic strain $\bar{\varepsilon}^p_{n+1} = \bar{\varepsilon}^p_n$

  EXIT

end

- **else**

  Return mapping required:

  - Compute the plastic multiplier via Eq. (9.16): $\dot{\gamma} = \dfrac{\Phi(\boldsymbol{\sigma}^{trial}_{n+1}, \sigma_{y,n})}{3G + H}$
  - Calculate the updated acumulated plastic strain by Eq. (9.11): $\bar{\varepsilon}^p_{n+1} = \bar{\varepsilon}^p_n + \dot{\gamma}$
  - Compute the updated uniaxial yield stress By Eq. (9.6): $\sigma_{y,n+1} = \sigma_0 + H \cdot \bar{\varepsilon}^p_{n+1}$
  - Update the plastic strain via Eq. (9.10): $\varepsilon^p_{n+1} = \varepsilon^p_n + \dot{\gamma}\sqrt{\dfrac{3}{2}}\dfrac{\mathbf{s}}{\|\mathbf{s}\|}$
  - Update stresses: $\boldsymbol{\sigma}_{n+1} = \boldsymbol{\mathcal{C}}_0(\varepsilon_{n+1} - \varepsilon^p_{n+1})$

  EXIT

end

of composite materials (see an extensive description in Car [Car00] and Zalamea [Zal00]), one of them is the already mentioned RoM (Trusdell and Toupin [TT60]) that is usually limited elastic behaviour and, if certain modifications are added, non-linear constitutive models can be used in the material components. Additionally, this theory states that the materials that coexist in a certain point of the space are submitted to the same strain state (parallel behaviour). This hypothesis implies a strong limitation when simulating general composite materials. In order to overcome this limitation, a general rule of mixtures or SPRoM [Cor+18; Bar+19; Jim+20; JBO18] was developed that is capable of simulating serial and parallel behaviour between the different components of the composite material. The SPRoM combined with the general anisotropy described in Chapter 8 represents a very powerful tool when highly anisotropic composite materials are involved.

The following is a description of the classical and the generalized serial/parallel

mixing theories. The first is a coarser approach but with a much more moderate computational cost. The second theory generalises the behaviour of the classical theory in order to represent highly anisotropic and fibre-oriented composites.

9.2.1 Classical rule of mixtures

The classical mixing theory (also called parallel mixing theory) was initially proposed by Trusdell and Toupin [TT60] in the 1960s and subsequently served as the basis for future work in the field, namely Green and Naghdi [GN65], Ortiz and Popov [OP82], Oller et al. [Oll+96], Oller and Oñate [OO96].

The classical RoM is based on the mechanics of the continuous medium locally, i.e. it is suitable for representing the behaviour of composite materials at one location in the solid. The theory implies the following basic hypotheses [Oll03]:

- i. Each point of the composite material involves a set of component materials
- ii. Each component material contributes to the behaviour of the compound in the same proportion as its volumetric participation
- iii. All the components have the same strain state (iso-strain condition)

The second hypothesis implies that the component materials are uniformly distributed along the composite volume. The interaction between the different constituent components depends on the volumetric participation ($k_i = V_i / V_t$) and its geometrical distribution. This allows the combination of different constitutive models for each constituent material.

The third hypothesis states the following condition (in small strain framework) for the n constituents

$$\varepsilon = \varepsilon_1 = ... = \varepsilon_n \tag{9.17}$$

and, according to the constitutive model of each material component, the stress of the constituent can be obtained ($\sigma_i = \mathfrak{C}_{law,i}(\varepsilon_i)$). Finally, the stress of the composite can be calculated as

$$\boldsymbol{\sigma} = \sum_{i=1}^{n} k_i \cdot \boldsymbol{\sigma}_i. \tag{9.18}$$

Analogously, the elastic constitutive tensor of the composite is obtained with

$$\mathcal{C}_0 = \sum_{i=1}^{n} k_i \cdot \mathcal{C}_{0,i}. \tag{9.19}$$

The previous expression can be used when computing the tangent constitutive tensor but, in order to ensure a quadratic convergence rate, a numerical derivation of the tangent constitutive tensor is required (see Appendix C).

9.2.2 Serial/Parallel rule of mixtures

The SPRoM [Cor+18; Bar+19; Jim+20; JBO18; Ras+08] defines two different compatibility conditions between the strain and stress states of the composite constituent materials: it formulates an iso-strain condition on the parallel direction, usually the fibre direction, and it defines an iso-stress condition on the serial direction, usually the remaining directions. Using these compatibility equations in a composite made of matrix and fibre, if the matrix structural capacity is lost due to excessive shear stresses, the iso-stress condition also reduces the shear capacity of the fibre, and, consequently, the composite serial strength is also reduced.

Since the behaviour of the composite is different depending on the serial or parallel direction, one must split the strain and stress tensors in their serial and parallel parts (denoted with the subscript "s" and "p" correspondingly). This is done with two complementary fourth order projector tensors, one corresponding to the serial direction ($\mathbb{P}_s$) and the other to the parallel direction ($\mathbb{P}_p$). These tensors are defined from the fibre axial direction in the composite. Thus,

$$\boldsymbol{\varepsilon} = \boldsymbol{\varepsilon}_p + \boldsymbol{\varepsilon}_s, \tag{9.20}$$

being $\boldsymbol{\varepsilon}_p$ the strain in the parallel direction, i.e.

$$\boldsymbol{\varepsilon}_p = \mathbb{P}_p : \boldsymbol{\varepsilon} \tag{9.21}$$

and ε_s the strain in the serial direction:

$$\varepsilon_s = \mathbb{P}_s : \varepsilon. \tag{9.22}$$

The fourth order projector tensors in the serial and parallel direction are computed as

$$\mathbb{P}_p = \mathbf{N}_p \otimes \mathbf{N}_p \text{ with } \mathbf{e}_1 \otimes \mathbf{e}_1 \tag{9.23}$$

and

$$\mathbb{P}_s = \mathbf{I} - \mathbb{P}_p \tag{9.24}$$

where $\mathbf{e}_1$ the director vector that determines the parallel behaviour (fibre direction), and $\mathbf{I}$ the identity tensor. The stress state may be split analogously, finding its parallel and serial parts using also the 4th order tensors $\mathbb{P}_p$ and $\mathbb{P}_s$:

$$\boldsymbol{\sigma} = \boldsymbol{\sigma}_p + \boldsymbol{\sigma}_s, \tag{9.25}$$

with

$$\boldsymbol{\sigma}_p = \mathbb{P}_p : \boldsymbol{\sigma} \text{ and } \boldsymbol{\sigma}_s = \mathbb{P}_s : \boldsymbol{\sigma}. \tag{9.26}$$

9.2.2.1 Main hypothesis for the numerical formulation

The SPRoM assumes the following hypothesis in order to take into account the strain-stress states defined in the previous paragraphs:

- i. The composite is composed by only two components: fibre and matrix
- ii. Component materials have the same strain in parallel (fibre) direction.
- iii. Component materials have the same stress in serial direction.
- iv. Composite material response is in direct relation with the volume fractions of compounding materials.
- v. Homogeneous distribution of phases is considered in the composite.
- vi. Perfect bonding between components is considered.

9.2.2.2 Constitutive models of simple materials (components)

Each composite component material is computed by means of its own constitutive equation $\mathfrak{C}_{law}$. So, the stresses in the matrix and fibre materials are obtained using:

$$ {}^{m}\boldsymbol{\sigma} = {}^{m}\mathfrak{C}_{law}({}^{m}\varepsilon) \text{ and } {}^{f}\boldsymbol{\sigma} = {}^{f}\mathfrak{C}_{law}({}^{f}\varepsilon) \tag{9.27} $$

where the superscript ${}^{m}[\cdot]$ and ${}^{f}[\cdot]$ corresponds to the matrix or fibre variable, correspondingly. In the case of linear elasticity in small strains one can rewrite Eq. (9.27) as

$$ {}^{m}\boldsymbol{\sigma} = {}^{m}\boldsymbol{\mathcal{C}}_0\,{}^{m}\varepsilon \text{ and } {}^{f}\boldsymbol{\sigma} = {}^{f}\boldsymbol{\mathcal{C}}_0\,{}^{f}\varepsilon. \tag{9.28} $$

where ${}^{m}\boldsymbol{\mathcal{C}}_0$ and ${}^{f}\boldsymbol{\mathcal{C}}_0$ are the elastic constitutive tensors in the matrix and fibre, respectively. The previous equations can be rewritten taking into account the serial-parallel split of the strain and stress tensors:

$$ \begin{bmatrix} \boldsymbol{\sigma}_P \\ \boldsymbol{\sigma}_S \end{bmatrix} = \begin{bmatrix} \boldsymbol{\mathcal{C}}_{PP} & \boldsymbol{\mathcal{C}}_{PS} \\ \boldsymbol{\mathcal{C}}_{SP} & \boldsymbol{\mathcal{C}}_{SS} \end{bmatrix} : \begin{bmatrix} \varepsilon_P \\ \varepsilon_S \end{bmatrix} \tag{9.29} $$

Where:

$$ \begin{aligned} \boldsymbol{\mathcal{C}}_{PP} &= \mathbb{P}_p : \boldsymbol{\mathcal{C}} : \mathbb{P}_p = \frac{\partial \boldsymbol{\sigma}_P}{\partial \varepsilon_P} & \boldsymbol{\mathcal{C}}_{PS} &= \mathbb{P}_p : \boldsymbol{\mathcal{C}} : \mathbb{P}_s = \frac{\partial \boldsymbol{\sigma}_P}{\partial \varepsilon_S} \\ \boldsymbol{\mathcal{C}}_{SP} &= \mathbb{P}_s : \boldsymbol{\mathcal{C}} : \mathbb{P}_p = \frac{\partial \boldsymbol{\sigma}_S}{\partial \varepsilon_P} & \boldsymbol{\mathcal{C}}_{SS} &= \mathbb{P}_s : \boldsymbol{\mathcal{C}} : \mathbb{P}_s = \frac{\partial \boldsymbol{\sigma}_S}{\partial \varepsilon_S} \end{aligned} \tag{9.30} $$

Using the compatibility conditions written above, the following expressions can be derived for a composite material with only two components: fibre and matrix.

$$ \varepsilon = {}^{f}k\,{}^{f}\varepsilon + {}^{m}k\,{}^{m}\varepsilon \qquad \boldsymbol{\sigma} = {}^{f}k\,{}^{f}\boldsymbol{\sigma} + {}^{m}k\,{}^{m}\boldsymbol{\sigma} \tag{9.31} $$

$$ \text{Parallel direction} : \begin{cases} {}^{c}\varepsilon_P = {}^{f}\varepsilon_P = {}^{m}\varepsilon_P \\ {}^{c}\boldsymbol{\sigma}_P = {}^{f}k\,{}^{f}\boldsymbol{\sigma}_P + {}^{m}k\,{}^{m}\boldsymbol{\sigma}_P \end{cases} \tag{9.32} $$

$$\text{Serial direction}: \begin{cases} {}^{c}\varepsilon_S = {}^{f}k\,{}^{f}\varepsilon_S + {}^{m}k\,{}^{m}\varepsilon_S \\ {}^{c}\boldsymbol{\sigma}_S = {}^{f}\boldsymbol{\sigma}_S = {}^{m}\boldsymbol{\sigma}_S \end{cases} \tag{9.33}$$

where superscripts c, m and f stand for composite, matrix and fibre, respectively and k corresponds to the volume fraction coefficient of each constituent in the composite.

9.2.2.3 Algorithm for the solution of the SPRoM problem

The known variable that enters the algorithm (input) is the strain state ${}^{c}\varepsilon$ of the composite material at time $t + \Delta t$. From this input, the SPRoM has to find a pair of strain/stress tensors for each component that fulfils the equilibrium, compatibility and the constitutive equations in each integration point (see Fig. 9.3). The first thing done by the algorithm is to split the strain tensor into its parallel and its serial parts, in order to compute the strain state in the matrix and the fibre. The parallel strain component is, the same for both materials and for the composite. On the other hand, the serial strain component requires a prediction of the strains expected in one of the composite components. If this prediction is done for the matrix (could be the fibre), the increment of its serial strains can be computed as:

$$\left[{}^{m}\Delta\varepsilon_S\right]_0 = \boldsymbol{\mathcal{A}} : \left[{}^{t}\left[{}^{f}\mathcal{C}_{SS}\right] : [\Delta\varepsilon_S]_0 + {}^{f}k\left({}^{t}\left[{}^{m}\mathcal{C}_{SP}\right] - {}^{t}\left[{}^{f}\mathcal{C}_{SP}\right]\right) : [\Delta\varepsilon_P]_0\right] \tag{9.34}$$

being $\boldsymbol{\mathcal{A}} = \left({}^{f}k^{t}\left[{}^{m}\mathcal{C}_{SS}\right] + {}^{m}k^{t}\left[{}^{f}\mathcal{C}_{SS}\right]\right)^{-1}$.

The initial approximation of the independent variable ${}^{m}\varepsilon_S$, proposed by Rastellini et al. [Ras+08] and described in the Eq. (9.34), is computed considering that the distribution of total strain, in its parallel and serial parts. Its computation is done using the composite tangent stiffness matrix from the previous time step. With the prediction of the matrix serial strains, the fibre serial strains can be computed, in the iteration step n, according to Eq. (9.33).

The first thing to do before the serial stress imbalance could be estimated, is to determine the total strains for each component:

$$\begin{aligned} \left[{}^{m}\varepsilon\right]_k &= \left[{}^{m}\varepsilon_P\right] + \left[{}^{m}\varepsilon_S\right]_k, \text{ where: } \left[{}^{m}\varepsilon_P\right] = \left[{}^{f}\varepsilon_P\right] = [\varepsilon_P] \\ \left[{}^{f}\varepsilon\right]_k &= \left[{}^{f}\varepsilon_P\right] + \left[{}^{f}\varepsilon_S\right]_k, \text{ where: } \left[{}^{f}\varepsilon_S\right]_k = \frac{1}{{}^{f}k}[\varepsilon_S] - \frac{{}^{m}k}{{}^{f}k}\left[{}^{m}\varepsilon_S\right]_k \end{aligned} \tag{9.35}$$

Finally, the stresses and the internal variables are computed based on the real constitutive model of each component material via Eq. (9.27) (the elastic hypothesis used at step 1 is no longer valid) and the residual $\Delta\boldsymbol{\sigma}_S = {}^{m}\boldsymbol{\sigma}_S - {}^{f}\boldsymbol{\sigma}_S$ is evaluated.

If the residual stress is lower than a certain tolerance, the equilibrium is achieved and the structural Newton-Raphson can continue. However, if $\Delta\boldsymbol{\sigma}_S > tol$, the initial approximation of the ${}^{m}\boldsymbol{\varepsilon}_s$ must be updated like in any Newton-Raphson strategy. Using this strategy, the update is made using the Jacobian of the residual forces. It is obtained deriving the residue function with respect to the unknown. According to Rastellini et al. [Ras+08], the expression for the Jacobian is given as follows:

$$ {}^{t+\Delta t}[\mathcal{J}]_k = {}^{t+\Delta t}\left[{}^{m}\mathcal{C}_{SS}\right]_k + \frac{{}^{m}k}{{}^{f}k}\,{}^{t+\Delta t}\left[{}^{f}\mathcal{C}_{SS}\right]_k \tag{9.36} $$

and the correction of the matrix serial strains becomes

$$ {}^{t+\Delta t}\left[{}^{m}\boldsymbol{\varepsilon}_S\right]_{k+1} = {}^{t+\Delta t}\left[{}^{m}\boldsymbol{\varepsilon}_S\right]_k - {}^{t+\Delta t}[\mathcal{J}]_k^{-1} : [\Delta\boldsymbol{\sigma}_S]_k \,. \tag{9.37} $$

In order to compute the tangent constitutive tensor of the composite material ${}^{c}\mathcal{C}$ we take advantage of the numerical derivation described in Appendix C, which is general and can adapt to any combination of component materials and constitutive models.

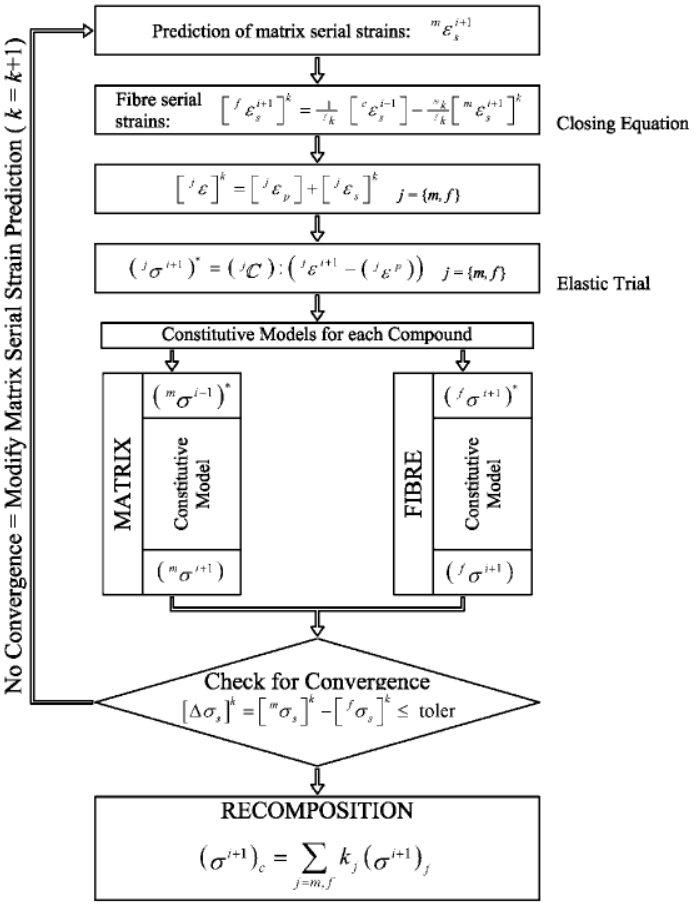

Figure 9.3: Serial Parallel rule of mixtures algorithm. Source: Oller (2003) [Oll03].

Chapter 10

The discrete element method (DEM)

Since the FEM-DEM formulation implies the generation of DE inside the FE mesh, it is necessary to review the principal characteristics of the DEM.

Extensive research work on the DEM has been carried out in the last decades since the first ideas were presented by Cundall and Strack [CS79]. Much of the research efforts have focused on the development of adequate DEM models for accurately reproducing the correct behaviour of non cohesive and cohesive granular assemblies as well as of solid materials. In recent years the DEM has also been effectively applied to the study of multi-fracture and failure of geo-materials (soils and rocks), concrete, masonry and ceramic materials, among others.

10.1 Introduction to the DEM

Within the analysis of solids with the DEM the material is typically represented as a collection of rigid particles (spheres in 3D and discs in 2D) interacting among themselves at the contact interfaces in the normal and tangential directions. Material deformation is assumed to be concentrated at the contact points. Appropriate contact laws are defined in order to obtain the desired macroscopic material properties. The contact law can be seen as the formulation of the material model of the underlying continuum at the microscopic level. For frictional cohesive material the contact law

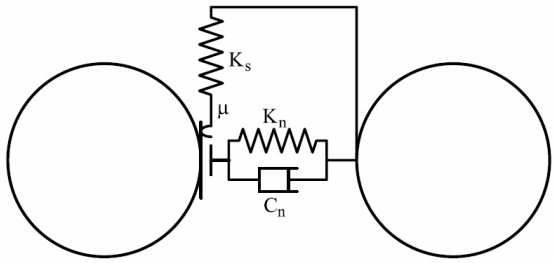

Figure 10.1: Model of the contact interface in the DEM. Image from [Oña+15]

takes into account the cohesive bonds between rigid particles. Cohesive bonds can be broken, thus allowing to simulate fracture of the material and its propagation.

A challenge in the failure analysis of solid materials, such as cement, shale rock and concrete, with the DEM is the definition of the limit strengths in the normal and shear directions at the contact interfaces, and the characterization of the non-linear relationship between forces and displacements at these interfaces beyond the onset of fracture, accounting for frictional effects, damage and plasticity.

10.2 Earliest Formulations DEM

Because this chapter's objective is to introduce the DEM, the earliest and simplest formulations are presented, which are, additionally, the better way to understand the procedures of the DEM. The first formulations of the DEM were based on rigid circular 2D solids with deformable contacts. The general solving scheme is direct, typically formulated by means of a explicit time integration [CS79]. The solid movement is governed by the external loads and the contact forces acting on a certain particle. The method carry out a loop over all the solids and, for each time step, compute all the forces acting on them. The unbalanced forces (or moments) produce accelerations (translational or rotations) that determines the movement of that solid in the next time step.

The simplest computational procedure for the DEM solves the movement equations on a certain discrete element and then updates the contact forces due to the contact between another particle or the boundary.

As is shown in Fig. 10.2, at each time step, the coordinates of the two particles

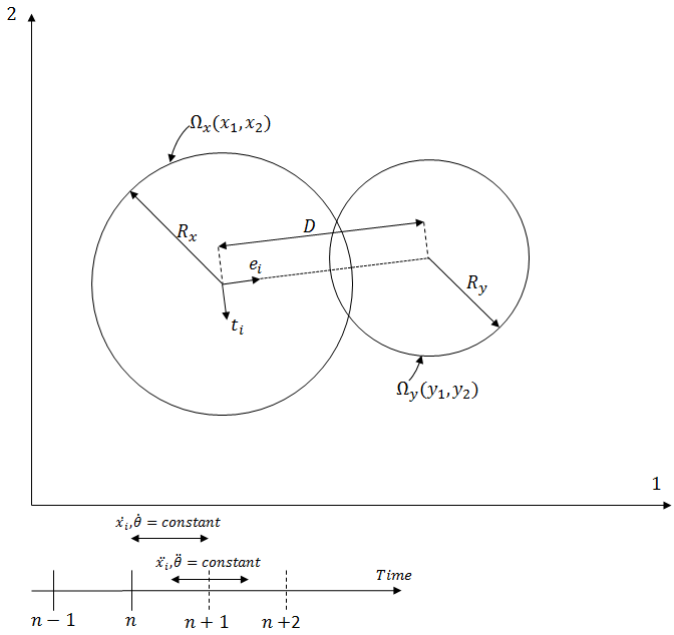

Figure 10.2: Discrete element method scheme

(Ω_x, Ω_y) are known ((x_1, x_2) and (y_1, y_2) respectively). The radius of the particles are the R_x and R_y and the distance between the centres of the particles is D. Additionally, the translational velocity $(\dot{x}_i, \dot{y}_i)$ and the angular velocity $(\dot{\theta}_i, \dot{\theta}_i)$ of each particle must be known for each i direction. Finally, in the same figure can be identified the unitary vectors (e_i and t_i) that connects the two centres of the particles.

Once the previous variables have been presented, the relative velocities in the i direction can be calculated as:

$$\dot{X}_i = (\dot{x}_i - \dot{y}_i) - (\dot{\theta}_x R_x + \dot{\theta}_y R_y) t_i \tag{10.1}$$

In this context, the relative displacements (Δn and Δs) can be obtained with:

$$\dot{n} = \dot{X}_i e_i \qquad \dot{s} = \dot{X}_i t_i \tag{10.2}$$

$$\Delta n = \dot{n} \Delta t \qquad \Delta s = \dot{s} \Delta t \tag{10.3}$$

so the contact force increments:

$$\Delta F_n = k_n(\Delta n + \beta \dot{n}) \qquad \Delta F_s = k_s(\Delta s + \beta \dot{s}) \tag{10.4}$$

Adding the contact force increments (Eq. (10.4)) to the previous time step (n):

$$F_n = F_n^n + \Delta F_n \qquad F_s = F_s^n + \Delta F_s \tag{10.5}$$

After this process, the sliding between particles must be checked:

$$F_s = min(F_s, C + F_n tan(\phi)) \tag{10.6}$$

and the moments:

$$M_x = \sum F_x R_x \qquad M_y = \sum F_y R_y \tag{10.7}$$

At this point, all the forces acting on the particles are known so the movement equations can be solved. Firstly, the accelerations are obtained solving the following equations:

$$m\ddot{x}_i = \sum F_i \qquad I\ddot{\theta}_i = \sum M_i \tag{10.8}$$

In the same way the velocities are updated

$$\dot{x}_i^{n+1/2} = \dot{x}_i^{n-1/2} + \ddot{x}_i \Delta t \qquad \dot{\theta}_i^{n+1/2} = \dot{\theta}_i^{n-1/2} + \ddot{\theta}_i \Delta t \tag{10.9}$$

and, in the end, the new positions:

$$x_i^{n+1} = x_i^n + \dot{x}_i^{n+1/2}\Delta t \qquad \theta_i^{n+1} = \theta_i^n + \dot{\theta}_i^{n+1/2}\Delta t \tag{10.10}$$

With this simple and direct algorithm, proposed initially by Cundall and Strack [CS79], one can obtain, at each time step, the displacements, accelerations and velocities according to an unbalanced system of equations at each particle.

10.3 DEM formulation within the FEM-DEM

The DEM methodology used within the FEM-DEM formulation is based on the work of Casas et al. [Cas+17], Oñate et al. [Oña+15] and Thornton et al. [TCC13].

The motion of the DE is computed by solving the dynamic equilibrium of forces at the centre of each particle using an explicit dynamic solution scheme (see Eqs. (10.8)-(10.10)). A *spring-dashpot type soft-sphere* approach for the contact between spheres has been selected. Considering two contacting spheres, which centres are $\mathbf{r_1}$ and $\mathbf{r_2}$, the normal vector that connects the centres of the spheres can be computed as follows:

$$\mathbf{n_{21}} = \frac{\mathbf{r_2} - \mathbf{r_1}}{\|\mathbf{r_2} - \boldsymbol{r_1}\|}\,,\ \mathbf{n_{21}} = -\mathbf{n_{12}} \tag{10.11}$$

The normal indentation δ_n between the discrete particles is computed as:

$$\delta_n = R_1 + R_2 - \|\mathbf{r_{21}}\| \tag{10.12}$$

where R_i are the radii of the particles. The total contact force between two particles is defined as the sum of a normal and a tangential force:

$$\mathbf{F} = F_n\,\mathbf{n} + F_t\,\mathbf{t} \tag{10.13}$$

The normal contact force F_n is obtained as a combination of an elastic and a viscous contribution:

$$F_n = F_{n,el} + F_{n,damp} \tag{10.14}$$

Where the elastic part can be computed as (assuming the classical Hertzian model):

$$F_{n,el} = \frac{4}{3}\tilde{R}^{\frac{1}{2}}\tilde{E}\delta_n^{\frac{3}{2}} \tag{10.15}$$

where $\tilde{R} := \left(1/R_1 + 1/R_2\right)^{-1}$, $\tilde{E}_i := E_i/(1-\nu^2)$, $\tilde{E} = \left(1/\tilde{E}_1 + 1/\tilde{E}_2\right)^{-1}$. The corresponding viscous damping contribution is modelled as:

$$F_{n,damp} = c_n \, \delta_n^{1/4} \, \dot{\delta}_n \tag{10.16}$$

For particle-particle contact the constant c_n can be expressed as:

$$c_n = \gamma \sqrt{8 \, \tilde{E} \, \tilde{M} \sqrt{\tilde{R}}} \tag{10.17}$$

being $\tilde{M} := \left(1/m_1 + 1/m_2\right)^{-1}$ and γ a viscous damping coefficient.

On the other hand, the tangential force is computed as:

$$\mathbf{F_t} = F_{t,el} \, \mathbf{t}_d + F_{t,damp} \mathbf{t}_\nu \tag{10.18}$$

where the directions $\mathbf{t_d}$ and $\mathbf{t}_\nu$ are based on the kinematics during tangential deformation [Oña+15].

The elastic tangential contribution is obtained by:

$$F_{t,el} = \delta_n^{1/2} \int a(t) \, dt \tag{10.19}$$

and the tangential viscous contribution as

$$F_{t,damp} = c_t \, \delta_n^{1/4} \dot{\delta}_t \tag{10.20}$$

with

$$c_t = 2 \gamma \sqrt{8 \, \tilde{G} \, \tilde{M} \, \sqrt{\tilde{R}}} \tag{10.21}$$

where $\tilde{G} = G/(4-2\nu)$ and $G = E/(2+2\nu)$.

All this computations have been implemented by the DEM developer team in *Kratos Multi-physics* `DEMApplication`. Programmatically, the `FemToDemApplication` imports all the necessary routines and methods from the `DEMApplication` in order to perform the necessary DEM operations and, additionally, carries out the coupling with the FEM. More information about how the different applications inside *Kratos Multi-physics* are interacting is given in the next chapter (Chapter 11) and in Appendix E.

10.4 Contact search

The potential contact detection between particles is a key issue in the DEM. Depending on the number of discrete elements (DE) and its shape, the cost of this operation can represent from de 60% to the 90% of the calculation time. This contact detection basically consists in determining, for each of the particles in the domain, which other neighbouring particles have and, in case that there is overlapping, then they must interact. Indeed, since this contact search is a very expensive part of the calculation, one must limit the number of searches only when it is necessary.

In general, the contact detection algorithms can be divided in two main stages:

- **Global contact search**: Consists in determining a list of potential contact neighbours to a certain particle. In this regard, two main approaches are available:
  - Grid based algorithm: This approach defines a rectangular grid in the domain and assigns a certain cell to each particle. Then, the potential neighbours of a particle are determined by selecting the surrounding cells of it (see Fig. 10.3).
  - Tree based algorithm: Within this approach, each element is represented by a point. The algorithm starts from a centered point and splits the domain y two: one covering the points that have greater x, y or z coordinate and the other including the points with less x, y or z coordinate. This methodology is repeated for all the points and alternates the coordinates until obtaining sa tree structure like the one depicted in Fig. 10.4. Once finished the computation of this tree, for every particle, the nearest neighbours have to be determined following the tree in upwind direction.
- **Local Resolution of the contact**: The aim of this stage is to compute the actual contact forces between those particles that have been tagged as potential contact neighbours in the previous stage. This is the most difficult and expensive part of the detection.

Inside the *Kratos Multi-physics* `DEMApplication`, the used methodology for the contact detection is the so-called *Bintree* method, which can be classified inside the tree based algorithms.

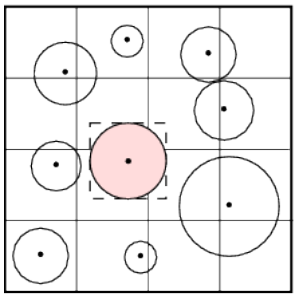

Figure 10.3: Grid based search, Image from Santasusana and Oñate [SO12]

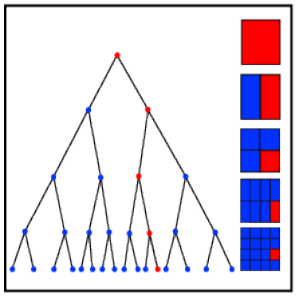

Figure 10.4: Tree based search, Image from Santasusana and Oñate [SO12].

Chapter 11

Coupled FEM-DEM methodology

11.1 Introduction to the FEM-DEM

The coupled FEM-DEM formulation was developed by Zárate and Oñate [ZO15] as an effective procedure for predicting the onset and propagation of cracks in concrete and rocks. Zárate et al. [ZCO18] extended the formulation to 3D problems.

Initially the continuum is modelled with simplex FE (3-noded triangles in 2D and 4-noded tetrahedra in 3D). The FE solution is obtained by reaching the dynamic equilibrium via an implicit transient dynamic solution scheme. An isotropic damage constitutive law is chosen in order to verify failure at the edges of the FE (using the SPR technique [ZZ92c]). Once one of the failure modes of the FE is achieved (which means that the elemental damage is greater than a certain threshold ≈ 0.98), that FE is removed from the mesh and DE are placed at the nodes of the removed FE (see Fig. 11.1 and [ZO15; ZCO18]).

The coupling or information exchange between the two solutions (DEM and FEM) can be one-way or two way. In this work the two approaches have been studied. In the one-way approach, after convergence of the implicit FEM time-scheme, the kinematic information from the FEM (displacements, velocities and position) nodes is transferred to the attached DE and then the contact forces between the particles and the skin of the FEM part (or between particles as it was originally, see Appendix D) are computed

in order to be included in the next time step as an equivalent nodal force in the FEM. In the two-way coupling approach, the iterative scheme of the FEM Newton-Raphson has been modified in order to recompute the contact forces coming from the DEM at each non-linear iteration. This adds an strong non-linearity to the problem but efficiently increases the accuracy and consistency of the contact forces. Must be said that this two-way coupling is especially used for contact driven problems since it adds a sensible computational cost in comparison with the one-way version.

In Zárate and Oñate [ZO15], Zárate et al. [ZCO18] and Cornejo et al. [Cor+19] the authors described a sub-stepping procedure in which the DEM performs several explicit time steps after an implicit step. This is done in order to smooth the contact forces along time and stabilize the solution because the contact forces transferred to the FEM have been averaged over all the DEM explicit steps. Without the sub-stepping, in order to stabilize the solution and converge, a reduced young modulus for the DE has to be applied (one or two order of magnitude lower in general) or a two-way coupling must be employed. Indeed, each particle is attached to a FEM node as long as this node exists. Once all the elements that share one node have been erased, the associated DE is allowed to move freely as in the standard DEM. In this case is especially useful to add the sub-stepping for this particle, otherwise the kinematics of the free particles are unstable and consequently not properly tackled. Must be said that the two-way coupling approach combined with the sub-stepping procedure has not been explored in this work due to its high computational cost.

At each time step, after the convergence of the FEM implicit calculation, a sub-stepping of the explicit DEM calculation is performed. This means that, at each explicit time step, the solid FEM part must be interpolated between the initial (previous time step) and the converged updated configuration (current converged time step) so the explicit contacts/kinematics can be tackled in a more stable and consistent way. For each particle, one can evaluate the contact impulses within the explicit steps and, once the sub-stepping is finalized, the averaged contact forces are computed and transferred as equivalent nodal forces for the FEM in the following time step.

11.2 Main improvements to the standard FEM-DEM methodology

Since the initial development of the FEM-DEM by Zárate and Oñate [ZO15], several improvements of the original methodology have been made within the development

of this work. In the next paragraphs, some of the most important contributions are highlighted.

The DEM employed is more efficient and sophisticated than the original one.

As explained in Chapter 10, the DEM implementation used for the coupling is currently being developed by a team inside the *Kratos Multi-physics* `DEMApplication`. This means that, only by implementing the FEM-DEM methodology in *Kratos Multi-physics*, the DEM procedure employed will be always at the forefront of science. In fact, currently, the particles interact between each other in a more complex way than before in terms of contact constitutive law (linear/Hertzian contact) but also in terms of friction and rotation of particles.

The repulsive contact forces preventing the indentation has been improved

In the current implementation of the FEM-DEM, the contact of frictional repulsive forces to prevent the indentation of the crack faces has been improved so it is no longer a DE-DE contact (contact between particles) but a DE-FE contact (contact between a DE and a FE face). This new feature is studied in Appendix D and implies a reduction of the apparent gap between the two crack faces of a 50%. Additionally, the contact surface with the DE-FE contact is flat, which improves the quality, robustness and accuracy of the contact interface. The reader is referred also to the example performed in Section 12.6 in order to see the improvements of the new contact procedure.

The tangent constitutive tensor estimation has been improved notably.

In the initial version of the FEM-DEM, the option used for computing the constitutive tangent tensor was the so-called secant tensor. This secant tensor has the advantage of being robust (this is why it is still available to be used in the current implementation) but slow, it requires a lot of iterations to converge (linear rate of convergence).

In order to overcome this issue, a tangent constitutive tensor numerical approximation has been implemented which, in most cases, reaches a quadratic rate of convergence. The numerical technique developed is available in small and finite deformations and can be studied in Appendix C and in Cornejo et al. [Cor+19].

All the operations have been parallelized.

Indeed, the FEM part and the DEM operations have been fully parallelized by means of the OpenMP architecture [MP]. This is a big improvement because in the

original version of the code the algorithm was no scalable with the number of threads available. This enhancement allows the proposed methodologies to face problems involving large geometries and challenging FE meshes.

A wide set of yield surfaces is now available.

In the implementation performed and, taking advantage of the object-oriented programming (c++), a wide set of yield surfaces (see a more detailed description in Appendix B) have been implemented without any condition inside the code, avoiding in this way the overhead of the yield surface selection (they are set via template):

- Rankine
- Mohr-Coulomb
- Simo-Ju
- Modified Mohr-Coulomb
- Drucker-Prager
- Von Mises
- Tresca

A rule of mixtures with j2-plasticity has been included.

In fact, in order to simulate the effect of steel rebars in the model, a phenomenological rule of mixtures (classical and the generalized serial/parallel rule of mixtures) which combines the effect of several material components according to its own constitutive model. Additionally, the fibre can exhibits plastic deformations by means of an isotropic j2-plasticity model.

The formulation has been extended to be used in anisotropic materials.

As shown in Chapter 8, the FEM-DEM has been enhanced to be able of performing non-linear constitutive calculations involving oriented anisotropic materials. This can increase the applicability of the method, especially in mining/blast simulations where general anisotropic materials and rocks can be found.

A more sophisticated sub-stepping procedure has been developed.

In this work, a more consistent and robust sub-stepping has been developed in order to better capture the movement and kinematics of the free particles meanwhile we can use an implicit time step for the FEM part. In order to accomplish this, an interpolation between the converged and the last implicit solution has to be used as a boundary for the particles explicit time steps (Section 11.3.3).

A consistent two-way coupling between the FEM and the DEM has been implemented.

In order to better estimate the contact forces between bodies, a more consistent strong coupling approach between the FEM and the DEM has been studied and developed. As will be demonstrated, the time step required to obtain consistent results is considerably lower than the one required in a one-way coupling approach.

11.3 FEM-DEM algorithm

This section will detail all the operations involved in the FEM-DEM algorithm, for the one-way and for the two-way coupling. As will be seen below, there is a basic version of the methodology without sub-stepping, which is notably faster but inconsistent for cases where there are *free particles*[1]. On the other hand, a more robust version has been developed in which, after the implicit FEM calculation, a sub-stepping procedure is related where the explicit DEM method solves n time steps while the FEM solid is interpolating its position between the initial (previous implicit time step) and the converged configuration (current implicit time step).

it is important to mention that DEM particles will be able to move freely only if they do not have an associated FEM node, that is, all FE containing a certain node have been eliminated. In that case, the kinematics and the particle position will be calculated by the explicit time advance scheme. Otherwise, if a particle is associated with a certain FEM node (*slave particles*), then the kinematics and position of the particle will be controlled by those of the FEM node[2].

11.3.1 FEM-DEM basic algorithm: one-way coupling

The FEM-DEM formulation without the sub-stepping procedure can be summarized in the algorithm below. As is shown in the aforementioned algorithm, the Newton-

[1] Free particles are DEM particles without any associated FEM node

[2] In this way, the particle is always attached to the FE skin node

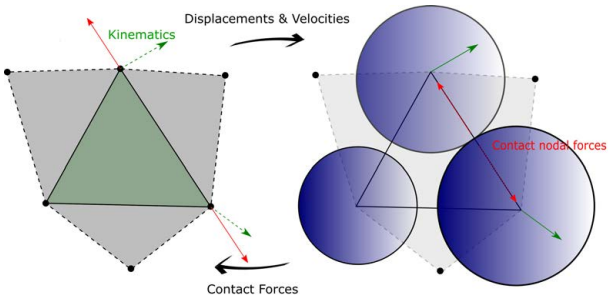

Figure 11.1: DE generation after removing a FE. Image from [Cor+19].

Raphson linearises the residual $\mathbf{r}_{\text{eff,dyn}}$ and updates the displacement increment $\Delta\mathbf{u}_k^t$ until a tolerance criterion is reached. In order to do so, the algorithm requires the computation of the external forces $\mathbf{F}_{\text{ext}}$ (which include the contact forces) and internal forces $\mathbf{F}_{\text{int}}$ that intrinsically depends on the computation of stresses and damage at elemental level[3].

After convergence of the non-linear Newton-Raphson, an automatic generation of particles is performed for those FE whose damage is greater than a certain threshold ($d_e \approx 0.98$), which are erased from the FE mesh.

Subsequently, the contact forces between the particles and the FE faces are computed and, in the case of free particles, the kinematics and position are integrated via a unique explicit time step (which in general provides unstable results since the explicit time scheme requires very small time steps).

11.3.2 FEM-DEM basic algorithm: two-way coupling

The two-way FEM-DEM approach without the sub-stepping procedure is summarized below. As has been explained, this strong coupling implies that at each non-linear iteration of the FEM, the contact forces estimated from the DEM must be updated and included in the external forces vector. In this way, the contact forces resulting of this non-linear iterative scheme are more accurate and consistent in comparison with the ones obtained in the with the algorithm 4. Of course, this increase of stability

[3]Since the FE used are linear triangles and tetrahedra, performing a loop over the nodes is equivalent to do a loop over the IP

implies a higher computational cost and an added non-linearity to the system which, subsequently, increases the complexity of the problem.

11.3.3 FEM-DEM consistent algorithm: inclusion of a sub-stepping

In this case, the inclusion of a sub-stepping procedure makes the kinematics of the free particles and the calculation of contact forces more consistent and accurate. Indeed, at each explicit time step, the explicit contact forces $\mathbf{F}_{contact,expl}$ are estimated and the impulses are added as $\mathbf{I}_e = \mathbf{I}_e + \Delta t_e \cdot \mathbf{F}_{contact,expl}$. Subsequently, at the end of the sub-stepping, the implicit contact forces that will be applied as a set of nodal forces to the FEM are computed as $\mathbf{F}_{contact,FEM} = \dfrac{\mathbf{I}_{t_e}}{\Delta t_i}$.

For this case, if one includes the sub-stepping procedure, the FEM-DEM algorithm can be summarized in Algorithm 5.

11.3.4 Comparison between the one-way and the two-way coupling approaches

In section, a quantitative analysis of the different coupling approaches between the FEM and the DEM is performed. In order to do so, a numerical example using the mentioned alternatives is carried out. Several time steps are used to ensure the consistency of the proposed methodologies.

The geometry of the problem is depicted in Fig. 11.3. As can be seen, it consists in two elastic bodies in which one of the is submitted to a gravitational acceleration in the horizontal direction. The initial gap between the two bodies is 0.1 m. An initial skin of particles has been created in order to detect the contact between the bodies -contact between DE and FE in this case-.

The material properties used for the continuum part (FEM) and the discrete part (DEM) are given in Table 11.1. The distributed particles have no mass since the body forces are taken into account by the continuum part. The restitution coefficient e is related to the energy loss due to the contact ($e = 1$ implies elastic contact), in fact can be defined as the ratio of the final to initial relative velocity between two objects after they collide. Since the contact is frictional, some sliding friction (friction coefficient) and rolling friction must be defined[4]

[4]The rolling friction is a source of energy dissipation involved in deformation of rolling objects.

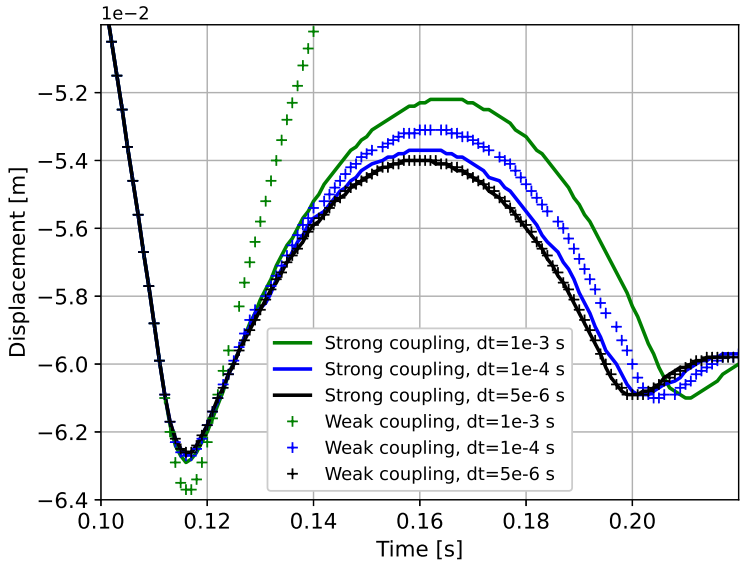

Figure 11.2: Displacement evolution of the colliding block along time for different time steps and coupling approaches.

Fig. 11.2 shows the horizontal displacement evolution of the moving block along time for different time steps (ranging from 10^{-3} to $5 \cdot 50^{-6}$ s) and different coupling approaches. As can be seen in the previous figure, the two-way coupling approach converges faster -employing a smaller time step- an estimates with more accuracy the contact forces for the same time step in comparison to the one-way coupling. However, the two approaches converge to the same solution if a sufficient small time step is used, as expected.

FEM Parameter	Value
Young's modulus (E)	35 GPa
Poisson's ratio (ν)	0.2
Density (ρ)	2400 kg/m^3
DEM Parameter	**Value**
Young Modulus (E_{DE})	10 Mpa
Poisson's ratio (ν)	0.2
Restitution coefficient (e)	0.1
Friction coefficient	0.58
Rolling friction	0.1

Table 11.1: Material properties used in the collision of deformable blocks and the DE.

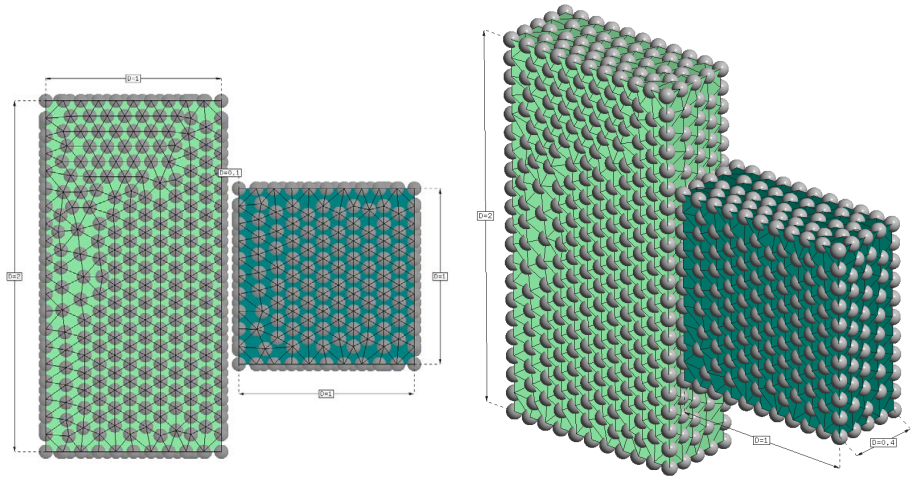

(a) (b)

Figure 11.3: Test case, 14,642 FE and 1,030 particles.

Algorithm 3 Standard FEM-DEM algorithm

• Initialization of the implicit transient dynamic scheme for the FEM: $t_i = t_i + \Delta t_i$, $k = 0$ being t_i the current time of the implicit scheme.
• Apply the DE contact forces from the previous time step as equivalent nodal force for the FEM
while $\left\| r_{\text{eff,dyn}} \right\| = \left\| \mathbf{F}_{\text{int}} - \mathbf{F}_{\text{ext}} \right\| < tol$ **do**
  for *Elements* **do**
    • Compute the effective stresses $\bar{\mathbf{S}} = \mathcal{C}_0 : \mathbf{E}$
    • Smoothing of the effective stress field at the FE edges
    • Compute the damage d at the edges by Eq. (7.6)
    • Obtain the elemental damage by Eq. (7.10)
    • Calculate the tangent stiffness matrix $\mathbf{K}_T^{(e)}$ via Eq. (6.72) and the updated internal forces vector $\mathbf{F}_{\text{int}}^{(e)}$
  end
  • Assemble the global expression of $\mathbf{K}_T$ and $\mathbf{F}_{\text{int}}$
  • Calculate the displacement increments $\Delta \mathbf{u}_k^t = \mathbf{K}^{-1} \Delta \mathbf{F}$
  • Check convergence $\left\| \mathbf{r}_{\text{eff,dyn}} \right\| < tol$
  • $k = k + 1$
end
for *Elements* **do**
  if *Damage > 0.98* **then**
    • ERASE the FE
    • Generate the DE at the nodes of the erased FE
  end
end
• Initialization of the explicit transient dynamic scheme for the DEM
• Import the kinematic information from the FEM nodes to the particles as an initial condition
• Compute the contact forces (between DE-DE or DE-FE) via Eq. (10.13)
• Integrate the equations of motion for the free particles (Eqs. (10.8)-(10.10))
• Compute the displacements, velocities and accelerations at the free particles
• Transfer the contact forces as equivalent nodal forces to the FEM nodes

Algorithm 4 Standard FEM-DEM algorithm: two-way coupling

• Initialization of the implicit transient dynamic scheme for the FEM: $t_i = t_i + \Delta t_i$, $k = 0$ being t_i the current time of the implicit scheme.
• Apply the DE contact forces from the previous time step as equivalent nodal force for the FEM
while $\left\| \boldsymbol{r}_{\text{eff,dyn}} \right\| = \left\| \mathbf{F}_{\text{int}} - \mathbf{F}_{\text{ext}} \right\| < tol$ **do**
  • Initialization of the explicit transient dynamic scheme for the DEM
  • Import the kinematic information from the FEM nodes to the particles as an initial condition
  • Compute the contact forces (between DE-DE or DE-FE) via Eq. (10.13)
  • Integrate the equations of motion for the free particles (Eqs. (10.8)-(10.10))
  • Compute the displacements, velocities and accelerations at the free particles
  • Transfer the contact forces as equivalent nodal forces to the FEM nodes
  for *Elements* **do**
    • Compute the effective stresses $\bar{\mathbf{S}} = \mathcal{C}_0 : \mathbf{E}$
    • Smoothing of the effective stress field at the FE edges
    • Compute the damage d at the edges by Eq. (7.6)
    • Obtain the elemental damage by Eq. (7.10)
    • Calculate the tangent stiffness matrix $\mathbf{K}_T^{(e)}$ via Eq. (6.72) and the updated internal forces vector $\mathbf{F}_{\text{int}}^{(e)}$. The external force vector must be updated with the current contact forces.
  end
  • Assemble the global expression of $\mathbf{K}_T$ and $\mathbf{F}_{\text{int}}$
  • Calculate the displacement increments $\Delta \mathbf{u}_k^t = \mathbf{K}^{-1} \Delta \mathbf{F}$
  • Check convergence $\left\| \mathbf{r}_{\text{eff,dyn}} \right\| < tol$
  • $k = k + 1$
end
for *Elements* **do**
  if *Damage > 0.98* **then**
    • ERASE the FE
    • Generate the DE at the nodes of the erased FE
  end
end

Algorithm 5 Standard FEM-DEM algorithm with sub-stepping

• Initialization of the implicit transient dynamic scheme for the FEM: $t_i = t_i + \Delta t_i$, $k = 0$ being t_i the current time of the implicit scheme.
• Apply the DE contact forces from the previous time step as equivalent nodal force for the FEM
while $\left\| \boldsymbol{r}_{\text{eff,dyn}} \right\| = \| \mathbf{F}_{\text{int}} - \mathbf{F}_{\text{ext}} \| < tol$ **do**
  for *Elements* **do**
    • Compute the effective stresses $\bar{\mathbf{S}} = \mathcal{C}_0 : \mathbf{E}$
    • Smoothing of the effective stress field at the FE edges
    • Compute the damage d at the edges by Eq. (7.6)
    • Obtain the elemental damage by Eq. (7.10)
    • Calculate the tangent stiffness matrix $\mathbf{K}_T^{(e)}$ via Eq. (6.72) and the updated internal forces vector $\mathbf{F}_{\text{int}}^{(e)}$
  end
  • Assemble the global expression of $\mathbf{K}_T$ and $\mathbf{F}_{\text{int}}$
  • Calculate the displacement increments $\Delta \mathbf{u}_k^t = \mathbf{K}^{-1} \Delta \mathbf{F}$
  • Check convergence $\left\| \mathbf{r}_{\text{eff,dyn}} \right\| < tol$
  • $k = k + 1$
end
for *Elements* **do**
  if *Damage > 0.98* **then**
    • ERASE the FE
    • Generate the DE at the nodes of the erased FE
  end
end
• Initialization of the explicit transient dynamic scheme for the DEM
while $t_e = t_e + \Delta t_e < t_i$ **do**
  • Interpolate the coordinates, displacements and velocities of the FEM nodes between the reference (t_{i-1}) and the converged values (t_i)
  • Import the kinematic information from the FEM nodes to the particles as an initial condition
  • Compute the contact forces $\mathbf{F}_c$ via Eq. (10.13)
  • Add the explicit contact impulses at each particle as $\mathbf{I}_{t_e} = \mathbf{I}_{t_e - 1} + \Delta t_e \cdot \mathbf{F}_c$
  • Integrate the equations of motion for the free particles (Eqs. (10.8)-(10.10))
  • Compute the displacements, velocities and accelerations of free particles
end
• Transfer the contact forces as equivalent nodal forces to the FE computed as $\mathbf{F}_{contact,FEM} = \dfrac{\mathbf{I}_{t_e}}{\Delta t_i}$

Chapter 12

Numerical examples of the basic FEM-DEM formulation

In this chapter, several numerical examples performed with the FEM-DEM formulation are presented. Some of them are compared against an analytical expression or, if an alternative numerical solution is available in the literature, checked with respect to the proposed methodologies results.

These study cases are meant to ensure the correctness of the implementation performed and they also serve as a validation of the formulation. Some of the examples are focused on predicting the behaviour of a certain sample of material subjected to a classical test such as the Brazilian test and the Uni-axial tension test, etc. Other examples try to asses the accuracy and consistency of the proposed frictional contact between solids.

It is also important to mention that the simulations have been performed in 2D and 3D in order to compare the behaviour of the sample in different dimensions. Complementary, in order to asses the mesh-dependency of the method, several FE discretizations have been used.

12.1 Tensile test

In this example a conventional 3D tensile test has been reproduced. The geometry of the sample is depicted in Fig. 12.1 with a thickness equal to 0.2 m. The left end

Parameter	Value
Young's modulus (E)	35 GPa
Poisson's ratio (ν)	0.2
Tensile strength (f_t)	1.5 MPa
Fracture energy (G_f)	30 J/m^2
Friction angle (ϕ)	32 deg

Table 12.1: Material properties used in the tensile test.

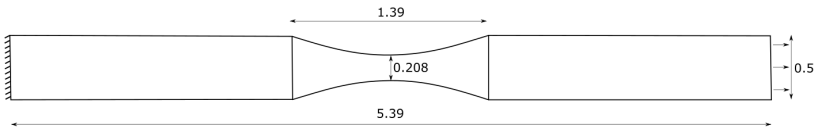

Figure 12.1: Tensile test sample geometry [m].

is clamped and the right one has a monotonic imposed displacement. The Modified Mohr-Coulomb yield surface (Appendix B) has been used. The material parameters are defined in Table 12.1. Three different meshes have been used in order to study the mesh dependence of the solution. The mentioned meshes are depicted in Fig. 12.2. The fractures geometry of the intermediate sample can be analysed in Fig. 12.3. As can be seen, the fracture appears and propagates at the centre of the sample, as expected. In order to assess quantitatively the accuracy of the calculation one can see the force-displacement evolution depicted in Fig. 12.4, indeed, the error committed with respect to the analytical solution for the coarse, intermediate and fine meshes reaches the 1.37%, 0.52% and 0.36%, respectively.

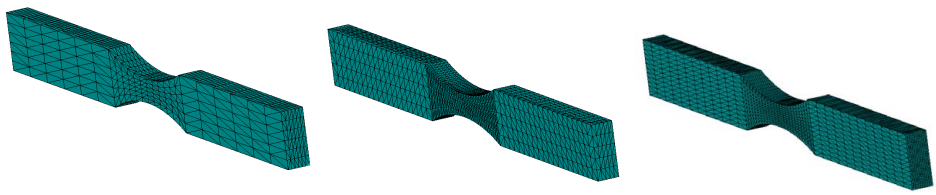

(a) (b) (c)

Figure 12.2: FE meshes used in the tensile test. a) 5184 FE b) 12000 FE c) 41472 FE.

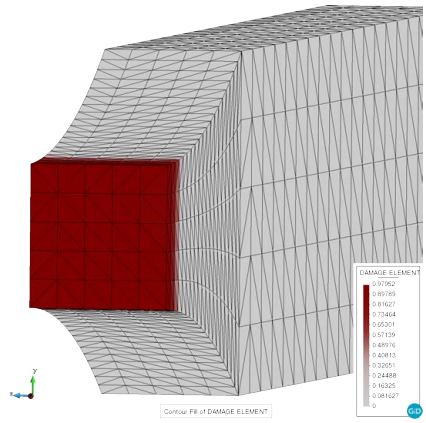

Figure 12.3: Fractured geometry of mesh b), Elemental damage variable d.

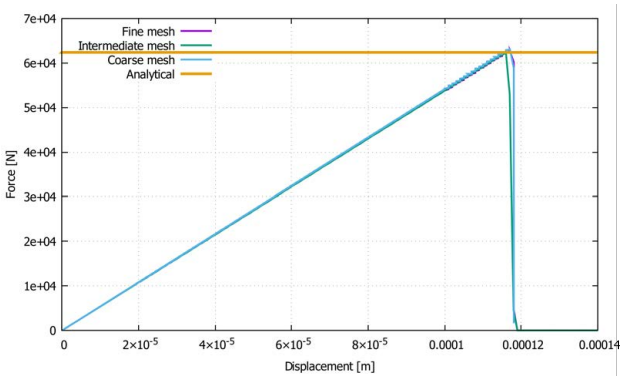

Figure 12.4: Force-displacement plot of the tensile test.

12.2 Brazilian test

The Brazilian tensile strength test is a very practical and simple experimental procedure to evaluate the tensile strength of brittle materials. In this case a cylinder with 15 cm of diameter (ϕ) and 30 cm height (H) is analysed. The described sample is loaded diametrically (loading width of 1 cm) by a press with an imposed velocity of 1 mm/s. The theoretical tensile strength of the material can be computed using the following expression [Car]:

$$f_t^{theory} = \frac{2P}{\pi H \phi} \tag{12.1}$$

being P the total applied load. The geometry used can be seen in Fig. 12.5. 2D plane stress formulation has been employed. Two different FE meshes have been used, which are depicted in Fig. 12.6. The material properties of the material are given in Table 12.2.

The force-displacement evolution of the simulation is depicted in Fig. 12.8. As can be seen, the two meshes converge to the almost equal peak strength. The error committed with respect to the analytical solution reaches the 7.16%, which is a reasonable value. Qualitatively, the fracture paths depicted in Fig. 12.7 are very similar, which ensures the stability and consistency of the formulation with different mesh sizes.

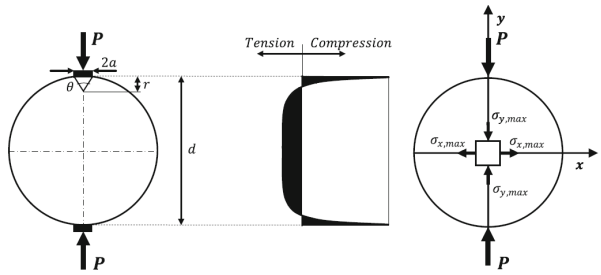

Figure 12.5: Brazilian test geometry and distribution of horizontal stresses. Image from [CA12].

Parameter	Value
Young's modulus (E)	35000 MPa
Poisson's ratio (ν)	0.2
Compressive strength (f_c)	15 MPa
Tensile strength (f_t)	1.5 MPa
Fracture energy (G_f)	100 J/m^2

Table 12.2: Material properties used in the Brazilian tensile test.

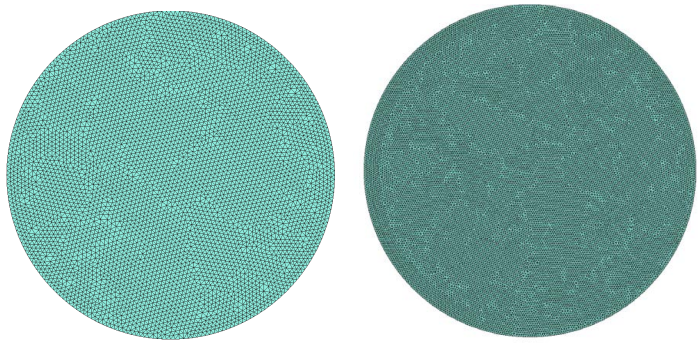

(a) (b)

Figure 12.6: Brazilian test FE meshes used. a) 10156 FE b) 40590 FE.

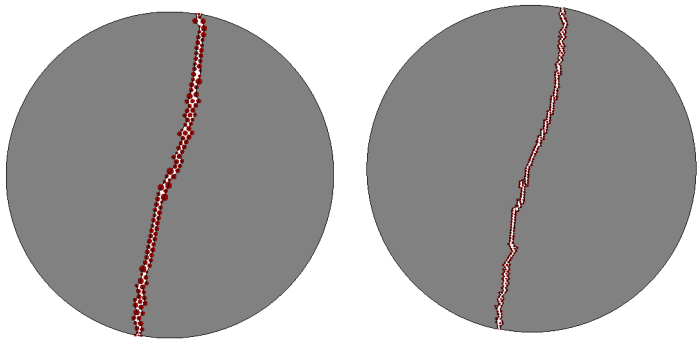

(a) (b)

Figure 12.7: Intermediate (a) and fine (b) mesh fractured geometries.

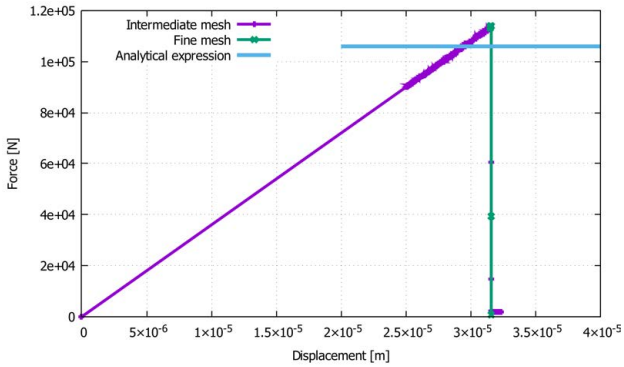

Figure 12.8: Force-displacement evolution of the Brazilian tensile test.

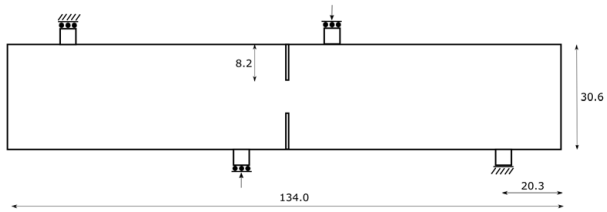

Figure 12.9: Four point bending test geometry [cm].

12.3 Four point bending test

This example is a plane stress four point supported beam with a double notch. In the two central supports a vertical displacement is imposed whereas in the exterior supports only the vertical displacement is enforced to be zero (one of them must be clamped, as depicted in Fig. 12.9. The yield surface used is the Modified Mohr-Coulomb [Oll88]. The material properties used are given in Table 12.3. This problem is especially appealing since it represents a good example of mixed mode fracture. This problem is based on the one proposed by Cervera et al. [CCC11] in which a mixed ε/u formulation is employed. Indeed, this mixed formulation improves the quality of the strain field (it is continuous element-wise) so it is interesting to compare the capabilities of the proposed FEM-DEM against this mixed formulation since it is remarkably cheaper in terms of computational time.

The domain is discretized in three FE meshes that are depicted in Fig. 12.10. As can be seen, only in the central zones (where the fracture is expected) is refined. Qualitatively, the three crack patterns (see Fig. 12.11) are close between each other and in agreement with the results obtained by Cervera et al. [CCC11] (Fig. 12.12). In Fig. 12.13 one can see the Force-displacement evolution of one of the central supports for the three different FE meshes, which are close to the results given in [CCC11].

It is true that, in the non-linear branch, the behaviour of the three different meshes are slightly different due to the fact that, unlike in the conventional continuum based damage formulations, the FEM-DEM effectively creates the crack and, consequently, the kinematics and the forces distribution of the problem can differ for each mesh.

Parameter	Value
Young's modulus (E)	30000 MPa
Poisson's ratio (ν)	0.2
Compressive strength (f_c)	20 MPa
Tensile strength (f_t)	2 MPa
Fracture energy (G_f)	100 J/m^2
Friction angle (ϕ)	32 *deg*
Thickness (t)	0.3 *m*

Table 12.3: Material properties used in the four point bending test.

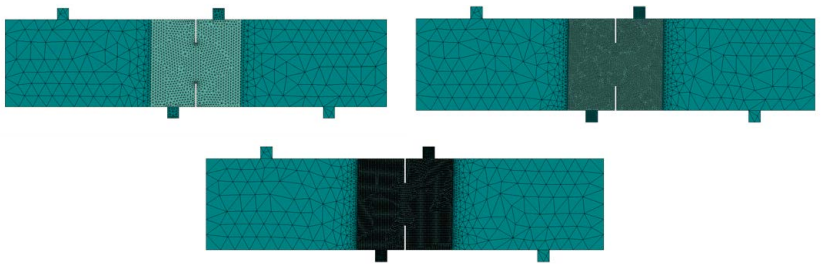

Figure 12.10: Four point bending test FE meshes used (coarse 2,912 FE, intermediate 15,112 FE and fine mesh with 58,368 FE).

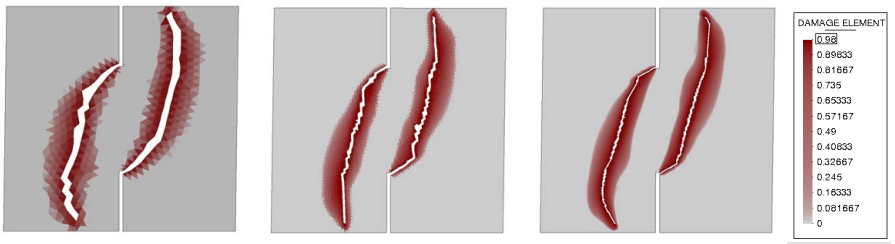

Figure 12.11: Four point bending test crack paths for the coarse, intermediate and fine mesh, respectively.

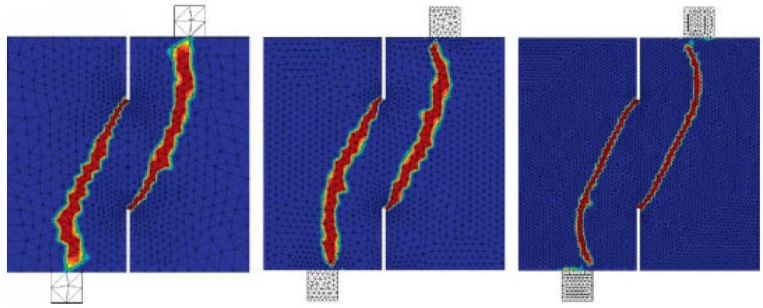

Figure 12.12: Four point bending test results from Cervera et al. [CCC11].

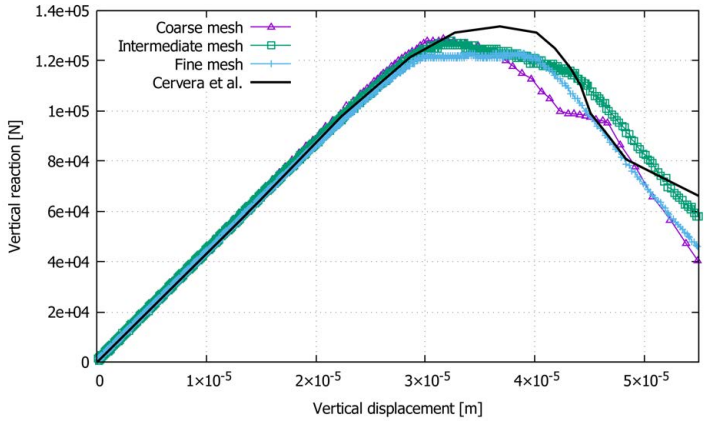

Figure 12.13: Force-displacement evolution of the four point bending test.

Parameter	Value
Young's modulus (E)	25.85 GPa
Poisson's ratio (ν)	0.18
Tensile strength (f_t)	2.7 MPa
Fracture energy (G_f)	160 J/m^2
Thickness (t)	0.1m

Table 12.4: Material properties used in the L-shaped panel.

12.4 L-shaped panel

In this section, a numerical simulation of a concrete L-shaped panel like the one proposed by Cervera et al. [CBC17] is performed (also in Mang et al. [MWW19], Dumstorff and Meschke [DM07] and Annavarapu et al. [Ann+16]). The geometry and loading procedure is shown in Fig. 12.14 and the material properties are given in Table 12.4. The solution reported in [CBC17] proposes a mixed ε/u formulation, Mang et al. employs a PF methodology, Dumstorff et al. used the XFEM and Annavarapu et al. proposed an embedded crack method with tracking procedure for simulating this test. Since this is a 2D calculation, plane stress conditions are assumed.

The FE mesh used is depicted in Fig. 12.15. Fig. 12.17 shows the damage field when the imposed displacement reaches 1 mm for the proposed method and for the solution given in [CBC17]. As one can see in the same figure, the crack path is almost identical and the crack propagates as expected from the experimental and available numerical test.

It is important to note that the FEM-DEM formulation does not require any crack tracking technique, nor any initial notch/imperfection to ensure the correct initiation of the crack as it is done in [Ann+16] and [DM07]. The evolution of the crack path is numerically derived and does not require any additional numerical procedures.

Fig. 12.17 shows the force-displacement evolution of the l-shaped panel test for the proposed method and the results obtained in [DM07] and [CBC17]. As can be seen, the general shape of the curve is captured as well as the peak load achieved in comparison with the literature.

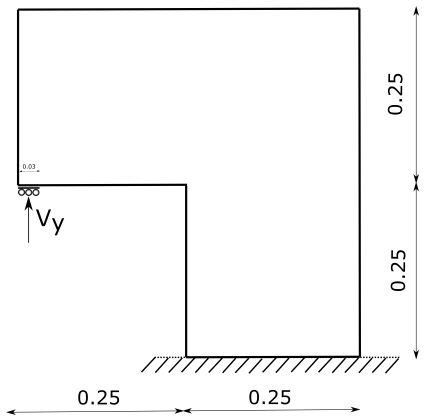

Figure 12.14: L-shaped panel geometry [m].

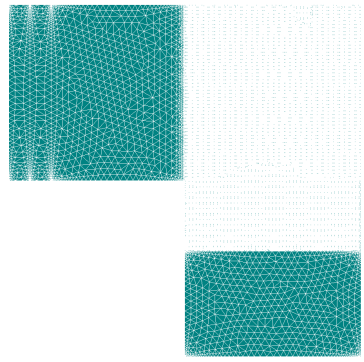

Figure 12.15: L-shaped test FE mesh in 2D (206,018 FE).

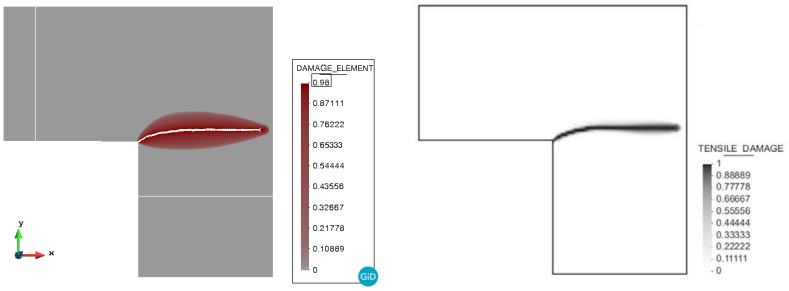

Figure 12.16: L-shaped crack path in 2D obtained with the FEM-DEM and in Cervera et al. [CBC17], respectively.

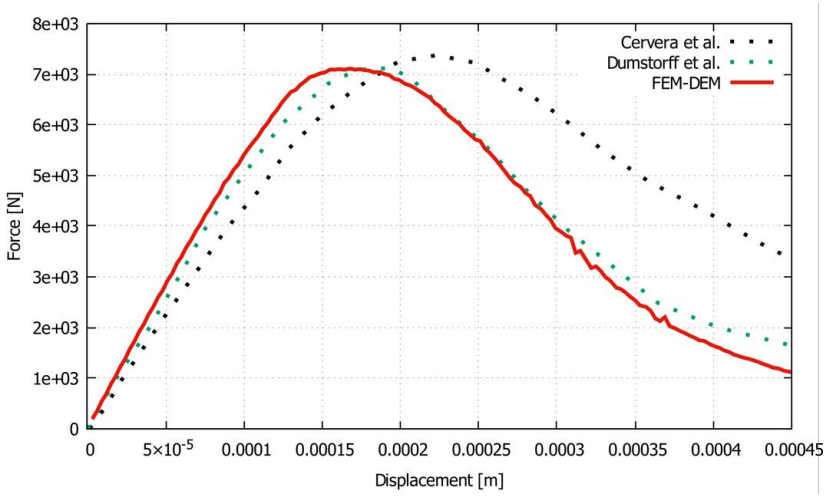

Figure 12.17: L-shaped panel test force-displacement evolution.

Parameter	Value
Young's modulus (E)	3.102 GPa
Poisson's ratio (ν)	0.35
Tensile strength (f_t)	7.0 MPa
Fracture energy (G_f)	500 J/m^2

Table 12.5: Material properties used in the three point bending test.

12.5 Three point bending test

In this example, a three point bending test with a non-centered notch is considered. This problem has been studied by Cervera et al. [CBC17] using a mixed ε/u formulation, Annavarapu et el. [Ann+16] employed crack tracking techniques and embedded methods and in Miehe et al. [MG07] using fracture mechanics. Figure 12.18 shows the geometry and boundary conditions of the test (the notch width is 0.002 m). The centered vertical load is introduced as an imposed vertical displacement in the middle of the sample. According to the physical experiment, the width of the sample is 0.5" [IG90].

The material properties used in the original experiment (Plexiglass material [IG90]) are given in Table 12.5. The FE mesh used is depicted in Fig. 12.19. For cost optimization, only the left half of the beam has been discretized with fine elements in order to capture properly the crack path.

As can be seen in Fig. 12.20, the results obtained with the FEM-DEM and the ones from Cervera et al. are almost identical, which demonstrates the correctness of the proposed formulation (since the solution in [CBC17] is very close to the experimental one). Figure 12.21 shows another perspective of the solution obtained and the DE elements generated during calculation. In this case, since the crack is always opening, the DE are not transmitting any contact force between the crack faces.

12.6 Colliding deformable blocks

In this example, the behaviour of the DE-DE contact and the improved DE-FE contact is studied, in the framework of a one-way coupling version of the FEM-DEM. The upper block's size is 1x1 m and the lower one's is 2x0.5 m. The lower body is fixed

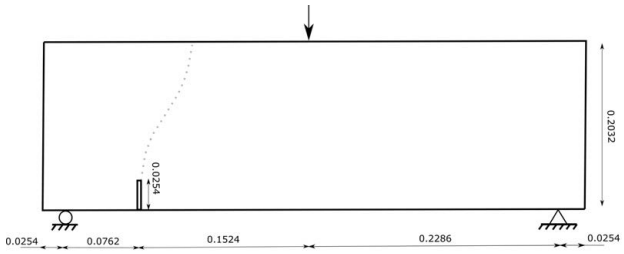

Figure 12.18: Three point bending test geometry and boundary conditions [m].

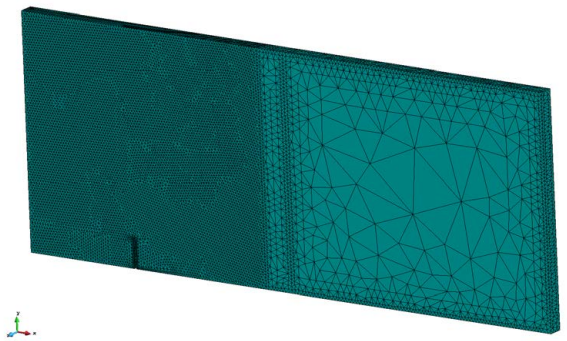

Figure 12.19: Three point bending test FE mesh used (314,278 FE).

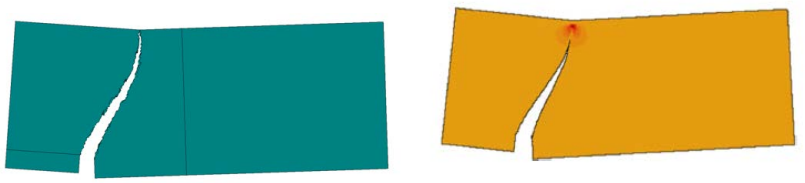

Figure 12.20: Three point bending test. FEM-DEM and Cervera et al. [CBC17] results, respectively.

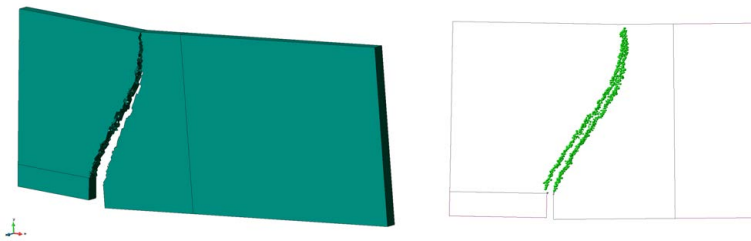

Figure 12.21: Three point bending fracture in perspective and DE generated.

in its lower boundary and the upper body is only submitted to its own weight. The initial gap between the bodies is 0.5 m. Fig. 12.22 shows the initial set up of the problem. As can be expected, a transient dynamic calculation is performed for this simulation. The material properties used are described in Table 12.6, using plane strain conditions.

Fig. 12.23 shows the position of the two blocks when the contact forces are activated. In the DE-DE case, active contact implies that there is an indentation between the particles located at the skin of the two bodies. On the other hand, for the DE-FE case, it means that the particles have entered inside the FE skin. The main improvement of the DE-FE contact is that the apparent gap between the two bodies has been reduced by half since the contact is activated when the particle indents the solid body.

Additionally, one of the inconvenients of the original DE-DE contact is the fact that the contacting surfaces are not flat (the DE generate a rough surface), which, in equilibrium, generates a locking between the particles.

As can be seen in Fig. 12.24, the bouncing of the moving block starts before for the DE-DE contact since the indentation is detected when the particles are in contact. Additionally, the value of the frictional repulsive forces are computed differently. This happens because the contact between particles only takes into account the material properties of the DE (which in general have a lower Young modulus) so the contact forces tend to be lower. Conversely, in the DE-FE contact, the material properties of the FE and the ones from the DE are used for the forces computation, which means that the repulsive forces estimation is more accurate. Additionally, the obtained solution is compared with the ALM contact procedure [Wri06; Pop12; Yas11; Mat20] results, which

Parameter	Value
Young's modulus (E)	35 GPa
Poisson's ratio (ν)	0.2
DE Young Modulus (E_{DE})	0.40 GPa

Table 12.6: Material properties used in the collision of deformable blocks and the DE.

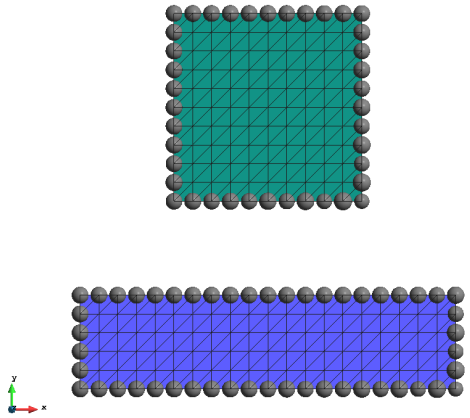

Figure 12.22: Initial geometry of the bodies to be collided and the initial skin of DE.

is the more exact formulation for contact mechanics. The ALM implementation used is located inside the *Kratos Multi-physics* `ContactStructuralMechanicsApp` based on the work of Mataix et al. [Mat20].

Fig. 12.24 shows how the ALM solution preserves the energy whereas the proposed methodologies does not preserve it with the same accuracy. Must be said that with the new contact procedure (DE-FE contact) the solution improves notably after a minor calibration of the penalty (DE stiffness) is performed. This improvement is greater in frictional problems where with the original DE-DE contact the particles are interlocked and prevents the sliding between the skin faces.

With this example, has been proved that the contact model implemented by using the DE-FE procedures is suitable to prevent the indentation after a minimal calibration of the stiffness of the particles and the time step of the simulation.

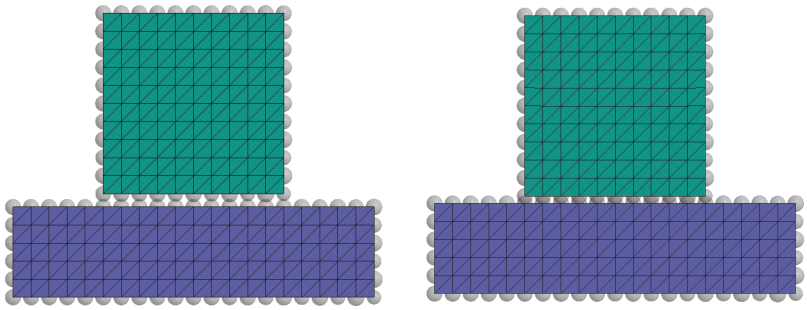

Figure 12.23: Contacting blocks when the repulsive forces are activated by using the DE-DE and the DE-FE contact procedures, respectively.

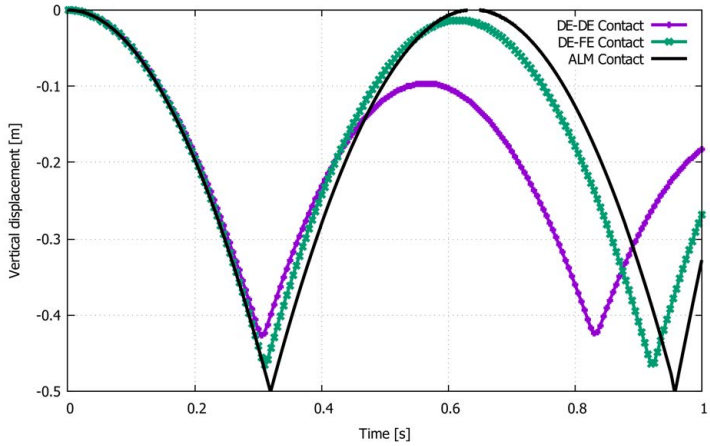

Figure 12.24: Displacement-time evolution of the lower part of the moving block for the DE-DE and the DE-FE contact procedures.

Parameter	Value
Young's modulus (E)	5 GPa
Poisson's ratio (ν)	0.4
Tensile strength (f_t)	0.5 MPa
Fracture energy (G_f)	150 J/m^2
Friction angle (ϕ)	32 deg

Table 12.7: Material properties used for the sinkhole simulation.

12.7 Sinkhole simulation

Sinkholes are a catastrophic collapse of the ground induced by a complex interplay between dissolution, erosion and mechanical stability in karst aquifers of the underlying rock layer [RKA20; Che+20; Fab+19]. In general, sinkholes are more prone to develop where the rock below land is limestone, salt beds, carbonate rock, or rocks that can be easily dissolved by groundwater.

The sinkhole simulated in this work can be classified within the cover-collapse sinkholes. These kind of processes can develop abruptly (hours or days) and cause potential catastrophic damages. Over time, the surface drainage, erosion and deposition of sediment can generate a bowl-shaped depression (see Fig. 12.25) and collapse dramatically.

The geometry and dimensions of the dynamic simulation performed can be seen in Fig. 12.26. Initially, the whole volume is submitted to its own weight. For simplicity, the erosion of the central brown zone has been assumed to be instantaneous and, due to this abrupt disequilibrium, the dynamic collapse of the upper part of the hole is developed.

The material properties of the problem are defined in Table 12.7. As can be seen in Fig. 12.27, the fracturing and collapse of the rock starts around $t \approx 5.1s$ and, meanwhile the crack propagates upwards, the damaged solid is transformed into DE due to the collision between blocks and boundaries. Finally, at the end of the simulation, the debris (mainly DE) are deposited in the lower part of the initial sinkhole. Indeed, the collapse mechanism developed via numerical method coincides with the one described in Galloway et al. [GJI13] depicted in Fig. 12.25.

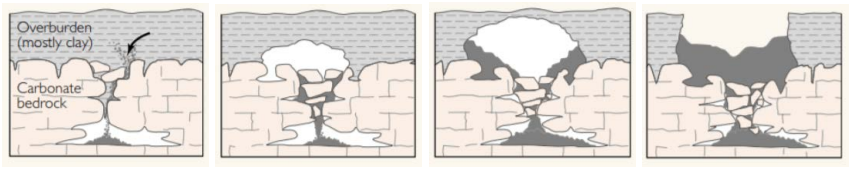

Figure 12.25: Cover-Collapse sinkhole type. Source: Galloway et al. [GJI13].

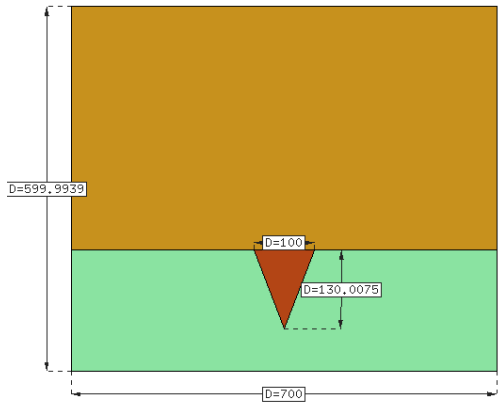

Figure 12.26: Sinkhole initial geometry [m].

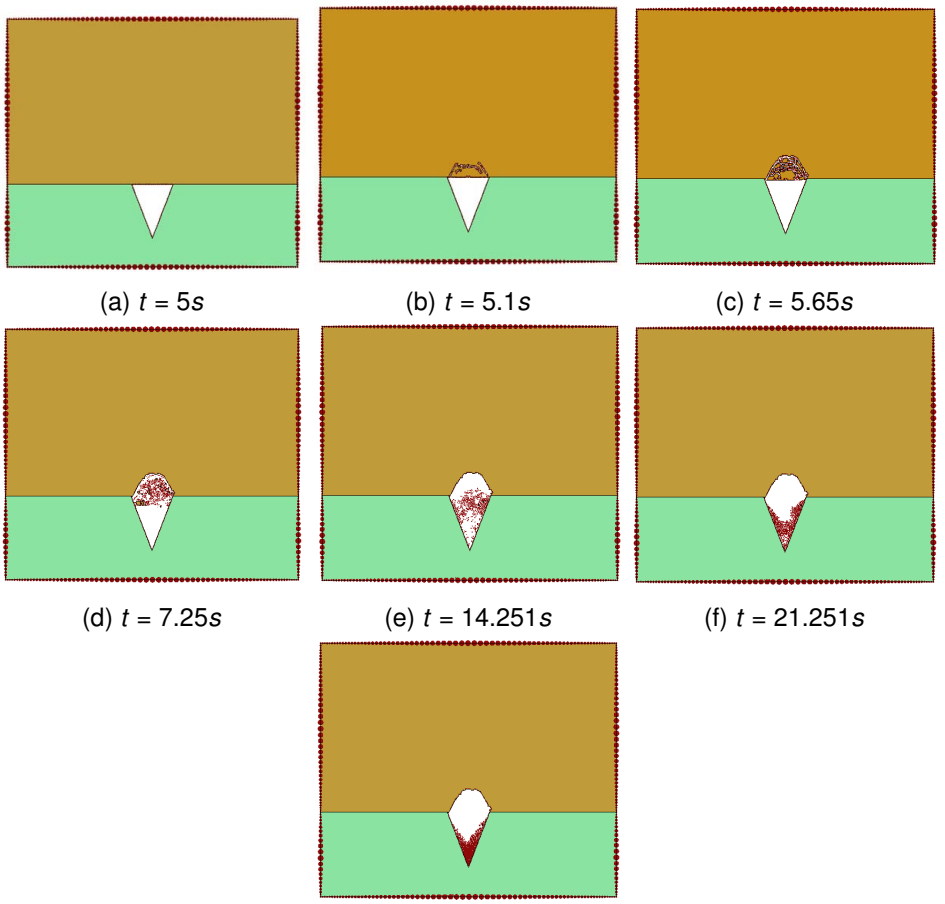

(a) $t = 5s$ (b) $t = 5.1s$ (c) $t = 5.65s$

(d) $t = 7.25s$ (e) $t = 14.251s$ (f) $t = 21.251s$

(g) $t = 30s$

Figure 12.27: Time-lapse of the collapse due to the sinkhole.

Part III bibliography

[Ann+16] C. Annavarapu et al. “A local crack-tracking strategy to model three-dimensional crack propagation with embedded methods”. *Comput. Methods Appl. Mech. Engrg*. Vol. 311, pp. 815–837 , 2016.

[Bar+19] LG. Barbu et al. “Methodology for the analysis of post-tensioned structures using a constitutive serial-parallel rule of mixtures: large scale non-linear analysis”. *Composite Structures*. Vol. 216, pp. 315–330 , 2019.

[Bar76] J. Barlow. “Optimal stress locations in finite element models”. *Int. J. Numer. Methods Eng*. Vol. 10, pp. 243–251 , 1976.

[Bas77] J.L. Bassani. “Yield characterization of metals with transversely isotropic plastic properties”. *Int. J. Mech. Sci.*. Vol. 19, p. 651 , 1977.

[BLB91] F. Barlat, D.J. Lege, and J.C. Brem. “A six-component yield function for anisotropic materials”. *Int. Journal of Plasticity*. Vol. 7, p. 693 , 1991.

[BPP] Z.P. Bazant, G. Pijaudier-Cabot, and P.C. Prat. *Distributed damage and application of non-local and microplane aspects*.

[BW97] J. Bonet and R. D. Wood. *Nonlinear continuum mechanics for finite element analysis*. 1997.

[CA12] S. Carmona and A. Aguado. “A new method to determine the tensile strength of concrete.” *Materials and Structures*. Vol. 45, pp. 1473–1485 , 2012.

[Car] FLLB. Carneiro. “A new method to determine the tensile strength of concrete.” *In Proceedings of the 5th meeting of the Brazilian Association for Technical Rules*. Pp. 126–129 ,

[Car00] E. Car. *Modelo constitutivo para el estudio del comportamiento mecánico de los materiales compuestos*. Universidad Politécnica de Cataluña. 2000.

[Cas+17] G. Casas et al. “A modular partitioned discrete element framework for industrial grain distribution systems with rotating machinery”. *Computational Particle Mechanics*. Vol. 4, pp. 181–198 , 2017.

[CBC17] M. Cervera, G.B. Barbat, and M. Chiumenti. “Finite element modelling of quasi-brittle cracks in 2D and 3D with enhanced strain accuracy”. *Computational Mechanics*. Vol. 60, pp. 767–796 , 2017.

[CCC11] M. Cervera, M. Chiumenti, and R. Codina. “Mesh objective modeling of cracks using continuous linear strain and displacement interpolations”. *Int. J. Numer. Meth. Engng*. Vol. 87, pp. 962–987 , 2011.

[CH93] J. Chung and G.M. Hulbert. “A time integration algorithm for structural dynamics with improved numerical dissipation: The generalized-alpha method”. *Journal of Applied Mechanics*. Vol. 60, pp. 371–375 , 1993.

[Che+20] H. Chen et al. “Experimental study on sinkhole collapse monitoring based on distributed Brillouin optical fiber sensor”. *Optik*. Vol. 216, p. 164825 , 2020.

[Chu80] Chen Chuan-miao. “Optimal points of the stresses for triangular linear element”. *Numerical Math. J. Chinese Univ.*. Vol. 2, pp. 12–20 , 1980.

[Cor+15] A. Cornejo et al. “High-cycle fatigue constitutive model and a load-advance strategy for the analysis of unidirectional fiber reinforced composites subjected to longitudinal loads”. *Composite Structures*. Vol. 220, pp. 622–641 , 2015.

[Cor+18] A. Cornejo et al. “Methodology for the analysis of post-tensioned structures using a constitutive serial-parallel rule of mixtures”. *Composite Structures*. Vol. 200, pp. 480–497 , 2018.

[Cor+19] A. Cornejo et al. “Combination of an adaptive remeshing technique with a coupled FEM-DEM approach for analysis of crack propagation problems”. *Computational Particle Mechanics*. Pp. 1–18 , 2019.

[Cor17] A. Cornejo. *Master Thesis: Evaluación de la técnica acoplada de elementos finitos y elementos discretos en problemas de fractura de rocas. Aplicación a voladuras en el frente de túneles*. Centro Internacional de Métodos Numéricos en Ingeniería - UPC. Barcelona. 2017.

[CS79] P.A. Cundall and D.L. Strack. “A discrete numerical model for granular assemblies.” *Geotechnique*. , 1979.

[CT17] M. Cervera and C. Tesei. “An Energy-Equivalent d+/d- Damage Model with Enhanced Microcrack Closure-Reopening Capabilities for Cohesive-Frictional Materials”. *Materials*. Vol. 10, p. 433 , 2017.

[DB82] G.J. Dvorak and Y.A. Bahei-El-Din. “Plasticity analysis of fibrous composites”. *J. App. Mech.*. Vol. 49, pp. 327–335 , 1982.

[DM07] P. Dumstorff and G. Meschke. “Crack propagation criteria in the framework of X-FEM-based structural analyses”. *Int. J. Numer. Anal. Meth. Geomech*. Vol. 31, pp. 239–259 , 2007.

[EY84] M. Eisenberg and C.F. Yen. “The anisotropic deformation of yield surfaces”. *J. Engng. Mater. Techn.*. Vol. 106, p. 355 , 1984.

[Fab+19] Ivan Fabregat et al. “Subsidence mechanisms and sedimentation in alluvial sinkholes inferred from trenching and ground penetrating radar (GPR). Implications for subsidence and flooding hazard assessment”. *Quaternary International*. Vol. 525, pp. 1–15 , 2019. DOI: https://doi.org/10.1016/j.quaint.2019.09.008.

[GJI13] D. Galloway, D. R. Jones, and S.E. Ingebritsen. *Land Subsidence in the United States*. U.S. Geological Survey Circular 1182. 2013.

[GK00] H. Gu and M. Kitanmra. “A modified recovery procedure to improve the accuracy of stress at central area of bilinear quadrilateral element”. *J. Soc. Nav. Arch. Japan*. Vol. 188, pp. 489–496 , 2000.

[GN65] A. Green and P. Naghdi. “A dynamical theory of interacting continua”. *Journal Engineering Science*. Vol. 3, p. 231 , 1965.

[Gur81] M.E. Gurtin. *An introduction to continuum mechanics*. 1981.

[GW89] G. Goodsell and J.R. Whiteman. “A unified treatment of superconvergent recovered gradient functions for piecewise linear finite element approximations”. *International Journal for Numerical Methods in Engineering*. Vol. 27, pp. 469–481 , 1989.

[GZH04] H. Gu, Z. Zong, and K.C. Hung. “A modified superconvergent patch recovery method and its application to large deformation problems”. *Finite Elem. Anal. Des*. Vol. 40, pp. 665–687 , 2004.

[Her72] L.R. Herrmann. “Interpretation of finite element procedures in stress error minimization”. *Proc. Am. Soc. Civ. Eng*. Vol. 98, pp. 1331–1336 , 1972.

[Hil48] R. Hill. “A theory of the yielding and plastic flow for anisotropic metals”. *Proc. Roy. Soc. London*. Vol. 193, pp. 281–297 , 1948.

[Hil65] R. Hill. “Micro mechanics of elastoplastic materials”. *J. Mech. Phis. Solids*. Vol. 13, pp. 89–101 , 1965.

[Hil71] R. Hill. *The mathematical Theory of Plasticity*. Oxford University Press. 1971.

[Hil79] R. Hill. “Theoretical plasticity of textured aggregates”. *Math. Proc. Cambridge Philos. Soc*. Vol. 85, pp. 179–191 , 1979.

[Hil90] R. Hill. “Constitutive modelling of orthotropic plasticity in sheet metals”. *J. Mech. Phis. Solids*. Vol. 38, pp. 405–417 , 1990.

[Hol00] G.A. Holzapfel. *Nonlinear solid mechanics: a continuum approach for engineering*. 2000.

[Hug00] T.J.R. Hughes. *The finite element method: linear static and dynamic finite element analysis*. 2000.

[IG90] A. Ingraffea and M. Grigoriu. *Probabilistic fracture mechanics: a validation of predictive capability*. 1990.

[JBO18] S. Jiménez, LG. Barbu, and S. Oller. *Analysis of post-tensioned structures by means of a constitutive serial-parallel rule of mixtures*. CIMNE. 2018.

[Jim+20] S. Jimenez et al. “Analysis of the mock-up of a reactor containment building: comparison with experimental results”. *Nuclear Engineering and Design*. Vol. 359, p. 110454 , 2020.

[KG07] A.R. Khoei and S.A. Gharehbaghi. “The superconvergence patch recovery technique and data transfer operators in 3D plasticity problems”. *Finite Elements in Analysis and Design*. Vol. 43, pp. 630–648 , 2007.

[KGN00] M. Kitanmra, H. Gu, and H. Nobukawa. “A study of applying the superconvergent patch recovery method in large deformation problem”. *J. Soc. Nav. Arch. Japan*. Vol. 187, pp. 208–210 , 2000.

[Kri89] M. Krizek. “Superconvergence results for linear triangular elements”. *Mathematical Institute, Czechoslovak Academy of Sciences*. , 1989.

[Kri94] M. Krizek. “Superconvergence phenomena in the finite element method”. *Comput. Methods Appl. Mech. Engrg*. Vol. 116, pp. 157–163 , 1994.

[Lev82] N. Levine. *Stress Sampling Points for Linear Triangles in the Finite Element Method*. University of Reading, Department of Mathematics. 1982.

[LZ99] B. Li and Z. Zhang. “Analysis of a class of superconvergence patch recovery techniques for linear and bilinear elements”. *Numerical Methods PDEs*. Vol. 15, pp. 151–167 , 1999.

[Mat20] V. Mataix. *Development of innovative mathematical and numerical models for the study of shells deformation during industrial forming processes employing the Finite Element Method*. Universitat Politècnica de Catalunya. 2020.

[Mau92] G.A. Maugin. *The thermodynamics of plasticity and fracture*. Cambridge University Press. 1992.

[MG07] C. Miehe and E. Gürses. “A robust algorithm for the configurational-force-driven brittle crack propagation with R-adaptative mesh alignment”. *Int. J. Numer. Anal. Meth. Geomech*. Vol. 72, pp. 127–155 , 2007.

[MH94] J.E. Marsden and T.J.R. Hughes. *Mathematical foundations of elasticity*. 1994.

[MP] OPEN MP. *https://www.openmp.org*.

[MR94] F.L. Matthews and R.D. Rawlings. *Composite Materials: Engineering and Science*. Chapman and Hall. 1994.

[MWW19] K. Mang, T. Wick, and W. Wollner. “A phase-field model for fractures in nearly incompressible solids”. *Computational Mechanics*. Pp. 1–18 , 2019.

[New59] N.M. Newmark. “A method of computation for structural dynamics”. *Journal of the Engineering Mechanics Division*. Vol. 85, pp. 67–94 , 1959.

[Ogd97] R.W. Ogden. *Non-linear elastic deformations*. 1997.

[Oli+90] J. Oliver et al. “Isotropic damage models and smeared crack analysis of concrete”. *Second international conference on Computer Aided Analysis and Design of Concrete Structures*. , 1990.

[Oll+93] S. Oller et al. “A finite element model for analysis of multiphase composite materials”. *Ninth International Conferences on Composite Materials. Zaragoza - Spain*. , 1993.

[Oll+95] S. Oller et al. “An anisotropic elastoplastic model based on an isotropic formulation”. *Engineering Computations*. Vol. 12, pp. 245–262 , 1995.

[Oll+96] S. Oller et al. “A plastic dmaage constitutive model for composite materials”. *Int. J. Solids and Structures*. Vol. 33(17), pp. 2501–2518 , 1996.

[Oll02] S. Oller. *Non-linear dynamics*. 2002.

[Oll03] S. Oller. *Simulación numérica del comportamiento mecánico de los materiales compuestos*. CIMNE - Barcelona. 2003.

[Oll88] S. Oller. *Un modelo de daño continuo para materiales friccionales*. 1988.

[Oña+15] E. Oñate et al. “A local constitutive model for the discrete element method. Application to geomaterials and concrete”. *Computational Particle Mechanics*. No. 2, Vol. 2, pp. 139–160 , 2015.

[Oña92] E. Oñate. *Cálculo de estructuras por el método de elementos finitos: Análisis elástico lineal.* Centro Internacional de Métodos Numéricos en Ingeniería. Barcelona. 1992.

[OO96] S. Oller and E. Oñate. “A Hygro-Thermo-Mechanical constitutive model for multiphase composite materials”. *Int. J. Solids and Structures*. Vol. 33(20-22), pp. 3179–3186 , 1996.

[OP82] M. Ortiz and E. Popov. “A physical model for the inelasticity of concrete”. *Proc. Roy. Soc. London*. Vol. 383, pp. 101–125 , 1982.

[Pop12] A. Popp. *Mortar Methods for Computational Contact Mechanics and General Interface Problems*. TECHNISCHE UNIVERSITAT MUNCHEN. 2012.

[QR89] Lin Qun and Xie Rui-feng. “Error expansion for FEM and superconvergence under natural assumption”. *Journal of Computational Mathematics*. Vol. 7, pp. 402–411 , 1989.

[Ras+08] F. Rastellini et al. “Composite materials non-linear modelling for long fibre reinforced laminates: continuum basis, computational aspects and validations”. *Comnput. Struct*. Vol. 86(9), pp. 879–896 , 2008.

[RKA20] D. Romanov, G. Kaufmann, and D. Al-Halbouni. “Basic processes and factors determining the evolution of collapse sinkholes A sensitivity study”. *Engineering Geology*. Vol. 270, p. 105589 , 2020.

[SG11] B. Singh and R.K. Goel. *Engineering Rock Mass Classification*. Butterworth-Heinemann. 2011.

[SH98] J.C. Simo and T.J.R. Hughes. *Computational inelasticity*. 1998.

[SJ87a] J.C. Simo and J.W. Ju. “Strain and stress based based continuum damage models I. Formulation”. *International Journal of Solids and Structures*. Vol. 23, pp. 821–840 , 1987.

[SJ87b] J.C. Simo and J.W. Ju. “Strain and stress based based continuum damage models II. Computational aspects”. *International Journal of Solids and Structures*. Vol. 23, pp. 841–869 , 1987.

[SL78] C.F. Shih and D. Lee. “Further developments in anisotropic plasticity”. *J. Engng. Mater. Techn.*. Vol. 105, p. 242 , 1978.

[SO12] M. Santasusana and E. Oñate. *Numerical Techniques for non-linear analysis of structures combining Discrete Element and Finite Element Methods*. 2012.

[Sos+17] A. Sosa et al. “Analyzing a suitable elastic geomechanical model for Vaca Muerta Formation”. *Journal of South American Earth Sciences*. Vol. 79, , 2017. DOI: 10.1016/j.jsames.2017.09.011.

[SPO08] E. de Souza, D. Peric, and R.J. Owen. *Computational Methods for Plasticity: Theory and Applications*. Wiley. 2008.

[TCC13] C. Thornton, SJ. Cummins, and PW. Cleary. “An investigation of the comparative behaviour of alternative contact force models during inelastic collisions”. *Powder Technology*. Vol. 233, pp. 30–46 , 2013.

[TFR96] G. B. Thomas, Jr. Finney, and L. Ross. *Calculus and Analytic Geometry (9th ed.)* 1996.

[TT60] C. Truesdell and R. Toupin. *The Classical Field Theories*. Springer, Berlin, Heidelberg. 1960.

[VF90] G.Z. Voyiadjis and M. Foroozesh. “The anisotropic deformation of yield surfaces”. *J. App. Mech.*. Vol. 57, p. 537 , 1990.

[WC11] W.A. Wall and C.J. Cyron. *Nichtlineare Kontinuumsmechanik, Institute for Computational Mechanics*. Institute for Computational Mechanics, Technische Universitĺat Mĺunchen. 2011.

[Wri06] P. Wriggers. *Computational Contact Mechanics*. 2006.

[Yas11] V. Yastrebov. *Computational contact mechanics: geometry, detection and numerical techniques*. Ecole Nationale Superieure des Mines de Paris. 2011.

[Zal00] F. Zalamea. *Tratamiento numérico de materiales compuestos mediante la teoría de homogenización*. Universidad Politécnica de Cataluña. 2000.

[ZBZ99] O.C. Zienkiewicz, B. Boroomand, and J.Z. Zhu. “Recovery procedures in error estimation and adaptivity, part I: adaptivity in linear problems”. *Comput. Methods Appl. Mech. Eng*. Vol. 176, pp. 111–115 , 1999.

[ZCO18] F. Zárate, A. Cornejo, and E. Oñate. “A three-dimensional FEMDEM technique for predicting the evolution of fracture in geomaterials and concrete”. *Comput Methods Appl Mech Eng*. Vol. 5, pp. 411–420 , 2018.

[Zha00] Z. Zhang. “Ultraconvergence of the patch theory recovery technique II”. *Math Comput*. Vol. 69, pp. 141–158 , 2000.

[ZO15] F. Zárate and E. Oñate. “A simple FEMDEM technique for fracture prediction in materials and structures”. *Computational Particle Mechanics*. Vol. 2, pp. 301–314 , 2015.

[ZT13] O. C. Zienkiewicz and R. L. Taylor. *The finite element method for solid and structural mechanics*. 2013.

[ZZ92a] O.C. Zienkiewicz and JZ. Zhu. “The superconvergence patch recovery and a posteriori error estimates, part I: the recovery techniques”. *Int. J. Numer. Methods Eng*. Vol. 33, pp. 1331–1364 , 1992.

[ZZ92b] O.C. Zienkiewicz and JZ. Zhu. “The superconvergence patch recovery and a posteriori error estimates, part II: error estimates and adaptivity”. *Int. J. Numer. Methods Eng*. Vol. 33, pp. 1365–1380 , 1992.

[ZZ92c] O.C. Zienkiewicz and JZ. Zhu. “The superconvergent patch recovery (SPR) and adaptive finite element refinement”. *Comput Methods Appl Mech Eng*. Vol. 101, pp. 207–224 , 1992.

[ZZ95] O.C. Zienkiewicz and JZ. Zhu. “Superconvergence and the superconvergent patch recovery”. *Finite Elem. Anal. Des.*. Vol. 19, pp. 11–23 , 1995.

[ZZT13] O. C. Zienkiewicz, J.Z. Zhu, and Robert L. Taylor. *The Finite Element Method: its Basis and Fundamentals*. Butterworth-Heinemann. 7th ed. 2013.

Part IV

Enhanced FEM-DEM formulation via an adaptive remeshing technique

Chapter 13

Introduction to the enhanced FEM-DEM formulation

This Chapter presents an enhanced coupled approach between the FEM and the DEM in which an adaptive remeshing technique has been implemented. The remeshing technique is based on the computation of the Hessian of a selected nodal variable, i.e. the mesh is refined where the curvature of the variable field is greater. Once the Hessian is known, a metric tensor is defined node-wise that serves as input data for the remesher (MmgTools) that creates a new mesh. After remeshing, the mapping of the internal variables and the nodal values is performed and a regeneration of the discrete elements on the crack faces of the new mesh is carried out.

One of the most powerful characteristics of the implementation performed is the capability of remesh geometries that have experienced large displacements and rotations and even fully detachments [DDF13], which is a key feature in the FEM-DEM. The remesher creates a new mesh from scratch based on the updated configuration of the geometry.

The remesher MmgTools has two main remeshing strategies available: the Level-Set (gradient of a certain distance function) and the Hessian strategy which is based in the computation of the Hessian of any nodal variable. In the case of more than one variable or a variable by components is considered them the intersection of the corresponding tensors. In this work, only a Hessian-based remeshing technique is considered.

Once one has chosen to use a Hessian-based remeshing strategy, a proper nodal indicator of which Hessian is computed has to be defined. In fluid dynamics, one of the most used is the velocity or acceleration field but, in the author's experience, it is a bad choice for solids. In the end, the nodal indicator used is a normalized expression of the free energy dissipated over the total energy available (extrapolated to the nodes). In this way the non-linear dissipation of the damaging process is intrinsically taken into account as well as the effective stress concentration at the most damaged zones.

Regarding the internal variables mapping techniques available, several procedures are offered in *Kratos Multi-physics*: the closest point transfer, shape function projection transfer and least-square projection transfer, being the first one the method used in this work. The author of this work chose the closest point transfer because it is the one that does not add an artificial diffusion to the internal variable mapped and, in addition, is the computational cheapest one.

It is important to mention that the remesher used is capable of perform isotropic and anisotropic remeshing [Tre07; FA04; FA03]. In fluids is very useful the anisotropic remeshing but in solids (which is the case of this work) generates too distorted FE (due to the stretching in one direction) that can produce instabilities and eventually prevent the convergence of the problem.

All the implementations performed have been published in Cornejo et al. [Cor+19]. Several examples of fracturing problems using the enhanced FEM-DEM formulation are presented in the next chapters. Accurate results in comparison with analytical and experimental solutions are obtained.

Finally, all the operations described regarding the remeshing process are implemented inside the `MeshingApp` in *Kratos Multi-physics* whereas some necessary processes (computation of the nodal indicator, regeneration of DE, etc...) can be found inside the `FemToDemApplication`.

13.1 State of the art in adaptive remeshing

In the last decades, in order to optimize the FE meshes as well as to improve the accuracy of the obtained solutions, several re-meshing methodologies have been developed. Additionally, these adaptive remeshing techniques can capture the physical behaviour of the problem [FA04] while reducing the computational cost -by reducing

the number of DoF- without a significant loss of accuracy associated.

These procedures allow to accelerate the process of mesh generation as it can be generated initially in a simple way and later adapted depending on the problem behaviour. Indeed, this automation can greatly facilitate the pre-processing of a finite element problem [ZZT13] as well as ease the implementation of more robust and autonomous algorithms, which adapt - in terms of mesh - to the study problem without the need for human decision making.

Despite its powerful advantages, re-meshing implies an added cost in terms of mesh generation, calculation of re-meshing indicators[1] mapping of nodal and internal variables from the old to the new mesh, among others. Additionally, the process of mapping nodal and integration point variables induces an interpolation error that causes the newly calculated mesh to be out of balance in the first instance. This error can generate oscillations and convergence losses in cases where the mesh changes too drastically [Cor+19].

As mentioned before, one of the main objectives of an adaptive remeshing technique regarding solid mechanics problems is to reduce the error exhibit in the displacement and stress fields. These error estimations were introduced by Babuska and Rheinboldt [BR78; BR79] in the 70's. One of the most used methodologies is the SPR developed by Zienkiewicz and Zhu [ZZ92] (see Section 7.2.1.2). Also from Zienkiewicz and Zhu one can find the so-called *recovery methods* [ZZ87] which are based on the calculation of a global energy norm followed by an estimation of local errors. This technology combined with an automatic mesh generator developed a very powerful tool for adapting the FE to the error requirements of the problem. Babuska and Rheinboldt [BR78; BR79] proposed the *residual based methods* which involved the residual obtained from the implicit FE calculation. A very complete and exhaustive description of the different error-controlled adaptive FE methods can be seen in Stein et al. [Ste+03].

More recently, some *Hessian* based techniques have been developed like in Wessner et al. [Wes+13] that involve the second derivatives of the error estimate which implies that the error estimation variable must be twice differentiable. One of the main advantages of this methodology is the capability of anisotropic remeshing, which means that the elements not only are can be refined but also stretched independently

[1] These remeshing indicators are used as a way of estimating the FE size of the new mesh according to a certain error level, curvature, gradient, etc., of a certain nodal value.

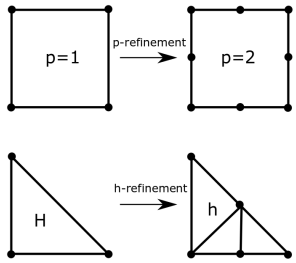

Figure 13.1: Graphical representation of an *h-refinement* and *p-refinement*

in each geometrical direction when necessary. This *Hessian* based methodologies are the ones adopted in this work.

Lastly, the remeshing techniques can be classified in the following categories [Wri08; Mat20]:

- **h-refinement:** The same type of FE is used -in terms of integration order and shape- but its size is modified (see Fig. 13.1). Within this category, one can find two main procedures [PC09]:
  - Enrichment: this procedure refines certain zones of the geometry by dividing the existing elements into smaller ones.
  - Remeshing: a new mesh is created from scratch, adapting the size of the new FE to the error requirements.
- **p-refinement:** in this case the size of the element remains constant but the polynomial order is enhanced. As can be seen in Fig. 13.1, the size of the element has not changed but the number of nodes is increased, with the consequent increase of DoF in the problem to solve [SG03; WB17].
- **hp-refinement:** this methodology combines the features of the previous refinement techniques. This means that both the element size and order can be modified to adapt to the problem requirements [Ste+08; Zan+16].
- **r-refinement:** the number of mesh nodes and cells remains constant, but nodes are relocated to areas where needed to increase resolution [McR00; Kuo12].

Within this work, the methodology employed coincides with the *h-refinement*, in particular we consider the remeshing procedure. This means that, whenever is necessary, according to the Hessian of a certain nodal variable, a new FE mesh will be generated, always maintaining its polynomial order.

Chapter 14

Hessian based adaptive remeshing technique

In this section we analyse in detail the techniques considered for remeshing. We introduce first the concepts of metrics (Section 14.1) and general *Hessian* based error measures (Section 14.2). Then we present the transfer operators for the internal variables of the damage model.

14.1 Metric based remeshing

In order to understand the concept involving the *Hessian* metric [Ala07][Wes+13], we first introduce the concept of metric. Then, we will show the intersection operations needed in case than more that one metric is taken into consideration.

14.1.1 Concept of metric

The notion of length in a metric space is related to the notion of metric [AFP03] and therefore to an adequate definition of the scalar product in the vector space considered. We define a metric tensor at a point P, respect an element K from a mesh $\mathcal{T}_h$, represented by a matrix $\mathcal{M}$ ($d \times d$) defined symmetric positive and not degenerated. In 3D, the following definition of $\mathcal{M}$ (Eq. (14.1)) is used, which can be assimilated to the analogy of an ellipsoid (Fig. 14.1).

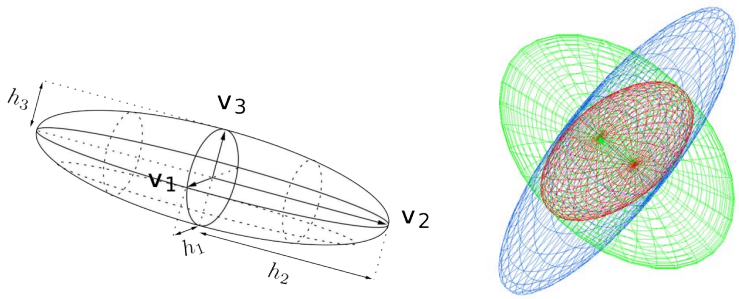

Figure 14.1: Metric analogy and intersection of metrics. Images from Alauzet [Ala07].

$$\mathcal{M} = \begin{bmatrix} a & b & c \\ b & d & e \\ c & e & f \end{bmatrix} \text{ such that } a > 0, d > 0, f > 0 \quad \text{and } \det(\mathcal{M}) > 0, \text{ considering } a, b, c, d, e \in \mathbb{R} \tag{14.1}$$

Tensor $\mathcal{M}$ can be diagonalized because it is symmetrical. Then, $\mathcal{M}$ can be written as $\mathcal{M} = \mathcal{R}\mathbf{\Lambda}\mathcal{R}^{-1}$, where $\mathcal{R}$ and $\mathbf{\Lambda}$ are the matrix of the eigenvectors and eigenvalues of $\mathcal{M}$, respectively.

Fig. 14.2 illustrates the effect of the metric on the mesh. The tetrahedra presented gets sketched accordingly to the metric computed at each node, represented with ellipsoids (Fig. 14.1).

14.1.1.1 Metric intersection

In the case that several metrics are specified at the same point of the mesh (for example if we want to use various nodal variables whose Hessians return different metrics) one have to define a procedure of intersection of all these metrics into one.

To define the intersection of two metrics, we use the fact that a metric tensor is represented geometrically by an ellipse (in 2D) or an ellipsoid (in 3D). The metric intersection consists then in keeping the most restrictive size constraint in all the

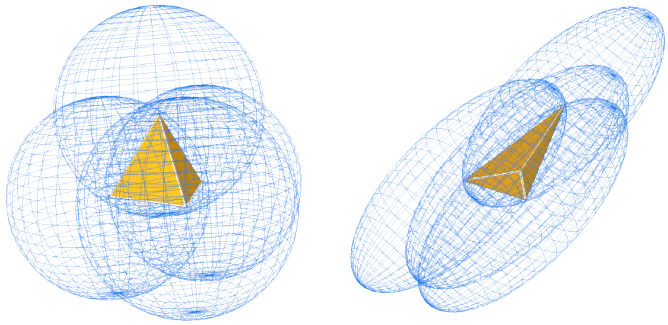

Figure 14.2: Effects of the metric on a tetrahedra

directions imposed by this set of metrics [Ala07] (Fig. 14.1).

The simultaneous reduction enables us to find a common basis ($\mathbf{e}_1$, $\mathbf{e}_2$, $\mathbf{e}_3$) such that $\mathcal{M}_1$ and $\mathcal{M}_2$ are congruent to a diagonal matrix. In this basis we can define a new tensor $\mathcal{N}$, whose expression is:

$$\mathcal{N} = \mathcal{M}_1^{-1}\mathcal{M}_2 \tag{14.2a}$$

$\mathcal{N}$ can be diagonalized in $\mathbb{R}$ because it is symmetrical in the metric $\mathcal{M}_1$. The base in question is given by the normalized eigenvectors of $\mathcal{N}$ that we denote $\mathbf{e}_1$, $\mathbf{e}_2$ and $\mathbf{e}_3$ (they form a base because $\mathcal{N}$ is diagonalisable) . The eigenvalues of $\mathcal{M}_1$ and $\mathcal{M}_2$ are found in this base using the *Rayleigh* quotient:

$$\lambda_i = \mathbf{e}_i^t \mathcal{M}_1 \mathbf{e}_i \text{ and } \mu_i = \mathbf{e}_i^t \mathcal{M}_2 \mathbf{e}_i \tag{14.2b}$$

Considering $\mathcal{P} = (\mathbf{e}_1, \mathbf{e}_2, \mathbf{e}_3)$ be the matrix the columns of which are the eigenvectors of $\mathcal{N}$ (common basis) one can obtain

$$\mathcal{M}_1 = \mathcal{P}^{-t} \begin{bmatrix} \lambda_1 & 0 & 0 \\ 0 & \lambda_2 & 0 \\ 0 & 0 & \lambda_3 \end{bmatrix} \mathcal{P}^{-1} \text{ and } \mathcal{M}_2 = \mathcal{P}^{-t} \begin{bmatrix} \mu_1 & 0 & 0 \\ 0 & \mu_2 & 0 \\ 0 & 0 & \mu_3 \end{bmatrix} \mathcal{P}^{-1} \tag{14.2c}$$

The metric intersection can be computed as:

$$\mathcal{M}_{1\cap 2} = \mathcal{M}_1 \cap \mathcal{M}_2 = \mathcal{P}^{-t} \begin{bmatrix} \max(\lambda_1, \mu_1) & 0 & 0 \\ 0 & \max(\lambda_2, \mu_2) & 0 \\ 0 & 0 & \max(\lambda_3, \mu_3) \end{bmatrix} \mathcal{P}^{-1} \tag{14.2d}$$

14.2 Hessian based error measure

Before introducing the theory involving the *Hessian* based metric, we summarize the following properties [AFP03]:

- The analysis and results obtained by this methodology are not asymptotic. This means that the size of the mesh h does not tend to zero, avoiding potential errors, like the collapse of the mesh at certain points.
- The metric is based in the *Hessian* of the solution.
- The metric is anisotropic.
- It is independent of the nature of the operator, so it can be used with any type of equation.

14.2.1 Theory

We compute the *Hessian* [Wes+13] matrix $\mathbf{H}$ of a scalar function f of vectorial variable as

$$\mathbf{H} = \begin{bmatrix} \frac{\partial^2 f}{\partial x_1^2} & \cdots & \frac{\partial^2 f}{\partial x_1 \partial x_n} \\ \vdots & \ddots & \vdots \\ \frac{\partial^2 f}{\partial x_n \partial x_1} & \cdots & \frac{\partial^2 f}{\partial x_n^2} \end{bmatrix} \text{ or just: } \mathrm{H}_{ij} = \frac{\partial^2 f}{\partial x_i \partial x_j} \tag{14.3}$$

Once the *Hessian* matrix has been computed we compute the corresponding anisotropic metric by [Ala07]:

$$\begin{aligned} &\mathcal{M} = \mathcal{R}^t \tilde{\mathbf{\Lambda}}^t \mathcal{R} \text{ where } \tilde{\Lambda} = \mathrm{diag}(\tilde{\lambda}_i) \text{ being} \\ &\tilde{\lambda}_i = \min\left(\max\left(\frac{c_d|\lambda_i|}{\epsilon}, \frac{1}{h_{max}^2}\right), \frac{1}{h_{min}^2}\right) \end{aligned} \tag{14.4a}$$

Being λ_i the eigenvalues of $\mathbf{H}$ and ϵ the error threshold and c_d a constant ratio of a mesh constant. The interpolation ratio ϵ has been taken as 10^{-6}. On the other hand

c_d can be taken as $\frac{2}{9}$ and $\frac{9}{32}$ for 2D and 3D cases, respectively. For an isotropic mesh the metric will be,

$$\mathcal{M}_{iso} = \text{diag}(\max(\tilde{\lambda}_i)) = \begin{bmatrix} \max(\tilde{\lambda}_i) & 0 & 0 \\ 0 & \max(\tilde{\lambda}_i) & 0 \\ 0 & 0 & \max(\tilde{\lambda}_i) \end{bmatrix} \tag{14.4b}$$

For an anisotropic mesh we have

$$\begin{aligned} \mathcal{M}_{aniso} &= \mathcal{R}^t \tilde{\mathbf{\Lambda}}_{aniso} \mathcal{R} \text{ with} \\ \tilde{\mathbf{\Lambda}}_{aniso} &= \text{diag}(\max(\min(\tilde{\lambda}_i, \tilde{\lambda}_{max}), R_{\lambda rel})) \text{ being} \\ R_{\lambda rel} &= |\tilde{\lambda}_{max} - R_\lambda| \text{ where } R_\lambda = (1-\rho)|\tilde{\lambda}_{max} - \tilde{\lambda}_{min}| \end{aligned} \tag{14.4c}$$

14.2.2 Example

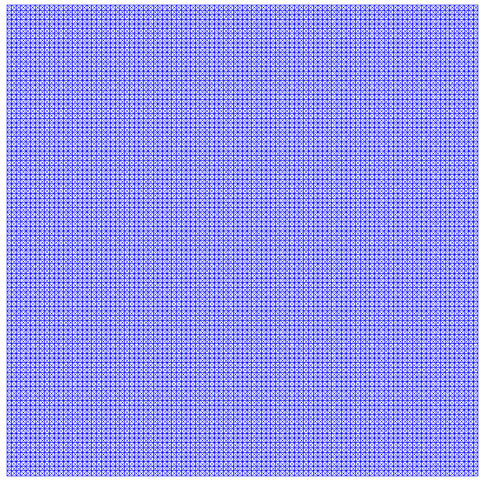

Figure 14.3: Initial mesh

The objective is to remesh the structured mesh of Fig. 14.3 according to the Hessian of the nodal variable (objective function) defined in Eq. (14.5). The original mesh has 40,000 structured triangular FE. Our objective is to obtain an unstructured mesh where the smaller elements will be in the vicinity of the objective function. This example was initially published in Cornejo et al. [Cor+19].

The nodal variable values are computed according to:

$$f(x,y) = \tanh(-100(y - 0.5 - 0.25\sin(2\pi x))) + \tanh(100(y - x)) \tag{14.5}$$

The results obtained are depicted in Fig. 14.5, using a mesh of 15,000 elements. The smaller elements are located around the χ shape displayed in Fig. 14.5 showing also the nodal value of the function defined in Eq. (14.5).

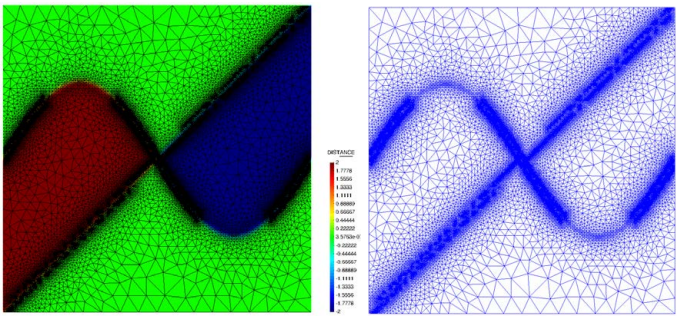

Figure 14.4: Nodal values of the remeshed mesh for the error function from Eq. (14.5). Source: Cornejo et al. [Cor+19].

14.3 Hessian nodal indicator

In order to optimize the remeshing technique and refine the elements close to the crack opening we define a proper nodal variable Υ of which *Hessian* is computed. Initially, the nodal extrapolation of the predictive Cauchy's stress tensor was selected but the meshes generated with this indicator were suboptimal, as it refines the zones near the boundary conditions where, in general, there is no interest. In the end, a normalized energetic nodal variable indicator was selected. The expression of the mesh refinement indicator is:

$$\Upsilon = \frac{1}{2\rho}\left(\varepsilon : \mathcal{C}_0 : \varepsilon\,(1-d)\left(\frac{r}{g_t} + \frac{1-r}{g_c}\right)\right) \tag{14.6}$$

where ρ is the material density, d is the damage internal variable, g_t and g_c are the normalized fracture energies in tension and compression (total fracture energy

divided by the characteristic length of the element), respectively and r is a tension indicator computed as:

$$r = \frac{\sum_{i=1}^{3} \langle \sigma_i \rangle}{\sum_{i=1}^{3} |\sigma_i|}, \ \langle \sigma_i \rangle = \frac{1}{2} \left(\sigma_i + |\sigma_i| \right) \tag{14.7}$$

being σ_i the principal components of the stress tensor. The mesh refinement indicator can be interpreted as the energy dissipated, normalized with the total energy available.

In some cases it is useful to use an alternative nodal indicator that does not take into account the damage and the density:

$$\Upsilon = \varepsilon : \mathcal{C}_0 : \varepsilon \tag{14.8}$$

This indicator refines a more reduced zone around the crack path but eventually can refine also the zones near the boundary conditions, which may not be necessary in all cases.

14.4 Internal variables interpolation

Once a new FE mesh has been created, nodal values and history-dependent variables need to be mapped or transferred from the old FE mesh to the new one. The state variables consist of the nodal displacements and the history-dependent variables such as the damage internal variable, which is stored at integration point level. Several important aspects of the mapping process have to be taken into account, i.e. [Kho+07],

- The mapping has to be consistent with the constitutive equations.
- The equilibrium of the structure can be altered.
- Compatibility with evolving boundary conditions.
- Minimizations of the numerical diffusion of the transferred fields (damage).

Fig. 14.5 shows graphically how each one of the *transfer operators* works [Jir] (all of them are available in *Kratos* [DRO10]).

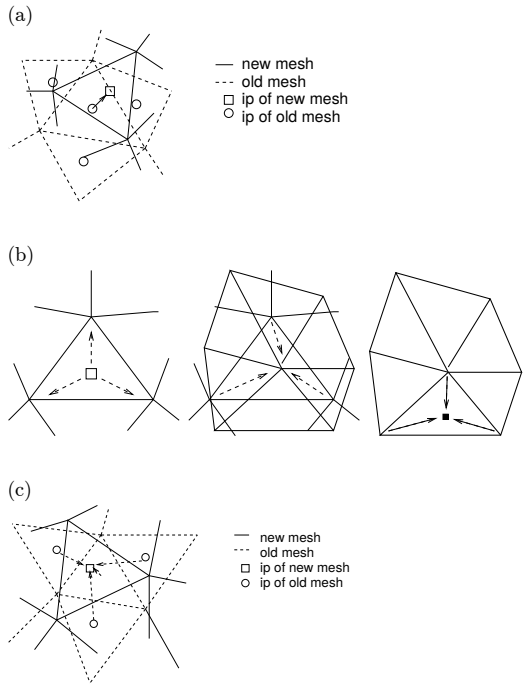

Figure 14.5: Transfer operators: a) Closest Point Transfer b) Shape Function Projection Transfer c) Least-Square Projection Transfer. Image from Jirásek [Jir].

- CPT: **Closest Point Transfer**. **(a)**. It takes the value from the closest point. It provides acceptable results at low cost.
- SFT: **Shape Function Projection transfer**. **(b)**. It interpolates the values using the standard FEM shape functions. It leads to an artificial damage diffusion, but preserves the original shape of the damage profile.
- LST: **Least-Square Projection transfer**. **(c)**. It considers a *least-square* transfer across the closest points. Probably it is the most accurate technique but also the most expensive from a computational point of view.

In the simulations performed, only the **CPT** technique was used.

14.5 Implemented algorithm of the FEM-DEM and the adaptive remeshing technique

The enhanced FEM-DEM formulation presented with the inclusion of an adaptive remeshing technique si summarized in the algorithm below.

Algorithm 6 Enhanced adaptive remeshing FEM-DEM algorithm with sub-stepping

• Initialization of the implicit transient dynamic scheme for the FEM: $t_i = t_i + \Delta t_i$, $k = 0$ being t_i the current time of the implicit scheme.
• Apply the DE contact forces from the previous time step as equivalent nodal force for the FEM
if *It is time to remesh* **then**
  • Compute nodal indicator $\Upsilon = \frac{1}{2\rho}\left(\varepsilon : \mathcal{C}_0 : \varepsilon(1-d)\left(\frac{r}{g_t} + \frac{1-r}{g_c}\right)\right)$ via Eq. (14.6)
  • Evaluate the *Hessian* matrix **H** via Eq. (14.3)
  • Calculate the metric tensor $\mathcal{M}$ by Eq. (14.4)
  • Perform the remeshing
  • Mapping of the internal variables and nodal values (Fig. 14.5)
  • Regenerate the DEM particles of the new mesh
end
• Do Alg. 3 if one-way coupling, Alg. 4 if two-way coupling or Alg. 5 is substepping is required

Chapter 15

Numerical examples with the enhanced FEM-DEM via an adaptive remeshing technique

In this section, a set of examples including the novel FEM-DEM formulation with the adaptive remeshing technique are shown. The first example is the well-known four point bending test whose fracture path is theoretically known and the force-displacement evolution has been compared with the results from Cervera et al. [CCC11]. The second example is a tensile test whose analytical solution is trivial, so it is very useful in order to validate the formulation. Finally, a three-point bending test on skew notched beam has been performed. The FEM-DEM results have been compared with those obtained by Cervera et al. [CBC17]. For the 2D examples, 3-noded triangles have been used. The 3D problems have been solved using 4-noded linear tetrahedra.

15.1 Four point bending test

In this section, the already exposed four point bending test (see Section 12.3) has been reproduced with the inclusion of the adaptive remeshing technique. The geometry of the test is depicted in Fig. 12.9 and the initial FE mesh can be seen in Fig. 12.10, being the coarser one. The material properties used are defined in Table 12.3.

Fig. 15.1 shows that the remeshing technique and the Hessian variable indicator defined in Eq. (14.6) are performing excellently as far as capturing the crack path is concerned. Another interesting feature is that the number of FE does not increase indefinitely. Fig. 15.1 shows that the number of FE in the mesh increases with respect to the initial coarse mesh but during the calculation is bounded up to a reasonable value (even decreasing at the end of the simulation) so the computational cost is balanced. It is important to note that the finer elements are located at the crack front, where the energy dissipation is greater, and not at the supports, where concentration of stresses can occur but no energy dissipation is occurring.

Quantitatively, the force-displacement evolution in one of the central supports is depicted in Fig. 15.2. In this figure the results from [CCC11] and the ones from the FEM-DEM formulation, with or without remeshing, are compared, showing a good agreement between them.

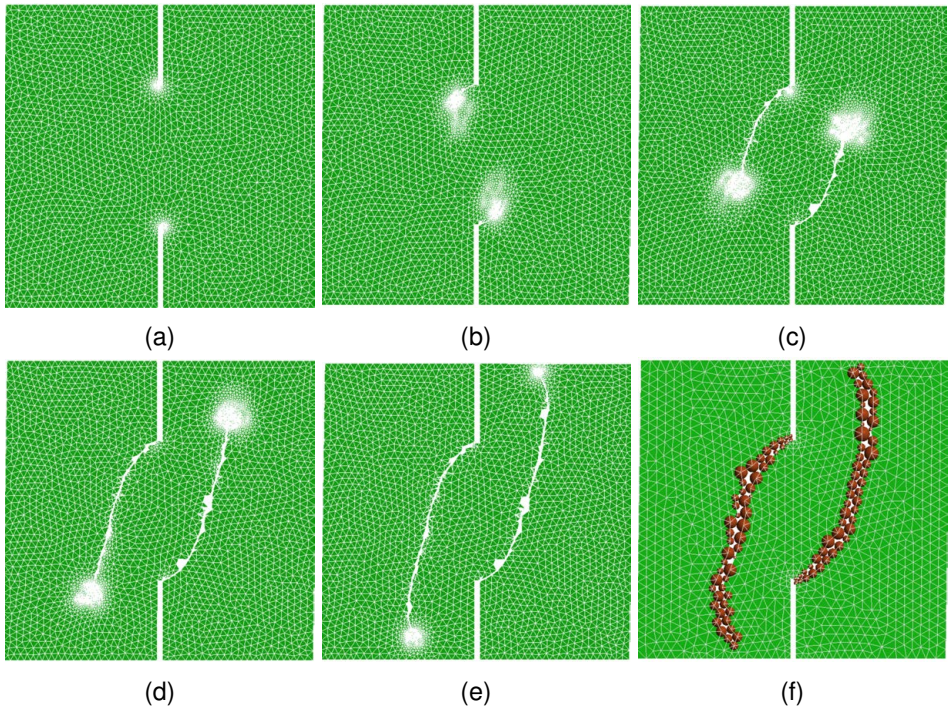

Figure 15.1: FE meshes during calculation (a) 5388 FE, b) 6276 FE, c) 8985 FE, d) 8188 FE, e) 6252 FE and f) Final result without remeshing technique.

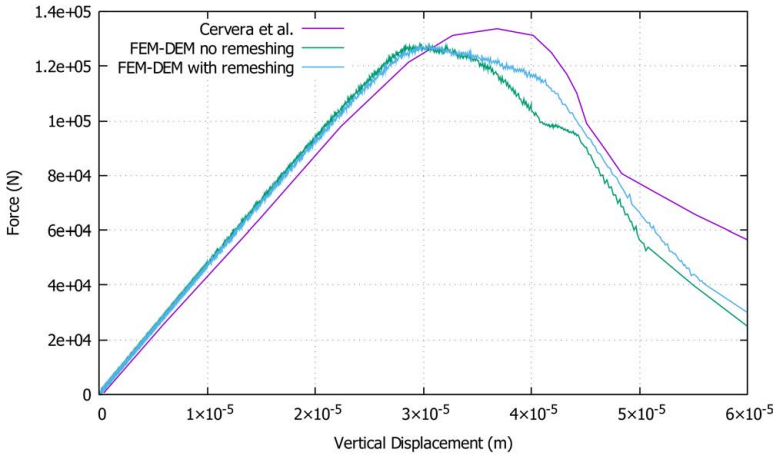

Figure 15.2: Force-displacement evolution in the four point bending test at one of the inner supports.

15.2 Tensile test

In this example a conventional 3D tensile test has been reproduced (see Section 12.1). The geometry of the sample is depicted in Fig. 12.1. The left end is clamped and the right one has a monotonic imposed displacement that introduces a tensile stress state. The material properties used are defined in Table 12.1.

Fig. 15.3 shows that the mesh refinement is concentrated at the centre zone, where all the energy dissipation is taking place due to the damage in the necking zone. The force-displacement evolution at one of the ends of the sample is depicted in Fig. 15.6 The results are in good agreement with the analytical expected solution.

In Fig. 15.4 the final fracture of the sample is depicted. As expected, fracture occurs at the centre of the necking. It is important to notice that the remeshing technique improves the quality of the cracking path (see the comparison in Fig. 15.5) but quantitatively is always consistent (Fig. 15.6), even when using coarse meshes.

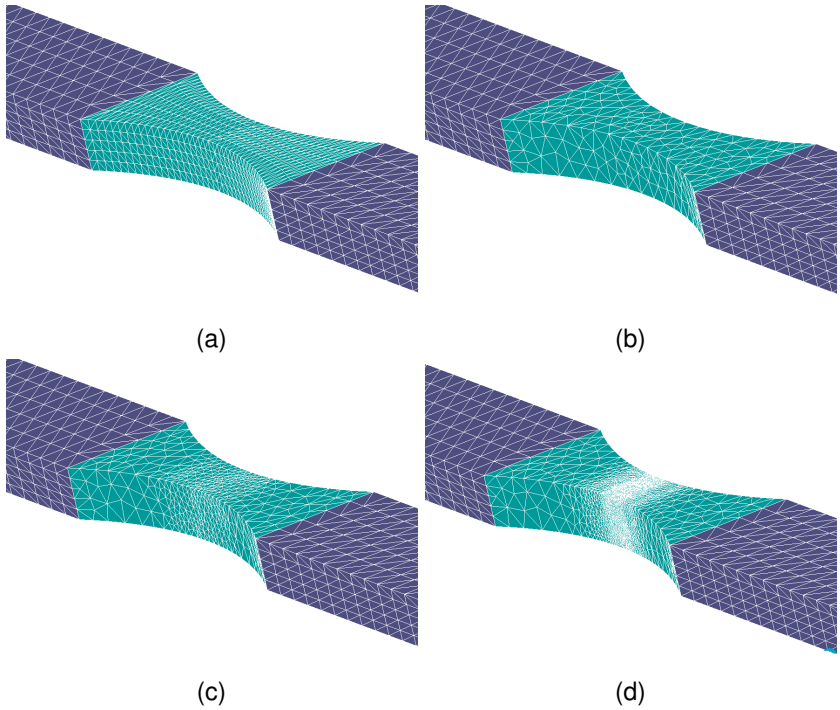

Figure 15.3: Tensile test FE meshes during the remeshed FEM-DEM calculation using 4-noded tetrahedra (a) 12000 FE, b) 8248 FE, c) 14092 FE and d) 70749 FE.

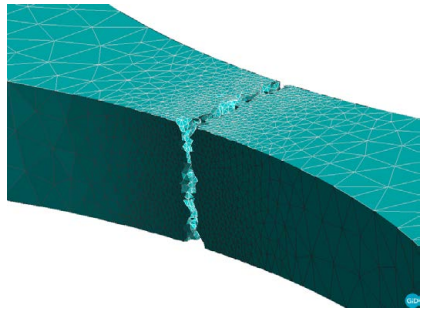

Figure 15.4: Tensile test fracture in the sample at the end of the calculation.

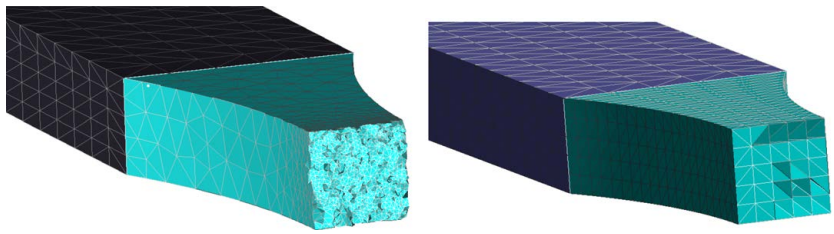

(a) With adaptive remeshing (b) Without adaptive remeshing

Figure 15.5: Tensile test comparison of the crack pattern between the solution with (a) or without (b) the remeshing technique.

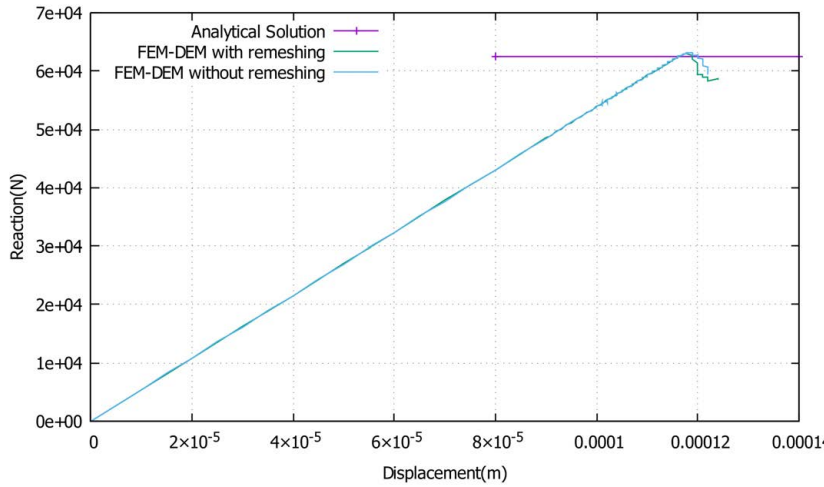

Figure 15.6: Force-displacement evolution for the tensile test at one of the ends of the sample.

Parameter	Value
Young's modulus (E)	28 GPa
Poisson's ratio (ν)	0.38
Tensile strength (f_t)	40 MPa
Fracture energy (G_f)	3000 J/m^2

Table 15.1: Material properties used in the Three-point bending skew notched beam.

15.3 Three-point bending skew notched beam

In this section, a skew notched beam subjected to three-point bending is analysed. The same problem was studied by Cervera et al. [CBC17]. The original experiment was performed by Buchholz et al. [BCR04] using Plexiglass in order to identify the fracture path along the sample. The geometry of the sample is shown in Fig. 15.7 in which the deviation of the notch can be seen. The Rankine yield surface was used in this test as in [CBC17].

The analysed problem is symmetric with respect to the notch and it fractures under a mixed Mode I and Mode III. Initially the crack path twists around the vertical axis until it is oriented perpendicular to the longitudinal direction of the beam. The initial mesh is depicted in Fig. 15.8. The FE meshes generated during the calculation using the remeshing technique can be analysed in Fig. 15.9. As it can be seen, the remeshing technique refines the elements near the notch due to the high dissipation that takes place in these zones. As the crack propagates, the remeshing follows the expected path by refining the front of the fracture at each remeshing step.

If one compares the results obtained with the simulation (Fig. 15.10) with the experimental results (Fig. 15.11) it is clear that the crack path follows the pattern obtained by the experiment accurately. As stated before, the solution obtained is skew-symmetrical. Also, the crack surface is perpendicular to the longitudinal axis at the end of the propagation as expected. The force-displacement evolution can be seen in Fig. 15.12. No numerical results regarding the force-displacement evolution was provided by the authors of this experiment.

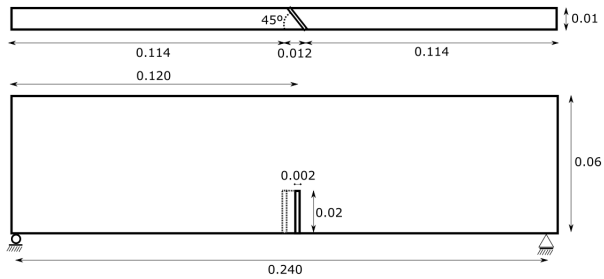

Figure 15.7: Three point bending skew notched beam geometry (units in m).

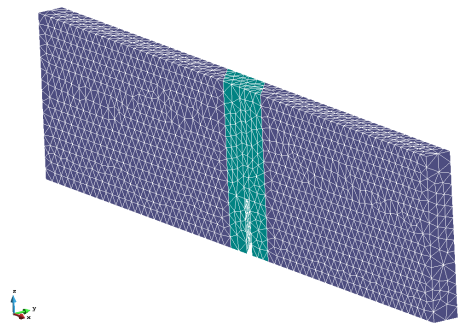

Figure 15.8: Three point bending skew notched beam initial FE mesh (15546 4-noded tetrahedra).

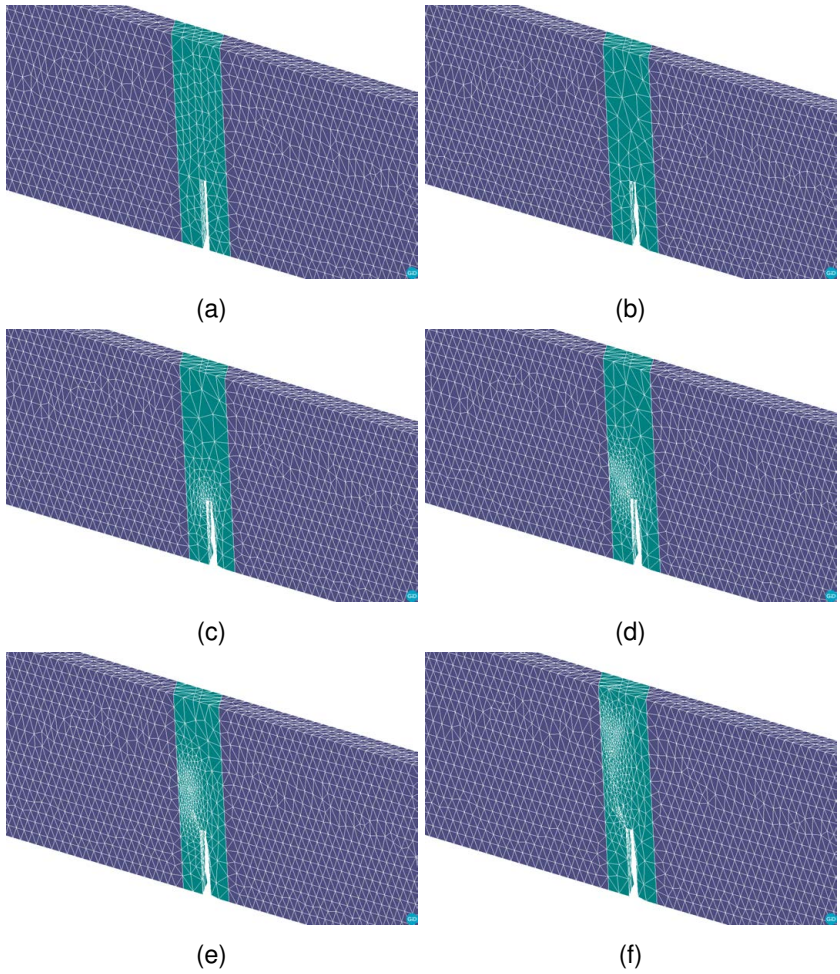

Figure 15.9: Adaptive FE meshes of 4-noded tetrahedra during calculation a) 15546 FE, b) 14436 FE, c) 16707 FE, d) 25811 FE, e) 27478 FE and f) 29738 FE.

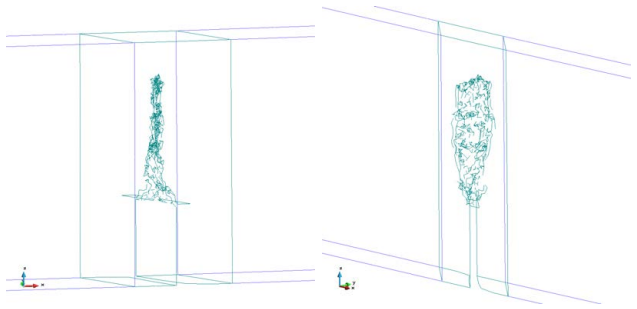

Figure 15.10: 3-Point bending beam test skew fracture path obtained with the simulation.

Figure 15.11: 3-Point bending skew beam experimental results with Plexiglass [BCR04].

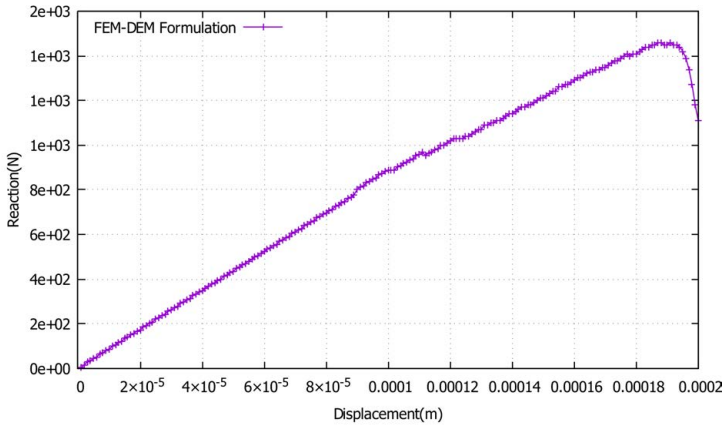

Figure 15.12: 3-Point bending skew beam force-displacement evolution at the centre of the beam.

Part IV bibliography

[AFP03] F. Alauzet, Frey, and Pascal. *Estimateur d'erreur géométrique et métriques anisotropes pour l'adaptation de maillage. Partie I : aspects théoriques*. 2003.

[Ala07] F. Alauzet. *Metric-Based Anisotropic Mesh Adaptation. Course material*. 2007.

[BCR04] F.G. Buchholz, A. Chergui, and H.A. Richard. "Analyses and experimental results of crack growth under general mixed mode loading conditions". *Eng Fract Mech*. Vol. 7, pp. 455–468 , 2004.

[BR78] I. Babuka and W. C. Rheinboldt. "A-posteriori error estimates for the finite element method". *International Journal for Numerical Methods in Engineering*. No. 10, Vol. 12, pp. 1597–1615 , 1978. DOI: 10.1002/nme.1620121010.

[BR79] I. Babuka and W. C. Rheinboldt. "Adaptive approaches and reliability estimations in finite element analysis". *Computer Methods in Applied Mechanics and Engineering*. Vol. 17-18, pp. 519–540 , 1979. DOI: https://doi.org/10.1016/0045-7825(79)90042-2.

[CBC17] M. Cervera, G.B. Barbat, and M. Chiumenti. "Finite element modelling of quasi-brittle cracks in 2D and 3D with enhanced strain accuracy". *Computational Mechanics*. Vol. 60, pp. 767–796 , 2017.

[CCC11] M. Cervera, M. Chiumenti, and R. Codina. "Mesh objective modeling of cracks using continuous linear strain and displacement interpolations". *Int. J. Numer. Meth. Engng*. Vol. 87, pp. 962–987 , 2011.

[Cor+19] A. Cornejo et al. “Combination of an adaptive remeshing technique with a coupled FEM-DEM approach for analysis of crack propagation problems”. *Computational Particle Mechanics*. Pp. 1–18 , 2019.

[DDF13] C. Dapogny, C. Dobrzynski, and P. Frey. *Three-dimensional adaptive domain remeshing, implicit domain meshing, and applications to free and moving boundary problems*. 2013.

[DRO10] P. Dadvand, R. Rossi, and E. Oñate. “An Object-oriented Environment for Developing Finite Element Codes for Multi-disciplinary Applications”. *Computational Methods in Engineering*. Vol. 17, pp. 253–297 , 2010.

[FA03] P.J. Frey and F. Alauzet. “Anisotropic mesh adaptation for transient flows simulations”. *Conference Paper*. , 2003.

[FA04] P.J. Frey and F. Alauzet. “Anisotropic mesh adaptation for CFD computations.” *Comput. Methods Appl. Mech.* , 2004.

[Jir] M. Jirásek. *Chapter 8 Nonlocal Damage Models 8.1 Basic Types of Nonlocal Damage Formulations*.

[Kho+07] A.R. Khoei et al. “Error estimation, adaptivity and data transfer in enriched plasticity continua to analysis of shear band localization”. *Applied Mathematical Modelling*. No. 6, Vol. 31, pp. 983–1000 , 2007. DOI: https://doi.org/10.1016/j.apm.2006.03.021.

[Kuo12] Yong-Lin Kuo. “The Enhanced r -Refinement Finite Element Analysis of Two-Dimensional Elastic Problems”. *Journal of Computational and Theoretical Nanoscience*. Vol. 9, pp. 908–917 , 2012. DOI: 10.1166/jctn.2012.2116.

[Mat20] V. Mataix. *Development of innovative mathematical and numerical models for the study of shells deformation during industrial forming processes employing the Finite Element Method*. Universitat Politècnica de Catalunya. 2020.

[McR00] D. Scott McRae. “r-Reőnement grid adaptation algorithms and issues”. *Comput. Methods Appl. Mech. Engrg*. Vol. 189, pp. 1161–1182 , 2000.

[PC09] J. Pitt and F. Costanzo. “An Adaptive h-Refinement Algorithm for Local Damage Models”. *Algorithms*. Vol. 2, , 2009. DOI: 10.3390/a2041281.

[SG03] S. D. Suchuan and E.K. George. “P-refinement and P-threads”. *Computer Methods in Applied Mechanics and Engineering*. No. 19, Vol. 192, pp. 2191–2201 , 2003. DOI: https://doi.org/10.1016/S0045-7825(02)00653-9.

[Ste+03] E. Stein et al. *Error-controlled Adaptive Finite Elements in Solid Mechanics*. Wiley. 2003.

[Ste+08] H. Sterck et al. “Efficiencybased h and hprefinement strategies for finite element methods”. *Numerical Linear Algebra with Applications*. Vol. 15, pp. 89–114 , 2008. DOI: 10.1002/nla.567.

[Tre07] P. Tremblay. *2-D, 3-D and 4-D Anisotropic Mesh Adaptation for the Time-Continuous Space-Time Finite Element Method with Applications to the Incompressible Navier-Stokes Equations*. 2007.

[WB17] D. Wells and J. Banks. “Using p-Refinement to Increase Boundary Derivative Convergence Rates”. . , 2017.

[Wes+13] W. Wessner et al. “Anisotropic Mesh Adaption Governed by a Hessian Matrix Metric”. . , 2013.

[Wri08] P. Wriggers. *Nonlinear finite element methods*. Springer. 2008.

[Zan+16] N. Zander et al. “The multi-level hp-method for three-dimensional problems: dynamically changing high-order mesh refinement with arbitrary hanging nodes”. *Numerical Linear Algebra with Applications*. Vol. 310, pp. 252–277 , 2016. DOI: https://doi.org/10.1016/j.cma.2016.07.007.

[ZZ87] O. C. Zienkiewicz and J. Z. Zhu. “A simple error estimator and adaptive procedure for practical engineerng analysis”. *International Journal for Numerical Methods in Engineering*. No. 2, Vol. 24, pp. 337–357 , 1987. DOI: 10.1002/nme.1620240206.

[ZZ92] O.C. Zienkiewicz and JZ. Zhu. “The superconvergent patch recovery (SPR) and adaptive finite element refinement”. *Comput Methods Appl Mech Eng*. Vol. 101, pp. 207–224 , 1992.

[ZZT13] O. C. Zienkiewicz, J.Z. Zhu, and Robert L. Taylor. *The Finite Element Method: its Basis and Fundamentals*. Butterworth-Heinemann. 7th ed. 2013.

Part V

Interaction of free-surface flows and structures by coupling the PFEM and FEM-DEM approaches

Chapter 16

Introduction to the interaction of free-surface flows and structures

In recent years, there has been a growing need for knowledge in relation to complex processes involving different coupled physical processes. This is why intensive work has been done to develop numerical models capable of capturing such processes in a reliable and efficient way. This work presents a new coupled numerical method for the simulation of structures collapsing and fracturing under the impact of free-surface fluids.

This type of FSI problems is of high interest for different engineering and industrial branches and can be found in several real-world situations, such as in the undesired case of civil structures and infrastructures affected by natural hazards, like floods, tsunami waves, or landslides.

The numerical simulation of these multi-coupled problems is challenging due to their high non-linearity and the complexity of the involved phenomena. Indeed, the numerical method must be able to deal with free-surface fluids undergoing large changes of topology and interacting with structures that can break and desegregate into smaller solid debris which, in turn, may eventually hit other structures.

The complexity of this scenario explains the reduced number of computational

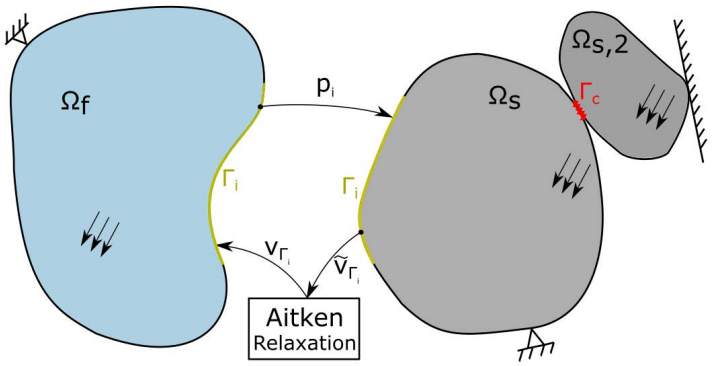

Figure 16.1: Strong coupling between the fluid (Ω_f) and the solid (Ω_s) with the Aitken relaxation technique. Exchange of pressures **p** and relaxed velocities **v** at the interface Γ_i. Schematic representation of the contact between two solids in Γ_c.

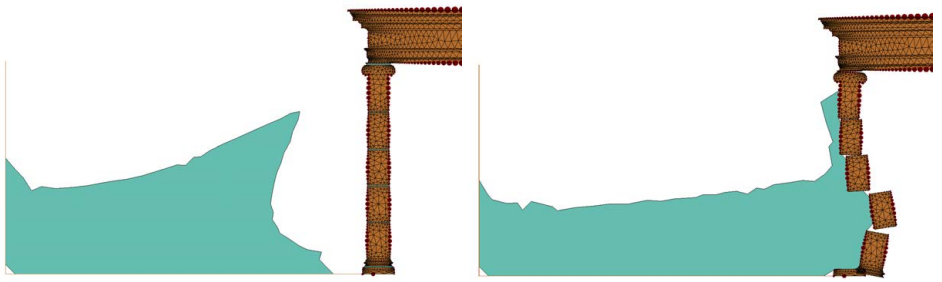

Figure 16.2: Fluid impact over a historical building.

methods for FSI problems with fracture phenomena present in the literature. Most of these works are focused on the structural failure of pipes or vessels subjected to shocks and explosions, *e.g*. [CDM07; Rab+07; Nor+12; WLF15; Dua+19; Kei+19; Tal+19].

Another important research area in this field refers to the simulation of hydraulic fracture processes, see *e.g* [Ada+07; SS12; PO17; DO18]. On the other hand, a smaller number of works analysed the collapse of civil structures caused by the impact of free-surface fluid flows, which is the main focus of the present work. In [Wic16], an FSI formulation with a PF fracture model was proposed for the structural failure caused by the impact of fluid flows in closed domains. In [SW18], similar problems were analysed considering also the fragmentation of the structure due to the cracks propagation. In [Ren+14], also free-surface fluids were considered using a coupled SPH-DEM model. Other SPH-based works analysed the effect of tsunami waves on civil infrastructures, especially bridges, although fracture phenomena of the structures were not taken into account [CA16; MA16; LA18]. Still in this research line, it is worth to mention the following coupled method based on SPH [AGS07], Inmersed Particle Method (IBM) [Rab+07; RB07] and DEM-LBM (Lattice Boltzman Method) [HFO07].

The PFEM [Cre+20] has also been used to model similar fluid-solid interaction phenomena, such as in [IOP04; OIA04]. but without modelling fracture processes. On the other hand, in the coupled PFEM-DEM model proposed in [OCI06; Oña+08] for bed erosion processes in river dynamics, the solid domains were also allowed to suffer changes of topology due to the erosion produced by the fluid flow. However, the detached parts could be modelled either as a set of dimensionless DEM particles or as rigid bodies, and not as deformable solids capable of fracturing again, as it is done in the present work.

The FSI problem is here solved with a novel hybrid strategy that combines three different Lagrangian numerical methods. The free-surface fluid dynamics problem is solved with the stabilized PFEM formulation presented in [OIA04], while the solid deformation, fracture and mutual contact are modelled by combining a FEM) with smoothed isotropic damage model [Cor+19; Oli+90] with a DEM [WO99; Cel+17; Cel+19], in the spirit of the so-called FEM-DEM method [ZO15; ZCO18; Cor+19].

In the specific type of FSI problems considered in this work, the solution accuracy strictly depends on the capability of the numerical method to track the evolving fluid-solid interface. This task is particularly critical for the problems analysed here because,

on the one hand, the fluids have a free surface which changes continuously during the analysis and, on the other hand, the solids can undergo large displacements/rotations and their contours can change significantly due to the propagating cracks and the consequent fragmentation of the structure. In this work, the fluid-solid interface is detected automatically with the PFEM during its remeshing step.

Remarkably, the remeshing procedure used in the PFEM not only improves the quality of the finite element discretization and defines the updated fluid free surface, but also allows to detect the new contact surfaces with the solid bodies. The Lagrangian nature of the PFEM guarantees also that all the nodes of the interface belong to both the fluid and the solid meshes. This allows us to avoid projecting nodal variables between the solid and the fluid domains. In this sense, this coupled approach can be classified as a body-fitted conforming-mesh FSI method [HWL12]. Compared to mesh-free [Ari+12], non-conforming mesh [Pes02; Gil+10] and embedded [Zor+20] FSI approaches, body-fitted algorithms allow for an easier transmission of boundary conditions between fluid and solid domains. Nevertheless, these methods generally require a similar size of fluid and solid elements at the interface zone and may lead to mesh distortion issues when applied to large deformation problems. In the case of large and arbitrary motion of the interface, this latter task can become critical for conforming-mesh methods basing on ALE) techniques [DH03].

On the contrary, the PFEM can naturally track the evolving interface and, at the same time, maintain a good discretization, also in the presence of large and unpredictable motion of the fluid-solid interface. This feature represents one of the main advantages of the PFEM for coupled fluid-solid mechanics analysis and also explains the extended use of the method for FSI problems, *e.g.* [Ryz+10; Ide+08; CFP10; FOC16; Med+17; ZS17; Cer+19].

In some cases its not possible, or very difficult, to ensure convergence for the staggered iterative problem exposed. This is typically the case when the densities of the solid and the fluid are similar (added-mass effects). In order to overcome this issue, an Aitken relaxation technique [Cer+19; Bre78; BZ90; DG80; SF82] for the velocities at the interface Γ_i has been employed (Section 18.2 and Fig. 16.1). Additionally, in Fig. 16.2 how the fluid can impact against any general structure, damage certain zones of it and drag rock debris that can contact between themselves.

Once the contact interfaces between fluids and solids have been detected, the FSI time step solution is performed through an Aitken iterative scheme [IT69]. A staggered method has been preferred to a monolithic one to avoid the ill-conditioning of the

linear system which could arise due to different orders of magnitude of the physical parameters of the involved materials. We note that this situation is prone to occur in the problems of interest of this work which involves civil structures that are generally characterized by high values of stiffness.

Concerning the solid mechanics solution scheme, the used FEM-DEM approach can be classified as a hybrid continuum-discrete formulation for fracture mechanics. The crack inception is detected using a continuum FEM model according to an isotropic damage model [Oli+90], while the DEM is used to compute the repulsion forces due to the contact interaction between different solid contours, including those of propagating cracks. Before fracturing, the stiffness degradation of the material and the crack initialization are approached in a smeared way. During this phase, the mesh topology is not changed and the fracture is represented by stress softening and localization. When the inelastic energy dissipation reaches the fracture energy in some zones of the solid, the finite elements contained therein are removed from the mesh and a replaced by a mass-equivalent set of particles, or discrete elements. These particles are used to prevent the indentation of the crack boundaries and to manage the frictional contact with the other solid bodies, using a standard DEM solution algorithm. In the case that larger solid areas are removed, could happen that some particles are no longer dependent on a certain FE node. In this case, a sub-stepping procedure has to be performed in order to capture properly the movement and kinematics of these particles (by using an explicit time integration as is commonly done in standard DEM).

A sub-stepping procedure is also employed in the time marching scheme to synchronize the FEM implicit solution and the DEM explicit one.

One of the main advantages of the FEM-DEM methodology lays in its capability to model in a natural way not only the onset, evolution, merging and branching of fractures, but also the eventual detachment of solid blocks, their mutual contact, and their independent motion under the effect of the fluid flow. This feature is particularly important for the problems of interest for this work, because loose solid debris may be at the origin of other damages on structures or living beings.

In the following chapters, the main characteristics of the PFEM formulation are presented, namely its general methodology, its governing equations as well as its solution in finite elements. Then, the operations performed in the coupling between the fluid and the solid and its relaxation procedure are detailed. Finally, some numerical examples are discussed.

Chapter 17

PFEM formulation for free-surface flow

17.1 Fluid dynamics problem

17.1.1 Remeshing procedure with the PFEM

The fluid governing equations are solved using a Lagrangian mesh. For fluid dynamics problems, this strategy leads inevitably to a deterioration of the mesh quality. With the PFEM, this inconvenience is circumvented by building a new discretization from the nodes of the previous FE mesh, whenever this has exceeded a threshold level of distortion. The remeshing step of the PFEM is done combining Delaunay Triangulation [ET93] and the Alpha Shape Method [EM99]. Figs. 17.1 and 17.2 show graphically the PFEM remeshing steps for two different situations of an FSI analysis. In particular, Fig. 17.1 shows a time instant in which the fluid and the solid domains are not interacting, whereas Fig. 17.2 represents a situation in which the fluid-solid interaction is active.

As shown in Figs. 17.1a and 17.2a, the first step of PFEM remeshing consists of erasing all the fluid elements of the previous distorted mesh. It is important to note that the nodes of the previous mesh are preserved together with all the problem information (nodal unknowns and physical parameters) and the solid mesh is not affected by the PFEM remeshing.

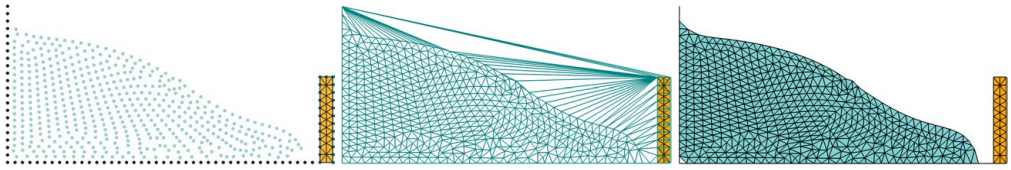

(a) Erase elements (b) Delaunay triangulation (c) Alpha Shape method

Figure 17.1: PFEM remeshing steps. Not active fluid-structure interaction.

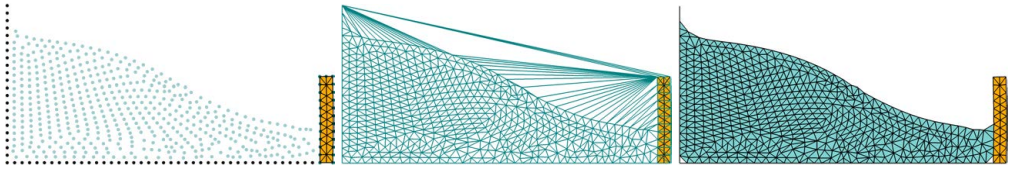

(a) Erase elements (b) Delaunay triangulation (c) Alpha Shape method

Figure 17.2: PFEM remeshing steps. Active fluid-structure interaction.

In the second step of remeshing, the Delaunay triangulation is built over the cloud of points formed by the nodes of the previous mesh. As shown in Figs. 17.1b and 17.2b, the Delaunay mesh is built also considering the nodes belonging to rigid contours and the boundary nodes of the solid domain (interface nodes).

In order to recognize the actual boundaries of the fluid domain (both the free surface and the new interface with the solid and rigid boundaries), the Alpha Shape Method is applied. This technique evaluates the quality of all the elements created by the Delaunay triangulation and removes from the mesh those elements that exceed a limit value of distortion or size. This way, the algorithm is capable to recognize the updated boundaries of the computational domain with good accuracy, as shown in Fig. 17.1c and 17.2c. Note that this step is crucial to establish whether the fluid and the solid domains are in contact or not. In the positive case, the fluid and the solid solutions will be coupled, as in the situation described in Fig. 17.2. In the opposite case (Fig. 17.1), the fluid solution will not be affected by the solid one and vice versa, at least for the duration of the next time step increment. More details about the PFEM remeshing process and its implications are given in [ICO03; OIA04; FC16].

17.1.2 Governing equations

The governing equations for the fluid dynamics problem are the linear momentum balance and the mass conservation equations. The problem is solved in an Updated Lagrangian framework as it is commonly done in the standard PFEM [IOP04]. Calling Ω_f the updated fluid domain and being $(0, T)$ the considered time interval, the fluid governing equations read

$$\rho_f \frac{\partial \mathbf{v}}{\partial t} - \bigtriangledown \cdot \boldsymbol{\sigma}_f - \rho_f \mathbf{g} = \mathbf{0} \qquad \text{in } \Omega_f \times (0, T) \tag{17.1}$$

$$\bigtriangledown \cdot \mathbf{v} - \frac{1}{\kappa_f} \frac{\partial p}{\partial t} = 0 \qquad \text{in } \Omega_f \times (0, T) \tag{17.2}$$

where $\mathbf{v}$ is the velocity vector, t is the time, $\boldsymbol{\sigma}_f$ is the fluid Cauchy stress tensor, $\mathbf{g}$ is the gravity acceleration vector, and ρ_f and κ_f are the fluid density and bulk modulus, respectively.

For Newtonian fluids, the Cauchy stress tensor is computed as

$$\boldsymbol{\sigma}_f = p\mathbf{I} + 2\,\mu_f\,\mathbf{d'} \tag{17.3}$$

where p is the pressure, $\mathbf{I}$ is the 2^{nd} order identity tensor, μ_f is the fluid dynamic viscosity, and $\mathbf{d'}$ is the deviatoric part of the deformation rate tensor $\mathbf{d}$ and it is computed as

$$\mathbf{d'} = \frac{1}{2}\left(\bigtriangledown \mathbf{v} + (\bigtriangledown \mathbf{v})^T\right) - \frac{1}{3} d_v \mathbf{I} \tag{17.4}$$

where $d_v = \bigtriangledown \cdot \mathbf{v}$ is the volumetric deformation rate.

Following [OIA04; ROI12; FOC15], the mass conservation equation (Eq. (17.2)) is here solved not in the standard divergence-free form of the Navier-Stokes problem ($\bigtriangledown \cdot \mathbf{v} = 0$), but considering a certain (small) compressibility of fluid material. For values of bulk modulus going to infinity the divergence-free form of the continuity equation is recovered.

The fluid governing equations are completed by the following boundary conditions at the Dirichlet (Γ_f^v) and Neumann (Γ_f^t) contours

$$\begin{aligned} \mathbf{v} - \hat{\mathbf{v}} &= \mathbf{0} \qquad && \text{on } \Gamma_f^v \\ \boldsymbol{\sigma} \cdot \mathbf{n} - \hat{\mathbf{t}} &= \mathbf{0} \qquad && \text{on } \Gamma_f^t \end{aligned} \tag{17.5}$$

being $\mathbf{n}$ the normal vector to fluid boundaries, $\hat{\mathbf{v}}$ the prescribed velocities at Dirichlet boundaries and $\hat{\mathbf{t}}$ the prescribed tractions at the Neumann ones.

17.1.3 Finite element solution

The fluid governing equations are solved in a standard FEM fashion and following the implicit stabilized velocity-pressure strategy presented in Oñate et al. [OFC14]. The domain is discretized with simplicial elements (triangles in two dimensions and tetrahedra in three dimensions) and linear shape functions are used for both velocity and pressure fields. The used stabilization method belongs to the family of Finite Calculus (FIC) methods [Oña98; OFC14; PO17]. According to the FIC scheme [OFC14], the stabilization terms are added to the continuity equation only, while the linear momentum equations are left unchanged. The derivation of the FIC-FEM form of the fluid governing equations is considered out of the scope of this work and it has already been detailed in [OFC14]. Hence, in this section, only the final fully-discretized and linearised form is given.

The time step solution is obtained through an iterative two-step procedure where the linear momentum equations are solved for the increments of nodal velocities $\mathbf{\Delta \bar{v}}$ and the stabilized continuity equation is solved for the nodal pressures $\bar{\mathbf{p}}$[1].

Considering a generic time step $[t^n; t^{n+1}]$ of duration Δt, at each iteration k, the increment of nodal velocities are obtained from the fully-discretized form of the linear momentum equations (Eq.(17.1)) as

$$\left(\mathbf{K}^{\rho} + \mathbf{K}^{m}\right) \mathbf{\Delta \bar{v}}_{k+1} = \mathbf{R}_k \tag{17.6}$$

with

$$\begin{aligned} \mathbf{K}^{\rho}_{IJ} &= \mathbf{I} \int_{\Omega} \frac{2\rho_f}{\Delta t} N_I N_J d\Omega, \quad \mathbf{K}^{m}_{IJ} = \int_{\Omega} \mathbf{B}_I^T \mathbf{C} \mathbf{B}_J d\Omega \\ R_{Ii} &= \int_{\Omega} \rho_f N_I N_J d\Omega \; \bar{\dot{v}}_{Ji} + \int_{\Omega} \frac{\partial N_I}{\partial x_j} \sigma_{ij} d\Omega - \int_{\Omega} \rho_f g_i N_I d\Omega \end{aligned} \tag{17.7}$$

where N_I is the linear shape functions for node I and matrices $\mathbf{B}$ and $\mathbf{C}$ are defined for a two dimensional problem as follows

$$\mathbf{B}_I = \begin{bmatrix} \dfrac{\partial N_I}{\partial x} & 0 \\ 0 & \dfrac{\partial N_I}{\partial y} \\ \dfrac{\partial N_I}{\partial y} & \dfrac{\partial N_I}{\partial x} \end{bmatrix}, \quad \mathbf{C} = \begin{bmatrix} \hat{\kappa_f} \Delta t + \dfrac{4\mu_f}{3} & \hat{\kappa_f} \Delta t - \dfrac{2\mu_f}{3} & 0 \\ \hat{\kappa_f} \Delta t - \dfrac{2\mu_f}{3} & \hat{\kappa_f} \Delta t + \dfrac{4\mu_f}{3} & 0 \\ 0 & 0 & \mu_f \end{bmatrix} \tag{17.8}$$

[1] $\bar{\cdot}$ denotes a nodal variable

The pseudo-bulk modulus $\hat{\kappa_f}$ used in the fluid constitutive matrix $\boldsymbol{c}$ is obtained by reducing *ad hoc* the real fluid bulk modulus κ_f to avoid ill-conditioning the algebraic linear system. Details about this technique are given in Franci et al. [FOC15].

After solving solution of Eq. (17.6) and updating the fluid kinematic with the new velocities, the fluid nodal pressures $\bar{\mathbf{p}}$ are computed from the fully-discretized and FIC-Stabilized form of the continuity equation (Eq. (17.2)) as follows

$$(\mathbf{M} + \mathbf{S}^{\tau})\,\bar{\mathbf{p}}_{k+1} = \mathbf{M}\bar{\mathbf{p}}^{n} - \mathbf{Q}^{T}\,\bar{\mathbf{v}}_{k+1} + \mathbf{f}^{\tau}_{k+1} \tag{17.9}$$

with

$$M_{IJ} = \int_{\Omega} \frac{N_I N_J}{\kappa_f \Delta t} d\Omega, \quad \mathbf{Q}_{IJ} = \int_{\Omega} \mathbf{B}_I^T \mathbf{m} N_J d\Omega \tag{17.10}$$

where, for two dimensional problems, $\mathbf{m} = [1, 1, 0]^T$.

$\mathbf{S}^{\tau}$ and $\mathbf{f}^{\tau}$ are stabilizing terms arising from the FIC method [OFC14]. The terms are detailed in Section 17.1.4.

Eq. (17.6) and Eq. (17.9) are solved iteratively within each fluid time step increment until the fulfilment of the established convergence criterion.

17.1.4 FIC stabilized terms

Here, the FIC terms used for the fluid problem stabilization and introduced in Section 17.1.3 are detailed. The stabilization terms of the FIC technique [OFC14] affect the continuity equation (Eq. (17.9)) only, while the linear momentum equations ((17.6)) are not modified.

In Eq. (17.9), the FIC stabilization terms $\mathbf{S}^{\tau}$ and $\mathbf{f}^{\tau}$ are computed as [OFC14]

$$\mathbf{S}^{\tau} = \left(\frac{1}{\Delta t^2} \mathbf{M}^{c} + \mathbf{L} + \mathbf{M}^{b} \right) \tag{17.11}$$

$$\mathbf{f}^{\tau} = \frac{\mathbf{M}^{c}}{\Delta t^2} \left(\bar{\mathbf{p}}^{n} + \dot{\bar{\mathbf{p}}}^{n} \Delta t \right) + \mathbf{f}^{p} \tag{17.12}$$

with

$$
\begin{aligned}
M^c_{IJ} &= \int_\Omega \tau \frac{\rho_f}{\kappa_f} N_I N_J d\Omega, \\
L_{IJ} &= \int_\Omega \tau (\boldsymbol{\nabla}^T N_I) \boldsymbol{\nabla} N_J d\Omega, \\
M^b_{IJ} &= \int_{\Gamma_t} \frac{2\tau}{h_n} N_I N_J, \\
f^p_I &= \int_{\Gamma_t} \tau N_I \left[\rho_f \frac{Dv_n}{Dt} - \frac{2}{h_n}(2\mu_f d_n - \hat{t}) \right] d\Gamma - \int_\Omega \tau \boldsymbol{\nabla}^T N_I \rho \mathbf{g} d\Omega
\end{aligned}
\tag{17.13}
$$

where Γ_t is the free-surface contour and the stabilization parameter τ is defined as

$$
\tau = \left(\frac{8\mu_f}{h^2} + \frac{2\rho_f}{\delta} \right)^{-1} \tag{17.14}
$$

where h and δ are characteristic distances in space and time. More details about the derivation of the stabilization terms can be found in [OFC14].

17.1.5 FIC Stabilized mixed velocity-pressure algorithm

The algorithm of the stabilized mixed $v - p$ formulation for quasi-incompressible fluids is shown in Alg. 7.

Algorithm 7 Non-linear solution scheme for the FIC Stabilized mixed velocity-pressure formulation for Newtonian fluids

1. Compute the nodal velocities increments $\boldsymbol{\Delta}\bar{\mathbf{v}}$:
   $\mathbf{K}^i \boldsymbol{\Delta}\bar{\mathbf{v}} = \mathbf{R}^i({}^{n+1}\bar{\mathbf{v}}^i,\ {}^{n+1}\boldsymbol{\sigma'}^i,\ {}^{n+1}\bar{\mathbf{p}}^i)$
2. Update the nodal velocities: ${}^{n+1}\bar{\mathbf{v}}^{i+1} = {}^{n+1}\bar{\mathbf{v}}^i + \boldsymbol{\Delta}\bar{\mathbf{v}}$
3. Update the nodal coordinates: ${}^{n+1}\bar{\mathbf{x}}^{i+1} = {}^{n+1}\bar{\mathbf{x}}^i + \bar{\mathbf{u}}(\boldsymbol{\Delta}\bar{\mathbf{v}})$
4. Compute the nodal pressures ${}^{n+1}\bar{\mathbf{p}}^{i+1}$:
   $(\mathbf{M} + \mathbf{S}^\tau)\ {}^{n+1}\bar{\mathbf{p}}^{i+1} = \mathbf{M}\,{}^{n}\bar{\mathbf{p}} - \mathbf{Q}^T\ {}^{n+1}\bar{\mathbf{v}}^{i+1} + {}^{n+1}\mathbf{f}^{\tau\,i+1}$
5. Compute the updated stress measures (Newtonian fluid):
   ${}^{n+1}\boldsymbol{\sigma}^{i+1} = 2\mu\mathbf{d}'({}^{n+1}\bar{\mathbf{v}}^{i+1}) + {}^{n+1}\bar{\mathbf{p}}^{i+1}\mathbf{I}$
6. Check convergence of the problem $\left\|\mathbf{R}^{i+1}({}^{n+1}\bar{\mathbf{v}}^{i+1},\ {}^{n+1}\bar{\mathbf{p}}^{i+1})\right\| <$ tolerance

If condition 6 is not fulfilled (not converged), return to 1 and $i = i + 1$

if *Mesh distortion* $>$ *tolerance* **then**

Erase the fluid elements and maintain the nodes (Figs. 17.1a and 17.2a).
Create Delaunay Triangulation over the cloud of nodes (Figs. 17.1b and 17.2b).
Do Alpha Shape check to recognize the free-surface boundaries and fluid-solid interface (Figs. 17.1c and 17.2c).

end

Chapter 18

Coupling of the FEM-DEM with the PFEM

18.1 The PFEM-FEM-DEM formulation

In this work, the PFEM will simulate the free-surface fluid flow dynamics problem and the FEM-DEM will be in charge of the computations regarding the non-linear solid mechanics problem and fracture. As has been exposed in previous chapters, the PFEM is formulated in a Lagrangian description of motion, which facilitates the transmission of information between the fluid and solid interfaces[1]. This means that several non-trivial problems usually related to the use of Eulerian or Arbitrary Lagrangian Eulerian (ALE) formulations have been avoided .

The interaction between the PFEM and the FEM-DEM consists in an staggered strong coupling (two way coupling) scheme. This means that the PFEM detects the solid boundary (which is being updated at each time step) and computes the kinematics of the fluid part as well as the pressures field. Then, these pressures at the solid boundary are transferred to the FEM-DEM as standard line/surface loads depending on the dimension of the problem. Indeed, these loads have to be regenerated at each time step because either the free-surface has changed and/or the pressure values have evolved (due to the PFEM calculation). This bidirectional transmission of

[1] In fact, the PFEM and the FEM-DEM share the nodes at the interface so there is no need of using any projector operator in order to transfer the kinematics and/or the pressures between the domains

information has to be performed iteratively at each time step until a certain convergence criterion[2] is reached at the interface of the solid and fluid domains. In order to ensure the convergence of this iterative staggered scheme, a relaxation technique (see Section 18.2) at the interface must be conducted in order to avoid a huge number of iterations between the solid and the fluid strategies.

It is also important to remark the fact that the nodes belonging to the interface are governed by the solid mechanics kinematics and not both. Indeed, during the PFEM calculations, the velocity and position of the coupling nodes are considered as fixed. After the convergence of the implicit PFEM strategy, these coupling nodes are free now to move under the solid mechanics computations.

Regarding the boundary detection of the solid, two approaches were considered: the first one consists in assuming the whole volume of the solid as a boundary for the PFEM. This is computationally cheaper and easier to implement (the nodes are added only once at the beginning of the simulation) but, in general, the algorithm tends to lose robustness because the PFEM remeshing step can generate fluid FE with the nodes in the interior of the solid domain, which is a very serious issue. The second option, which is the one eventually used, consists in recomputing the boundary of the solid at each time step (only when the topology of the solid has changed due to fracturing) and updating this boundary nodes to the PFEM when necessary. This is a more expensive option but the most robust.

Related to the fluid pressures transfer to the solid part, at each Aitken iteration, just before the FEM-DEM calculation starts, there is a process that detects the nodes at the interface with non-zero pressure and generate line/surface loads which value is the average pressure of the nodal pressures involved in that load. Must be said that, in order to increase the efficiency of the methodology, the line/surface loads are generated only once per step but its value is updated at each iteration, according to the new pressure values obtained from the PFEM.

Lastly, it is important to mention that, even though the simulation of flexible solids is not the scope of this work, it has been proved that the presented formulation is capable of simulating these kind of processes with the inclusion of a hyperelastic law for the solid part (see Eq. (6.26)).

[2] In this work, the convergence criterion is based on the residual of the velocities at the interface Γ_i of the fluid and solid domains. Indeed, the norm of the residual $\mathbf{R} = \mathbf{v}_{\Gamma_i} - \tilde{\mathbf{v}}_{\Gamma_i}$ is compared with a certain tolerance $\epsilon_v = \dfrac{tol}{NumDof}$

18.2 Aitken relaxation technique

In order to avoid instabilities inherent in the sequential staggered schemes, a relaxation procedure has been used [Cer+19]. Every time step requires iterations between the two fields until convergence is reached of the respective interface velocities is reached (see Fig. 16.1).

At the beginning of the current time step t_{n+1}, according to the information of the previous time step t_n, the fluid strategy ($\mathfrak{F}$) computes the new velocities $\bar{\mathbf{v}}^{i+1}_{t_{n+1}}$, pressures $\bar{\mathbf{p}}^{i+1}_{t_{n+1}}$ and positions $\bar{\mathbf{x}}^{i+1}_{t_{n+1}}$ of the fluid domain (iteration $i+1$). Next, the pressures at the interface Γ_i are transferred to the structure as pressure loads $\bar{\mathbf{p}}^{i+1}_{t_{n+1},\Gamma_i}$ and the solid strategy ($\mathfrak{S}$) solves the non-linear solid mechanics problem. The result of the solid strategy $\mathfrak{S}(\bar{\mathbf{p}}^{i+1}_{t_{n+1},\Gamma_i})$ is the updated set of displacements $\tilde{\mathbf{u}}^{i+1}_{t_{n+1}}$, velocities $\tilde{\mathbf{v}}^{i+1}_{t_{n+1}}$ and accelerations $\tilde{\mathbf{a}}^{i+1}_{t_{n+1}}$. The next step is to *relax* the solid velocities $\tilde{\mathbf{v}}^{i+1}_{t_{n+1}}$ at the interface via an Aitken scheme ($\mathfrak{A}$) as:

$$\mathbf{v}^{i+1}_{t_{n+1},\Gamma_i} = \omega_i \, \tilde{\mathbf{v}}^{i+1}_{t_{n+1},\Gamma_i} + (1-\omega_i)\mathbf{v}^{i}_{t_{n+1},\Gamma_i} \tag{18.1}$$

being $\mathbf{v}^{i+1}_{t_{n+1},\Gamma_i}$ the relaxed velocity at the interface Γ_i and ω_i is the Aitken relaxation parameter which calculation is:

$$\omega_{i+1} = -\omega_i \frac{\mathbf{R}^{i^T}(\mathbf{R}^i - \mathbf{R}^{i-1})}{\left\|\mathbf{R}^i - \mathbf{R}^{i-1}\right\|^2} \tag{18.2}$$

where $\mathbf{R}^i$ is the residual of the velocities at the interface $\mathbf{R}^i = \tilde{\mathbf{v}}^{i}_{t_{n+1},\Gamma_i} - \mathbf{v}^{i}_{t_{n+1},\Gamma_i}$ and the initial value of the Aitken parameter has been taken as 0.825 in this work.

This iterative scheme has to be repeated until the norm of the residual is lower than a certain predefined tolerance. In this work, the convergence is achieved when:

$$\frac{\left\|\mathbf{R}^i\right\|}{\text{Number of DoF}} <? \text{tol} \tag{18.3}$$

18.3 PFEM-FEM-DEM solution scheme

Summarizing all the information exposed in the previous sections, all the operations and processes performed for coupling the PFEM and the FEM-DEM formulations are presented in Alg. 8.

Algorithm 8 PFEM-FEM-DEM coupled solution scheme for a time step

- Time step initialization $t = t + \Delta t$.
- PFEM performs remeshing (only once per step)

while $\left\| \boldsymbol{R}^i \right\| / Number\ of\ DoF > tol$ **do**

- Fix the velocity and position of the interface nodes of the solid.
- Solve the PFEM part of the calculation (see Alg. 7)
- Free the velocities and position of the boundary nodes of the solid
- Regenerate and update the values of the fluid induced pressure loads on the solid part
- Solve the FEM-DEM part of the calculation (do Alg. 3-4 or Alg. 5 if substepping is required)
- Relax the velocities at the interface via Aitken relaxation (see Eq. (18.1))
- Check convergence of velocities at the interface Γ_i (Eq. (18.3))

end

Chapter 19

Numerical examples of the coupled PFEM-FEM-DEM methodology

Several numerical examples are presented to validate the proposed PFEM-FEM-DEM formulation and to highlight specific features of the method. The first example validates the correct transmission of pressures in a controlled hydrostatic example. Next, the accurate exchange of information in terms of solid skin and boundaries is assessed in the second example (Section 19.2). Section 19.3 and 19.4 ensures that the proposed method is capable of simulating strong added-mass effects and flexible solids submitted to a wave impact.

For validating the capacity of the formulation to deal with submerging solid objects in a free surface fluid, the wedge water entry example described in Section 19.5 has been reproduced.

Next, the progressive collapse of a 2D and 3D solid slab due to the accumulation of a free-surface fluid is reproduced. Finally, the structural failure of a framed 2D structure and a 3D concrete wall under the action of a tsunami wave is presented.

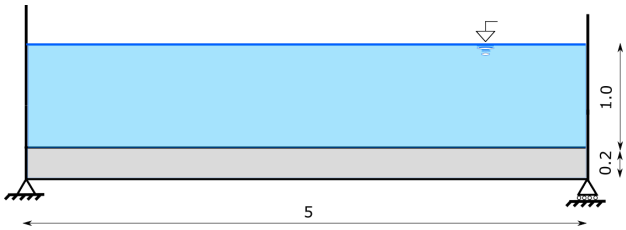

Figure 19.1: Initial setup of the beam submitted to a hydrostatic load. Units in [m].

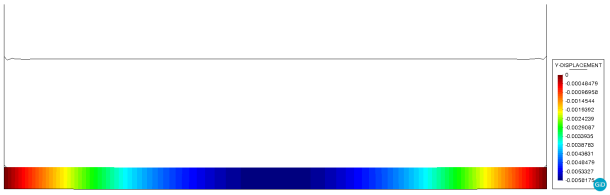

Figure 19.2: Displacement field obtained for the solid part [m].

19.1 Hydrostatic load over a beam

In order to validate the transmission of pressures between the fluid and the solid parts, a simply supported beam submitted to a hydrostatic loading of a fluid has been simulated. The geometry of the problem is shown in Fig. 19.1. In this 2D problem, a plane strain formulation has been employed. The material properties used are defined in Table 19.1.

Analytically, the self weight of the beam is $q_{sw} = 0.2 \times 1.0 \times \rho_s \times g = 4708.8\, N/m$. Additionally, the fluid pressure at the bottom reaches a value of $q_{fluid} = H \times \rho_f \times g = 9810\, N/m$. Knowing this, one can estimate analytically the maximum deflection of the beam as:

$$\delta_{\max} = \frac{5\, q_{tot} l^4}{384 EI} = 5.907 \cdot 10^{-3} m. \tag{19.1}$$

being $q_{tot} = q_{sw} + q_{fluid}$. On the other hand, the PFEM-FEM-DEM solution of this problem is depicted in Fig. 19.2, obtaining a displacement of $5.817 \cdot 10^{-3} m$. This means that the FEM solution has a error of 1.5 % approximately, which is reasonable.

Parameter	Value
Solid Young's modulus (E)	30 GPa
Solid Poisson's ratio (ν)	0.0
Solid Density (ρ_s)	2400 kg/m^3
Fluid Viscosity (μ)	0.001 $Pa \cdot s$
Fluid Density (ρ_f)	1000 kg/m^3

Table 19.1: Problem data for the simply supported beam submitted to a hydrostatic loading.

19.2 Dam break against a stiff step

In this section, a collapse of a water column against a rigid step has been solved. This example is widely known in the literature, like in Franci et al. [FC16], and has been reproduced in laboratories like in Greaves [Gre06]. The initial geometry of the problem can be seen in Fig. 19.3 and the material properties of the solid and fluid parts are given in Table 19.2. The time step used is $\Delta t = 0.001s$.

In this problem, the gravity is the only external load over the solid and fluid materials. Initially, the solid part has been meshed with 1255 FE and 834 nodes whereas the fluid part is composed by 6204 FE and 3159 nodes. Fig. 19.4 shows the time evolution of the fluid previously and after the impact against the rigid step. The results are in agreement with the ones given by Franci et al. [FC16] and the ones coming from the laboratory (see Greaves [Gre06] and Fig. 19.5). With this example it is shown that the coupling between the fluid and the solid parts behave as expected.

Additionally, we have recomputed the example assuming that the solid part can be damaged and eventually fractured (reducing the time step to $\Delta t = 0.0001s$). In that case, the results can be found in Fig. 19.6 in which one can see how the solid step has been fractured at its base and moved a certain distance. In order to prevent the indentation of the rigid step against the ground, an initial set of DE is placed over the skin of the solid.

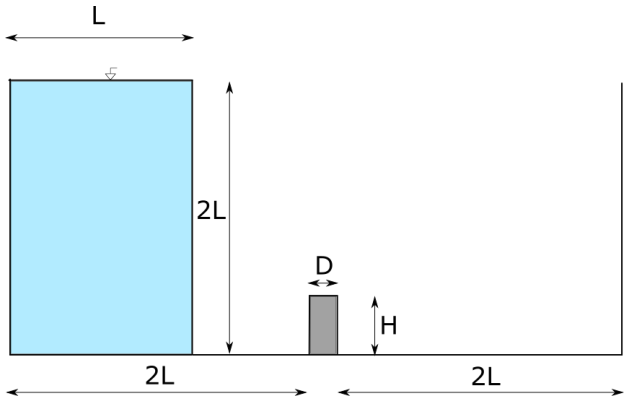

Figure 19.3: Dam break against a stiff step. Initial setup.

Parameter	Value
Solid Young's modulus (E)	10 GPa
Solid Poisson's ratio (ν)	0.2
Solid Density (ρ_s)	2400 kg/m^3
Fluid Viscosity (μ)	0.01 $Pa \cdot s$
Fluid Density (ρ_f)	1000 kg/m^3
L	0.146 m
H	0.048 m
D	0.024 m

Table 19.2: Problem data for the water dam break against a rigid step.

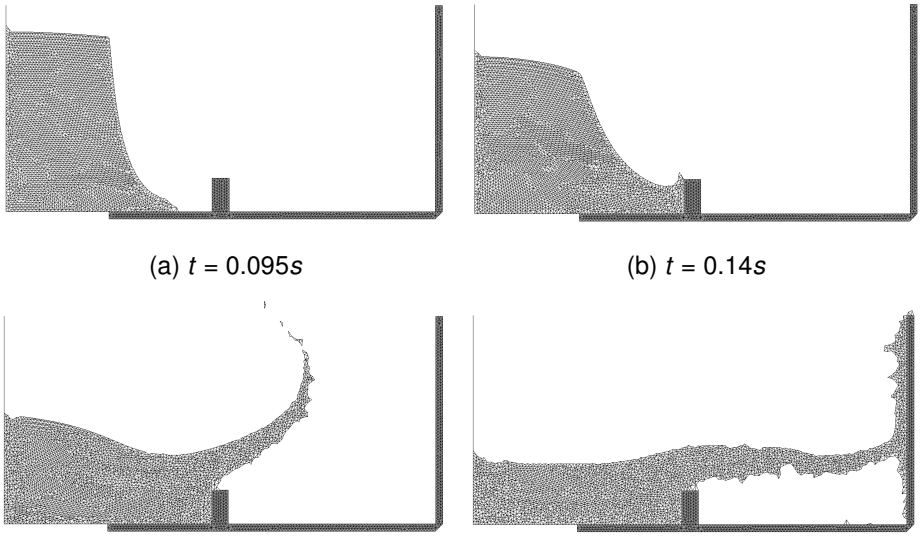

(a) $t = 0.095s$ (b) $t = 0.14s$

(c) $t = 0.24s$ (d) $t = 0.38s$

Figure 19.4: Time lapse of the water impacting over the stiff step.

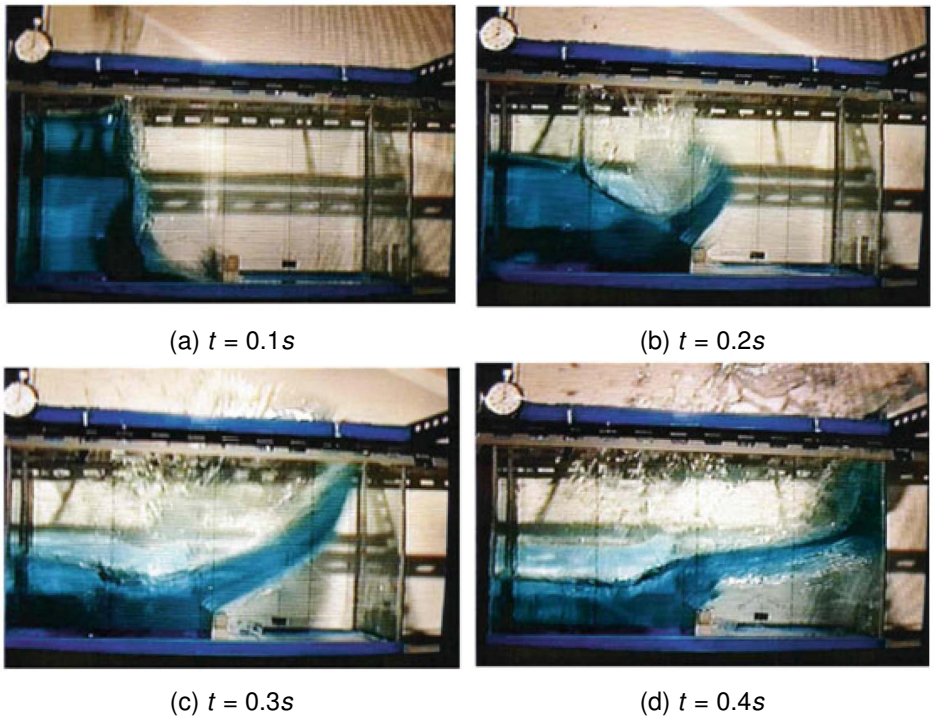

(a) $t = 0.1s$ (b) $t = 0.2s$

(c) $t = 0.3s$ (d) $t = 0.4s$

Figure 19.5: Time lapse of the water impacting over the stiff step in the laboratory. Images from Greaves [Gre06].

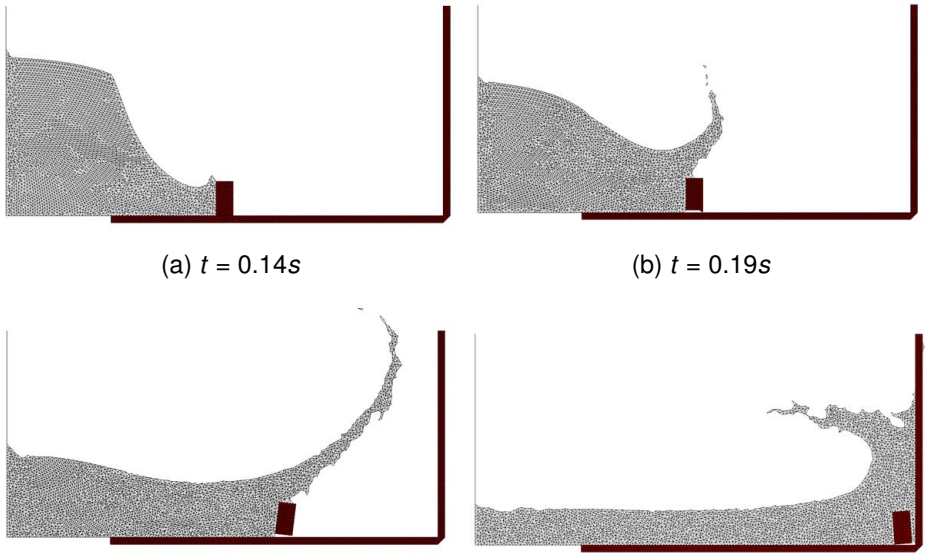

(a) $t = 0.14s$ (b) $t = 0.19s$

(c) $t = 0.30s$ (d) $t = 0.54s$

Figure 19.6: Time lapse of the water impacting over the stiff inelastic step.

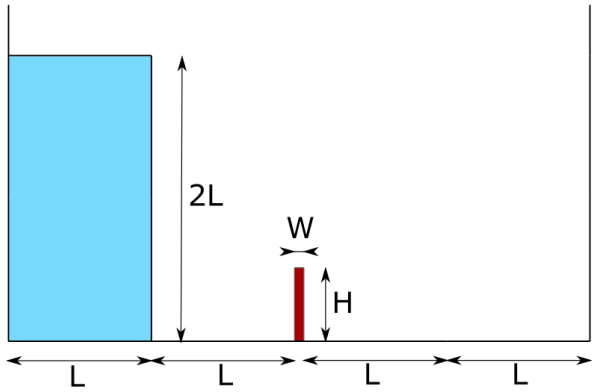

Figure 19.7: Initial setup of the dam break against a flexible wall.

19.3 Dam break against a flexible wall

Another validation example for the implemented FSI consists in a model of a dam breaking against a deformable obstacle. This benchmark example was initially proposed by Walhorn et al. [Wal+05] and subsequently reproduced by Cerquaglia et al. [Cer+19], Meduri et al. [Med+17] and Ryzhakov et al. [Ryz+10]. The initial setup of the example is shown in Fig. 19.7 in which at the beginning of the calculation the fluid is free to flow towards the solid wall. A highly flexible wall is located in the middle of the geometry whose horizontal displacement is tracked along time meanwhile is being hit by the fluid column. The material properties used and the geometry data is given in Table 19.3. For the solid, a Neo-hookean large strain constitutive law and a total Lagrangian FE kinematics have been used. The mesh used for the solid contains 3982 FE whereas the fluid is simulated with 3964 FE.

Regarding the problem data, the time step used is Δt = 1e-3s, the relaxation procedure used is the Aitken methodology assuming a tolerance of 1e-7 and a maximum relaxation of ω_{max} of 0.9.

As can be seen in Fig. 19.8, the amplitude of the initial impact and its subsequent time evolution is well represented with the proposed method in comparison with the literature. Additionally, the results shown in Fig. 19.9 are very close to the proposed by Cerquaglia et al. [Cer+19] which ensures the correctness of the formulation exposed.

Parameter	Value
Solid Young's modulus (E)	1 MPa
Solid Poisson's ratio (ν)	0
Solid Density (ρ_s)	2500 kg/m^3
Fluid Viscosity (μ)	0.001 $Pa \cdot s$
Fluid Density (ρ_f)	1000 kg/m^3
L	0.146 m
H	0.080 m
W	0.012 m
Gravity	9.81 m/s^2

Table 19.3: Problem data for the dam break against a flexible wall.

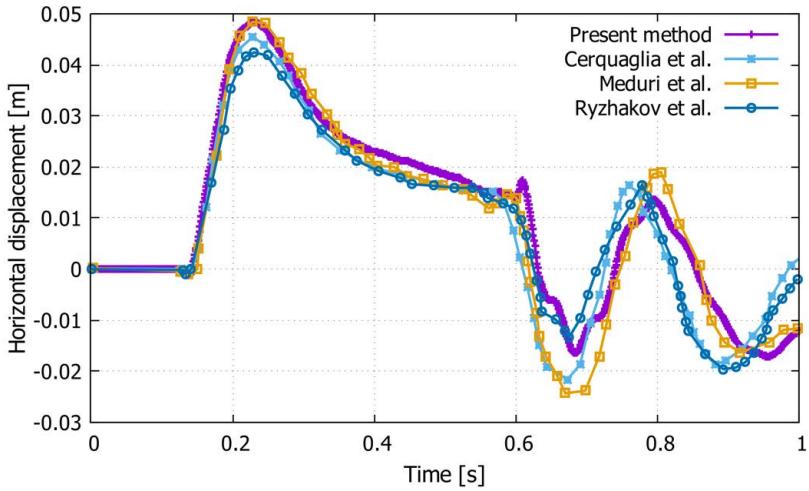

Figure 19.8: Evolution of the horizontal displacement of the tip of the wall along time.

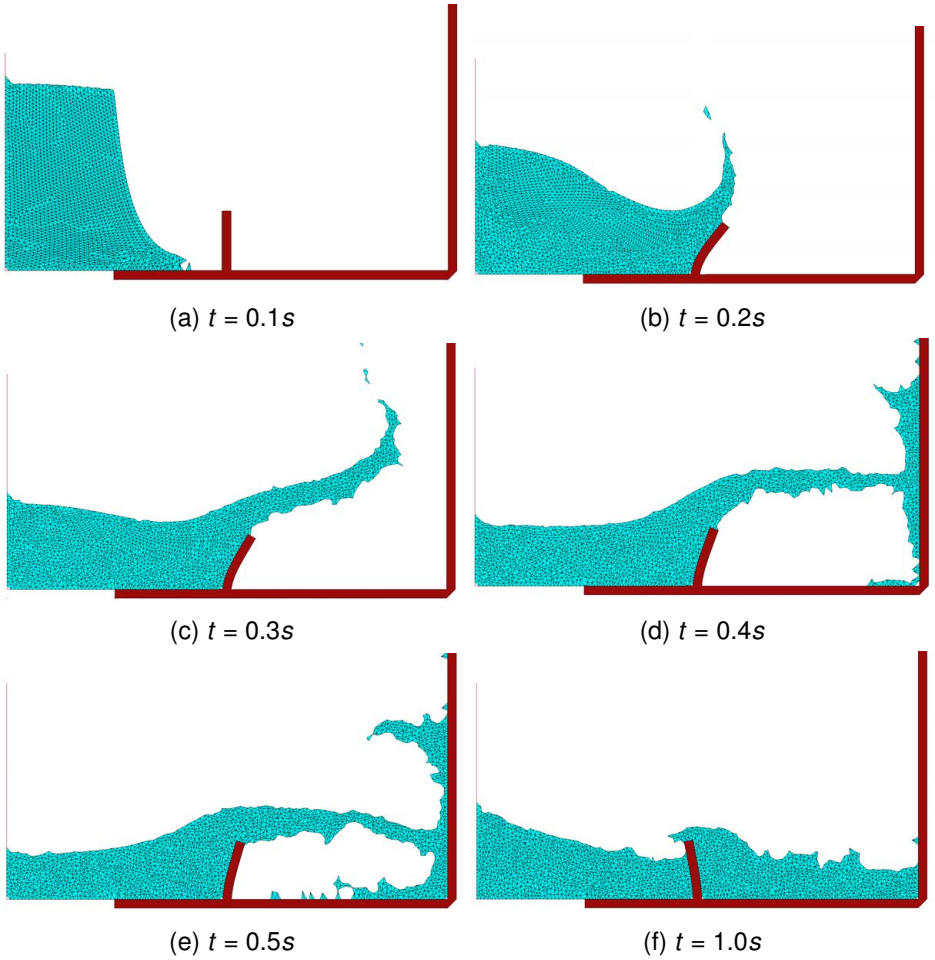

(a) $t = 0.1s$ (b) $t = 0.2s$

(c) $t = 0.3s$ (d) $t = 0.4s$

(e) $t = 0.5s$ (f) $t = 1.0s$

Figure 19.9: Time lapse of the water impacting over the flexible wall.

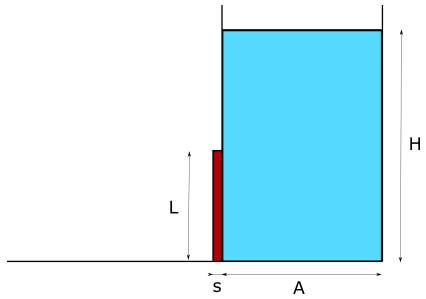

Figure 19.10: Initial setup of the dam breaking against a flexible gate.

19.4 Dam break through a flexible elastic gate

Similarly to the example shown in Section 19.3, the collapse of a water column against a flexible gate is analysed. The geometrical parameters used are defined in Antoci et al [AGS07] in which several experimental results are given. The material properties are defined in Table 19.4. The Young modulus of the solid part has been calibrated to this problem since no further information was given in Antoci et al [AGS07]. This issue is extensively discussed in Cerquaglia et al. [Cer+19]. In this case, a Neo-Hookean constitutive law has been used.

Must be said that, since the densities of the solid and the fluid are very similar (ρ_s/ρ_f = 1.1) and the gate is a highly slender and flexible structure, the added-mass effects can be critical if no relaxation strategy is used in the partitioned staggered scheme.

Initially the gate is fixed and a hydrostatic regime is achieved for the fluid part. Then, the gate is released and starts deforming under the action of the water pressure. The gate increases its deformation under the action of water pressure up to $t \approx 0.12s$. Afterwards the gate starts closing due to the reduced water level, which implies a reduction of the water pressures applied over the gate.

The geometry is depicted in Fig. 19.10. As can be seen in Fig. 19.12, the proposed methodology correctly captures the evolution of the horizontal and vertical displacement of the gate according to the numerical simulation (Cerquaglia et al. [Cer+19]) and with the experiments (Antoci et al [AGS07]). Additionally, the numerical results at several time steps are depicted in Fig. 19.11 showing a very good agreement with respect to the reference literature.

Parameter	Value
Solid Young's modulus (E)	5 GPa
Solid Poisson's ratio (ν)	0.0
Solid Density (ρ_s)	1100 kg/m^3
Fluid Viscosity (μ)	0.001 $Pa \cdot s$
Fluid Density (ρ_f)	1000 kg/m^3
L	0.079 m
H	0.14 m
A	0.1 m
s	0.005 m

Table 19.4: Problem data for the dam break through a flexible elastic gate.

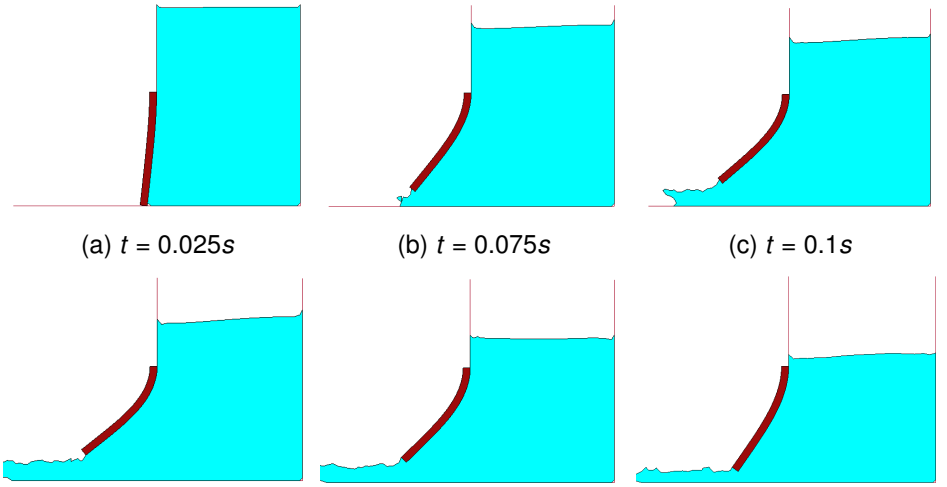

(a) t = 0.025s (b) t = 0.075s (c) t = 0.1s

(d) t = 0.12s (e) t = 0.2s (f) t = 0.4s

Figure 19.11: Time lapse of the water impacting over the flexible gate.

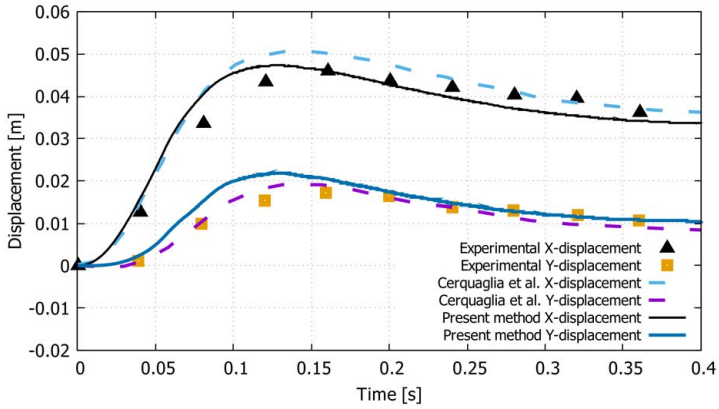

Figure 19.12: Horizontal and vertical displacement of the gate along time.

19.5 Wedge water entry

Here, an experimental test performed in [YDC06] is reproduced. In this case, a solid wedge falling on the water from an initial height of 1.3 m is simulated. The initial geometry of the example is depicted in Fig. 19.13. The material properties used are defined in Table 19.5. The time step used has a duration of $10^{-4}s$.

The solid domain has been discretized with 5833 FE whereas the fluid part is composed of 65586 FE. The numerical results have been compared with the ones obtained by Franci et al. [Fra20] and Sun et al. [SMZ15] and the experimental data provided by Yettou et al. [YDC06].

In Fig. 19.14 the numerical results obtained for four time steps are shown. It is important to note that the results obtained are in good agreement with the ones given by Franci et al. [Fra20]. Fig. 19.15 shows the time evolution of the obtained velocity of the wedge and the expected solution. Additionally, Fig. 19.16 and Fig. 19.17 depict the time evolution of the velocity and pressure, respectively, at the point A of the wedge taking as initial time the instant that the wedge initiates the contact with the fluid.

Figs. 19.16-19.17 demonstrate that the PFEM-FEM-DEM algorithm behaves correctly when simulating inertial-driven problem such as the one proposed since the results are close to the ones given in the literature.

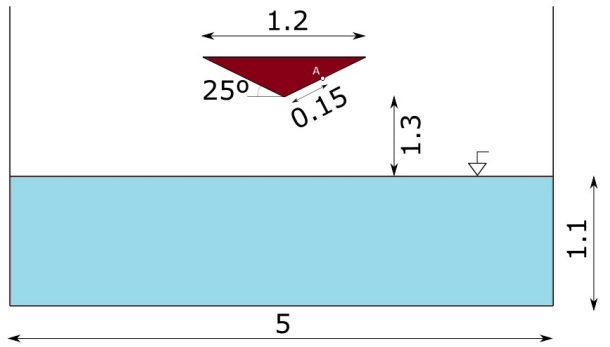

Figure 19.13: Wedge water entry. Initial setup [m].

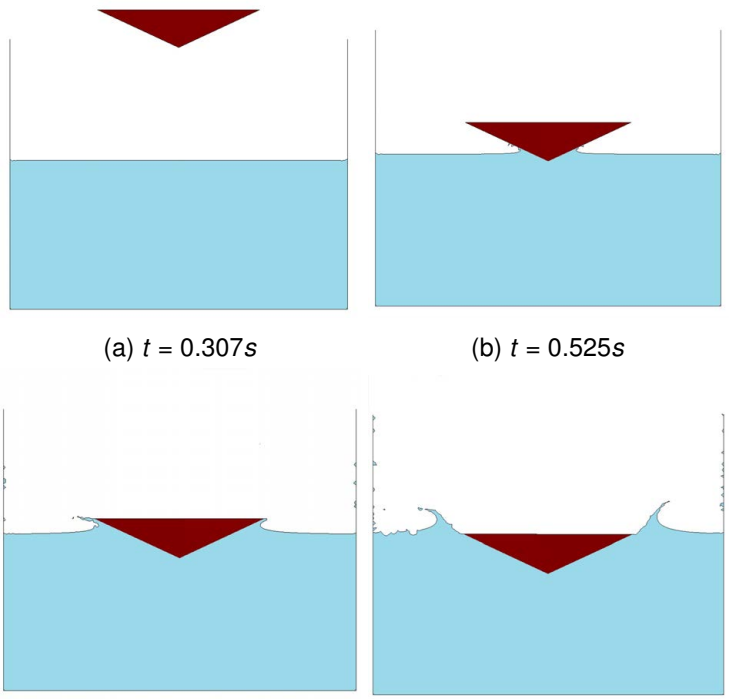

(a) $t = 0.307s$ (b) $t = 0.525s$

(c) $t = 0.590s$ (d) $t = 0.698s$

Figure 19.14: Wedge water entry. Numerical results obtained.

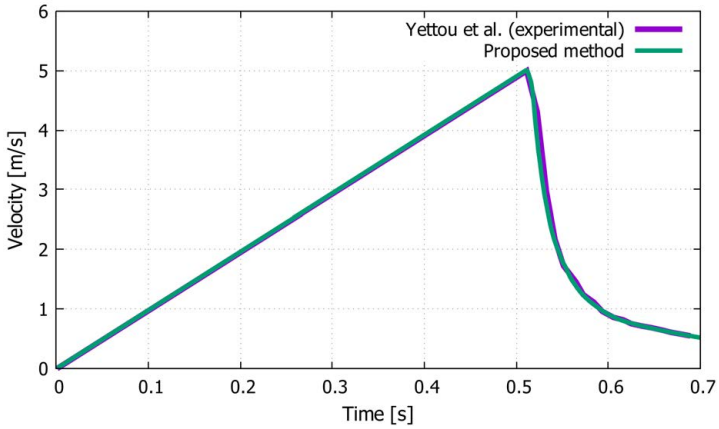

Figure 19.15: Time evolution of the vertical velocity of the wedge. Comparison between the results obtained with the proposed method and the experimental ones (Yettou et al. [YDC06]).

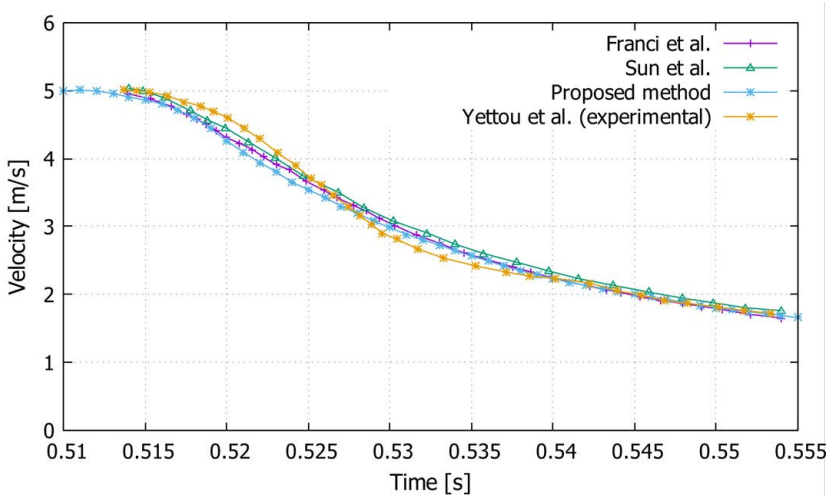

Figure 19.16: Time evolution of the vertical velocity of the wedge. Comparison between the results obtained with the proposed method and the ones from Franci [Fra20], Sun et al. [SMZ15] and Yettou et al. [YDC06].

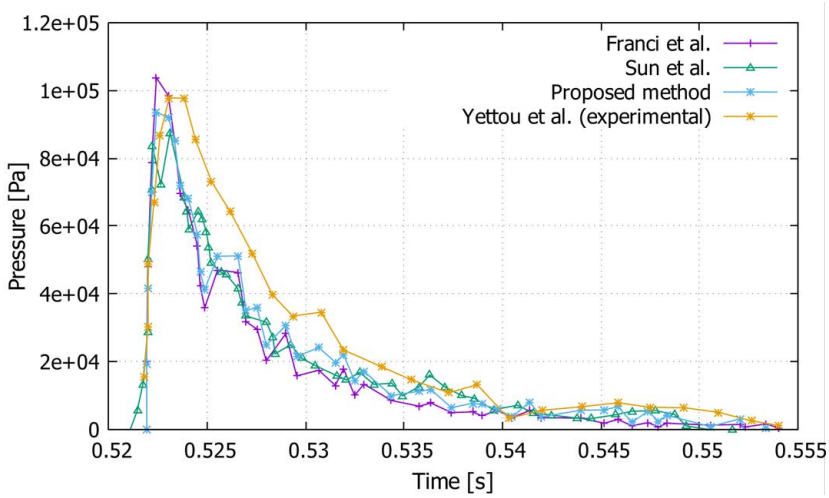

Figure 19.17: Time evolution of the pressure at the point A of the wedge. Comparison between the results obtained with the proposed method and the ones given in [SMZ15], [Fra20] and Yettou et al. [YDC06].

Parameter	Value
Solid Young's modulus (E)	10 GPa
Solid Poisson's ratio (ν)	0.0
Solid Density (ρ_s)	466.07 kg/m^3
Fluid Viscosity (μ)	0.001 $Pa \cdot s$
Fluid Density (ρ_f)	1000 kg/m^3

Table 19.5: Problem data for the Wedge water entry.

19.6 Dam break against a fracturing wall

In this case the example performed in Section 19.3 has been reproduced but changing the material properties of the solid and allowing the degradation and breakage of the material. The material properties can be found in Table 19.6 and, as can be seen, the material is stiffer than previously and more similar to a concrete type of structure. An initial layer of discrete elements have been placed at the contour of the solid body in order to prevent the indentation between the detached wall and the ground/walls of the geometry.

As can be seen in Fig. 19.18, the impact of the water on the wall causes it to crack at its base and then be dragged downstream until it hits the contours of the domain. In this case, due to the added complexity of the non-linear constitutive and geometrical behaviour, a lower time step was used: $\Delta t = 10^{-4}s$. Fig. 19.20 shows the error decrease for two time steps in terms of velocities at the interface for each Aitken iteration. As expected, the convergence rate of the proposed Aitken relaxation scheme is consistently linear.

This example shows one of the potentialities of the proposed method: simulating the breakage of a structure due to a violent impact of a free-surface water flow. Indeed, this example includes fluid-structure interaction, contact between deformable solids, and geometrical and constitutive non-linearity. Additionally, in order to asses the consistency and stability of the proposed FSI methodology, this examples has been run with different time steps (10^{-4}-50^{-6}s). The comparison of the horizontal displacement of the wall along time for the different time steps is depicted in Fig. 19.19. As can be seen, the similarity between the results of different time steps is very high, which ensures the correctness and the stability of the proposed methodology.

Finally, this example has been reproduced using four different FE meshes (3722, 9694, 35980 and 135270 DoF). The fractured geometries are depicted in Fig. 19.23. As expected, the crack is located at the lower part of the vertical wall in all cases. The horizontal displacement of the upper end of the wall can be seen in Fig. 19.21. Additionally, in Fig. 19.22, a convergence analysis of the horizontal displacement of the wall at $t = 0.2s$ is plotted. One can see how the solution converges to the most accurate result (fine mesh) as long as we use meshes with a greater number of DoF.

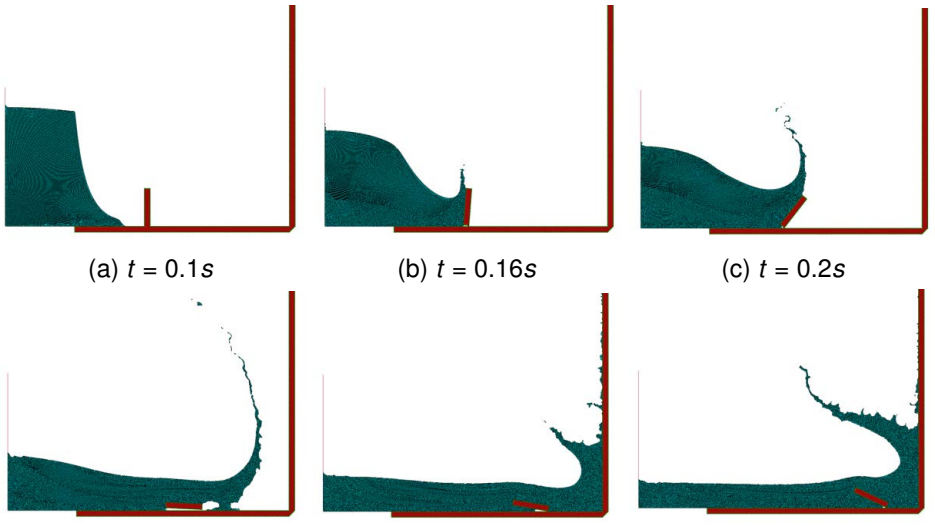

(a) $t = 0.1s$ (b) $t = 0.16s$ (c) $t = 0.2s$

(d) $t = 0.3s$ (e) $t = 0.4s$ (f) $t = 0.5s$

Figure 19.18: Time lapse of the water impacting over the flexible gate.

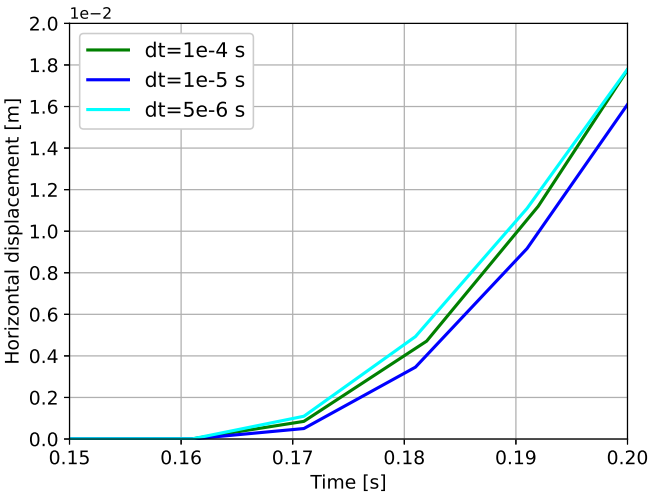

Figure 19.19: Comparison of the computed horizontal displacement of the wall for different time steps.

Parameter	Value
Solid Young's modulus (E)	30 GPa
Solid Poisson's ratio (ν)	0.0
Solid Density (ρ_s)	2400 kg/m^3
Solid Tensile strength (f_t)	0.5e5 Pa
solid Fracture energy (G_f)	10 J/m^2
Fluid Viscosity (μ)	0.001 $Pa \cdot s$
Fluid Density (ρ_f)	1000 kg/m^3
L	0.079 m
H	0.14 m
A	0.1 m
s	0.005 m

Table 19.6: Problem data for the dam break against a fracturing wall.

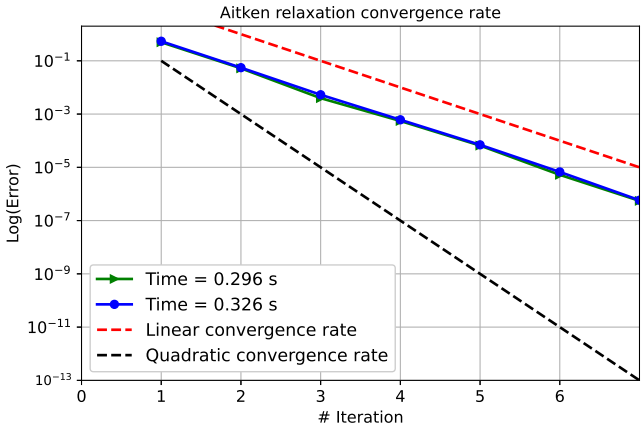

Figure 19.20: Aitken convergence rate for different time steps.

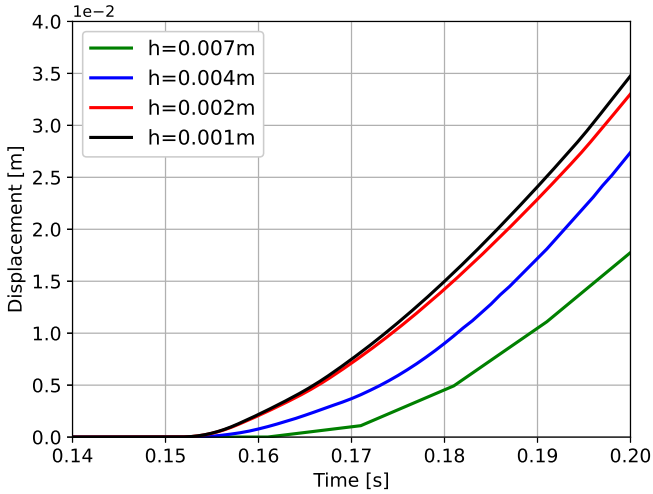

Figure 19.21: Time evolution of the horizontal displacement for different FE meshes.

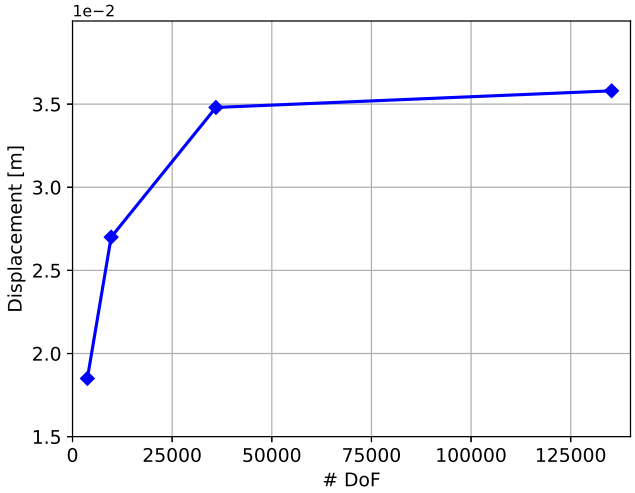

Figure 19.22: Horizontal displacement obtained for different FE discretizations at $t = 0.2s$.

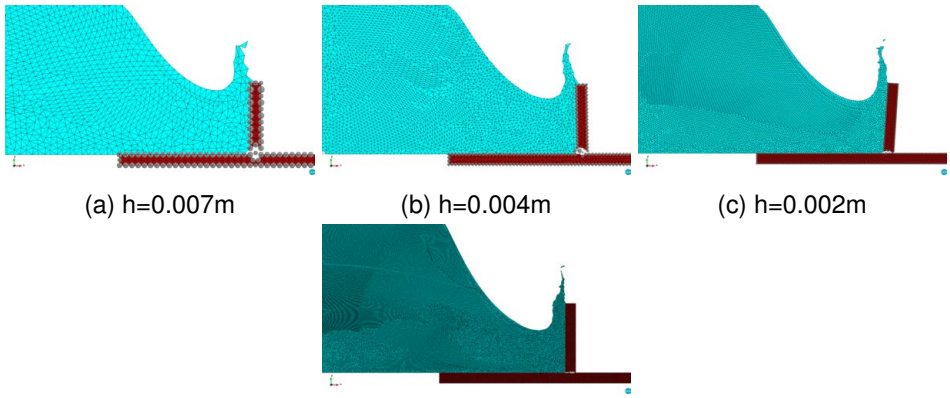

(a) h=0.007m (b) h=0.004m (c) h=0.002m

(d) h=0.001m

Figure 19.23: Fractured geometry for different FE discretizations.

19.7 Slab collapse due to fluid-weight

The present example consists of simulating the failure of a slab with a central notch due to the weight of a fluid flow that accumulates on top of it. The geometry used is depicted in Fig. 19.24. The fluid inlet is located 1m above the slab level and generates a constant flow of fluid with an initial velocity of 1.5 m/s. The beam has a central notch of 0.05 m in order to promote the crack to develop at this zone. The concrete slab is simply supported at its upper ends and it is submitted to its own weight. The material properties of the solid and fluid domains are defined in Table. 19.7. Initially, the solid part consists in 5,162 FE and the fluid is generated as long as the inlet flow is adding fluid mass to the system. The time step used is Δt = 1e-3s.

Fig. 19.25 shows the collapse process of the structure. As can be seen, the viscous fluid accumulates on the top of the concrete slab until the tension stresses at the central notch exceed the yield stress. At this stage the crack starts to develop (see Fig. 19.26 in order to see the crack evolution within the thickness of the slab) and eventually propagates up to the top of the slab. Finally, when the fracture has extended through the entire thickness of the structure, the two parts of the structure can rotate independently and all the accumulated fluid is evacuated by gravity.

Parameter	Value
Solid Young's modulus (E)	35 GPa
Solid Poisson's ratio (ν)	0.0
Solid Density (ρ_s)	2400 kg/m^3
Solid Tensile strength (f_t)	2e6 Pa
Solid Fracture energy (G_f)	1 J/m^2
Fluid Viscosity (μ)	10 $Pa \cdot s$
Fluid Density (ρ_f)	1500 kg/m^3

Table 19.7: Problem data for the slab collapse.

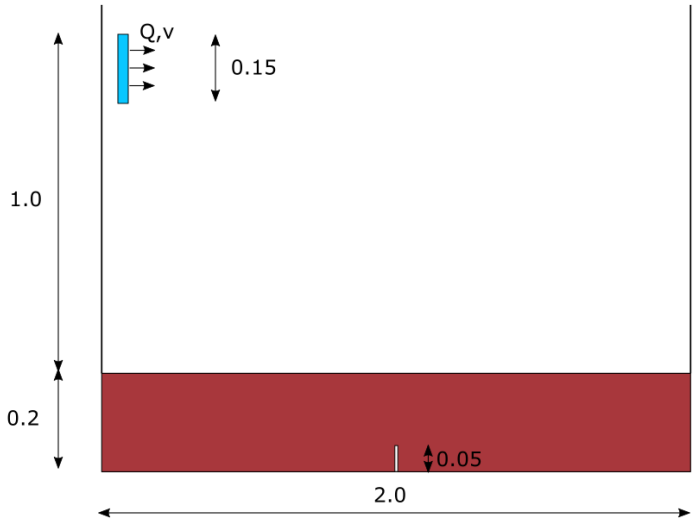

Figure 19.24: Slab collapse geometry. Units in m.

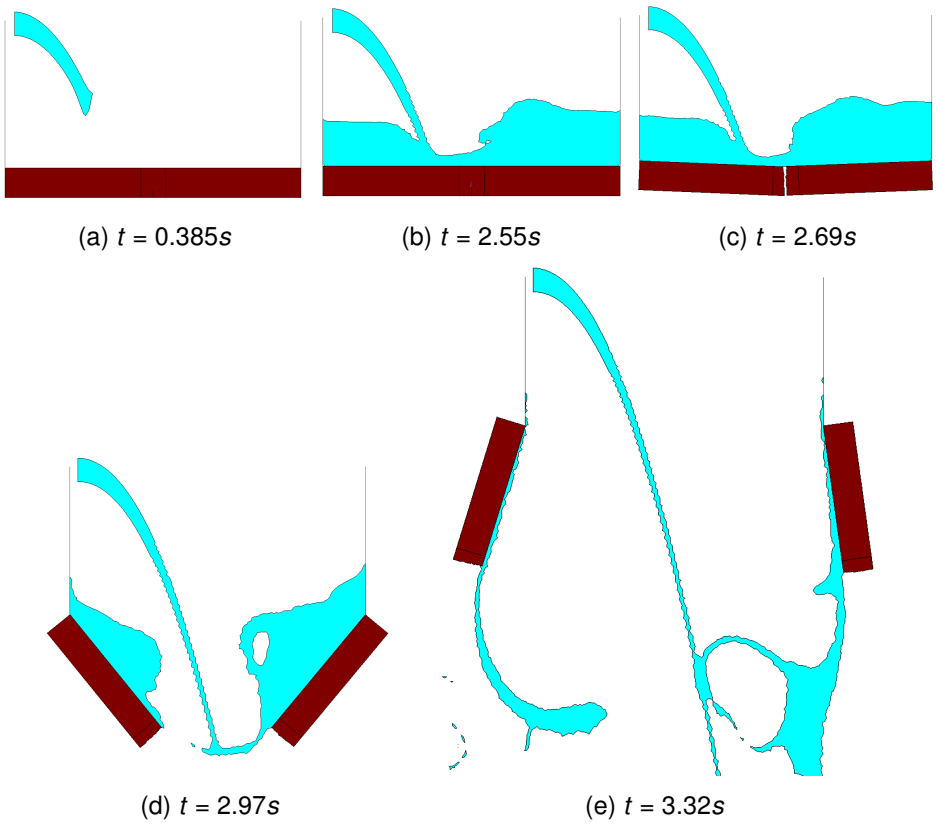

(a) $t = 0.385s$ (b) $t = 2.55s$ (c) $t = 2.69s$

(d) $t = 2.97s$ (e) $t = 3.32s$

Figure 19.25: Time lapse of the slab collapse.

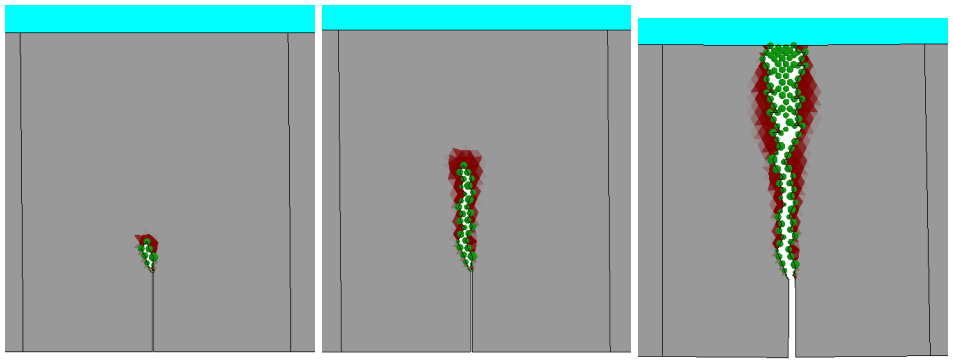

(a) t = 2.38s (b) t = 2.59s (c) t = 2.66s

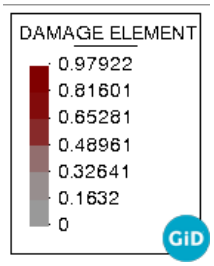

(d) Damage variable, d

Figure 19.26: Crack propagation at the central notch. Damage field.

19.8 Wave impact against an structure

In this example it has been sought to apply the proposed methodology in a case of real application. This problem consists of the impact of a wave against a realistic concrete structure. The geometry of the problem is depicted in Fig. 19.27. Initially, the fluid column has an initial horizontal velocity of 10 m/s until it reaches the left wall of the structure. The material properties used for the fluid and solid domain are described in Table 19.8. The time step used is $\Delta t = 10^{-3}$s and, after the collision of the wave against the solid wall, a $\Delta t = 10^{-4}$ is required for capturing properly the contacts between the debris or solid blocks generated.

Fig. 19.28 shows the collapse mechanism of the structure due to the pressures forces induced by the fluid wave impact. As can be seen, the left wall is initially fractured in three blocks that contact between themselves. Next, the upper frame starts falling due to gravity until it collides with the bottom boundary, fracturing into several blocks during the process.

This problem implies a great computational difficulty since the fluid-structure interaction must be solved taking into account that the fluid can experience great changes in its topology while the solid implies other levels of non-linearity, namely constitutive non-linearity (damage and fracture model), geometrical non-linearity (large displacements and rotations) and non-linear boundary conditions (contacts between blocks).

This example demonstrates the capabilities and potential application of the proposed method to natural hazards phenomena acting against human activities and structures.

19.9 3D slab collapse due to fluid weight

The present example consists of simulating the failure of a slab with a central notch due to the weight of a fluid flow that accumulates on top of it. The inlet used for the fluid is inclined 45 degrees and has been positioned in the middle of the slab section (in $z - y$ plane) in order to recreate a full three-dimensional problem. The inlet lower edge is located at 0.86 m above the slab upper level. The solid slab has an initial imperfection - an artificial notch with 0.1 m height - that will propitiate the onset of the crack at the central part of the structure. The slab is fixed in the upper axis that are aligned with the initial notch.

Parameter	Value
Solid Young's modulus (E)	35 GPa
Solid Poisson's ratio (ν)	0.2
Solid Density (ρ_s)	2400 kg/m^3
Solid Tensile strength (f_t)	1.5e6 Pa
Solid Fracture energy (G_f)	20 J/m^2
Fluid Viscosity (μ)	0.001 $Pa \cdot s$
Fluid Density (ρ_f)	1000 kg/m^3

Table 19.8: Problem data for the wave impact against an structure.

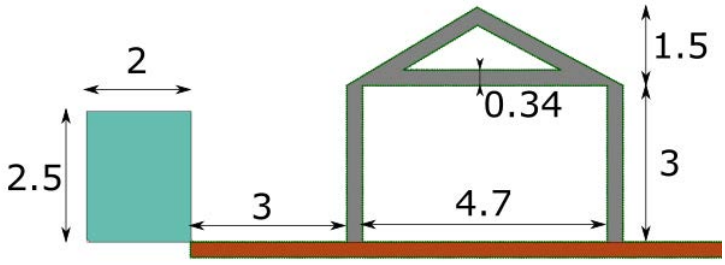

Figure 19.27: Initial set up of the problem. Units in m.

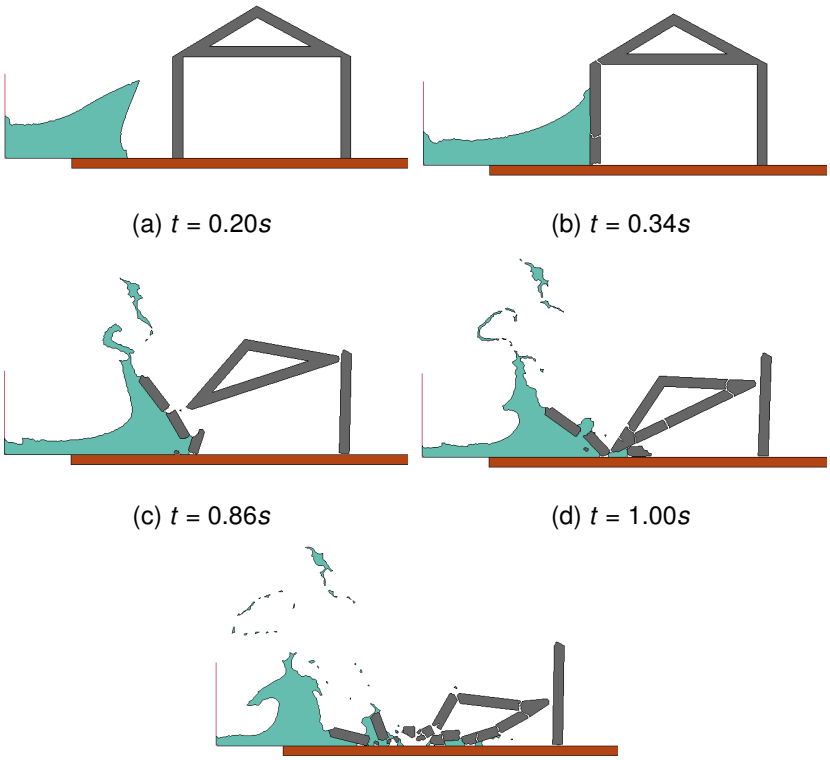

(a) $t = 0.20s$ (b) $t = 0.34s$

(c) $t = 0.86s$ (d) $t = 1.00s$

(e) $t = 1.25s$

Figure 19.28: Numerical results obtained of the collapse of the framed structure. Cracked geometry along time.

Parameter	Value
Solid Young's modulus (E)	35 GPa
Solid Poisson's ratio (ν)	0.2
Solid Density (ρ_s)	2400 kg/m^3
Solid Tensile strength (f_t)	0.5e6 Pa
Solid Fracture energy (G_f)	100 J/m^2
Fluid Viscosity (μ)	100 $Pa \cdot s$
Fluid Density (ρ_f)	2400 kg/m^3

Table 19.9: Problem data for the 3D slab collapse example.

The geometry of the problem is depicted in Fig. 19.29. The material properties used for the solid and the fluid domains are given in Table. 19.9. The yield surface used in the solid part is Rankine. A Newtonian fluid with high viscosity ($\mu = 100 Pa \cdot s$) and density ($\rho_f = 2400 kg/m^3$) has been considered. The time step used ranges between $\Delta t = 10^{-3}$-10^{-4}s depending on the stage of the calculation. The Aitken velocity tolerance is 10^{-5} $m/(s \cdot DoF)$.

Fig. 19.30 shows the time evolution of the collapse of the concrete slab. The fluid accumulates on the top of the concrete slab and fills progressively the containment until the maximum strength capacity of the solid is reached (around $t \approx 1.9$ s). Then, as expected, the crack is generated at the central notch and it propagates vertically through the thickness of the slab and for all its length ($t \approx 2$ s). As shown in Fig. 19.30, a set of discrete particles is introduced on the fracture faces to avoid mutual solid penetration. Once the continuity of the solid structure is broken by the propagated fracture, the two parts of the slab starts moving independently rotating around the z axis aligned with their clamped edges. The fluid is then free to flow downwards due to gravity. The final number of finite elements used for the fluid part is 52,738 linear tetrahedral elements.

As has been demonstrated, the behaviour of the PFEM-FEM-DEM coupled formulation gives analogous results for 2D and 3D simulations (see Section 19.7 for a similar 2D case). this encourages its use for more complex geometries and problems as it is done in the next Section.

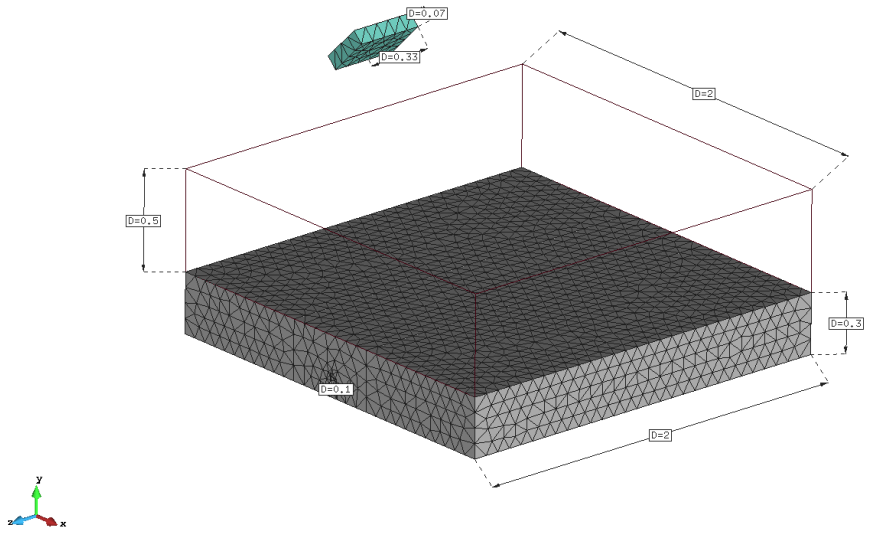

(a) Dimensions [m]

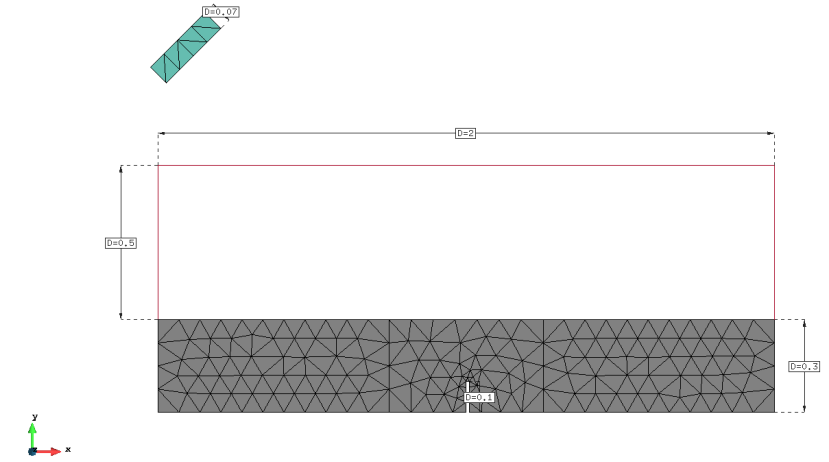

(b) FE mesh. Solid: 35,690 FE, Fluid: 153 FE.

Figure 19.29: Initial geometry of the problem.

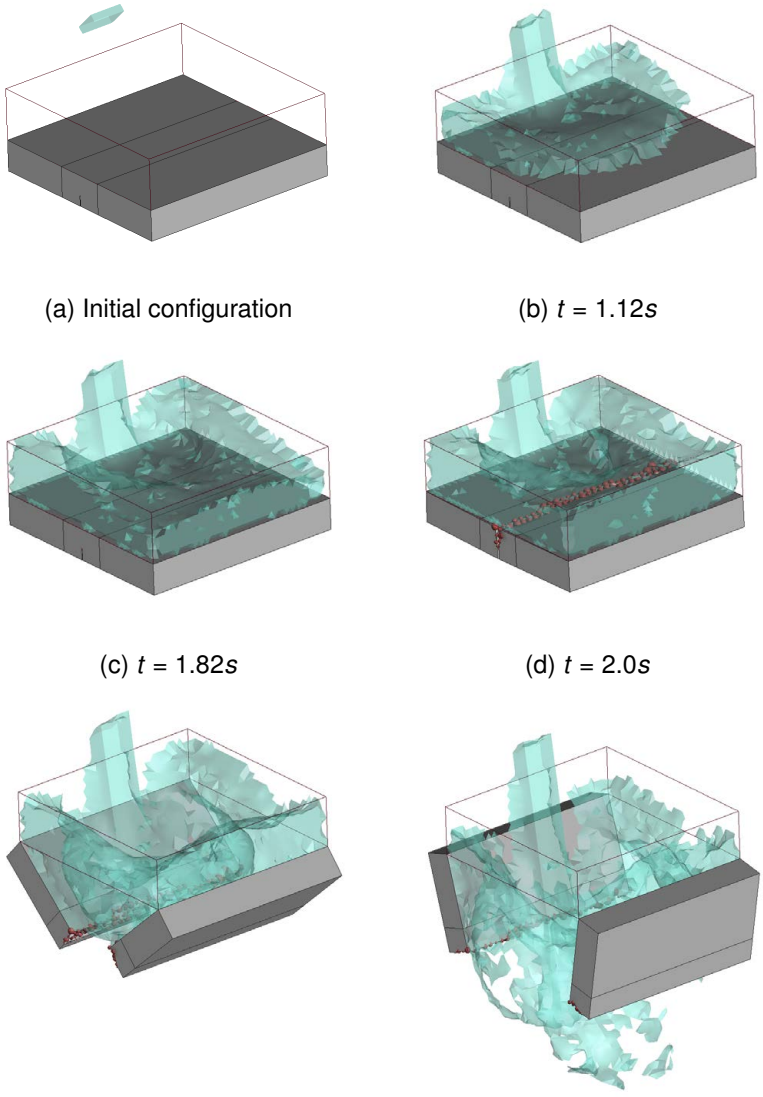

(a) Initial configuration

(b) t = 1.12s

(c) t = 1.82s

(d) t = 2.0s

(e) t = 2.32s

(f) t = 2.48s

Figure 19.30: Time evolution of the collapse of the structure.

19.10 Failure of a concrete wall due to a tsunami force

This numerical test aims to model the failure of a concrete structure subjected to a tsunami-type impulse force. The problem is inspired by the experimental tests conducted by Arikawa et al. [ASI12] in a $184m$ long channel. In the experimental test, the tsunami wave was produced through a piston-type wave maker capable of generating a maximum wave 3.5 m height. The concrete plate was clamped at its lateral sides over two concrete columns, while the upper and lower sides were free to move. The geometry of the wall, its boundary conditions and the material parameters (Table 19.10) here considered are the same as in [ASI12]. Nevertheless, to limit the high computational cost of the fully 3D model, only a reduced geometry of the channel is here analysed, and the water wave is reproduced in an approximate way via an inlet condition applied to the water volume. The inlet velocity has been taken equal to $2m/s$, which was the peak value of the velocity measured experimentally at the impact zone.

Fig. 19.31 shows the FE mesh used for the fluid and the solid body and some useful distances. At the beginning of the analysis, the mesh is composed of 37359 solid elements and 17275 fluid ones.

An adaptive time step has been used, ranging from $\Delta t = 2 \cdot 10^{-3} s$ to $\Delta t = 10^{-4} s$, in order to better capture the cracking of the wall while reducing the computational cost. The velocity tolerance used for the Aitken relaxation is $10^{-4}\ m/(s \cdot DoF)$.

Fig. 19.32 shows some representative results of the analysis. To better appreciate the fluid motion, also the velocity vectors are plotted over the fluid domain. The pictures show how the fluid advances through the channel until it hits the concrete wall (Fig. 19.32.d). The impulsive force produced by the fluid impact induces the sudden failure of the lower part of the solid plate which detaches from the rest of the structure. After this, the fluid can pass through the solid plate dragging almost half part of the wall. Fig. 19.33 shows, from different perspectives, detailed views of the fractured geometry of the concrete wall.

The resulting collapse mechanism of the wall is a punching-shear mode. This is in agreement with the experimental data provided by Arikawa et al. [ASI12]. The fractured geometry of the wall obtained in the experiment is shown in Fig. 19.34.

Despite the simplifications assumed in this analysis, this 3D test shows the high potential of the proposed formulation for predicting and analysing the damages of real

Parameter	Value
Solid Young's modulus (E)	21 GPa
Solid Poisson's ratio (ν)	0.2
Solid Density (ρ_s)	2400 kg/m^3
Solid Tensile strength (f_t)	3e6 Pa
Solid Fracture energy (G_f)	100 J/m^2
Fluid Viscosity (μ)	0.001 $Pa \cdot s$
Fluid Density (ρ_f)	1000 kg/m^3

Table 19.10: Problem data for the large scale structural failure.

structures under the impact of natural hazards, such as tsunami or floods.

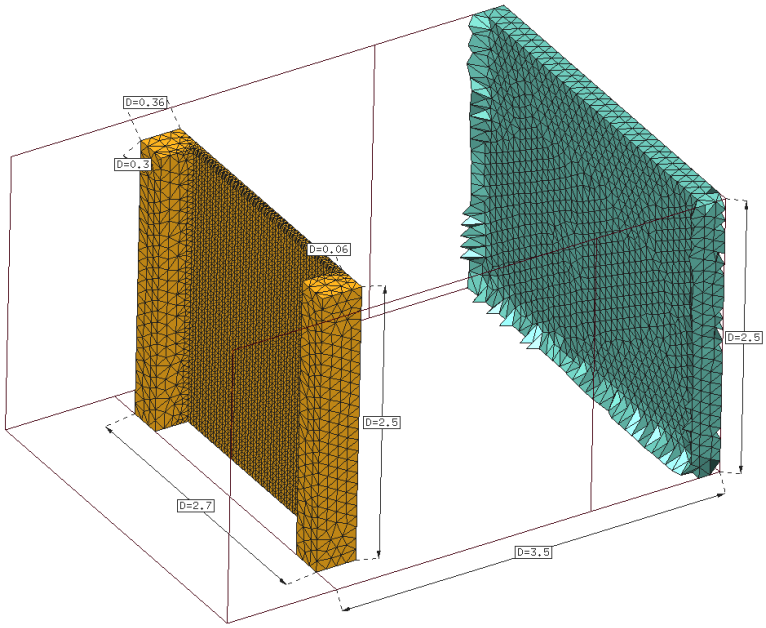

Figure 19.31: Initial geometry of the problem. FE mesh. Solid: 37359 FE, Fluid: 17275 FE

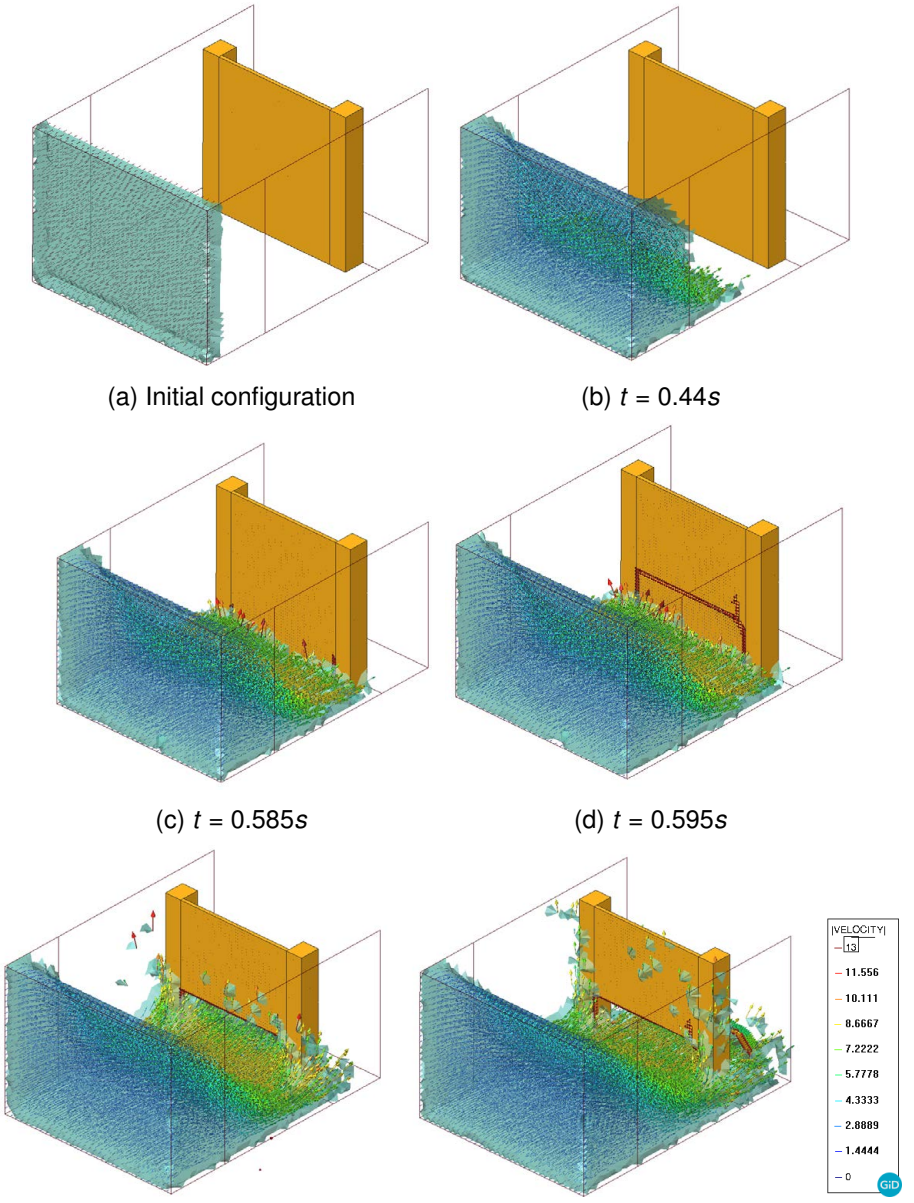

(a) Initial configuration (b) $t = 0.44s$

(c) $t = 0.585s$ (d) $t = 0.595s$

(e) $t = 0.70s$ (f) $t = 0.81s$ (g)

Figure 19.32: Velocity vectorial field of the fluid domain and cracked geometry of the structure.

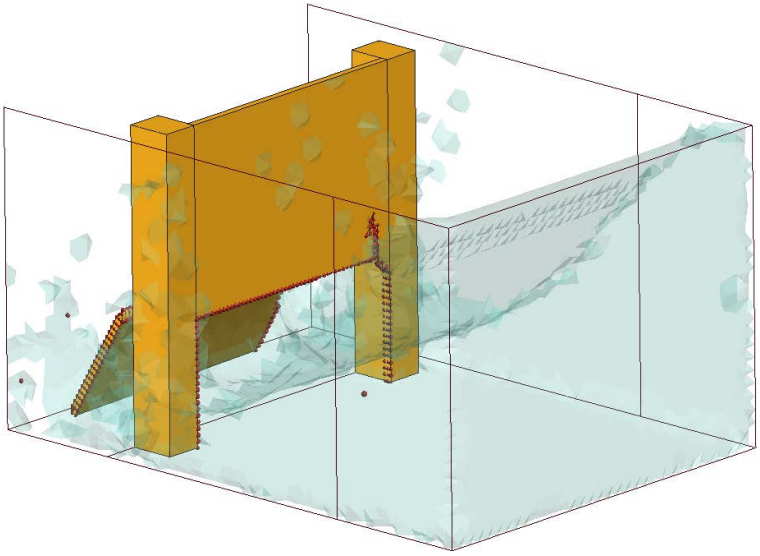

(a) Final configuration, isometric

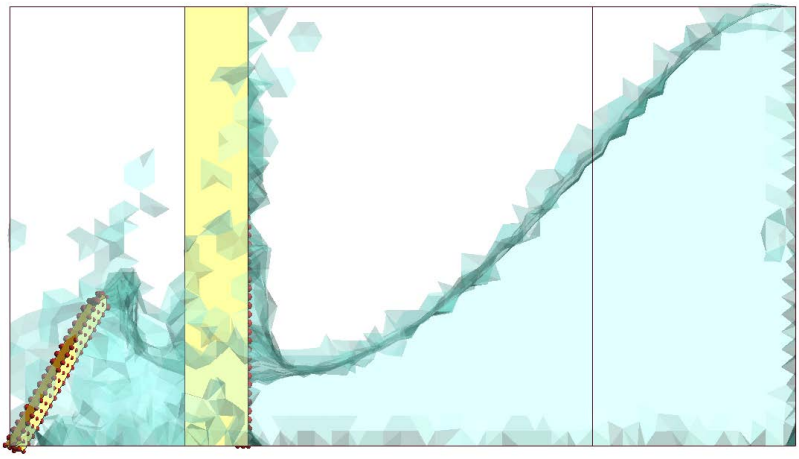

(b) Final configuration, lateral view.

Figure 19.33: Fractured geometry of the wall.

Figure 19.34: Cracked geometry of the wall after the experiment conducted in Arikawa et al. [ASI12].

Part V bibliography

[Ada+07] J. Adachi et al. “Computer simulation of hydraulic fractures”. *International Journal of Rock Mechanics and Mining Science*. Vol. 44, pp. 739–757 , 2007.

[AGS07] C. Antoci, M. Gallati, and S. Sibilla. “Numerical simulation of fluidstructure interaction by SPH”. *Computers & structures*. Vol. 85, pp. 879–890 , 2007.

[Ari+12] M. Ariane et al. “Discrete multi-physics: A mesh-free model of blood flow in flexible biological valve 2017 solid aggregate formation”. *Plose One*. Vol. 12(4), e0174795 , 2012.

[ASI12] T. Arikawa, K. Shimosako, and N. Ishikawa. “Structural failure by impulsive force”. *5th International Conference on Protection of Structures against Hazards*. , 2012.

[Bre78] C. Brezinski. *Algorithmes d’Accélération de la Convergence, Étude Numérique*. Editions Technip. 1978.

[BZ90] C. Brezinski and M.R. Zaglia. *Extrapolation Methods, Studies in Computational Mathematics*. North Holland. 1990.

[CA16] B. Chandra and M. Asai. “Verification and validation of the fluid-rigid body interaction simulation by the smoothed particle hydrodynamics method”. *Proceedings of computational engineering conference JSCES 21*. , 2016.

[CDM07] F. Cirak, R. Deiterding, and S.P. Mauchand. “Large-scale fluidstructure interaction simulation of viscoplastic and fracturing thin-shells subjected to shocks and detonations”. *Computers and Structures*. Vol. 85, pp. 1049–1065 , 2007.

[Cel+17] MA. Celigueta et al. “Accurate modelling of the elastic behavior of a continuum with the Discrete Element Method”. *Computational Mechanics*. Vol. 60, pp. 997–1010 , 2017.

[Cel+19] MA. Celigueta et al. “An accurate nonlocal bonded discrete element-method for nonlinear analysis of solids: application to concrete fracture tests”. *Comp. Part. Mech.* , 2019.

[Cer+19] M.L. Cerquaglia et al. “A fully partitioned Lagrangian framework for FSI problems charcterized by free surfaces, large solid deformations and displacements,and strong added-mass effects”. *Comput. MEthods Appld. Mech. Engnr.*. Vol. 348, pp. 409–442 , 2019.

[CFP10] M. Cremonesi, A. Frangi, and U. Perego. “A Lagrangian finite element approach for the analysis of fluidstructure interaction problems”. *International Journal for Numerical Methods in Engineering*. Vol. 84(5), pp. 610–630 , 2010.

[Cor+19] A. Cornejo et al. “Combination of an adaptive remeshing technique with a coupled FEM-DEM approach for analysis of crack propagation problems”. *Computational Particle Mechanics*. Pp. 1–18 , 2019.

[Cre+20] M. Cremonesi et al. “A state of the art review of the Particle Finite Element Method”. *Archives of Computational Methods in Engineering*. , 2020.

[DG80] J. P. Delahaye and B. Germain-Bonne. “Resultats negatifs en acceleration de la convergence”. *Numer. Math*. Vol. 35, pp. 443–457 , 1980.

[DH03] J. Donea and A. Huerta. *Finite element method for flow problems*. Wiley. 2003.

[DO18] I DePouplana and E. Oñate. “Finite element modelling of fracture propagation in saturated media using quasi-zero-thickness interface elements”. *Computers and Geotechnics*. Vol. 96, pp. 103–117 , 2018.

[Dua+19] Y. Dua et al. “Consequence analysis of premixed flammable gas explosion occurring in pipe using a coupled fluid-structure-fracture approach”. *Journal of Loss Prevention in the Process Industries*. Vol. 57, pp. 81–93 , 2019.

[EM99] H. Edelsbrunner and E.P. Mucke. “Three dimensional alpha shapes”. *ACM Trans Graphics*. Vol. 13, pp. 43–72 , 1999.

[ET93] H. Edelsbrunner and T.S. Tan. “An upper bound for conforming delaunay triangulations”. *Discrete and Computational Geometry*. No. 2, Vol. 10, pp. 197–213 , 1993.

[FC16] A. Franci and M. Cremonessi. “On the effect of standard PFEM remeshing on volume conservation in free-surface fluid flows problems”. *Computational Particle Mechanics*. Vol. 4, pp. 331–343 , 2016.

[FOC15] A. Franci, E. Oñate, and J.M. Carbonell. “On the effect of the bulk tangent matrix in partitioned solution schemes for nearly incompressible fluids”. *International Journal for Numerical Methods in Engineering*. Vol. 102, pp. 257–277 , 2015.

[FOC16] A. Franci, E. Oñate, and J.M. Carbonell. “Unified Lagrangian Formulation for solid and fluid mechanics and FSI problems”. *Comput. Methods Appl. Mech. Engrg*. Vol. 298, pp. 520–547 , 2016.

[Fra20] A. Franci. “Lagrangian finite element method with nodal integration for fluidsolid interaction”. *Computational Particle Mechanics*. , 2020. DOI: https://doi.org/10.1007/s40571-020-00338-1.

[Gil+10] AJ. Gil et al. “The immersed structural potential method for haemodynamic applications”. *Journal of Computational Physics*. Vol. 229(22), pp. 8613–8641 , 2010.

[Gre06] DM. Greaves. “Simulation of viscous water column collapse using adapting hierarchical grids”. *Int J Numer Methods Eng*. Vol. 50, pp. 693–711 , 2006.

[HFO07] K. Han, YT. Feng, and DRJ. Owen. “Numerical simulations of irregular particle transport in turbulent flows using coupled LBM-DEM”. *Comp Model Eng Sci*. Vol. 18, p. 87 , 2007.

[HWL12] GN. Hou, J. Wang, and A. Layton. “Numerical Methods for Fluid-Structure InteractionA Review”. *Communications in Computational Physics*. Vol. 12(2), pp. 337–377 , 2012.

[ICO03] S. Idelsohn, N. Calvo, and E. Oñate. “Polyhedrization of an arbitrary point set”. *Computer Methods in Applied Mechanics and Engineering*. No. 22-24, Vol. 92, pp. 2649–2668 , 2003.

[Ide+08] S.R. Idelsohn et al. “Unified Lagrangian Formulation For Elastic Solids And Incompressible Fluids: Applications to Fluid-Structure Interaction Problems Via The PFEM”. *Computer Methods In Applied Mechanics And Engineering*. Vol. 197, pp. 1762–1776 , 2008.

[IOP04] S.R. Idelsohn, E. Oñate, and F. Del Pin. “The particle finite element method: a powerful tool to solve incompressible flows with free-surfaces and breaking waves”. *International Journal for Numerical Methods in Engineering*. Vol. 61, pp. 964–989 , 2004.

[IT69] B. Irons and R.C. Tuck. “A version of the Aitken accelerator for computer implementation”. *International Journal for Numerical Methods in Engineering*. Vol. 1, pp. 275–277 , 1969.

[Kei+19] V. Keima et al. “Fluid-structure-interaction modeling of dynamic fracture propagation in pipelines transporting natural gases and CO2-mixtures”. *International Journal of Pressure Vessels and Piping*. Vol. 175, p. 103934 , 2019.

[LA18] Y. Li and M. Asai. “Fluid-rigid body interaction simulation based on a stabilized ISPH method incorporated with the impulse-based rigid body dynamics”. *Transactions of the Japan Society for Computational Engineering and Science*. , 2018.

[MA16] Y. Miyagawa and M. Asai. “Multi-scale bridge wash out simulation during tsunami by using a particle method”. *MATEC Web of Conferences*. Vol. 47, p. 02019 , 2016.

[Med+17] S. Meduri et al. “A partitioned fully explicit Lagrangian finite element method for highly nonlinear fluidstructure-interaction problems”. *Internat. J. Numer. Methods Engrg*. Vol. 113, pp. 43–64 , 2017.

[Nor+12] H.O. Nordhagen et al. “A new coupled fluidstructure modeling methodology for running ductile fracture”. *Computers and Structures*. Vol. 94-95, pp. 13–21 , 2012.

[OCI06] E. Oñate, M.A. Celigueta, and S.R. Idelsohn. “Modeling bed erosion in free surface flows by the Particle Finite Element Method”. *Acta Geotechnia*. Vol. 1(4), pp. 237–252 , 2006.

[OFC14] E. Oñate, A. Franci, and J.M. Carbonell. “Lagrangian formulation for finite element analysis of quasi-incompressible fluids with reduced mass losses”. *International Journal for Numerical Methods in Fluids*. No. 10, Vol. 74, pp. 699–731 , 2014.

[OIA04] E. Oñate, S. Idelsohn, and R. Aubry. “The particle finite element method. An overview”. *International Journal of Computational Methods*. No. 2, Vol. 1, pp. 267–307 , 2004.

[Oli+90] J. Oliver et al. “Isotropic damage models and smeared crack analysis of concrete”. *Second international conference on Computer Aided Analysis and Design of Concrete Structures*. , 1990.

[Oña+08] E. Oñate et al. “Advances in the Particle Finite Element Method for the analysis of fluidmultibody interaction and bed erosion in free surface flows”. *Computer methods in applied mechanics and engineering*. Vol. 197(19-20), pp. 1777–1800 , 2008.

[Oña98] E. Oñate. “Derivation of stabilized equations for advective-diffusive transport and fluid flow problems”. *Computer methods in applied mechanics and engineering*. Vol. 151, pp. 233–267 , 1998.

[Pes02] CS. Peskin. “The immersed boundary method”. *Acta Num.*. Vol. 11, pp. 479–517 , 2002.

[PO17] I. Pouplana and E. Oñate. “A FIC based stabilized mixed finite element method with equal order interpolation for solidpore fluid interaction problems”. *International Journal for Numerical and Analytical Methods in Geomechanics*. Vol. 41, pp. 110–134 , 2017.

[Rab+07] T. Rabczuk et al. “Immersed particle method for fluidstructure interaction”. *International Journal for Numerical Methods in Engineering*. Vol. 81, pp. 48–71 , 2007.

[RB07] T. Rabczuk and T. Belytschko. “A three-dimensional large deformation meshfree method for arbitrary evolving crack”. *Comput Methods Appl Mech Eng*. Vol. 196, pp. 2777–2799 , 2007.

[Ren+14] B. Ren et al. “SPH-DEM Modeling of the Hydraulic Stability of 2D Blocks on a Slope”. *Journal of Waterway, Port, Coastal, and Ocean Engineering*. Vol. 140(6), p. 04014022 , 2014.

[ROI12] P. Ryzhakov, E. Oñate, and S.R. Idelsohn. “Improving Mass Conservation in Simulation of Incompressible flows”. *International Journal of Numerical Methods in Engineering*. Vol. 90, pp. 1435–1451 , 2012.

[Ryz+10] P.B. Ryzhakov et al. “A monolithic Lagrangian approach for fluidstructure interaction problems”. *Computational Mechanics*. Vol. 46, pp. 883–899 , 2010.

[SF82] D. A. Smith and W. F. Ford. “Numerical Comparisons of Nonlinear Convergence Accelerators”. *Mathematics of Computation*. Vol. 38, pp. 481–499 , 1982.

[SMZ15] P. Sun, F. Ming, and A. Zhang. “Numerical simulation of inter- actions between free surface and rigid body using a robust SPH method”. *Ocean Engineering*. Vol. 98, pp. 32–49 , 2015.

[SS12] S. Secchi and B.A. Schrefler. “A method for 3-D hydraulic fracturing simulation”. *International Journal of Rock Mechanics and Mining Science*. Vol. 178, pp. 245–258 , 2012.

[SW18] Y. Sudhakar and W.A. Wall. “A strongly coupled partitioned approach for fluid-structure-fracture interaction”. *International Journal for Numerical Methods in Fluids*. Vol. 87, pp. 90–108 , 2018.

[Tal+19] R. Talemi et al. “A fully coupled fluid-structure interaction simulation of three-dimensional dynamic ductile fracture in a steel pipeline”. *Theoretical and Applied Fracture Mechanics*. Vol. 101, pp. 224–235 , 2019.

[Wal+05] E. Walhorn et al. “Fluidstructure coupling within a monolithic model involving free surface flows”. *Computers & Structures*. Vol. 25-26, pp. 2100–2111 , 2005.

[Wic16] T. Wick. “Coupling fluidstructure interaction with phase-field fracture”. *Journal of Computational Physics*. Vol. 327, pp. 67–96 , 2016.

[WLF15] K.G. Wang, P. Lea, and C. Farhat. “A computational framework for the simulation of high-speed multi-material fluidstructure interaction problems with dynamic fracture”. *International Journal for Numerical Methods in Engineering*. Vol. 104, pp. 585–623 , 2015.

[WO99] J. Williams and R. OConnor. “Discrete element simulation and contact problem”. *Arch Comput Methods Eng*. Vol. 6, pp. 279–304 , 1999.

[YDC06] E. Yettou, A. Desrochers, and Y. Champoux. “Experimental study on the water impact of a symmetrical wedge”. *Fluid dynamics research*. Vol. 38, pp. 37–66 , 2006.

[ZCO18] F. Zárate, A. Cornejo, and E. Oñate. “A three-dimensional FEMDEM technique for predicting the evolution of fracture in geomaterials and concrete”. *Comput Methods Appl Mech Eng*. Vol. 5, pp. 411–420 , 2018.

[ZO15] F. Zárate and E. Oñate. “A simple FEMDEM technique for fracture prediction in materials and structures”. *Computational Particle Mechanics*. Vol. 2, pp. 301–314 , 2015.

[Zor+20] R. Zorrilla et al. “An embedded Finite Element framework for the resolution of strongly coupled FluidStructure Interaction problems. Application to volumetric and membrane-like structures”. *Computer Methods in Applied Mechanics and Engineering*. Vol. 368, p. 113179 , 2020.

[ZS17] M. Zhu and MH. Scott. “Direct differentiation of the quasi-incompressible fluid formulation of fluidstructure interaction using the PFEM”. *Computational Particle Mechanics*. Vol. 4(3), pp. 307–319 , 2017.

Part VI

Blast loading simulation applied to mining processes and risk assessment of structures

Chapter 20

Introduction to blast loading simulation

Excavation of the ground by drilling and blasting with explosives is a technique extensively used in the field of mining and civil engineering. Given the incipient importance of this methodology, it is necessary to develop tools that allow a design prior to blasting and a prognosis of the result of it [FL14; Wen+11; Gha+13; HRL10; MC04]. In addition, with the objective of assessing the effect of various blast design parameters and explosives types, an increasing number of publications conducted experimental and numerical simulations of blast loadings [Amb+02; BAG12; De12; Yin+13]. In recent years several numerical approaches have been developed in the field of blast damage over materials [MA08; LHY13; MP07; Gha+20; MA08; YJG17; Nin+11] to mention a few. The main relevant variables for blast fracturing are detailed in Chapter 21.

Another important field of application is the hydraulic fracturing or *fracking* in which the exploitation of natural gas reservoirs in shale rock is performed. The most used fracking techniques involve the use of explosives, gas or hydraulic pressure. The final configuration of the crack network is controlled by the initial stress state (confinement stresses), the peak pressure applied to the soil and the time of application of this pressure. The objective of this technique is to reach a brittle failure in which a wide, complex and fully connected network of cracks is formed. In this regard, Reza et al. [M+13; MJU13] developed a rate-dependent constitutive model for different blast loading by using a FE based method. Some of the results showed in Chapter 22 take

as a reference the ones proposed by Reza et al. in terms of cracking patterns for different confinement stresses and pressure peaks.

Once the interest and importance of having a numerical tool capable of simulating multi-fracture processes in solids due to blasting is known, the objective of this part of the work is to asses the capabilities and efficiency of the already presented FEM-DEM formulation within this field. The FEM-DEM formulation is used for the simulation of the onset and evolution of cracks in the continuum but, as the crack front advances through the solid, the pressure load must follow the same path. This implies that, at each time step, the pressure loads applied to the solid[1] must be updated in terms of topology (the contour over it is applied can be different due to cracking) and in terms of absolute value. In the next chapter an exhaustive description of the pressure load extrapolation and its value evolution as well as the main concepts in blast excavation techniques are exposed.

[1] In this work the blast pressure loads are applied as a set of line/surface loads whose value is controlled by an evolution function and a decay factor due to the volume increase when the crack opens.

Chapter 21

Blast loading numerical treatment

21.1 Theoretical background

21.1.1 Introduction

The excavation of rock slopes or underground tunnels generally involves the use of explosives and therefore blasting, especially when dealing with hard rocks or non-circular tunnels. The fragmentation of rock by means of explosives is a subject of paramount importance and therefore there are a large number of publications that deal with it in detail like Langefors and Kihlstrom [LK73], Hemphill [Hem81], Du Pont [Mem84], Wyllie and Mah [WM05] and Persson [Per75].

The excavation of rock for civil constructions in general requires the generation of cuttings that must remain stable throughout their useful life and at the same time be as steep as possible to reduce their cost. These two contradictory concepts imply that control over the blasting procedure must be as thorough as possible so that the rock mass behind the cutting plane is damaged as minimally as possible. This concepts are included within the *controlled blasting*[1].

[1] *Controlled blasting* must be differentiated from *production blasting*. The first is used to extract material from the rock mass to create an artificial cut, thus minimizing damage to the surrounding rock and reducing the risk of rock falls. Production blasting, on the other hand, is used to fracture a volume of intact rock, usually in a radial fashion, whose blast damage is pushed inwards beyond the final cut. The

When blasting in inhabited urban or industrial areas, special caution must be taken with the potential damage that could be caused to residences or other significant structures. In this respect, measures must be taken to limit induced vibrations, ground settlements, hazards of fly-rock, air blast and noise.

21.1.2 Rock fracturing mechanism by using explosives

Knowing the fracture mechanism of the rock is fundamental for correct blasting design, whether for production or for controlled blasting. It is directly related to the potential damage to nearby structures or even people living in inhabited zones.

When an explosive is detonated, in a matter of a few hundredths of a second, it is transformed into high temperatures and gas under high pressure. Since the explosive is confined within a hole, this reaction is capable of generating pressures that can reach 2 GPa. This pressure is transferred as a compression deformation along the rock at speeds ranging from 2000-6000 m/s. As the pressure wave enters the material surrounding the blast hole, the area at a distance of twice[2] the radius is completely fragmented due to the high compression it has been subjected to (see Fig. 21.1.a). As the compression wave advances through the medium, the tension level rapidly falls below the dynamic compressive elastic limit of the material and, beyond the pulverized zone, the material is subjected to high radial tension which induces tangential tensile stresses at that same location. When the mentioned tangential stresses exceed the dynamic tensile limit of the material, the process of radial cracking starts. The extent of these cracks depends on the available energy of the explosive and the mechanical properties of the rock and can reach a depth of up to 40-50 times the initial diameter of the hole. Parallel to the advance of the compression waves, concentric shells of material undergo a radial expansion. This causes a tangential discharge of the load in the vicinity of the hole. These concentric fractures follow a cylindrical pattern that gets closer and closer to the free faces of the rock mass. When a compression wave reaches a free face, it is reflected as a tensile strain wave. If this tensile wave is strong enough, *spalling* occurs from the free face towards the blast hole. This induces a discharge of the rock mass, producing an extension of the radial fractures described above (Fig. 21.1.b). Since the strength of rocks is much lower in tension than in compression, the effect of these reflected waves is particularly effective.

The complete generation of gases due to the explosion usually takes about 10

latter is capable of fracturing large volumes of material swiftly

[2] In hard rocks ranges between 1-2 times the radius. In soft rocks this distance is bigger

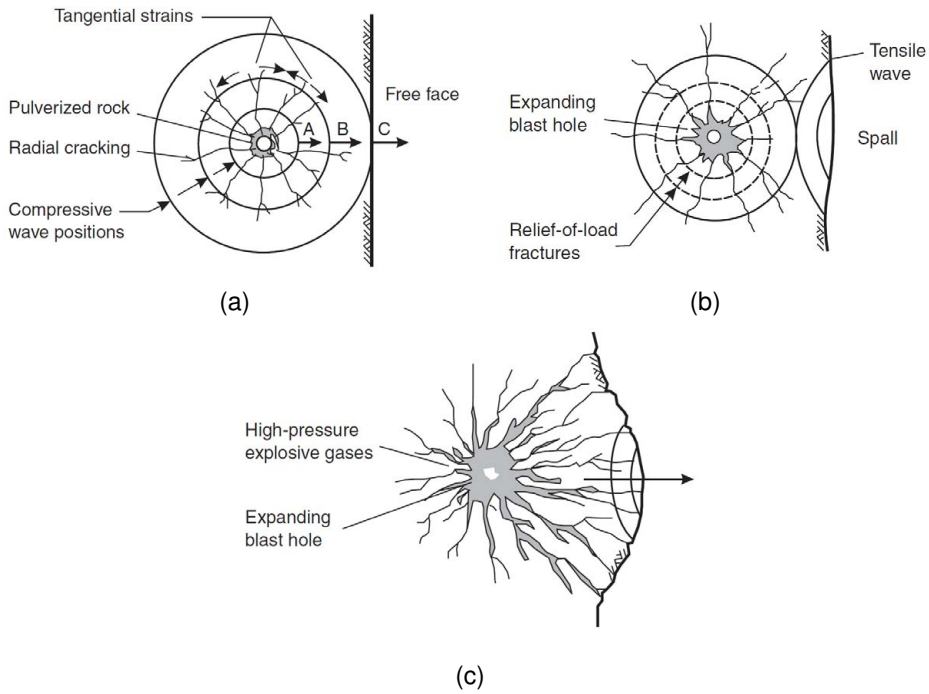

Figure 21.1: Time lapse of the fracturing process of rocks due to blast loading. Image from Wyllie and Mah [WM05]

ms while the fracturing due to the deformation wave usually takes only 1-2 ms. As the stresses in rock are decreasing due to radial expansion, is it possible now for the explosive gases the expand through the strain wave-generated cracks and begin to expel the rock. (Fig. 21.1.c). This stage is characterized by the formation of a dome around the blast hole [WM05] and, due to the pushing effect of the expanding gases, more fracturing occurs to shear failure as the rock mass is expelled towards the free face.

21.1.3 Design parameters of blasting processes

The fracturing process described in the previous section is controlled by a set of design parameters that will affect the efficiency of the blast fragmentation. The most relevant parameters to optimize the blasting process in general conditions can be

listed in:

- Type, weight and spatial distribution of the explosive
- Mechanical properties of the rock
- Bench height
- Blast hole diameter
- Burden distance
- Spacing between holes
- Sub-drill depth
- Stemming
- Sequence of detonation
- Powder factor

Each design factor will be studied in detail in the sections below.

Explosive properties

The power of an explosive can be seen as a measure of the work or energy it can release per unit of weight or volume. It is very common to express the strength of the explosive as relative to the ANFO[3] type. Another measure of the power of an explosive is the Velocity Of Detonation (VOD); the higher this value is, the more crushing. Must be noted that, in addition to the explosive strength, is crucial to control the confinement and density for an optimal execution. In Table 21.1 several explosive properties for the most used types are given.

The explosive power in usually defined by weight and bulk strength. The weight measuring is especially useful when several types of explosives with different strengths are used at the same time or when comparing the cost of the explosives, since they are sold by weight. Conversely, the Relative Bulk Strength (RBS) is related to the

[3] ANFO is the most used explosive type which consist in ammonium nitrate prills (0.5mm diameter spheres) and 5.5% fuel oil

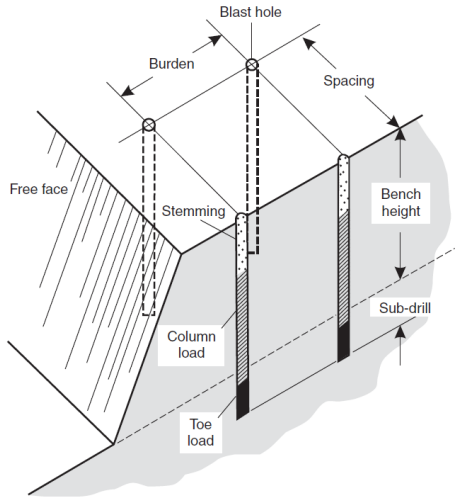

Figure 21.2: Graphical interpretation of the design parameters for blasting, image from Wyllie and Mah [WM05]

weight strength of the explosive by the specific gravity. This value is especially used when computing the required amount of energy for performing a certain operation. The higher this value is, the less blast hole capacity will be required. In general, ANFO is used for large scale operations in quarries and watergels or dynamites are more commonly used in smaller processes. As can be seen in Fig. 21.2, when using ANFO as main type of explosive, it is advisable to use a higher RBS explosive at the end of the hole (so called *toe load*) in order to ensure the correct detonation of the ANFO and, in addition, to ensure the fragmentation of the rock in the lower part, where is more confined.

Bench height

In general cases, the bench height is limited to 8-9 m. In higher benches the drilling accuracy becomes critical and increases substantially its cost. Since the hole diameter enlarges according to the height of the bench, an increase of the diameter of the blast induce a reduction of the drilling costs. In high slopes (more than 8 m), the toe burden (see Section 21.1.3) can be excessive and it is advisable to incline the blast holes for

Explosive type	Density [g/cc]	VoD [m/s]	Relative bulk strength (ANFO = 100)	Water re
Packaged, detonator-sensitive emulsions	1.12 - 1.2	4600-5200	115-170	Exce
Packaged, booster-sensitive emulsions	1.24-1.26	4300-5050	125-155	Exce
Watergels	1.20	4785	129	Exce
Dynamites	1.2-1.42	3350-5600	170-130	Good to
Wall control dynamites	0.75-1.3	1650-2600	76-114	Good
Boosters	1.34-1.6	5600-7900	167-280	Exce
ANFO	0.84	4000	100	No
Bulk emulsions	1.25	5200-5500	120-150	Exce

Table 21.1: Usual properties fo different explosive alternatives [WM05]

the front row.

Burden

the break mechanism defined in Section 21.1.2 is closely related to the spacing between rows of explosives and to the nearest free face. Blasting is more efficient when it is able to reflect off a free face and thus generate tensile waves. In this way the rock is fragmented and pushed out of the slope. An excessively small burden will cause radial cracks to reach the free face. This means that gases will be released quickly, reducing the efficiency of the explosion and inducing problems such as fly-rocks. On the other hand, a too large spacing can cause the shock wave not to be reflected on the free faces. In this case the blast will not reach a sufficient fragmentation level, with the loss of efficiency associated.

In general cases, the bench height H can be related with the burden B as

$$B = (0.33 \text{ to } 0.25) \cdot H, \tag{21.1}$$

obtaining good results within this range.

Blast hole diameter

Persson [Per75] states that the drilling cost decreases as the hole size increases. This is because the volume of explosive is proportional to the square of the hole diameter so that the same amount of explosive can be placed in fewer holes. The increased crushing of the rock due to a higher concentration of explosive may cause the slopes to be more unstable and the blasting to generate larger blocks of rock, with the increase of difficulty for the machinery to handle it. If the burden B has been set (accoring

to Eq. (21.1)), an appropriate diameter for the explosive d_{ex} can be estimated using [WM05]

$$d_{ex} \approx \frac{B \cdot 1000}{24\left(\gamma_{ex}/\gamma_r\right) + 18} \text{ in [mm]} \tag{21.2}$$

where γ_{ex} and γ_r are the specific weights of the explosive and rock, respectively. Additionally, if there is no correlation between the unit weight and the energy of the explosive, it is advisable to use the following equation in order to obtain an approximation of the blast hole diameter:

$$d_{ex} \approx \frac{B \cdot 1000}{8\left(RBS/\gamma_r\right)^{0.33}} \text{ in [mm]} \tag{21.3}$$

where RBS is the relative bulk strength, which has been defined in Section 21.1.3.

Characteristics of the rock

The natural heterogeneities of the rocks can significantly affect the optimal design of a blasting plan. Discontinuities in the rock mass such as faults, joints, weak/disaggregate areas, etc., can dissipate large amounts of blasting energy and thus reduce its efficiency. Such is the relevance of the geological structure that is common to be more influential than its mechanical properties in terms of blasting efficiency. In the case of closely spaced joints rock masses, low energy factors and low-velocity explosives such as ANFO are more recommended. The structural geology effects can be taken into account quantitatively by re-adjusting the value of the burden as proposed by Wyllei and Mah [WM05].

Sub-drill depth

Sub-drilling[4] is necessary in general cases in order to break the rock properly at bench level (see Fig. 21.3). If sub-drilling is not performed, a slightly fragmented area will be generated at the bottom of the blast hole resulting in high excavations costs afterwards. In general cases, a sub-drill depth of 0.2-0.5 times the burden shows good results.

[4] Sub-drilling means drilling up to a depth below the necessary level or bench floor

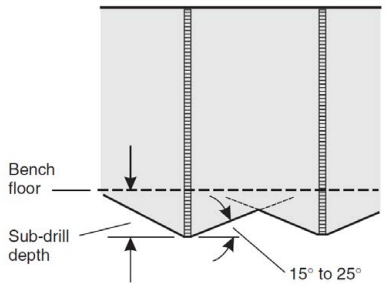

Figure 21.3: Rock blasting by using the sub-drilling methodology, image from Wyllie and Mah [WM05]

Stemming

In order to ensure the tightness of the hole at the top and avoid the lose of explosive gases, a layer of stemming is used. This stemming material is usually a well graded gravel whose optimum size increases with the blast hole diameter. For general purposes, an average size of the particles of 0.05 times the diameter of the blast hole is optimal. Analogously to the burden distance effect on the blast efficiency, a short stemming length can compromise blast tightness and facilitate the gases to vent while a too long stemming will lead to a low fragmentation level of the rock mass.

Hole spacing

In the event that fractures are generated parallel to the free face, the lateral extent that the crack can reach is dependent on the volume of gas available and the width of the crack. If the energy of an explosive is reinforced by the energy of a nearby explosive, the total thrust force is uniformed along the blasting face, making the process more efficient.

For a multiple series of delayed blast holes, the spacing S can be estimated as

$$\begin{cases} S = \dfrac{H + 7B}{8} & \text{if H/B between 1 and 4.} \\ S = 1.4B & \text{if H/B greater than 4.} \end{cases} \tag{21.4}$$

Blast detonation sequence

Detonation of all spatially arranged holes simultaneously is usually not the most efficient option. A simultaneous detonation of large quantities of explosives would cause insufficient fracturing as well as potentially damaging areas where subsequent stability is important or inducing large vibrations in adjacent structures. To mitigate this effect, explosives should be detonated sequentially (Fig. 21.4 show several detonation sequences) and with such a delay that the next detonation easily finds the free face generated by the previous detonation.

The most used relationships for calculating the delay interval are

$$\begin{cases} t_{delay} = (10\text{-}13)B & \text{for row-to-row detonation} \\ \\ t_{delay} = \kappa_t \cdot S & \text{for hole-to-hole detonation} \end{cases} \tag{21.5}$$

where t_{delay} is given in ms and the burden B and the spacing S must be introduced in m. Additionally, the constant κ_t depends on the rock type ranging from 3 to 7 ms/m [WM05].

Weight of explosive

The weight of the explosive is a vital parameter for obtaining a given level of fragmentation or avoiding excessive damage to the final face of a cut. It is also important to avoid excessive noise, vibrations or fly-rocks in these explosion zones. The most used parameter for this purpose us the *powder factor* , which is the weight of explosive material necessary to break a unit volume of rock (usually expressed in kg/m^3). The total weight of explosive per hole W_{ex} can be computed as [Per75]

$$W_{ex} = d_{ex} \cdot \gamma_{ex} \cdot (H - l_{stemming}) \cdot l_{subdrill} \tag{21.6}$$

where d_{ex} is the diameter of the explosive, γ_{ex} the unit weight of the explosive, H the bench height, $l_{stemming}$ the stemming length and $l_{subdrill}$ is the sub-drill depth. Additionally, the volume of rock per hole V_h can be estimated as

$$V_h = H \cdot B \cdot S \tag{21.7}$$

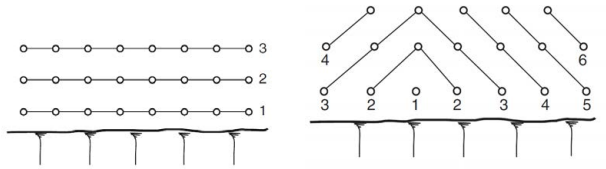

(a) square "row-by-row" detonation sequence

(b) square "V" detonation sequence

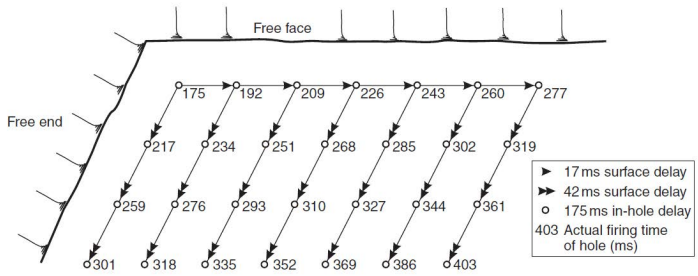

(c) "hole-by-hole" detonation

Figure 21.4: Most used detonation sequences. Image from Wyllie and Mah [WM05]

so the powder factor P_f is computed as

$$P_f = \frac{W_{ex}}{V_h} \tag{21.8}$$

An interesting feature of this powder factor parameter is its relation with the average boulder size [Per75]. Fig. 21.5 shows the graphical relationship between the powder factor and the desired average boulder size (according to several burden sizes).

21.1.4 Blast loading in tunnelling

The first effective application of *drill & blast* dates back to 1627 conducted by the Tyrolean Kaspar Weindl, who had marched to Italy with the Austrian army. At that time, Weindl noticed that he could use his knowledge of gunpowder to create new technologies in the civilian world [Kel04]. In a silver mine in the region of Schemmnitz (Slovakia), Weindl announced a a novel methodology for extracting minerals by taking advantage of the gunpowder. This methodology is especially suitable for very hard rocks (granite, gneiss, basalt, quartz) but work well also with soft rock such as marl,

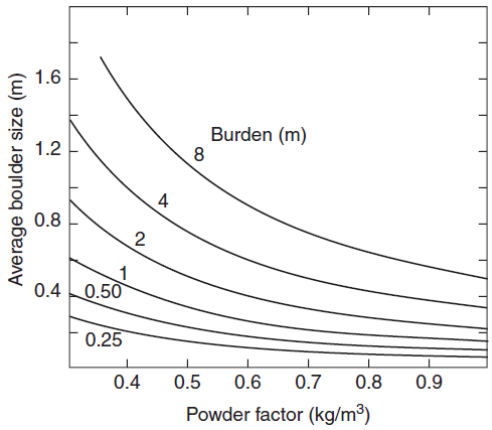

Figure 21.5: Rock blasting by using the sub-drilling methodology, image from Persson [Per75]

loam, clay and chalk. Can be applied also for rock with varying properties and/or anisotropy.

The drill & blast methodology used for tunnelling consist of several steps that must be followed in order to increase the efficiency of the excavation and prevent accidents. The first step consist in drilling the blastholes with 40mm of diameter in most cases by means of a rotary and percussion drilling. The orientations and lengths of the blastholes must be controlled very carefully, therefore the drilling equipment are mounted on tire carriages. The length of the blastholes is usually equal to the advancing step, which in general oscillates between 1-3 m. The next step is the charging and tamping (similar concept to the stemming defined in Section 21.1.3) of the explosive load. Then the distribution of charges and its posterior consecution of ignition control the result. In this regard, according to Kolymbas [Kol05], the most efficient excavation is obtained if the fume pushes the rock against a free surface. This can be achieved with a V-cut. In this way the blastholes in the central part of the face are conically arranged and ignited first (see Fig. 21.6). The surrounding blastholes are ignited consecutively with a delay of some milliseconds. Parallel blastholes are easier to drill precisely but require more explosive than the conically arranged ones. Several unloaded drill holes are placed in the parallel cut, creating thus a cavity (artificial free face) against which the detonation pushes the rock. For smooth blasting, the contour

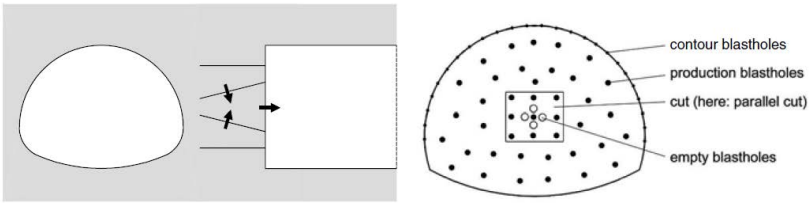

Figure 21.6: V-cut and distribution of blast holes, image from Kolymbas [Kol05]

holes must have a small spacing (40-50 mm). This procedure reduces considerably the post-profiling costs.

Finally, various ventilation and structural reinforcement operations are carried out. Since these procedures exceed the limits of this work, the reader is referred to Kolymbas [Kol05] in order to obtain a more detailed description.

21.2 Numerical implementation

The pressure due to the detonation of explosives is taken into account in the FEM model as a set of pressure loads normal to the internal faces of the blasthole. However, since the topology of the geometry is changing due to the degradation of the material[5], the mentioned loads must be adapted to the new contour each time it changes. Fig. 21.7 shows how the pressure load has adapted to the new fractured contour (initially was applied only within the initial blasthole R_0). It is important to mention that the explosive pressure must be extrapolated only through cracks that are connected to the main chamber, simulating in this way the expansion and movement of gases along the cracks. Fig. 21.8 depicts schematically how the explosive gas pressures are applied to the contours of the chamber, radial cracks and for isolated blocks.

In order to estimate the value of the blast pressure along time several semi-empirical state equations can be used. One of the most used is the Jones Wilkins Lee (JWL) [LHK68], which is considered as the most comprehensive and accurate. The JWL equation reads:

[5]Indeed, as explained in Chapter 11, when a FE reaches a certain damage threshold it is removed from the mesh

$$P = A\left(1 - \frac{\omega}{R_1 V}\right) e^{-R_1 V} + B\left(1 - \frac{\omega}{R_2 V}\right) e^{-R_2 V} + \frac{\omega E}{V} \tag{21.9}$$

where A, R_1, B, R_2 and ω are material constants, P is the pressure value, V is the relative volume (current volume over the initial one) and E is the specific energy whose initial value is E_0. To have an order of magnitude, Hu et al. [Hu+15] proposed the following values: $A = 200$ GPa, $B = 0.2$ GPa, $R_1 = 4.5$, $R_2 = 1.1, \omega = 0.35$ and $E_0 = 4.2$ GPa.

Another option is to use a more simple equation proposed in Ning et al. [Nin+11], whose expression is

$$P = P_0 \left(\frac{V_0}{V}\right)^{\gamma} \tag{21.10}$$

where P_0 and V_0 are the initial pressure and volume of the blasthole, respectively and γ is a calibration parameter ($\gamma \approx 1$). Additionally, P is the gas pressure at time t and V is the gas volume at the same instant.

In each time step, the explosive pressure loads must be checked in terms of topology (because the contour of the damaged rock may have changed) or in terms of value (since the volume will increase as long as the cracks evolve). This implies that the methodology must notice each time that one element is erased from the mesh, update the pressure loads according to the new contour (is the crack is connected to the main chamber) and storage the increment of volume due to the FE erasion. Fig. 21.9 shows of the pressure load is extrapolated along time to the new contour only for the connected cracks. Once the explosion gas reaches the free surface and leakage is produced, the pressure vanishes instantly.

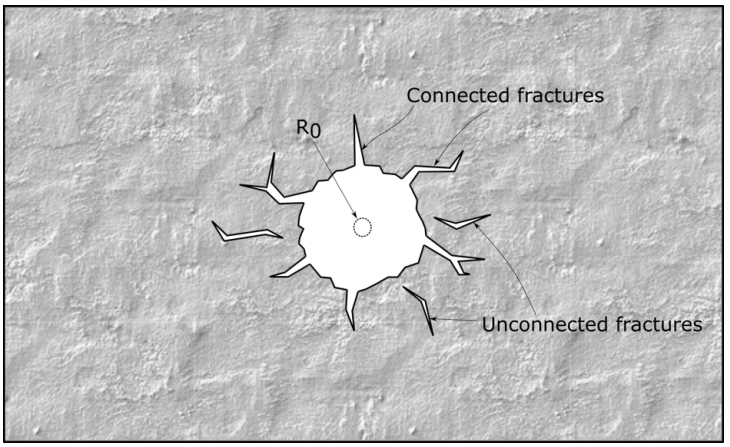

Figure 21.7: Blast chamber pressure extrapolation sketch.

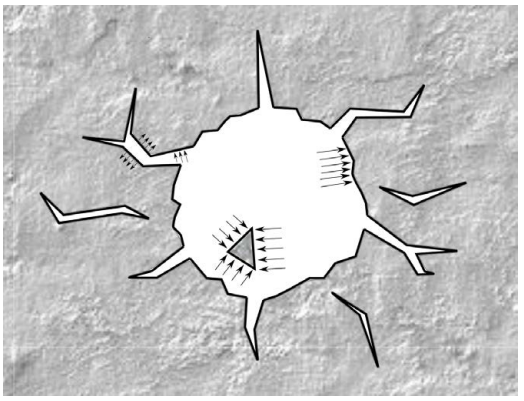

Figure 21.8: Gas pressure applied over the updated contour.

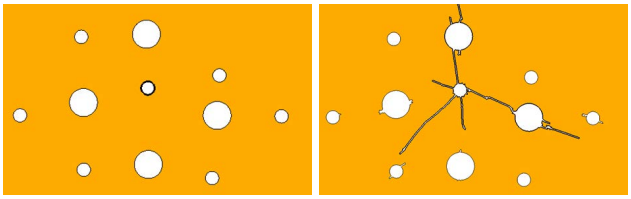

(a) Initial configuration (b) Time t configuration

Figure 21.9: Pressure load extrapolation example.

Chapter 22

Blast loading numerical examples with the FEM-DEM

In this chapter, several numerical examples regarding blasting and mining procedures are shown. The first example consists in a sinkhole collapse, which can demonstrate the capabilities of the proposed FEM-DEM methodology. Next, a collection of validation and application examples performed (as a collaboration between the author of this work and Dr. José Manuel González) within the framework of a Spanish project **TUÑEL** whose title is: "*Investigación para la mejora competitiva del ciclo de perforación y voladura en minería y obras subterráneas, mediante la concepción de nuevas técnicas de ingeniería, explosivos, prototipos y herramientas avanzadas*".

22.1 Sample test explosion

In the validation and calibration phase of the code, the experimental results obtained by Johansson et al. [Joh08] have been taken as a reference. In this document, different loads are applied to a cylindrical magnetic concrete specimen of 140 mm diameter and height h=280mm, in which a cylindrical hole of 5-12 mm diameter has been made. The study considers three assumptions for the analysis:

- Free concrete specimen.
- Concrete specimen embedded in granular material.

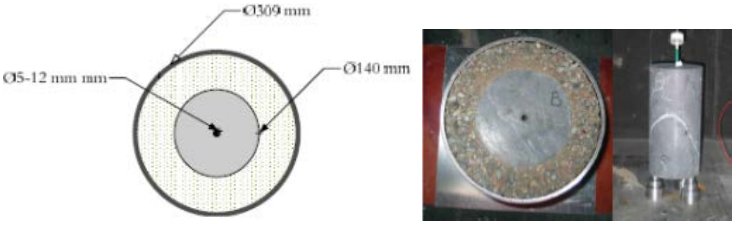

(a) (b)

Figure 22.1: Experimental set up. Specimen geometry.

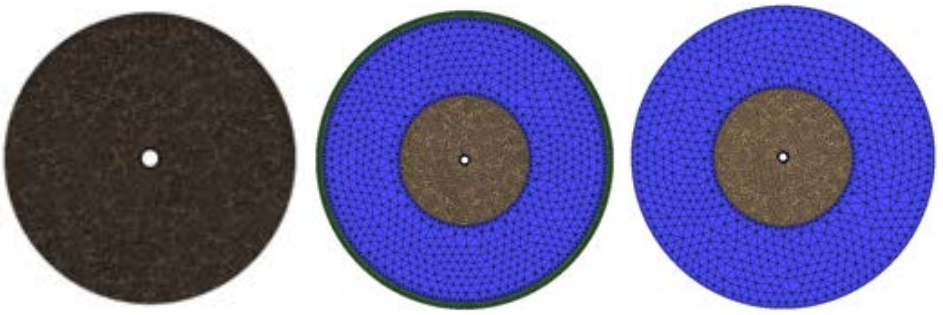

(a) (b) (c)

Figure 22.2: FE meshes used in the simulations.

- Concrete specimen embedded in granular material and confined with an external load.

In the second and third cases, the filling material is held in place by a steel liner 7 mm thick which acts as a container that also allows the application of confining pressure. Fig. 22.1 shows an outline of the specimen and an image for the three scenarios considered.

The results obtained are analysed in terms of the fragmentation and compaction of the material after the explosion. Visual information about the specimens after the explosion is available as shown in Fig. 22.4. Three numerical models have been considered for the assumptions considered assuming the problem in plane deformation as shown in Fig. 22.2. In the free concrete model (a) the specimen is modelled by 62820 triangular elements with a central 8mm diameter hole. The load is applied in a

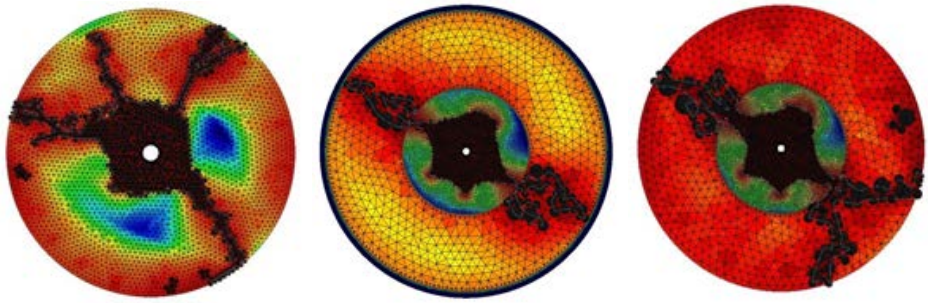

(a) Free concrete (b) Filled concrete (c) Confined filled concrete

Figure 22.3: Damage field obtained and cracked geometry.

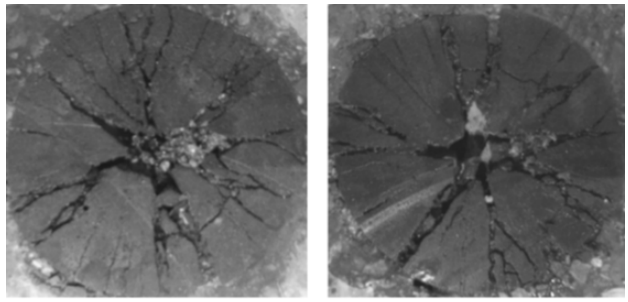

Figure 22.4: Fractured geometry of the sample after the explosion.

distributed way on its contour. In the filled concrete model (b) the filling is modelled by means of finite elements covered by a steel ring. The model has been built with a total of 10366 linear triangles. In the case of concrete with confined filling, the steel casing has been removed in order to apply the confinement by means of a load distributed over the filling itself, as is actually the case. The material properties used are the ones provided by Johansson et al. [Joh08].

The simulation has been performed by applying a prescribed load function depicted in Fig. 22.11. By means of a calibration process, the ideal load function for these cases has been determined for a maximum pressure P_{max} = 200 MPa. The numerical results obtained are shown in Fig. 22.3. As can be seen in the previous figure, the similarity between the experimental and numerical crack paths is significant.

22.2 Tunnel portal subjected to internal blast loading

In this example, a real blasting procedure has been simulated with the proposed FEM-DEM methodology. The real excavation is located in Bekkelaget (Norway) with approximately 8.5 m width and 8 m height. The theoretical cross-section area is 59.18 m^2. The blasting plan (Fig. 22.6) and material properties (Table 22.4) of the Bekkelaget excavation were given by the competent authority. The yield surface for the simulation is the Modified Mohr-Coulomb criterion [Oll02].

The Bekkelaget Tunnel is an underground construction site and therefore the material at the front is confined, i.e. it presents an initial stress state when the explosion takes place. The tensional state to which the rock is found determines the response to this phenomenon. The Bekkelaget tunnel is in the category of intermediate cover. In this case, the pressure on the tunnel and equivalently the confinement of the material can be estimated by the expression [Bud13; Per00]:

$$P = \gamma\alpha(b + h) \tag{22.1}$$

being b and h the width and the height of the tunnel, γ the specific weight and α the Terzaghi's proportionality factor [Per00].

The firing plan is composed of four 10 cm diameter shafts and 119 5 cm diameter holes distributed in different areas according to the activation delay time and the amount of explosive charge assigned to each hole. Table 22.2 details the distribution of holes in each zone delimited in the tunnel front (Fig. 22.6).

The function of variation of pressure applied in time is triangular, with a base of 0.25 ms in which the peak value is t_p = 0.10 ms. This time function is applied in all holes. Fig. 22.11 shows an outline of the pressure function considered, where P_{max} is the maximum pressure stated in Table 22.2. Fig. 22.5 depicts the FE mesh used in the simulation. The results obtained are shown in terms of material disaggregation and remaining cracking, referring to the degree of cracking left in the non-disaggregated rock.

Next, in Fig. 22.7, one can see the evolution of the blasting process for the Bekkelaget simulation performed. The results are shown in a series of significant time instants: 0.5, 1.5, 2.5, 3.5 and 4.5 ms. The evolution of the explosions in each hole can be seen in Fig. 22.7. Each of them creates an initial fracture that varies the pressure

acting on the walls, extending the fracture and the disaggregated material.

It can be seen that at the site of the hole where the explosion begins, the amount of damaged material is significantly greater. The connection between the fractures can also be seen in the images as the blast load progresses. This fact results in the variation of the acting pressure since the volume that is taken into account in the calculation is the one available, so the volume of the two incident cracks is also counted.

These results show the capacity of the mixed finite-discrete formulation FEM-DEM to simulate this blast-induced fracture paths in an adaptive way.

The numerical simulation of the blasting in the Bekkelaget tunnel has been validated by the measured blasting profile in the tunnel. Fig. 22.10 shows a comparison between the results of the numerical simulation (in red) and the field measurements (profile in blue). In 22.10.a, the entire blasting is shown with the profiles of the material fractions that have been broken down from the massif. In 22.10.b, the result has been specified for the external contour of the blasting, used to validate the accuracy of the numerical approach.

Fig. 22.10 shows how the numerical solution is conditioned by the location of the contour holes, so that the main fractures start from them. The numerical solution thus presents these oscillations around the theoretical profile so that the validation of the model takes into account the absolute value deviation between both curves. The error between the theoretical excavated profile and the numerical solution has been measured in terms of areas excavated with respect to the theoretical profile (see Fig. 22.9).

It can be seen how, in terms of the total area, the simulation and the field data are very similar. This is largely due to the fact that the difference is in the contour, not in the front end. The realistic comparison is made on the basis of the areas of over- and under-excavation with respect to the excavated profile (see Table 22.1), obtaining results of around 3 m^2 , which represents a variation with respect to the experimental one of 4.2% and 4.6% respectively.

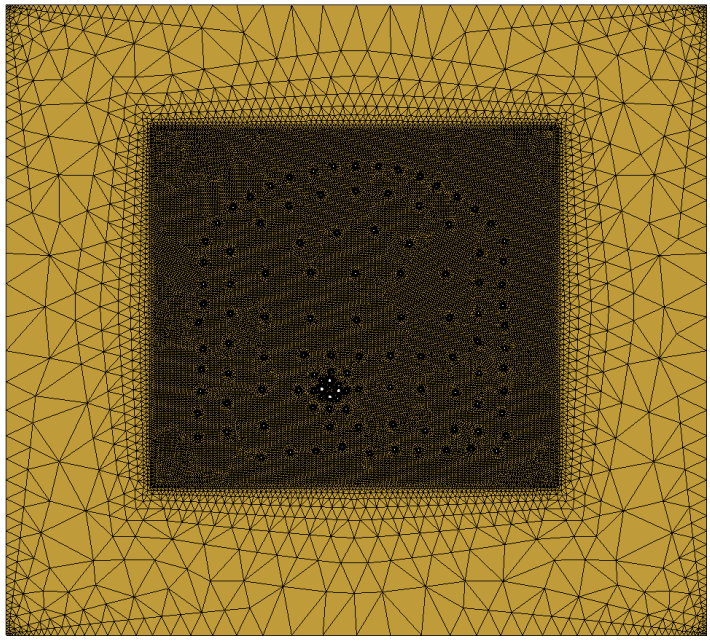

Figure 22.5: Bekkelaget FE mesh used (88,722 linear triangles and 45136 nodes).

Area	Measurement [m^2]
Experimental excavation area	71.9
Numerical excavation area	71.1
Under-excavation	3.3
Over-excavation	3.0

Table 22.1: Excavated areas for the simulated and excavated profiles. Validation of the model.

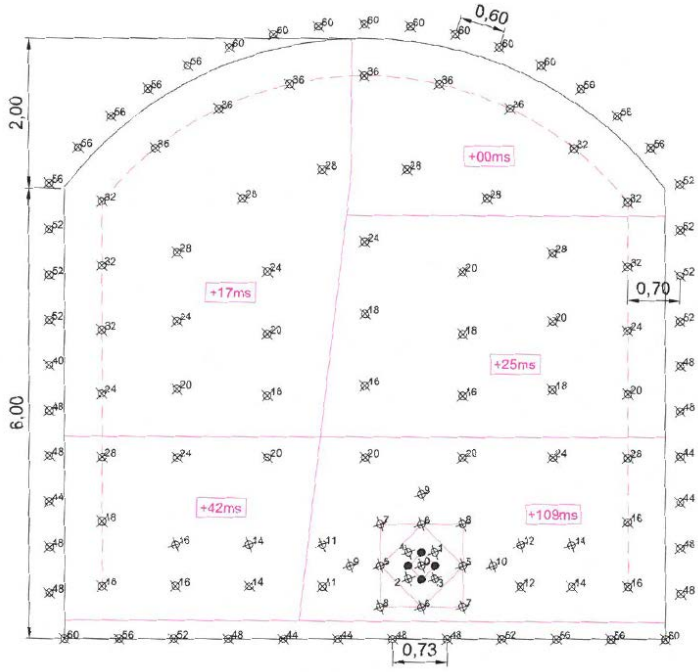

Figure 22.6: Blasting holes distribution of the Bekkelaget tunnel.

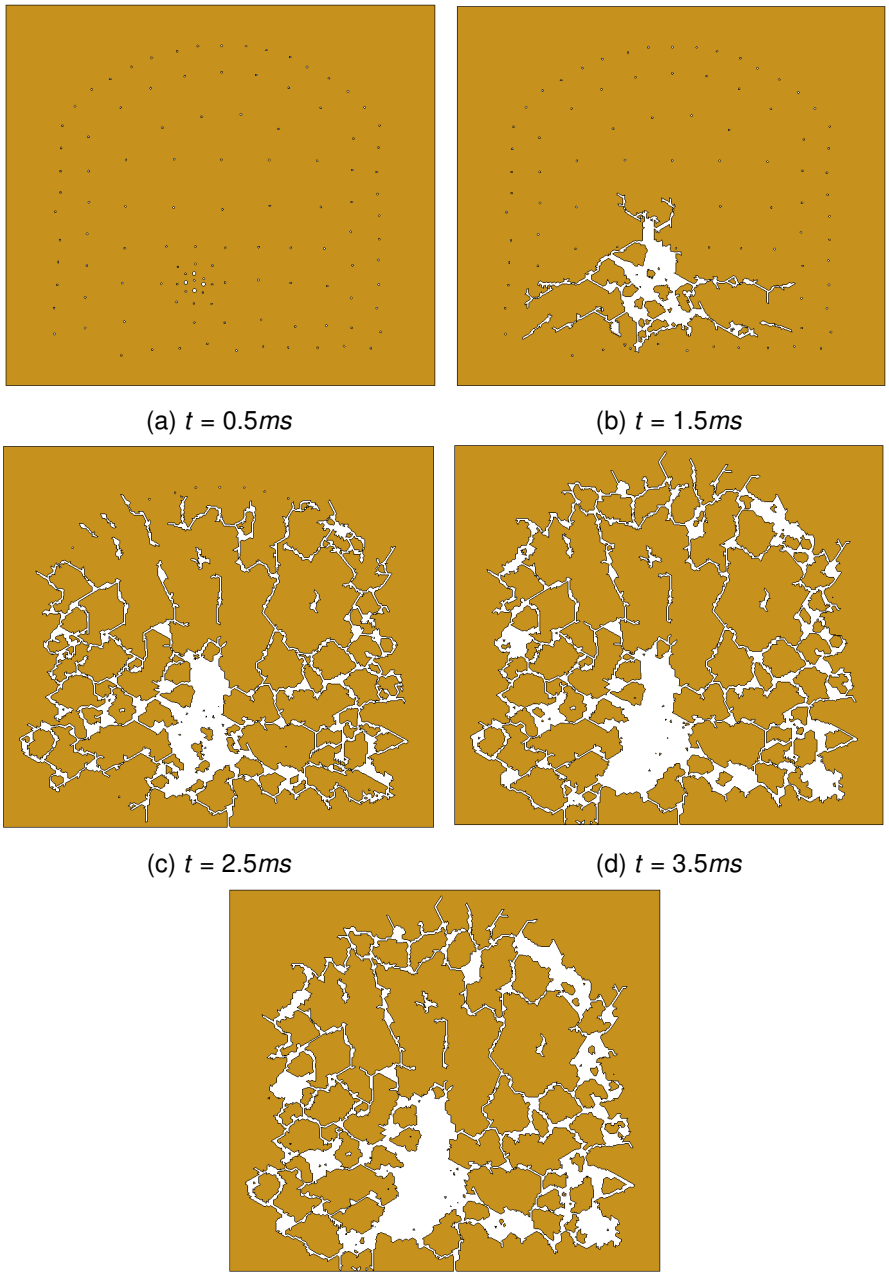

(a) $t = 0.5ms$ (b) $t = 1.5ms$

(c) $t = 2.5ms$ (d) $t = 3.5ms$

(e) $t = 4.5ms$

Figure 22.7: Bekkelaget tunnel excavation time lapse.

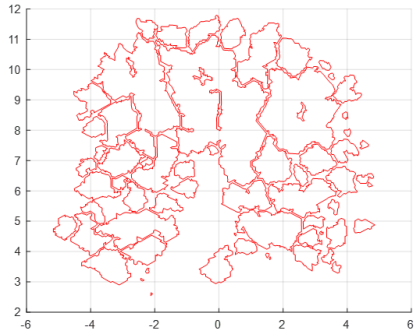

Figure 22.8: Blasting holes distribution of the Bekkelaget tunnel.

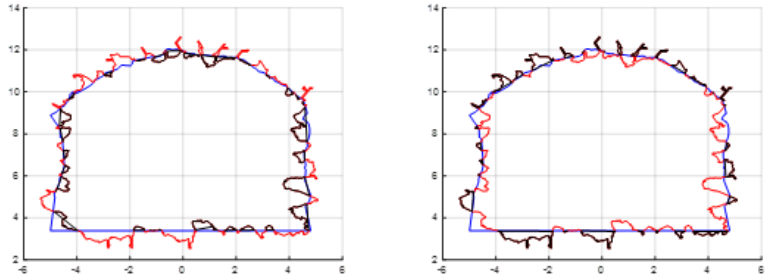

(a) under-excavation (b) over-excavation

Figure 22.9: Error measurements between the simulated profile (red) and the experimental (blue).

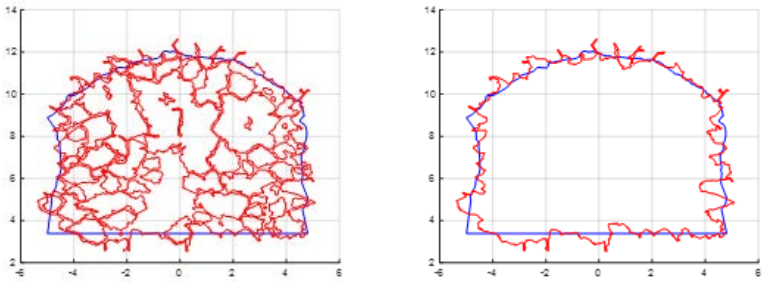

(a) (b)

Figure 22.10: Fracture distribution for the simulated (red) and the experimental excavation (blue).

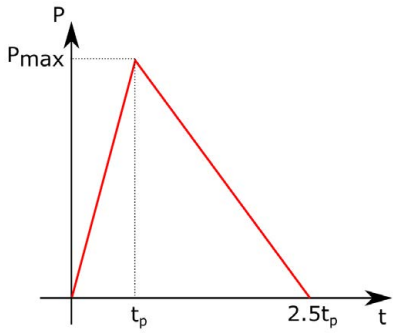

Figure 22.11: Time variation of the blasting pressure applied.

Blast	Blast Id	Zone	Pressure [MPa]	Delay [ms]
0	1	Cut	4217	0
1	1	Cut	4217	1
2	1	Cut	4217	2
3	1	Cut	4217	3
4	1	Cut	4217	4
5	2	Cut	4217	5
6	2	Cut	4217	6
7	2	Cut	4217	7
8	2	Cut	4217	8
9	2	Bottom	3568	9
10	1	Bottom	3568	10
11	2	Bottom	3568	11
12	2	Bottom	3568	12
14	4	Bottom	3568	13
16	4	Bottom	3568	14
16	2	Lifter	4217	14
18	2	Bottom	3568	15
18	3	Lifter	4217	15
18	1	Top	3197	15
20	3	Bottom	3568	16
20	3	Lifter	4217	16
20	2	Top	3197	16
24	2	Bottom	3568	17
24	2	Lifter	4217	17
24	3	Top	3197	18
28	2	Bottom	3568	18
28	3	Lifter	4217	18
28	3	Top	3197	18

Table 22.2: Pressure distribution for each blast zones. Part I.

Blast	Blast Id	Zone	Pressure [MPa]	Delay [ms]
32	1	Lifter	4217	19
32	5	Top	3197	19
36	6	Top	3197	20
44	2	Contour 2nd	2456	21
44	3	Contour	2124	21
48	3	Contour 2nd	2456	22
48	9	Contour	2124	22
52	2	Contour 2nd	2456	23
52	7	Contour	2124	23
56	3	Contour 2nd	2456	24
56	8	Contour	2124	24
60	2	Contour 2nd	2456	25
60	8	Contour	2124	25

Table 22.3: Pressure distribution for each blast zones. Part II.

Parameter	**Value**
Young's modulus (E)	85 GPa
Poisson's ratio (ν)	0.25
Tensile strength (f_t)	0.57 MPa
Compressive strength (f_c)	18 MPa
Fracture energy (G_f)	1.0 J/m^2
Friction angle (ϕ)	32 deg

Table 22.4: Material properties used in the tunnel portal subjected to internal blast loading.

Part VI bibliography

[Amb+02] R.D. Ambrosini et al. “Size of craters produced by explosive charges on or above the ground surface”. *Shock Waves*. Vol. 8(1), pp. 3–21 , 2002.

[BAG12] F.G. Bastante, L. Alejano, and J. Gonzalez-Cao. “Predicting the extent of blast-induced damage in rock masses”. *Int. J. Rock Mech. Min*. Vol. 56(2), pp. 44–53 , 2012.

[Bud13] Muni Budhu. *Soil mechanics and foundations*. JOHN WILEY and SONS. 2013.

[De12] Anirban De. “Numerical simulation of surface explosions over dry, cohesionless soil”. *Comput. Geotech*. Vol. 43, pp. 72–79 , 2012.

[FL14] A. Fakhimi and M. Lanari. “DEM-SPH simulation of rock blasting”. *Comput. Geotech*. Vol. 55, pp. 158–164 , 2014.

[Gha+13] E. Ghasemi et al. “Application of artificial intelligence techniques for predicting the flyrock distance caused by blasting operation”. *Arab. J. Geosci*. Vol. 7(1), pp. 193–202 , 2013.

[Gha+20] S. Gharehdash et al. “Blast induced fracture modelling using smoothed particle hydrodynamics”. *International Journal of Impact Engineering*. Vol. 135, p. 103235 , 2020.

[Hem81] G.B. Hemphill. *Blasting Operations*. McGrawHill Inc., New York. 1981.

[HRL10] E. Hamdi, N.B. Romdhane, and J.M. Lecléach. “A tensile damage model for rocks: application to blast induced damage assessment”. *Comput. Geotech*. Vol. 38(5), pp. 133–141 , 2010.

[Hu+15] Y. Hu et al. “Numerical simulation of the complete rock blasting response by SPHDAMFEM approach”. *Simulation Modelling Practice and Theory*. Vol. 56, pp. 55–68 , 2015.

[Joh08] D. Johansson. *Fragmentation and waste rock compactation in small-scale confined blasting*. Licenciate thesis. Lulea University of Technology. 2008.

[Kel04] Jack Kelly. *Gunpowder: Alchemy, Bombards and Pyrotechnics: The History of the Explosive That Changed the World*. Basic Books. 2004.

[Kol05] Dimitrios Kolymbas. *Tunelling and Tunnel Mechanics*. Springer. 2005.

[LHK68] EL. Lee, HC. Hornig, and JW. Kury. “Adiabatic expansion of high explosive detonation products”. *Report No. UCRL50422. California Univ., United States: Lawrence Radiation Lab*. , 1968.

[LHY13] W.B. Lu, Y.G. Hu, and J.H. Yang. “Spatial distribution of excavation induced damage zone of high rock slope”. *Int. J. Rock Mech. Min*. Vol. 64(5), pp. 181–191 , 2013.

[LK73] U. Langefors and B. Kihlstrom. *The Modern Technique of Rock Blasting*. John Wiley and Sons, New York, 2nd edn. 1973.

[M+13] Reza Safari M et al. “Pulsed fracturing in shale reservoirs: geomechanical aspects, ductilebrittle transition and field implications”. *Unconventional resources technology conference (URTeC), Denver, CO, USA*. Vol. 12-14, pp. 448–461 , 2013.

[MA08] G.W. Ma and X.M. An. “Numerical simulation of blasting-induced rock fractures”. *Int. J. Rock Mech. Min*. Vol. 45(2), pp. 966–975 , 2008.

[MC04] J.B. Martino and N.A. Chandler. “Excavation-induced damage studies at the underground research laboratory”. *Int. J. Rock Mech. Min*. Vol. 41(2), pp. 1413–1426 , 2004.

[Mem84] Du Pont De Memours. *TBlasters Handbook*. Du Pont, Wilmington, DE. 1984.

[MJU13] Reza Safari M, Huang J, and Mutlu U. “Ductile to brittle transition, generation of complex fracture networks and engineering implications”. *Applied geoscience conference, Houston (Texas)*. , 2013.

[MP07] S. Mohammadi and A. Pooladi. “Non-uniform isentropic gas flow analysis of explosion in fractured solid media”. *Finite Elem. Anal. Des*. Vol. 43(2), pp. 478–493 , 2007.

[Nin+11] Y. Ning et al. “Modelling rock fracturing and blast-induced rock mass failure via advanced discretisation within the discontinuous deformation analysis framework”. *Computers and Geotechnics*. Vol. 38, pp. 40–49 , 2011.

[Oll02] S. Oller. *Non-linear dynamics*. 2002.

[Per00] G. Perri. “Behavior category and design loads for conventionally excavated tunnels”. *VI Congreso suramericano de mecanica de rocas*. , 2000.

[Per75] P.A. Persson. “Bench drilling an important first step in the rock fragmentation process”. *Atlas Copco Bench Drilling Symposium, Stockholm*. , 1975.

[Wen+11] Lu Wenbo et al. “An equivalent method for blasting vibration simulation”. *Simul. Model. Pract. Theory*. Vol. 19(9), pp. 2050–2062 , 2011.

[WM05] D.C. Wyllie and C.W. Mah. *Rock Slope Engineering*. Spon Press. 2005.

[Yin+13] Hu Yingguo et al. “Comparison of blast-induced damage between presplit and smooth blasting of high rock slope”. *Rock Mech. Rock Eng*. Vol. 46(5), pp. 1–14 , 2013.

[YJG17] C. Yi, D. Johansson, and J. Greberg. “Effects of in-situ stresses on the fracturing of rock by blasting”. *Computers and Geotechnics*. Vol. 104, , 2017. DOI: 10.1016/j.compgeo.2017.12.004.

Part VII

Conclusions and future work

Chapter 23

Conclusions and future works

> *Tell me and I forget. Teach me and I may remember. Involve me and I learn.*
>
> *Benjamin Franklin*

23.1 Part III: FEM-DEM formulation

In this part, a novel methodology combining the FEM and the DEM has been presented. Since both methods have different time integration schemes -the FEM uses an implicit scheme while the DEM uses an explicit one- a sub-stepping procedure has been implemented by which the impulses generated by the contact between particles and the walls of finite elements can be calculated much more consistently. In this way, it is possible to use a large time step for the FEM, while to capture properly the kinematics of the particles in a stable way it is possible to apply a time step several orders of magnitude smaller on the DEM.

The original one-way coupling approach of the FEM-DEM published by Zárate et al. [ZO15] has been generalized to a two-way coupling approach. Additionally, for the non-linear anisotropic case, a spaces mapping theory [Oll+93; Oll+95; Oll03] has been used, so that the FEM-DEM is now applicable to mechanics of rocks that present

orthotropy axes and, therefore, differentiated mechanical properties depending on the direction. Additionally, a phenomenological rules of mixtures have been added to the FEM-DEM methodology, providing in this way the capability to deal with composite materials in which its material components can experience loads beyond the elastic regime.

The DEM formulation has been substantially improved. In the newly implemented version it is fully parallelized and the original frictionless particle-to-particle contact has been extended to a frictional particle-FEM wall contact. The use of particle-FEM wall contact reduces the gap by 50% and provides a smooth contact surface, preventing in this way an artificial locking between particles.

These improvements in the FEM-DEM methodology have led to the creation of a new powerful numerical tool: consistent, fast and versatile, as has been shown with the application examples. It is consistent because each method used in it is capable of working with a stable time frame, making each method and the interaction between them reliable. It is comparatively faster and computationally cheaper in relation to mixed formulations [CCC11; CBC17; Cer08] since, in this case, a calculation with an irreducible formulation is carried out and, subsequently, the stress field is enriched by means of SPR [ZZ92]. Obviously, the accuracy of the stress field smoothed by the SPR is not as high as the one obtained in more sophisticated formulations [CCC11; CBC17; Cer08]. This limitation has been addressed by two different ways: on the one hand we are capable of using more FE for the same quantity of DoF's, balancing in this way the cost and accuracy of the solution. On the other hand, an adaptive remeshing technique has been developed which increases the discretization quality at the zones where it is required.

The proposed methodology has been extensively tested and validated by means of a set of examples and benchmarks. The FEM-DEM has demonstrated to be an accurate and efficient methodology in comparison to the methodologies available in the literature.

Finally, it is important to highlight that the FEM-DEM formulation has demonstrated to be a versatile numerical tool since it is capable of simultaneously solving the degradation of the material (isotropic damage), initiation and evolution of fractures (elimination of elements and creation of particles), large displacements and fully detachments and, finally, impact of blocks against other domains of the problem by means of the frictional contact between particles and FEM walls.

23.2 Part IV: Enhanced FEM-DEM formulation via an adaptive remeshing technique

In this Part, a coupled FEM-DEM formulation enhanced with a novel adaptive remeshing technique has been presented. The proposed methodology has demonstrated a good performance: quantitatively, when comparing the force displacement curves obtained with the analytical ones, and qualitatively when analysing the crack paths obtained versus the expected or experimental results.

The standard FEM-DEM is an accurate numerical procedure due to its enhanced mesh-independence and consistency features [ZO15; ZCO18]. However, the adaptive remeshing technique here presented improves considerably the crack path geometry obtained and optimizes the calculation cost, because it only refines the zones of interest: where the non-linear dissipation takes place.

Regarding the remeshing technique, the Hessian-based methodology combined with the nodal variable indicator developed (normalized free energy) has behaved very well in all the examples performed, capturing the zones of interest where the mesh needs to be refined. In conclusion the FEM-DEM formulation, enhanced with the adaptive remeshing technique presented, is suitable for simulating complex fracture mechanics problems at an affordable computational cost.

23.3 Part V: Interaction of free-surface flows and structures by coupling the PFEM and FEM-DEM approaches

In this Part we have presented a coupled Lagrangian method for the simulation of FSI problems in presence of free-surface fluids and fracturing solids.

The formulation uses the PFEM to solve the free-surface fluid dynamics problem and to detect the fluid-solid interface, and a coupled FEM-DEM method to model crack formation and propagation in structures and the contact interaction between different solids. An iterative staggered scheme with Aitken relaxation is used to guarantee a strong coupling of the FSI problem and to avoid numerical inconveniences, such as the ill-conditioning of the linear system or added-mass effects. The numerical method presented has demonstrated its potential to estimate damages on civil constructions due to natural hazards like floods, tsunamis, landslides, or explosions.

Several academic and large scale experimental examples have been presented

to validate the proposed technology in the framework of FSI problems with fracture phenomena. The numerical tests have shown that the method is able to reproduce the dynamics of a solid object in the water, to solve accurately FSI problems with strong fluid impacts and large solid displacements, to model crack formation due to fluid hydrodynamic forces and its propagation in the structure, and to deal with solid fragmentation multi-body contact interaction, both in 2D and 3D.

23.4 Part VI: Blast loading simulation applied to mining processes and risk assessment of structures

In this part of the work, The FEM-DEM methodology has been applied to a set of engineering problems such as sample explosions and tunnel excavations. Some of the simulations performed have been conducted within the framework of an Spanish project **TUÑEL** whose title is: "*Investigación para la mejora competitiva del ciclo de perforación y voladura en minería y obras subterráneas, mediante la concepción de nuevas técnicas de ingeniería, explosivos, prototipos y herramientas avanzadas*".

In order to do so, a phenomenological procedure has been implemented in order to calculate the pressure load values to be applied at each time step on the updated cracked geometry. Additionally, an adaptive detection of the "wet" surface -surface in contact with the blast load pressure- has been developed that automatically generates the set of line/face loads to be applied at each load increment.

In addition, several numerical examples have been exposed, demonstrating the capabilities and application potential of the methodology. Indeed, the results of the Bekkelaget excavation tunnel, which can be compared with experimental results, exhibit a great resemblance in terms of excavated profile and total mass of rock fractured. These results demonstrate the capacity of the coupled finite-discrete formulation FEM-DEM to simulate this blast-induced fracture paths in an efficient and adaptive way.

23.5 Contributions

The main contributions of this work can be summarized in:

- **Generalization of the existing FEM-DEM**: The FEM-DEM now can use a wide

range of yield surfaces: Rankine, Von Mises, Drucker-Prager, Simo-Ju, Mohr-Coulomb, Modified Mohr-Coulomb. This will allow the formulation to adapt to different fracture modes and material behaviours.

- **The linearisation of the Newton-Raphson procedure has been greatly improved**: Thanks to the implementation of a numerical derivation procedure for obtaining the tangent constitutive tensor the algorithm is capable of achieving a quadratic convergence ratio.

- **Fully parallelization of the calculation**: Indeed, now the computations are fully parallelized. This allows for more challenging calculations to be performed at the lowest possible computational cost.

- **Anisotropic and composite rule of mixtures have been added**: Currently, a general non-linear anisotropic calculations can be performed within the FEM-DEM. Additionally, in order to analyse the behaviour of reinforced concrete, a phenomenological rules of mixtures have been implemented as well as an associative isotropic plasticity constitutive law for steel.

- **A Hessian-based adaptive remeshing technique has been added**: The existing FEM-DEM formulation has been enhanced with the inclusion of an adaptive remeshing technique. This inclusion can optimize the efficiency of the FE mesh and, additionally, reduce considerably the mesh dependence of the results.

- **A proper nodal indicator has been developed for remeshing purposes**. Indeed, a novel nodal variable (normalized energy dissipation) has been proposed of which Hessian matrix is used for tracking the zones to be refined.

- **The formulation is capable of simulating large displacements and rotations**: the numerical methodology has been implemented in a TL framework. This allows the solids to experience large displacements and rotations, crucial for the kind of simulations that the method is meant to be appealing.

- **A novel FSI coupled formulation has been developed**: The well established numerical methods, namely the PFEM and the FEM-DEM have been strongly coupled in order to perform free-flow fluid impacts over fracturing solids. In order to overcome the added-mass effects, an Aitken relaxation method [Cer+19] has been included.

- **A semi empirical methodology for blasting processes has been studied**: In order to simulate the blast pressure evolution through the cracks generated within the rock mass, a heuristic procedure has been included that updates the topology in which the pressure load is applied as well as the load reduction due to the increase of available space.

- **The DEM used is now far more sophisticated and allows the user to select the contact constitutive law (linear and Hertzian), a wide variety of time advancing schemes and including friction between particles.**

- **A new FE-DE contact is now available.** The new contact procedure detects the indentation between a particle and a FE edge instead of computing the conventional particle-particle contact. This new methodology reduces by half the apparent gap between the bodies and generates a flat contact surface, avoiding the artificial locking that occurred with the DE-DE contact.

- **An extensive validation and benchmarking study has been conducted for each of the implementations performed.** Indeed, for each proposed methodology, a wide set of numerical examples is given. Some of the tests are compared against other numerical solutions or against analytical/experimental data, if available.

- **A strong coupling between the FEM and the DEM has been explored and implemented.** This new development estimates with more accuracy and stability the contact forces calculated with the DEM. This is achieved by recomputing the frictional contact forces with the DEM at each non-linear iteration performed within the FEM.

23.6 Transversal contributions

As detailed in Annex E, a great effort has been made to develop a modular, polivalent and object oriented constitutive law library within the open source code Kratos-Multiphysics. Currently, these CL, the composite rules and the generic anisotropic law are being employed by several researchers in their own scientific fields in addition to its use in competitive international and national projects.

In this regard, with the collaboration of Dr. Vicente Mataix and Dr. Riccardo Rossi, has been the elaboration of a **object oriented modular library** of constitutive laws for

solids within the framework of Kratos-Multiphysics inside the `StructuralMechanicsApp`. A review of the CL library can be found here.

23.7 Future work

As we have seen, the FEM-DEM is a very appealing option when it comes to solving multi-fracture problems. The same goes for the multi-physic PFEM-FEM-DEM methodology for fluid structure interaction. Still, further research on some aspects is suggested:

- **Improve of the accuracy of the stress field.** The accuracy in the field of deformation or stress can be improved in order to gain mesh independence. This could be done by improving the existing SPR or by implementing a mixed formulation like the one proposed by Cervera et al. [CCC11; CC06], among other possible methodologies.
- **Extension to any kind of FE**. Currently the FEM-DEM is formulated only for linear triangles and tetrahedra. An extension to linear hexahedra or high order triangles and tetrahedra could definitely improve the discretization accuracy and generality of the methodology.
- **Extension of the FEM-DEM to plasticity processes**. Currently, the FEM-DEM methodology works internally according to an isotropic damage model. Could be interesting to generalize the proposed formulation to be able to use any kind of plasticity (kinematic-isotropic hardening) model and in this way apply the FEM-DEM to strain-driven plastic processes. In this regard, thanks to the transversal implementation performed within the Structural mechanics application (Appendix E), the extension of the FEM-DEM to any kind of constitutive model should be easy and re-usable.
- **Crack opening-re-closure.** The crack opening and re-closure behaviour is typical for cyclic loading conditions. The isotropic damage model is not capable of capturing this behaviour. An interesting implementation could be to use a directional or "$d+d-$" damage model [CTV18] to be able of simulating this effect.
- **Predict a good estimation for the DE material properties.** Since the material properties of the continuum (FEM) can differ from the ones used in the particles,

a good estimation procedure could ease the calibration process of the FEM-DEM simulations.

- **Improve the coupling approach within the FSI.** The Aitken relaxation procedure used does its work perfectly but there are more sophisticated relaxation techniques that may be more efficient and increase the convergence rate. One option could be to implement a Jacobian-Free Newton-Krylov method [KK04] or a Quasi-Newton procedure like Broyden [Sri84], MVQN [Bog+14], etc.

- **Implement a Arc-length strategy.** In order to perform load-controlled calculations in which softening and/or snap-through can appear, only by means of a Arc-length procedure [FM93] can be solved.

- **Consider the interaction of the fluid and the free particles**. In the current implementation, the free particles move according to an explicit time advancing scheme, as it is commonly done in the standard DEM. For those free particles, could be interesting to compute the interaction between the fluid flow (PFEM) and the DE. With this capability, the free particles could be dragged by the fluid flow like it happens in erosive rivers or problems regarding small debris generation.

- **Perform FSI simulations using the enhanced FEM-DEM methodology and its adaptive remeshing technique**. Indeed, if this technology is developed, a more efficient calculation can be performed and the mesh-dependency issue can be circumvented without any additional operations.

- **Increase the consistency and robustness of the adaptive remeshing analysis**. In this regard, several operations can be implemented. One interesting option consists in checking the equilibrium of the generated new mesh with the previously computed nodal and integration points values. In this way, and estimating the error committed -via the already explained SPR methodology for example-, one can track the quality of the new generated meshes and require a minimum accuracy threshold for them -since the Hessian is not related to the discretization error-.

- **Employ a more exact and energy conservative contact methodology**. An improvement that could be studied consists in using a proper contact model like the one proposed by Mataix et al. [Mat20] based on Augmented Lagrange Multipliers (ALM). In this case, the DEM would simulate only the debris generated

and the contact between particles. Conversely, the contact between different solid parts would be calculated by a variationally consistent contact formulation [Wri06; Pop12; Yas11; Mat20]. This new formulation would circumvent the current gap between the crack faces and would enforce the contact constraints in a variationally consistent way. One important drawback of this implementation is the computational cost added to the problem in order to detect the *master-slave* contacts, indentations and solving the enriched system of equations. Additionally, since the enriched system of equations is not well-conditioned is general cases, the iterative solvers used in this work would experience numerical instabilities and direct solvers should be used, with the associated increase of solving time associated.

- **Validate the blast pressure load extrapolation to the 3D case**. The implemenation performed for the blast load extrapolation for the 3D case is analogous to the one exposed for the 2D geometries. However, an extensive validation of the 3D version is still misssing, which would increase the applicability and generality of the proposed methodology.

Conclusions bibliography

[Bar+20] G. Barbat et al. “Structural size effect: Experimental, theoretical and accurate computational assessment”. *Engineering Structures*. Vol. 213, p. 110555 , 2020.

[Bog+14] Alfred Bogaers et al. “Quasi-Newton methods for implicit black-box FSI coupling”. *Computer Methods in Applied Mechanics and Engineering*. Vol. 279, pp. 113–132 , 2014. DOI: 10.1016/j.cma.2014.06.033.

[CBC17] M. Cervera, G.B. Barbat, and M. Chiumenti. “Finite element modelling of quasi-brittle cracks in 2D and 3D with enhanced strain accuracy”. *Computational Mechanics*. Vol. 60, pp. 767–796 , 2017.

[CC06] M. Cervera and M. Chiumenti. “Mesh objective tensile cracking via a local continuum damage model and a crack tracking technique”. *Computer Methods in Applied Mechanics and Engineering*. Vol. 196(1), pp. 304–320 , 2006.

[CCC11] M. Cervera, M. Chiumenti, and R. Codina. “Mesh objective modeling of cracks using continuous linear strain and displacement interpolations”. *Int. J. Numer. Meth. Engng*. Vol. 87, pp. 962–987 , 2011.

[Cer+19] M.L. Cerquaglia et al. “A fully partitioned Lagrangian framework for FSI problems charcterized by free surfaces, large solid deformations and displacements,and strong added-mass effects”. *Comput. MEthods Appld. Mech. Engnr.*. Vol. 348, pp. 409–442 , 2019.

[Cer08] M. Cervera. “An orthotropic mesh corrected crack model”. *Computer Methods in Applied Mechanics and Engineering*. Vol. 197, pp. 1603–1619 , 2008.

[CTV18] M. Cervera, C. Tesei, and G. Ventura. “Cracking of quasi-brittle structures under monotonic and cyclic loadings: a d+/d damage model with stiffness recovery in shear”. *International Journal of Solids and Structures*. Vol. 135, pp. 148–171 , 2018.

[FM93] M. FAFARD and B. MASSICOTTE. “GEOMETRICAL INTERPRETATION OF THE ARC-LENGTH METHOD”. *Computers and Structures*. Vol. 46, pp. 603–615 , 1993.

[KK04] D.A. Knoll and D.E. Keyes. “Jacobian-free NewtonKrylov methods: a survey of approaches and applications”. *Journal of Computational Physics*. No. 2, Vol. 193, pp. 357–397 , 2004. DOI: https://doi.org/10.1016/j.jcp.2003.08.010.

[Mat20] V. Mataix. *Development of innovative mathematical and numerical models for the study of shells deformation during industrial forming processes employing the Finite Element Method*. Universitat Politècnica de Catalunya. 2020.

[Oll+93] S. Oller et al. “A finite element model for analysis of multiphase composite materials”. *Ninth International Conferences on Composite Materials. Zaragoza - Spain*. , 1993.

[Oll+95] S. Oller et al. “An anisotropic elastoplastic model based on an isotropic formulation”. *Engineering Computations*. Vol. 12, pp. 245–262 , 1995.

[Oll03] S. Oller. *Simulación numérica del comportamiento mecánico de los materiales compuestos*. CIMNE - Barcelona. 2003.

[Pop12] A. Popp. *Mortar Methods for Computational Contact Mechanics and General Interface Problems*. TECHNISCHE UNIVERSITAT MUNCHEN. 2012.

[Sri84] G P Srivastava. “Broyden’s method for self-consistent field convergence acceleration”. *Journal of Physics A: Mathematical and General*. No. 6, Vol. 17, pp. L317–L321 , 1984. IOP Publishing. DOI: 10.1088/0305-4470/17/6/002.

[Wri06] P. Wriggers. *Computational Contact Mechanics*. 2006.

[Yas11] V. Yastrebov. *Computational contact mechanics: geometry, detection and numerical techniques*. Ecole Nationale Superieure des Mines de Paris. 2011.

[ZCO18] F. Zárate, A. Cornejo, and E. Oñate. “A three-dimensional FEMDEM technique for predicting the evolution of fracture in geomaterials and concrete”. *Comput Methods Appl Mech Eng*. Vol. 5, pp. 411–420 , 2018.

[ZO15] F. Zárate and E. Oñate. “A simple FEMDEM technique for fracture prediction in materials and structures”. *Computational Particle Mechanics*. Vol. 2, pp. 301–314 , 2015.

[ZZ92] O.C. Zienkiewicz and JZ. Zhu. “The superconvergent patch recovery (SPR) and adaptive finite element refinement”. *Comput Methods Appl Mech Eng*. Vol. 101, pp. 207–224 , 1992.

Appendices

Appendix A

Mesh independence and size-objectivity

In this appendix we will study the behaviour of the FEM-DEM formulation in regard to the structural size-objectivity and mesh-dependency of quasi-brittle materials submitted to fracturing. In order to do so, a Mode I and Mixed modes I-II fracture examples of 3-point bending notched beams have been performed. To study the size-objectivity, the same aspect ratio of the geometry and material properties have been used, but different global sizes are studied. On the other hand, to asses the mesh-dependency of the proposed method, the same geometry and material properties have been employed but with different FE discretizations. This study follows the structure of the research performed in [Bar+20], in which an exhaustive analysis of this issue is conducted.

Barbat et al. [Bar+20] state that "*Structural size effect refers to the variation, motivated by a change of size, of the load capacity of a structure from estimations made using stress failure criteria*". This implies that larger structures can dissipate a much lower energy than smaller geometries, like is shown in Fig. A.1. Indeed, several authors have shown how the size-effect can affect the ductility and peak load of structures [BP98; Baz00; Baz99; Bar+20], which denotes its importance and study interest. The structural size-effect is no taken into account in the current implementation of the FEM-DEM procedure, but it can be added in the future like it is done in [Bar+20].

The FEM-DEM methodology can be framed, at least before removing FE, within the *smeared crack approaches* (Section 4.2.1.2). These approaches have achieved size-objectivity by means of relating the energy dissipation with the element size of the problem (Eq. (7.7)). The numerical examples performed in this section for a wide range of structural sizes demonstrate the capability of the standard FEM-DEM (without any adaptive remeshing technique) of circumventing spurious mesh-size dependent results.

In addition to being able to be size-objective, it is also vitally important to analyse the mesh-dependence on the formulation when computing crack trajectories. In this case, since the fracture path is determined by the damage field and the subsequent removal of FE, the result is intrinsically dependent on the mesh used if no additional measures are taken. This is why the inclusion of an adaptive remeshing technique is crucial for the FEM-DEM methodology in order to avoid the mesh-dependency problem.

Although the implemented version of an SPR improves the stability and mesh independence from an irreducible formulation without stress smoothing, it will always be necessary to employ a higher number of FE to obtain consistent results compared to more sophisticated mixed formulations [Bar+20; CCC11; CBC17; CC06] that as a counterpart are computationally more expensive and, in the monolithic schemes, can lead to ill conditioning of the stiffness matrix. Indeed, in the 3D case, the employed irreducible formulation involves 3 DoF per node whereas in [Bar+20] is 9 DoF per node. This difference in the number of DoF per node allows the proposed methodology to use a finer mesh for the same number of DoF to be solved.

A.1 Size-objectivity

A.1.1 Mode I size-effect test: Grégoire test

The first numerical example consist in a three-point bending beam with a central notch. This is a classical Mode I example and has been experimentally performed by Grégoire et al. [GRP13] and reproduced numerically by Barbat et al. [Bar+20]. The generic geometry of the sample is depicted in Fig. A.2. The numerical simulations were conducted for different scales by modifying the depths of the beam as $D = 400mm$, $D = 200mm$, $D = 100mm$ and $D = 50mm$ but maintaining the same aspect ratios. Two different notch penetrations were studied, namely, half-notched case with $\lambda = 0.5$ and fifth-notched with $\lambda = 0.2$. Plane stress conditions are assumed with a

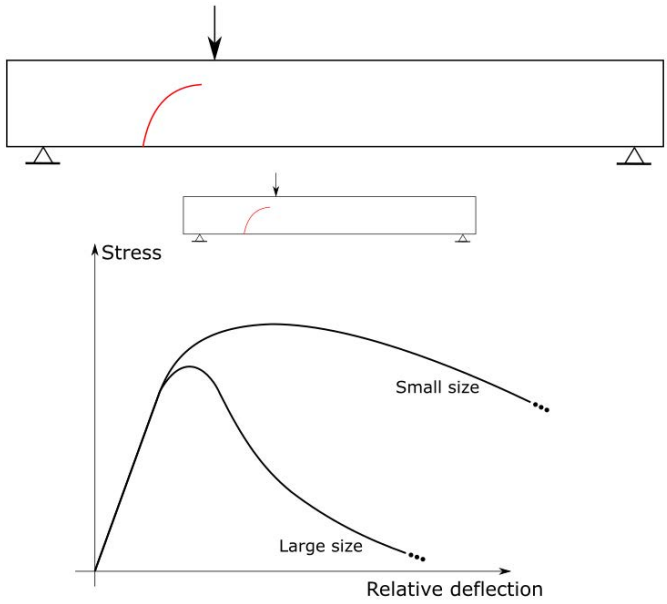

Figure A.1: Stress-deflection evolution for different structure sizes

thickness $t = 50mm$ for all cases. The notch width depends on the beam depth as $w = 1.25 \cdot 10^{-2} D$. The element size used is $l_{elem} = w/2$.

The material properties used were estimated in [Bar+20] and are given in Table A.1. As can be seen in Fig. A.2, the load is applied as an imposed vertical displacement at the midpoint of the beam. The yield surface used is the Rankine criterion.

Fig. A.3 shows the evolution of the reaction-CMOD (Crack Mouth Opening Displacement) at the midpoint and at the nodes of the notch, respectively. It can be seen how the proposed method is capable of capturing the peak force of the problem for the half-notched and for the fifth-notched cases according to the numerical result provided in [Bar+20].

It can be seen how the proposed methodology is mesh-objective, in the sense that all the curves are in homotethic. On the contrary, the post peak evolution of the curves corresponding to the smaller scales of the structure are in greater disagreement to the

Parameter	Value
Young's modulus (E)	37 GPa
Poisson's ratio (ν)	0.2
Tensile strength (f_t)	3.5 MPa
Fracture energy (G_f)	90 J/m^2

Table A.1: Material properties used in the Grégoire test

ones given in [Bar+20]. This can happen due to the stress smoothing performed within the FEM-DEM becuase it add a certain diffusion to the damage field and, subsequently, can affect to the energy dissipation.

Fig. A.4 shows how the crack propagated along the geometry of the sample. The crack path is in accordance to the one obtained in the literature [Bar+20], which corresponds to an straight line connecting the tip of the notch and the midpoint of the beam.

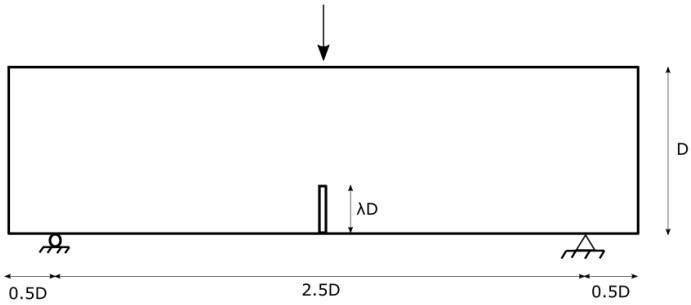

Figure A.2: Mode-I Grégoire test geometry.

A.1.2 Mixed Mode size-effect test: Garcia-Alvarez test

In this case, a three point beam with an eccentric notch is studied. This example was conducted in Garcia-Alvarez et al. [GGC12] and reproduced in Barbat et al. [Bar+20] as a mixed-mode fracture problem for assessing the mesh size-effect. Several similar geometries were analysed (see a generic geometry in Fig. A.5) in terms of depth: $D = 80mm$, $D = 160mm$ and $D = 320mm$. The λ factor of the notch is constant

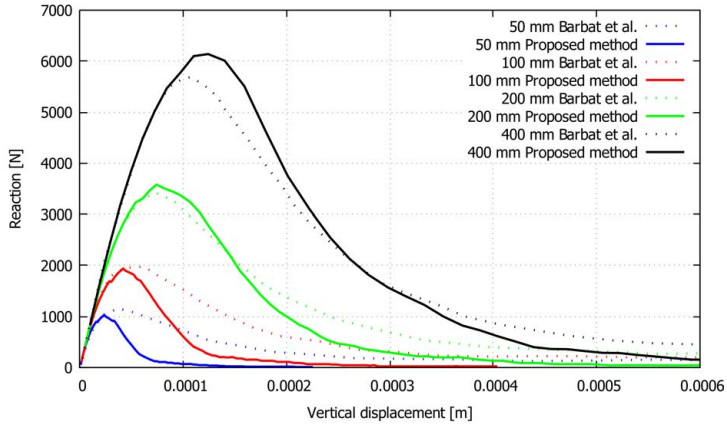

(a) half-notched beam

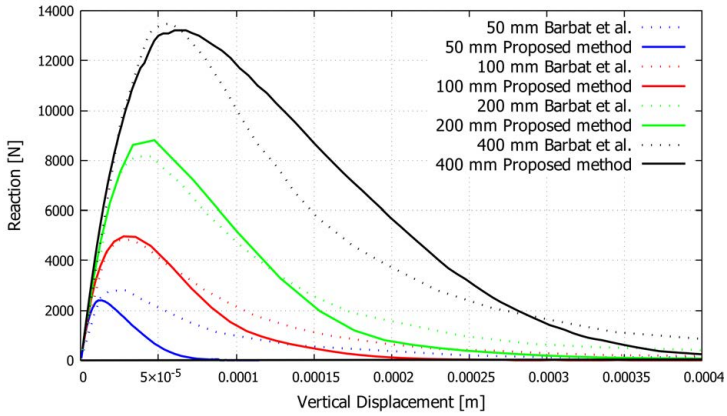

(b) fifth-notched beam

Figure A.3: Force-CMOD evolution for the a) half-notched and for the b) fifth-notched Grégoire test

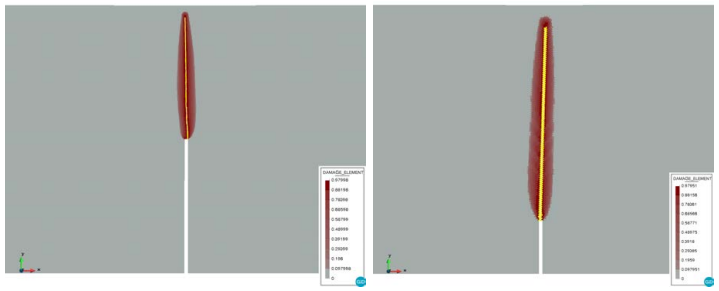

(a) half-notched beam (b) fifth-notched beam

Figure A.4: Crack trajectories for the half and fifth notched beams ($D = 400mm$) of the Grégoire test.

and equal to 0.25 in all cases. Two different notch eccentricities were considered: $\mu D = 0.625D$ and $\mu D = 0.3125D$. The material properties used are given in Table A.2 and the thickness of the plane stress problem is 50 mm in all the simulations. As in the previous example, a vertical imposed displacement is applied at the midpoint of the beam. The width of the notch is assumed to be $w = D/100$. The element size used is $l_{elem} = w/2$.

Fig. A.6 shows a good agreement between the proposed method and the mixed $\varepsilon - u$ formulation [Bar+20] in terms of peak load. Must be said that for the eccentricity $\mu D = 0.625D$ the peak load is consistently underestimated according to Barbat et al. [Bar+20] but, since the FE mesh used is finer (we use four elements instead of one to discretize the notch) the behaviour could be more ductile in the FEM-DEM simulation. Additionally, if one compares the crack paths obtained with the FEM-DEM in Fig. A.7 with the ones given in [Bar+20] (Fig. A.8) one can appreciate the high analyse between them.

As in the previous example, there is some misalignment of the post-peak behaviour in comparison the ones given in [Bar+20].

As far as the damage fields shown in Figs. A.7-A.8 are concerned, one can see how the FEM-DEM solution damage field is more "diffusive" or, in other words, involves a wider surface of damaged FE. This is mainly due to the stress smoothing performed which, as a side effect, adds a certain quantity of artificial diffusion to the damage field.

Parameter	Value
Young's modulus (E)	33.8 GPa
Poisson's ratio (ν)	0.2
Tensile strength (f_t)	3.5 MPa
Fracture energy (G_f)	80 J/m^2

Table A.2: Material properties used in the Garcia-Alvarez test.

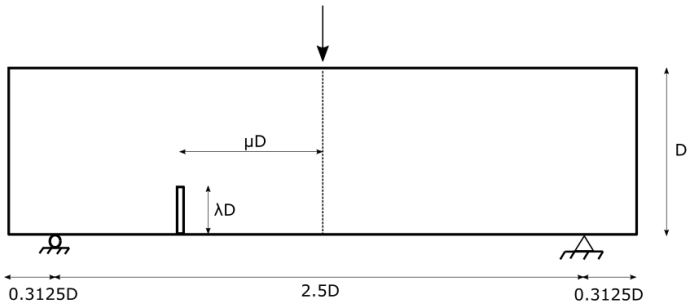

Figure A.5: Mixed Mode Garcia-Alvarez test geometry.

A.2 Mesh-dependence

With the aim of studying the mesh-dependence of the proposed FEM-DEM procedure, we have computed the already shown Garcia-Alvarez test (Section A.1.2) with a $\mu D = 0.3125D$ employing different FE mesh sizes and orientations.

The FE meshes used are depicted in Fig. A.10. As one can see, there are five different meshes, discretizing the notch with a certain number of elements, ranging from 8 (mesh 1) to 1 (mesh 5) FE.

Fig. A.11 shows the crack path for each FE mesh. In this figure, one can see how the simulated fracture path is practically the same for the three finer meshes (mesh 1, mesh 2 and mesh 3). Conversely, if one discretizes the notch with only one triangle (mesh 4 and mesh 5) the crack path diverges from the expected one, even though the global tendency is correct.

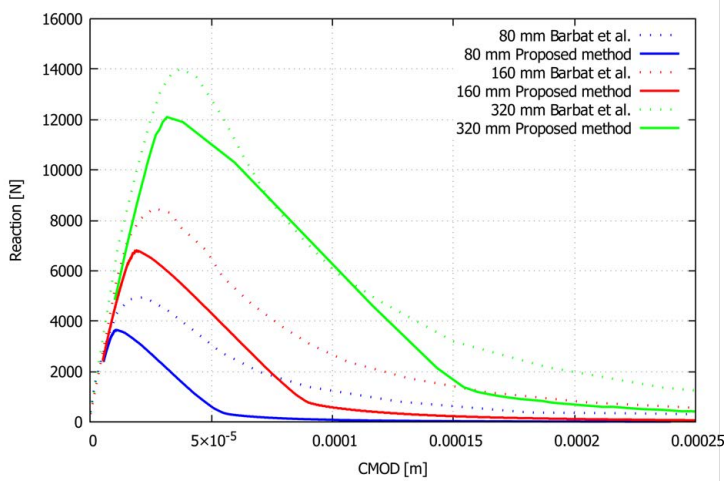

(a) $\mu D = 0.625D$

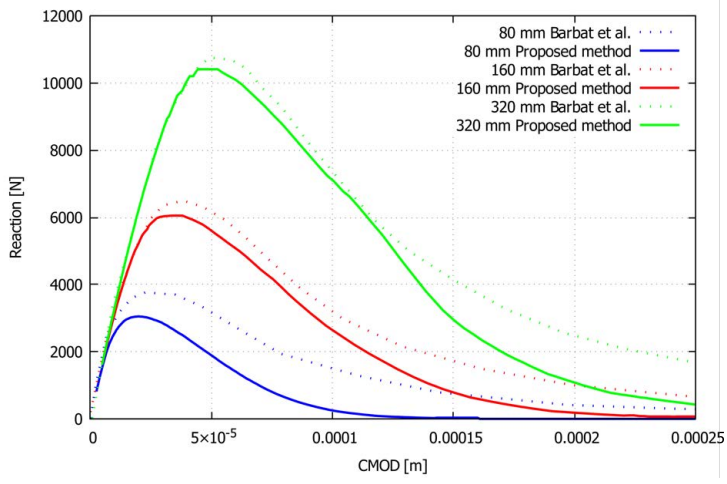

(b) $\mu D = 0.3125D$

Figure A.6: Force-CMOD evolution of the Garcia-Alvarez test for different eccentricities.

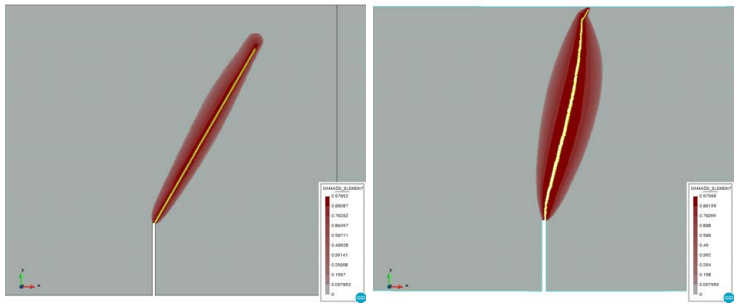

(a) $\mu D = 0.625D$ (b) $\mu D = 0.3125D$

Figure A.7: Crack trajectories for the Garcia-Alvarez test for different eccentricities.

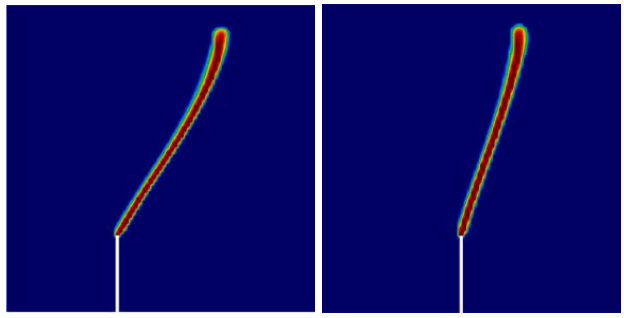

(a) $\mu D = 0.625D$ (b) $\mu D = 0.3125D$

Figure A.8: Crack trajectories for the Garcia-Alvarez in Barbat et al. [Bar+20].

The Force-displacement evolution (applied vertical load against the vertical displacement of one node of the notch) for each FE mesh is depicted in Fig. A.9. As can be seen in this figure, the force-displacement evolution is similar for the different FE meshes used. As expected, the finer the mesh is, the more ductile and smooth the solution becomes. Additionally, it can be seen how the solution converges in terms of peak force with the increase of the number of FE.

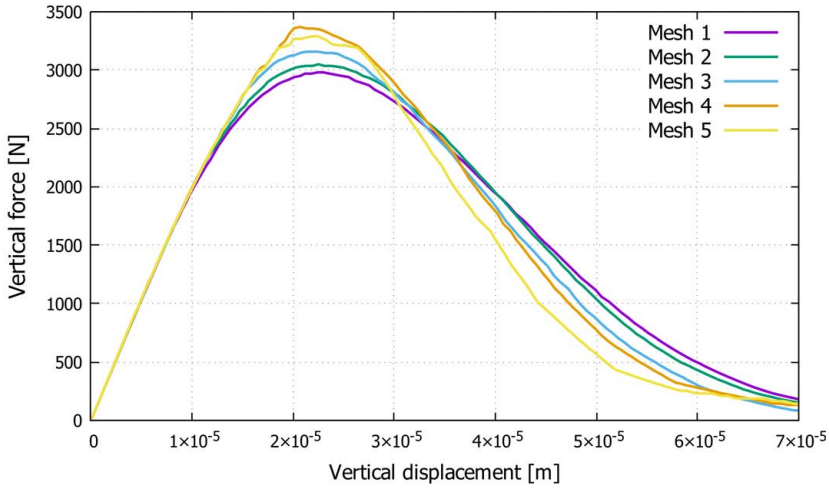

Figure A.9: Force-displacement evolution of the Garcia-Alvarez test for different FE meshes.

A.3 Conclusions

Based on the examples performed in this section, the following conclusions can be drawn:

- The structural size-objectivity problem is treated correctly within the proposed FEM-DEM. The results obtained (in terms of peak stress) are in reasonable accordance to the ones given in Barbat et al. [Bar+20] for the same mesh-sizes, which ensures the correctness of the proposed methodology. Must be said that, since the proposed methodology is based on an irreducible displacement-based formulation, a larger number of FE should be used in order to better capture the

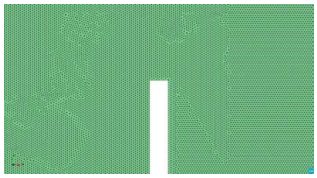

(a) Mesh 1: 711,354 FE and 357,353 nodes

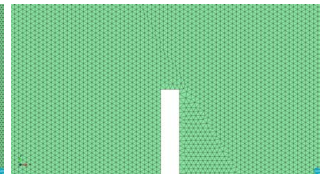

(b) Mesh 2: 179,684 FE and 90,184 nodes

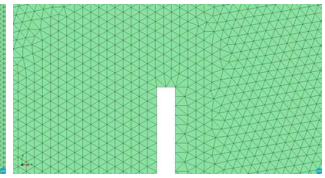

(c) Mesh 3: 46,045 FE and 23,213 nodes

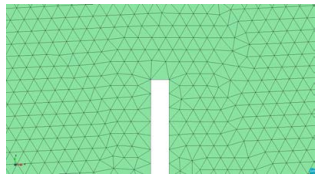

(d) Mesh 4: 21,024 FE and 10,653 nodes

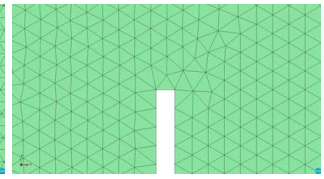

(e) Mesh 5: 12,264 FE and 6,247 nodes

Figure A.10: FE meshes used for the mesh-dependency study. FE discretization at the notch.

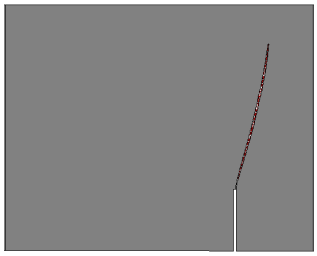

(a) Mesh 1 crack path

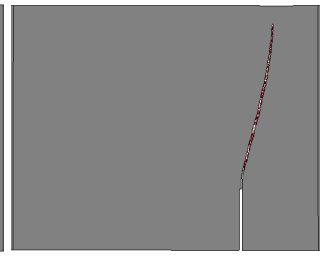

(b) Mesh 2 crack path

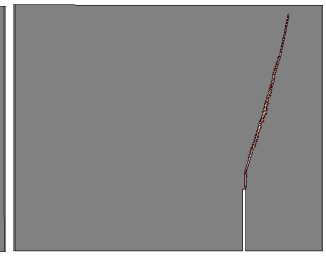

(c) Mesh 3 crack path

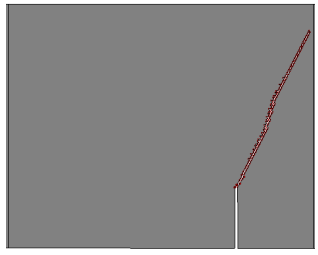

(d) Mesh 4 crack path

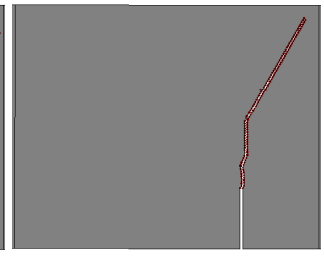

(e) Mesh 5 crack path

Figure A.11: Fracture trajectories for each FE mesh.

post-peak behaviour of some of the cases exposed in comparison to a more sophisticated and node-wise more expensive formulations.

- The post-peak behaviour of the proposed methodology shows a sensible misalignment with the ones given in [Bar+20]. The results obtained with the proposed methodology do not show a relative increase of the energy dissipated whereas this effect can be seen in [Bar+20]. This issue has to be studied but, since the smoothing procedure of stresses induces an increase of the diffusivity of the damage field, the SPR will be the main focus of this research.
- The mesh-dependency of the proposed method is higher than in more sophisticated formulations (i.e. mixed $u - \varepsilon$ formulations) but the SPR implemented is able to improve the accuracy and stability solution in comparison with the standard irreducible displacement based formulations [Lev82; Kri94; Kri89]. At this stage, as a future research line, could be interesting to explore the possibility to improve the stress recovery procedure or adapt the FEM-DEM to be based on a more mesh-independent formulation like the ones proposed in [Bar+20].

Appendix B

Yield surfaces used

A great number of criteria about yield and plastic discontinuity have been formulated during the last years to better represent the inelastic behaviour of ideal solids. There are other better suited criteria for the representation of the behaviour of metal and other materials that work better for geomaterials. In general, the formulation and/or use of these criteria require considering the following basic behaviour characteristics:

- **Metallic materials** have traction and compression strength of the same magnitude. The hydrostatic pressure, first invariant stress tensor I_1 , has very little influence on the determination of the plastic yield state.
- **Frictional materials** of the stony concrete type, soils, ceramics, etc., have less strength to traction than to compression. The hydrostatic pressure $p = I_1/3$ has more influence on the plastic yield condition for low and moderate stresses than on high hydrostatic stresses. The solid suffers unrecoverable volume changes showing dilatancy phenomena.

From this brief description the need to formulate different yield and plastic potential criteria to consider the requirements for each type of materials becomes obvious.

In this appendix, all the used and implemented yield surfaces are described. Some of them are widely-known yield criteria and can be found in Oller [Oll02] and in Souza et al. [SPO08].

Since the most of the yield surfaces exposed are formulated in terms of the stress invariants, a brief description of them and the so-called Lode's angle is given in the next paragraphs. Additionally, all the yield surfaces described follow the same structure:

$$\Psi = \mathfrak{F}(\boldsymbol{\sigma}) - \kappa \tag{B.1}$$

where Ψ defines the elastic domain (when lower than zero), $\mathfrak{F}(\boldsymbol{\sigma})$ is the uniaxial stress measure and κ is the material threshold.

B.1 Stress invariants and other computations

B.1.1 Stress invariants

$$I_1 = \sigma_{11} + \sigma_{22} + \sigma_{33} = \mathrm{tr}(\boldsymbol{\sigma}) \tag{B.2}$$

$$I_2 = \sigma_{11}\sigma_{22} + \sigma_{22}\sigma_{33} + \sigma_{11}\sigma_{33} - \sigma_{12}^2 - \sigma_{23}^2 - \sigma_{31}^2 \tag{B.3}$$

$$I_3 = \det(\boldsymbol{\sigma}) \tag{B.4}$$

B.1.2 Stress deviator invariants

The stress deviator tensor s_{ij} is defined as:

$$\mathbf{s} = \boldsymbol{\sigma} - \frac{I_1}{3}\mathbf{I} \tag{B.5}$$

Where I_1 is the first stress invariant (Eq. (B.2)) and $\mathbf{I}$ the identity tensor. Based on the deviator stress tensor, the following invariants can be defined:

$$J_1 = 0 \tag{B.6}$$

$$J_2 = \frac{1}{3}I_1^2 - I_2 \tag{B.7}$$

$$J_3 = \frac{2}{27}I_1^3 - \frac{1}{3}I_1 I_2 + I_3 \tag{B.8}$$

B.1.3 Lode's angle θ

Geometrically, the Lode Angle is the smallest angle between the line of pure shear and the projection of the stress tensor on the deviatoric plane. The mathematical expression is:

$$\theta = \frac{1}{3}\text{asin}\left(\frac{-3\sqrt{3}J_3}{2J_2\sqrt{J_2}}\right) \tag{B.9}$$

B.2 Mohr-Coulomb yield surface

This criterion was first formulated by Coulomb in 1773 and later developed more thoroughly by Mohr in 1882. It is based on two parameters: the cohesion c and the internal friction angle ϕ among particles. It includes the first invariant of the stress tensor in its mathematical expression I_1 and the second and third invariants of the deviatoric stress tensor J_2 , J_3 respectively.

Uniaxial stress

$$\mathfrak{F}(\boldsymbol{\sigma}) = \left(\cos\theta - \frac{\sin\theta\sin\phi}{\sqrt{3}}\right)\sqrt{J_2} + \frac{I_1\sin\phi}{3} \tag{B.10}$$

Material threshold

$$\kappa = c\cos\phi \tag{B.11}$$

B.3 Modified Mohr-Coulomb yield surface

The use of the original Mohr-Coulomb yield criterion for materials of the concrete type, has the disadvantage of not fulfilling the relationship between the uniaxial tensile and compressive strength for friction angles ϕ usually employed for concrete ($\phi \approx 30 - 35\,deg$).

Among the solutions usually adopted to solve the problem is to increase this internal friction angle ϕ until the required initial uniaxial resistance ratio is reached. However, this is not a valid solution when working with associative plasticity, since

the Mohr-Coulomb criterion defined as a surface of plastic potential with a dilatancy angle $\psi = \phi$, would produce in the solid an excessive effect of the dilatancy phenomenon.

In order to be able to operate with associative plasticity, and to avoid the inconvenience of using the Mohr-Coulomb function defined with a very high internal friction angle, a simple modification of the original criterion mentioned above is proposed in Oller et al. [Oll88; Oll02] is proposed as:

Uniaxial stress

$$\mathfrak{F}(\boldsymbol{\sigma}) = \frac{2\tan\left(\pi/4+\phi/2\right)}{\cos\phi}\left(\frac{I_1\mathbb{K}_3}{3}+\sqrt{J_2}\left(\mathbb{K}_1\cos\theta-\frac{\mathbb{K}_2\sin\theta\sin\phi}{\sqrt{3}}\right)\right) \tag{B.12}$$

being:

$$\mathbb{K}_1 = 0.5(1+\alpha_r) - 0.5(1-\alpha_r)\sin\phi \tag{B.13a}$$

$$\mathbb{K}_2 = 0.5(1+\alpha_r) - 0.5(1-\alpha_r)/\sin\phi \tag{B.13b}$$

$$\mathbb{K}_3 = 0.5(1+\alpha_r)\sin\phi - 0.5(1-\alpha_r) \tag{B.13c}$$

$$\alpha_r = \frac{f_c/f_t}{\tan\left(\pi/4+\phi/2\right)^2} \tag{B.13d}$$

Material threshold

$$\kappa = f_c \quad \text{(yield stress in compression)} \tag{B.14}$$

B.4 Circumscribed Drucker-Prager yield surface

This criterion formulated by Drucker and Prager in 1952 is considered as a smoothed approximation to the Mohr-Coulomb criterion. However, the mathematical formulation arises from a generalization of the Von Mises criterion to include the influence of pressure, through the first invariant of the stress tensor I_1 and the internal friction angle ϕ.

Uniaxial stress

$$\mathfrak{F}(\boldsymbol{\sigma}) = \left(\frac{-\sqrt{3}(3-\sin\phi)}{3\sin\phi-3}\right)\left(\frac{2I_1\sin\phi}{\sqrt{3}(3-\sin\phi)}+\sqrt{J_2}\right) \tag{B.15}$$

Material threshold

$$\kappa = f_t\left(\frac{3+\sin\phi}{3\sin\phi-3}\right) \tag{B.16}$$

B.5 Rankine yield surface

This criterion was formulated by Rankine in 1876 and is based on one single parameter, the maximum uni-axial tension strength f_t. Additionally, it is influenced by the first invariant of the stress tensor I_1 and by the second and third invariants of the deviatoric stress tensor J_2 , J_3 , respectively. This criterion helps to set in the limits in a simple way where the fracturing process starts in a point of a solid. This hypothesis leads to the assumption that fractures occur when the maximum main stress reaches the value of the uni-axial tension strength f_t.

Uniaxial stress

$$\mathfrak{F}(\boldsymbol{\sigma}) = \max(\sigma_I, \sigma_{II}, \sigma_{III}) \tag{B.17}$$

As a function of the invariants of the stress tensor and its deviatoric stress tensors:

$$\mathfrak{F}(I_1, J_2, \theta, f_t) = 2\sqrt{3J_2}\cos(\theta+\pi/6) + I_1 - 3f_t = 0 \tag{B.18}$$

where θ is the Lode's similarity angle $\theta = \operatorname{asin}\left(\frac{3\sqrt{3}J_3}{2J_2^{3/2}}\right)$.

Material threshold

$$\kappa = f_t \tag{B.19}$$

B.6 Simo-Ju yield surface

This yield surface was initially proposed by Simo and Ju in [SJ87] for strain based isotropic damage models. This criterion computes the energy norm of the strain, which was especially useful since this formulation lead to a symmetric elastic-damage moduli.

Uniaxial stress

$$\mathfrak{F}(\boldsymbol{\sigma}) = (r + n(1 - r))\sqrt{\varepsilon : \mathcal{C}_0 : \varepsilon} \tag{B.20}$$

where r can be computed according to Eq. (14.7) and n is the ratio between the compressive and tensile yield strengths.

Material threshold

$$\kappa = \frac{f_c}{\sqrt{E}} \tag{B.21}$$

B.7 Huber-Von-Mises yield surface

This criterion was formulated by Von Mises in 1913, and like the two former, depends only on one single parameter, the maximum octahedral shear strength τ_{oct}^{max}. Moreover, it only considers the second invariant of the stress deviatoric tensor J_2, neglecting hence the influence of the first invariant of the stress tensor I_1 and the third invariant of the stress deviatoric tensor J_3.

Uniaxial stress

$$\mathfrak{F}(\boldsymbol{\sigma}) = \sqrt{3\mathrm{J}_2} \tag{B.22}$$

Material threshold

$$\kappa = f_t \tag{B.23}$$

B.8 Tresca yield surface

This criterion was formulated by Tresca in 1864. Similarly to Rankine criterion, it also depends on one single parameter which is the maximum tangent strength f_t. Moreover, it considers the second and third invariants of the deviatoric stress tensor J_2 , J_3 , respectively, neglecting the influence of the first invariant of the stress tensor I_1.

Uniaxial stress

$$\mathfrak{F}(\boldsymbol{\sigma}) = 2\cos\theta\sqrt{\mathrm{J}_2} \tag{B.24}$$

Material threshold

$$\kappa = f_t \tag{B.25}$$

Appendix C

Tangent operator numerical derivation

The FEM solution is solved via an implicit transient dynamic solution scheme. Thus, the tangent constitutive matrix is required at each iteration of the loading step. For this purpose, several numerical techniques have been developed and adapted to the FEM-DEM formulation. The implementation of this procedure can be seen in tangent_operator_calculator_utility.h. Must be clarified that this procedure is only called when the formulation is in loading conditions. If the external forces induces unloading conditions, a secant type (damage) or elastic (plasticity) constitutive tensor must be used.

The most robust but slower option (linear rate of convergence) is to use the secant constitutive tensor $\mathcal{C}_s$, computed as a function of the initial constitutive tensor $\mathcal{C}_0$ and the damage d:

$$\mathcal{C}_s = (1 - d)\mathcal{C}_0 \tag{C.1}$$

Another alternative is based on the derivatives approximation via finite differences, i.e. the tangent constitutive tensor relationship can be expressed as $\dot{\boldsymbol{\sigma}} = \mathcal{C}_T : \dot{\boldsymbol{\varepsilon}}$. A column of the tangent constitutive tensor $\mathcal{C}_T$ is defined as [MOB11; Cor+19]:

$$\mathcal{C}_{T,j} = \frac{\delta^j \boldsymbol{\sigma}}{\delta \varepsilon_j} \tag{C.2}$$

An approximation of the tangent constitutive tensor can be obtained by defining n small perturbations of the strain tensor $\delta\varepsilon_j$ in order to obtain n stress tensor increments $\delta^j\boldsymbol{\sigma}$. This can be done in several ways, as stated below (depending on the finite difference scheme):

$$\boldsymbol{\mathcal{C}}_{T,j} \simeq \frac{\boldsymbol{\sigma}(\boldsymbol{\varepsilon} + \boldsymbol{\delta\varepsilon_j}) - \boldsymbol{\sigma}(\boldsymbol{\varepsilon})}{\delta\varepsilon_j} \quad ; \quad \boldsymbol{\mathcal{C}}_{T,j} \simeq \frac{\boldsymbol{\sigma}(\boldsymbol{\varepsilon} + \boldsymbol{\delta\varepsilon_j}) - \boldsymbol{\sigma}(\boldsymbol{\varepsilon} - \boldsymbol{\delta\varepsilon_j})}{2\delta\varepsilon_j} \tag{C.3}$$

where $\boldsymbol{\delta\varepsilon_j}$ is a zero vector except for the jth component whose value is the strain perturbation $\delta\varepsilon_j$. In the case of the FEM-DEM methodology, once the Gauss point perturbation of the strain has been done, one must reproduce the smoothing of the effective stress field as it is done in Alg. 3 and compute the damage of the perturbed strain field and, in this way, obtaining the corresponding column of the tangent tensor, according to Eq. (C.3). In the case of finite strains, the strain is no longer perturbed, but the deformation gradient tensor **F** is the one affected.

In order to compute the strain perturbation $\delta\varepsilon_j$, at each strain component j, one must verify the following conditions:

$$\text{if } \varepsilon_j \neq 0 \Rightarrow \delta\varepsilon_j = 10^{-5}\varepsilon_j \tag{C.4a}$$

$$\text{else } \Rightarrow \delta\varepsilon_j = \min\left(|\varepsilon_k|\right)10^{-5} \quad \forall k = 1, n \; ; \; \varepsilon_k \neq 0 \tag{C.4b}$$

With this procedure, it is ensured that the perturbation used is always small enough to produce a slight variation of the stress tensor. It is true that the procedure described in Eqs. C.4 can lead to a quasi-zero perturbation in some cases, this is why a final check must be added:

$$\delta\varepsilon_j > \max(\varepsilon_k)10^{-10} \quad \forall k = 1, n \tag{C.5}$$

By means of the indicated procedure one can obtain a good approximation of the tangent constitutive tensor. In addition, this is one of the the main advantages of the proposed method, this calculation is independent of the constitutive equation used for the material.

The most general option consists in perturbing the displacement field of the FEM solution [LP02]. This method is appropriate for small and large strain computations (the strain perturbation method is limited to small strains) and for any kind of constitutive model. In this way, the approximation of the tangent stiffness matrix can be computed as:

$$\mathbf{K}_{T,j} \simeq \frac{\mathbf{F}_{\text{int}}(\mathbf{u}^{n,i} + \epsilon \boldsymbol{\Delta}\mathbf{u}^n) - \mathbf{F}_{\text{int}}(\mathbf{u}^{n,i})}{\epsilon \Delta u^n} \tag{C.6}$$

Where $\mathbf{K}_{T,j}$ is the jth column of the tangent stiffness matrix, $\boldsymbol{\Delta}\mathbf{u}^n$ is the displacement increment of that node in the previous time step, $\mathbf{F}_{int}$ is the internal force vector that depends of the displacement field and ϵ is a small constant computed as:

$$\epsilon = \sqrt{\varkappa} \left(1 + \frac{\left\| \mathbf{u}^{n,i-1} \right\|}{\left\| \boldsymbol{\Delta}\mathbf{u}^{n,i-1} \right\|} \right) \tag{C.7}$$

being $\varkappa$ the computer precision. Note that the components of the vector $\boldsymbol{\Delta}\mathbf{u}^n$ are null except for the jth component whose value is Δu^n.

C.0.1 Minimal example

In this case we have analysed a plate (in 2D) with a circular void in the middle of it. The left edge is clamped and in the right one an increasing horizontal displacement is imposed. In Fig. C.1 the FE mesh used is depicted.

As can be analysed in Fig. C.2, for a certain time step in which the damage is occurring, the tangent tensor obtained via perturbation method (T1 and T2) achieves an average slope close to the expected quadratic behaviour whereas the classical secant tensor reduces linearly with the number of iterations performed.

It is true that, due to the smoothing of stresses, the performance of the perturbation method proposed is not optimal. The author of this work has implemented this procedure by using standard non-linear constitutive models and the quadratic convergence is achieved consistently (j2 plasticity, isotropic damage, visco-elasticity, etc...).

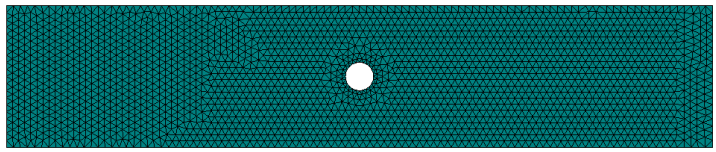

Figure C.1: FE mesh used for the tensile test

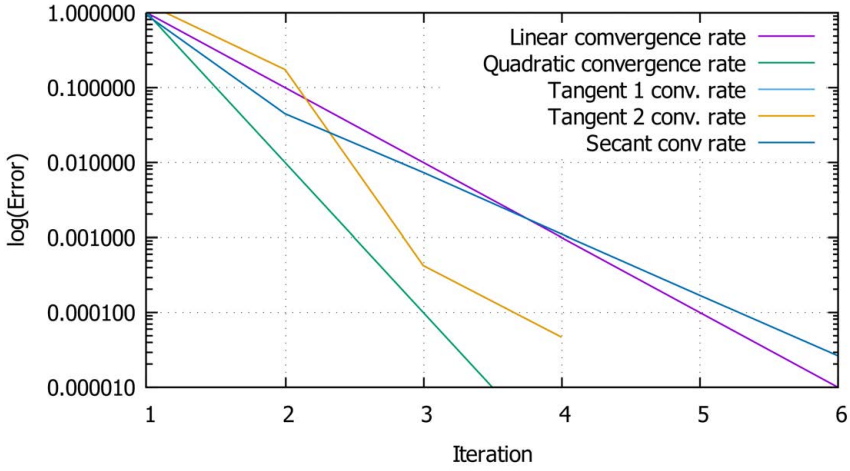

Figure C.2: Log(Error)-Iteration plot for different tangent tensor estimations

Appendix D

Contact model used: particle-particle or particle-wall

Contact between particles (DE) as well as contact between particles and solid FE walls is a problem of considerable difficulty since it depends on the shape of the particles, their material properties, relative kinematics between the bodies, etc.

Although according to Johnson [Joh87] the contact forces between two bodies can be calculated theoretically from their deformation over the contact time, within the DEM, we usually use approximations of it through various calibration parameters such as relative velocity, indentation, radius, Young's modulus, Poisson ratio and some others that represent the energy dissipation occurred during contact.

As explained in Part III, the contact model used within the FEM-DEM methodology can be either a contact model between particles or between particles and FE walls (see Fig. D.2). Since the details of the contact are not relevant -at least its micro effect on the particle- a linear contact law is usually used as a penalty technique, calibrated as a trade-off between calculation time (time step size) and admissible indentation.

Since the contact law between particles can be found in Section 10.3, only the particle-wall contact model is here exposed (see Fig. D.1). The particle-wall contact model used in the FEM-DEM is based on the work of Santasusana [San16].

In this case, since the tangential displacement of the wall is negligible in compari-

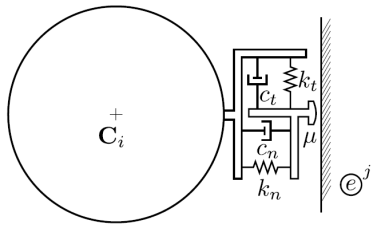

Figure D.1: Particle-FE wall contact rheology. Source: Santasusana [San16]

son with the exhibit by the particle, one can adopt the following simplifications:

$$R_{eq} = R_i \tag{D.1a}$$
$$m_{eq} = m_i \tag{D.1b}$$
$$E^*_{eq} = ((1 - \nu_i^2)/E_i + (1 - \nu_j^2)/E_j)^{-1} \tag{D.1c}$$
$$G^*_{eq} = G_i/(2 - \nu_i). \tag{D.1d}$$

If one introduces this modified parameters in Eqs. (10.15)-(10.21) can obtain the contact forces for the particle-wall contact model.

In general cases, it is always more accurate and consistent to use particle-wall contact. Indeed, the apparent gap is reduced by half, making the contact more accurate in all cases. Additionally, the contact surfaces are smooth and avoid the artificial locking between particles so characteristic of conventional particle contact. As can be seen in Fig. D.2, the contact between particles estimates contact forces whose directions are dependent on the line connecting the two centres. This implies that the directions of the forces are very dependent on the disposition of the particles on the surface of the solid. This is solved in the case of using the particle-wall model.

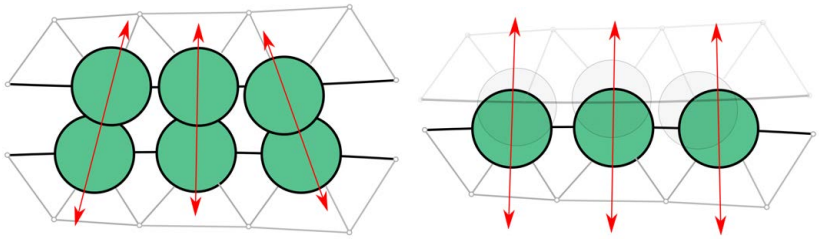

(a) DE-DE contact (b) DE-FE contact

Figure D.2: Different contact calculations within the FEM-DEM formulations

Appendix E

Finite element code Kratos-Multiphysics

All the implementations conducted and the external applications used have been included inside the open-source FEM code Kratos-Multiphysics (https://github.com/KratosMultiphysics/Kratos) [DRO10].

KRATOS Multiphysics ("Kratos") is a framework for building parallel, multi-disciplinary simulation software, aiming at modularity, extensibility, and high performance, under a BSD license. Kratos is written in C++, and counts with an extensive Python interface. CIMNE is one of the main contributors to this project, among others.

Kratos is a framework for building multi-disciplinary finite element programs. It provides several tools for easy implementation of finite element applications and a common platform providing effortless interaction between them. Kratos has an innovative variable base interface designed to be used at different levels of abstraction and implemented to be very clear and extendible. It also provides an efficient yet flexible data structure which can be used to store any type of data in a type-safe manner. The Python (see https://www.python.org) scripting language is used to define the main procedure of Kratos which significantly improves the flexibility of the framework in time of use.

The kernel and application approach is used to reduce the possible conflicts arising between developers of different fields. Also layers are designed to reflect the working

space of different people, considering their programming knowledge.

Kratos is Parallelized for Shared Memory Machines (SMM) and Distributed Memory Machines (DMM). In the same way it provides tools for its applications to adapt easily their algorithms to these architectures. Its scalability has been verified up to thousands of cores.

Figure E.1: Kratos Multiphysics logo (https://github.com/KratosMultiphysics/Kratos)

E.1 Who may use Kratos

Some potential users of Kratos are:

- **Finite Element Developers:** These developers are considered to be more expert in FEM, from the physical and mathematical points of view, than C++ programming. For this reason, Kratos provides their requirements without involving them in advanced programming concepts.

- **Application Developers:** These users are less interested in finite element programming and their programming knowledge may vary from very expert to higher than basic. They may use not only Kratos itself but also any other applications provided by finite element developers, or other application developers. Developers of optimization programs or design tools are the typical users of this kind.

- **Package Users Engineers:** and designers are other users of Kratos. They use the complete package of Kratos and its applications to model and solve their problem without getting involved in internal programming of this package. For these users Kratos has to provide a flexible external interface to enable them use different features of Kratos without changing its implementation.

E.2 Who is Kratos

The Kratos structure, due to its multi disciplinary nature, has to support the wide variety of algorithms involved in different areas. That's the principal reason that explain the variety of people, mostly engineers, composing the Kratos Community.

E.3 Keywords

Kratos is **MULTI-PHYSIC**. One of the main topics in engineering nowadays is the combination of different analysis (thermal, fluid dynamic, structural) with optimising methods in one global software package with just one user interface and, even more, the possibility to extend the implemented solution to new problems.

Kratos is **FINITE ELEMENT METHOD** based. Many problems in engineering and applied science are governed by Partial Differential Equations (PDE), easily handled by computer thanks to numerical methods. The FEM is one of the most powerful, flexible and versatile existing methods.

Kratos is **OBJECT ORIENTED**. An integration of disciplines, in the physical as well as in the mathematical sense, suggests the use of the modern object oriented philosophy from the computational point of view. The modular design, hierarchy and abstraction of these approaches fits to the generality, flexibility and re-usability required for the current and future challenges in numerical methods.

Kratos is **OPEN SOURCE**. The main code and program structure is available and aimed to grow with the need of any user willing to expand it. The BSD (Berkeley Software Distribution) licence allows to use and distribute the existing code without any restriction, but with the possibility to develop new parts of the code on an open or close basis depending on the developers.

Kratos is **FREE** because is devoted mainly to developers, researchers and students and, therefore, is the most fruitful way to share knowledge and built a robust numerical methods laboratory adapted to their users' needs. Free because you have the freedom to modify and distribute the software. The one thing you're not able to do with free software is take away other people's freedom. Please, read the license for more detailed information.

E.4 Interaction between applications regarding the FEM-DEM algorithm

In order to use the FemToDemApplication methodology, some other complementary applications must be compiled in order to be used afterwards. As can be see in Fig. E.2, the FemToDemApplication depends on the Discrete Element Method (DEM) methodology (DEMApplication), the remeshing operations (MeshingApplication), the Particle Finite Element Method (PFEM) algorithm (PFEMFluidDynamicsApp) and the solid mechanics part (SolidMechanicsApp).

The FemToDemApplication application includes all the operations used in the FEM-DEM method proposed. The damage Constitutive Law (CL), the smoothing of the stress field, the yield surfaces implemented (see Appendix B), the small displacement and the total Lagrangian FE, the blast load extrapolation for explosions, automatic generation of DE during calculation, the inclusion of the remeshing technique (recursive call of the MeshingApplication), the transference of the DE contact forces to the FEM, etc. are included in this app.

The DEMApplication includes all the operations and utilities used for the DEM. The explicit solution scheme, the particles kinematics, the contact search and the contact force estimation is performed by using this application.

The MeshingApplication takes the current FE mesh and, according to the Hessian (utility inside this application) of a certain nodal value, it generates a new mesh from scratch. Next, all the nodal and Integration Points (IP) information is mapped to the new mesh.

The PFEMFluidDynamicsApp includes all the implementations used for the Particle Finite Element Method (PFEM). The remeshing of the geometry, the Delaunay triangulation and the formulation shown in Chapter 17 is included here.

The SolidMechanicsApp includes all the operations used for the basic solid mechanics operations such as the elastic constitutive laws, the basic small strain and total Lagrangian elements and all the load conditions required for solving any kind of problem.

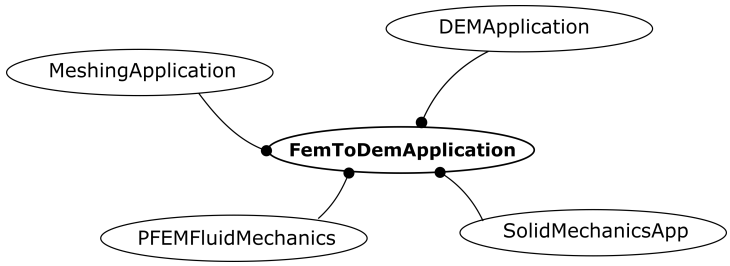

Figure E.2: Kratos Applications involved in the implementations performed

E.5 Transversal developments and implementations

Together with the development of the formulations presented in this work, numerous works have been conducted which, in one way or another, have had a very positive influence on the knowledge related to fracture mechanics and the constitutive modelling of materials.

The most relevant implementation performed, with the collaboration of Dr. Vicente Mataix and Dr. Riccardo Rossi, has been the elaboration of a **object oriented modular library** of constitutive laws for solids within the framework of *Kratos-Multiphysics* GitHub Website of Kratos inside the `StructuralMechanicsApp`. A review of the CL library can be found here.

The implemented CL within the `StructuralMechanicsApp` can be categorized in:

1. **Isotropic Elasticity**
2. **Hyper-elasticity**
3. **Associative and Non-Associative Isotropic Plasticity**
4. **Associative and Non-Associative Kinematic Plasticity and Combined Isotropic-Kinematic Plasticity**
5. **Isotropic Damage**
6. **Viscoelasticity**

7. **Viscoplasticity**

8. **d+d- Damage Model**

9. **Classical Rule of Mixtures (RoM) and Serial Parallel Rule of Mixtures (SPRoM) for composite materials**

10. **Generic Anisotropic CL formulation**

As can be seen in Fig. E.3, inside the `custom_advanced_constitutive` folder we can find three subfolders and the whole list of CL available. The `constitutive_law_i` are objects that effectively integrate the stress according to a certain CL rules. In this case, each CL storages its own internal variables, *i.e.* the damage in isotropic damage or plastic strain in plasticity, whereas the *integrator* returns the integrated stress without any memory consumption.

Next, one can see the `plastic_potentials` folder. These objects are mainly used in plasticity CL's in order to compute the plastic flow according to a certain plastic surface. The available plastic potential surfaces are: Circumscrived Drucker-Prager, Modified Mohr-Coulomb [Oll02], Mohr-Coulomb, Tresca and Von-Mises, .

Finally, there is the `yield_surfaces` folder, which contains all the yield criteria implemented to be used in damage, plasticity, viscoplasticity, etc. The available yield surfaces are: Circumscrived Drucker-Prager, Modified Mohr-Coulomb [Oll02], Rankine, Simo-Ju, Mohr-Coulomb, Tresca and Von-Mises.

E.5.1 Isotropic elasticity

Isotropic materials require two material parameters only, the Young modulus E and the Poisson's ratio ν. The constitutive matrix for isotropic materials can be directly written in global Cartesian axes. If initial strains and stresses are taken into account we can write

$$\boldsymbol{\sigma} = \mathcal{C}_0(\varepsilon - \varepsilon^0) + \boldsymbol{\sigma}^0 \tag{E.1}$$

where the isotropic constitutive matrix $\mathcal{C}_0$ is given by

$$\mathcal{C}_0 = \Xi \begin{bmatrix} 1 & \frac{\nu}{1-\nu} & \frac{\nu}{1-\nu} & 0 & 0 & 0 \\ & 1 & \frac{\nu}{1-\nu} & 0 & 0 & 0 \\ & & 1 & 0 & 0 & 0 \\ & & & \frac{1-2\nu}{2(1-\nu)} & 0 & 0 \\ & & & & \frac{1-2\nu}{2(1-\nu)} & 0 \\ & & \textit{Symmetrical} & & & \frac{1-2\nu}{2(1-\nu)} \end{bmatrix} \tag{E.2}$$

where $\Xi = \dfrac{E(1-\nu)}{(1+\nu)(1-2\nu)}$.

The initial strain vector due to thermal strains is, depending on the temperature increment ΔT and the expansion coefficient α:

$$\varepsilon^0 = \alpha(\Delta T)[1,1,1,0,0,0]^T. \tag{E.3}$$

The procedure is analogous with the 2D and axisymmetric case. The class definition of this CL inside *Kratos* is performed as shown in code E.5.1.

```
class KRATOS_API(STRUCTURAL_MECHANICS_APPLICATION) ElasticIsotropic3D
: public ConstitutiveLaw
{
    [...]
}
```

Listing E.1: Constructor of the ElasticIsotropic3D class inside elastic_isotropic_3d.h

E.5.2 Hyper-elasticity

Hyper-elastic or *Green* elastic materials such as elastomers, polymers, biological tissues, rubber, etc. have the capability of exhibit large deformations without any

internal energy dissipation. It is commonly said that these kind of materials have no memory -contrary to the usual non-linear damage, plasticity and other path-dependent CL-. This means that the strains and stresses are only dependent on the current state of the main variables. The Hyper-elastic CL currently available in *Kratos* are the Kirchoff and the Neo-Hookean laws.

Many engineering applications involve small strains and large rotations. In these problems the effects of large deformation are primarily due to rotations (such as in the bending of a marine riser or a fishing rod). The response of the material may then be modelled by a simple extension of the linear elastic laws by replacing the stress by the second Piola-Kirchoff stress **S** and the linear strain by the Green-Lagrange strain **E**. This is called a Saint Venant Kirchhoff material, or a Kirchhoff material for brevity. The most general Kirchhoff model is:

$$\mathbf{S} = \mathcal{C} : \mathbf{E}. \tag{E.4}$$

The definition of the constitutive tensor $\mathcal{C}$ is:

$$\mathcal{C} = \lambda \mathbf{I} \otimes \mathbf{I} + 2\mu \mathbf{I}. \tag{E.5}$$

being λ and μ the lamé constants (see Eq. (6.27)).

On the other hand, for the Neo-Hookean hyper-elastic law, the second Piola-Kirchoff stress tensor can be obtained by:

$$\mathbf{S} = \lambda \ln(J)\mathbf{I} + \mu(\mathbf{I} - \mathbf{C}^{-1}). \tag{E.6}$$

and the constitutive tensor $\mathcal{C}$ can be computed as:

$$\mathcal{C}_{ijkl} = \lambda C_{ij}^{-1} C_{kl}^{-1} + \mu \left(C_{ik}^{-1} C_{jl}^{-1} + C_{il}^{-1} C_{kj}^{-1} \right), \tag{E.7}$$

being **C** the left Cauchy-Green tensor. Both classes are implemented in *Kratos* as can be seen in code E.5.2 and E.5.2.

```
class KRATOS_API(STRUCTURAL_MECHANICS_APPLICATION)
    HyperElasticIsotropicKirchhoff3D
: public ConstitutiveLaw
{
    [...]
}
```

Listing E.2: Constructor of the HyperElasticIsotropicKirchhoff3D class inside hyper_elastic_isotropic_kirchhoff_3d.h

```
class KRATOS_API(STRUCTURAL_MECHANICS_APPLICATION)
    HyperElasticIsotropicNeoHookean3D
: public ConstitutiveLaw
{
    [...]
}
```

Listing E.3: Constructor of the HyperElasticIsotropicNeoHookean3D class inside hyper_elastic_isotropic_neo_hookean_3d.h

E.5.3 Non-associative isotropic plasticity

One of the most challenging implementations has been the modular non-associative isotropic plasticity. We will focus on the small strain implementation that has been extended to finite strains by Dr Vicente Mataix. The theoretical description of the implemented models can be found in Barbu et al. [Bar15].

The theory of plasticity is concerned with solids that, after being subjected to a loading programme, may sustain permanent (or plastic) deformations when completely unloaded. In particular, this theory is restricted to the description of materials (and conditions) for which the permanent deformations do not depend on the rate of application of loads and is often referred to as rate-independent plasticity.

Usually, the phenomenological plasticity models (see Souza et al. [SPO08], Hill et al. [Hil71; Hil48] and Mauguin [Mau92]) usually require to storage several internal variables that define the path dependant behaviour. Additionally, it is required to define a yield criterion in order to differentiate the elastic and the inelastic domains. Finally, a plastic potential surface is required for computing the plastic flow, which will determine the development of plastic strains.

This is why we have adopted a modular object oriented design in which we declare the plasticity CL with several levels of *templating*. In code E.5.3 one can see how the `TConstLawIntegratorType` is templated inside the `GenericSmallStrainIsotropicPl` class. This is done in order to allow the new developers to implement different *return mapping* procedures different to the already existing Backward Euler.

```
template <class TConstLawIntegratorType>
class KRATOS_API(STRUCTURAL_MECHANICS_APPLICATION)
    GenericSmallStrainIsotropicPlasticity
: public std::conditional<TConstLawIntegratorType::VoigtSize == 6,
    ElasticIsotropic3D, LinearPlaneStrain >::type
{
    [...]
}
```

Listing E.4: Constructor of the GenericSmallStrainIsotropicPlasticity class inside generic_small_strain_isotropic_plasticity.h

Additionally, within the generic_constitutive_law_integrator_plasticity.h object (see code E.5.3), which is the `constitutive_law_integrator` used for the non-associative isotropic plasticity CL, one can see that the `TYieldSurfaceType` is the templated object. This means that the implementation of the integrator is generic for all the yield surfaces defined in the previous paragraphs.

```
template<class TYieldSurfaceType>
class GenericConstitutiveLawIntegratorPlasticity
{
    [...]
}
```

Listing E.5: Constructor of the GenericConstitutiveLawIntegratorPlasticity class inside generic_constitutive_law_integrator_plasticity.h

If we select one arbitrary yield surface object, Von-Mises criterion for example, one can see that now the `TPlasticPotentialType` is the templated class. This means that for any given yield surface, a different -or equal- plastic potential surface can be defined, which is the definition of a non-associative plasticity. for example, one can define an isotropic plasticity using the Von-Mises criterion as a yield surface

but a Mohr-Coulomb plastic potential without affecting the implementation performed, thanks to the modular templated design.

```
template <class TPlasticPotentialType>
class VonMisesYieldSurface
{
    [...]
}
```

Listing E.6: Constructor of the VonMisesYieldSurface class inside von_mises_yield_surface.h

Finally, if we have a look to the implementation of the `mohr_coulomb_plastic_potential` (see code E.5.3), one can notice that only the `TVoigtSize` is templated. This is used only for defining whether the problem is conducted in 2D or in 3D.

```
template <SizeType TVoigtSize = 6>
class MohrCoulombPlasticPotential
{
    [...]
}
```

Listing E.7: Constructor of the MohrCoulombPlasticPotential class inside mohr_coulomb_plastic_potential.h

Additionally, several flow rules have been implemented inside the `generic_constitutive_` that controls the evolution of the uniaxial stress threshold that defines the elastic domain. Currently, the user can select to apply linear softening, exponential softening, parabolic hardening and posterior softening, perfect plasticity and curve fitting hardening. Code E.5.3 depicts a typical input data for the constitutive model in which one can see how the yield surface and the plastic potential are defined and, automatically, the FE code builds the correct non-associative CL for the simulation.

```
enum class HardeningCurveType
{
    LinearSoftening = 0,
    ExponentialSoftening = 1,
    InitialHardeningExponentialSoftening = 2,
```

```
    PerfectPlasticity = 3,
    CurveFittingHardening = 4
};
```

Listing E.8: enum definition for selecting one of the different flow rules inside generic_constitutive_law_integrator_plasticity.h

```
{
    "model_part_name" : "SolidBody",
    "properties_id"   : 1,
    "Material"        : {
    "constitutive_law" : {
        "name" : "SmallStrainIsotropicPlasticityFactory3D",
        "yield_surface" :  "VonMises",
        "plastic_potential" : "MohrCoulomb"
    },
    "Variables"        : {
        "DENSITY"       : 7850.0,
        "YOUNG_MODULUS" : 206900000000.0,
        "POISSON_RATIO" : 0.29,
        "YIELD_STRESS_TENSION" : 275e6,
        "YIELD_STRESS_COMPRESSION" : 275e6,
        "FRACTURE_ENERGY" : 1.0e5,
        "HARDENING_CURVE" : 1
    }
    }
}
```

Listing E.9: Example of an input data file for isotropic plasticity

E.5.4 Non-associative combined isotropic kinematic plasticity

The same class structure and templating system shown for the isotropic plasticity is the used for the combined isotropic kinematic plasticity (see generic_small_strain_kinematic_plasticity.h). the only difference is the fact that a different constitutive law integrator is used: generic_constitutive_law_integrator_plasticity.h. For the kinematic hardening, three diferent hardening rules have been implemented (see code E.5.4): linear hardening, Armstrong Frederick and Araujo Voyiadjis kinematic hardening. The theoretical description of the implemented models can be found in Barbu et al. [Bar15].

```
enum class KinematicHardeningType
{
    LinearKinematicHardening = 0,
    AmstrongFrederickKinematicHardening = 1,
    AraujoVoyiadjisKinematicHardening = 2
};
```

Listing E.10: enum definition for selecting one of the different flow rules inside generic_constitutive_law_integrator_plasticity.h

E.5.5 Small strain isotropic damage

Continuum damage mechanics is a branch of continuum mechanics that describes the progressive loss of material integrity due to the propagation and coalescence of micro-cracks, micro-voids, and similar defects. These changes in the microstructure lead to an irreversible material degradation, characterized by a loss of stiffness that can be observed on the macro-scale. The implemented formulation can be found in this work in Section 7.1.

The structure of the damage constitutive law is analogous to the plasticity case. Indeed, the damage constitutive law generic_small_strain_isotropic_damage.h has a template of an damage integrator (generic_constitutive_law_integrator_damage.h) that calculates the damage internal variable and computes the integrated or real stress according to the degradation of the material. This damage CL uses the yield surfaces previously described in an identical way as the plasticity.

E.5.6 Visco-elasticity

One of the behaviours responsible for the non-linearity in the materials response over the time field is due to viscoelasticity. Viscoelasticity studies the rheological behaviour of materials, in other words, behaviours affected by the course of time.

Up to now, we have developed two viscous models [Oll02]: the Generalized Maxwell model (used to simulate the stress relaxation of materials) and the Generalized Kelvin model (used to simulate creep and delayed strains).

The Generalized Maxwell model [Oll02] can be found in viscous_generalized_maxwell.h. The implementation details can be found in Cornejo et al. [Cor+18] and in Oller [Oll02]. The one-dimensional spring-damper analogy is depicted in Fig. E.4. Additionally, the

general behaviour of the model can be seen in Fig. E.5. Indeed, if a constant strain is applied to a material, a relaxation of the resulting initial stress is expected.

As far as the Generalized Kelvin model is concerned, one can find the implementation in viscous_generalized_kelvin.h. As for the Generalized Maxwell model, the mathematical derivation and expressions can be found in Oller [Oll02]. The one-dimensional spring-damper analogy is depicted in Fig. E.6 and its schematic behaviour is shown in Fig. E.7. In this case, if this material is submitted to a constant stress along time, a certain quantity of delayed strains will appear, simulating for example the creep phenomenon in concrete.

E.5.7 Visco-plasticity

This model is a generalization of an elastoplastic model including the viscosity parameter, ξ, which makes the model sensitive to time. Figure E.8 exemplifies the model response for the $1D$ case through a spring-damping analogy. The implementation can be found in generic_small_strain_viscoplasticity_3d.h.

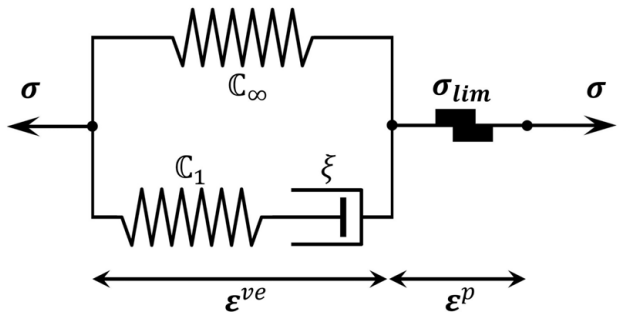

Figure E.8: Viscoplastic model representation through a spring-damping analogy.

At each point, the total strain, ε, is computed as

$$\varepsilon = \varepsilon^{ve} + \varepsilon^{p} \tag{E.8}$$

where ε^{ve} and $\varepsilon^{\boldsymbol{p}}$ are the visco-elastic and plastic strain components, respectively. The elastic response of the material is represented in Figure E.8 through a set of springs and a damper. On one hand, the springs are characterized by the constitutive tensor: $\mathbb{C}_1$ for the short-term and $\mathbb{C}_\infty$ for the long-term behaviour and, on the other hand, the viscous damper is controlled through the variable ξ that allows the stress

relaxation of the material. Finally, the plastic behaviour is controlled by a frictional device that activates once the stress level reaches a certain limit, σ_{lim}.

This visco-elasto-plastic constitutive law can be seen as a staggered procedure in which, at the beginning of each strain increment, the stress relaxation occurs via a Generalized Maxwell model [Cor+18; Oll02] (visco-elastic behaviour) and, if the relaxed predictor stress-state lies outside a certain yield surface, an isotropic plasticity constitutive law performs the return mapping of the stress predictor, locating the integrated stress state on the yield surface.

This methodology allows to simulate the relaxation of the material whether or not it has entered into a plastic regime, which is the general case of the prestressing steel.

E.5.8 d+d- damage model

In this case, we implemented a more sophisticated damage model that differentiates the behaviour of the material depending on the sign of the stresses. In other words, the damage behaviour is different in compression and in tension. This is done by performing an spectral decomposition of the stress tensor (see constitutive_law_utilities.h) in which we separate the tension/compression states [CT17].

Once we have decomposed the stress tensor we proceed to the calculation of the damage variables (now d^+ and d^- corresponding to the tension/compression states) and compute the integrated stress tensor as:

$$\boldsymbol{\sigma} = (1 - d^+)\bar{\boldsymbol{\sigma}}^+ + (1 - d^-)\bar{\boldsymbol{\sigma}}^- \tag{E.9}$$

In order to guarantee flexibility, we have designed an structure capable of combining different yield surfaces in tension and in compression. This has been achieved by templating two integrators named `TConstLawIntegratorTensionType` and `TConstLawIntegratorCompressionType` which define the tension/compression yield surfaces and flow rules. The implementation of this CL can be found in generic_small_strain_d_plus_d_minus_damage.h and in code E.5.8.

```
1 template <class TConstLawIntegratorTensionType, class
      TConstLawIntegratorCompressionType>
```

```
class KRATOS_API(STRUCTURAL_MECHANICS_APPLICATION)
    GenericSmallStrainDplusDminusDamage
: public std::conditional<TConstLawIntegratorTensionType::VoigtSize ==
    6, ElasticIsotropic3D, LinearPlaneStrain >::type
{
    [...]
}
```

Listing E.11: Constructor of the GenericSmallStrainDplusDminusDamage class inside generic_small_strain_d_plus_d_minus_damage.h

E.5.9 Classical Rule of Mixtures (RoM) and Serial Parallel Rule of Mixtures (SPRoM) for composite materials

The implementations made for the analysis of composite materials can be found in rule_of_mixtures_law.h for the classical Rule of Mixtures (RoM) and in serial_parallel_rule_of_mixtures_law.h for the more sophisticated Serial Parallel Rule of Mixtures (SPRoM). The formulation implemented can be reviewed in Chapter 9 and in Cornejo et al. [Cor+18], Barbu et al. [Bar+19], Oller [Oll03] and in Jiménez et al. [JBO18].

As can be seen in codes E.5.9 and E.5.9, in the given input files one can select the number of material components, its volumetric participation, the orientation of the layers (according to a set of Euler angles) and the constitutive law to be used in each material component. Regarding the constitutive laws for each component, one can select any of the CL described in this annex or even creating another nested composite material.

```
{
    "properties" : [{
        "model_part_name" : "Structure.Parts_Solid_Auto2",
        "properties_id"   : 1,
        "Material"        : {
            "constitutive_law" : {
                "name" : "SerialParallelRuleOfMixturesLaw",
                "combination_factors"          : [0.3, 0.7],
                "parallel_behaviour_directions" : [1,0,0,0,0,0]
        },
        "Variables" : {
            "LAYER_EULER_ANGLES": [0.0,0.0,0.0,0.0,0.0,0.0]
        }
        "sub_properties" : [{
```

```
            "properties_id"    : 10,
            "Material"         : {
            "constitutive_law" : {
                "name" : "LinearElastic3DLaw"
            },
            "Variables"        : {
                "DENSITY"       : 2000,
                "YOUNG_MODULUS" : 3.4e9,
                "POISSON_RATIO" : 0.38
            }
            }
        },{
        "properties_id"    : 11,
        "Material"         : {
            "constitutive_law" : {
                "name" : "LinearElastic3DLaw"
            },
            "Variables"        : {
                "DENSITY"       : 2000.0,
                "YOUNG_MODULUS" : 72.35e9,
                "POISSON_RATIO" : 0.22
            }
            }
        }]
    }
}
```

Listing E.12: Example of an input data file for the Serial/Parallel rule of mixtures. A simple example and the input data files can be found here.

```
{
    "properties" : [{
        "model_part_name" : "Main",
        "properties_id"    : 1,
        "Material"         : {
            "constitutive_law" : {
                "name" : "ParallelRuleOfMixturesLaw3D",
                "combination_factors"      : [0.4, 0.6 ]
            },
            "Variables"        : {
            },
            "Tables"           : {}
        },
        "sub_properties" : [{
```

```
            "properties_id"    : 11,
            "Material"         : {
                "constitutive_law" : {
                    "name" : "LinearElastic3DLaw"
                },
                "Variables"        : {
                    "DENSITY"       : 7850.0,
                    "YOUNG_MODULUS" : 206900000000.0,
                    "POISSON_RATIO" : 0.29
                },
                "Tables"           : {}
            }
        },{
            "properties_id"    : 12,
            "Material"         : {
                "constitutive_law" : {
                    "name" : "HyperElastic3DLaw"
                },
                "Variables"        : {
                    "DENSITY"       : 2000.0,
                    "YOUNG_MODULUS" : 30000000000.0,
                    "POISSON_RATIO" : 0.49
                },
                "Tables"           : {}
            }
        }]
    }]
}
```

Listing E.13: Example of an input data file for the Classical rule of mixtures. A simple example and the input data files can be found here.

E.5.10 Generic Anisotropic CL formulation

As has been described in detail in Chapter 8, the implemented *implicit general definition* developed by Oller et al. [Oll+93; Oll+95; Oll03] employs a bijective transformation between two spaces, namely *real anisotropic space* and *fictitious isotropic space*. This implies that it is not necessary to mathematically formulate an anisotropic criterion, but that this is defined in a conventional way in an isotropic space and to admit the existence of a numerical transformation that allows the exchange of information between both spaces. In this sense, the symmetric operators that allow the mapping of stresses ($\mathbf{A}^S$), deformations ($\mathbf{A}^E$) and internal variables from one space to another must be defined in detail, always guaranteeing the conditions of invariance.

The implementation can be studied in generic_anisotropic_3d_law.h. In code E.5.10 one can see how simple is to define an anisotropic material by only defining the ISOTROPIC_ANISOTROPIC_YIELD_RATIO variable that defines the ration between the base yield stregnth and the yield strength at each direction. Additionally, one can define the orthotropic elastic constants and the orientation of the local system of axes by filling the EULER_ANGLES vector.

```
{
    "properties" : [{
        "model_part_name" : "SolidBody",
        "properties_id"   : 1,
        "Material"        : {
            "constitutive_law" : {
                "name" : "GenericAnisotropic3DLaw"
            },
            "Variables"        : {
                "ORTHOTROPIC_ELASTIC_CONSTANTS" : [40e9, 10e9, 10e9,
    0.2, 0.2, 0.2],
                "EULER_ANGLES"     : [45,0,0],
                "ISOTROPIC_ANISOTROPIC_YIELD_RATIO"  :
    [2.0,0.667,0.667,1.0,1.0,1.0]
            }
        },
        "sub_properties" : [{
            "properties_id"   : 10,
            "Material"        : {
                "constitutive_law" : {
                    "name" : "
    SmallStrainIsotropicDamage3DVonMisesVonMises"
                },
                "Variables"        : {
                    "DENSITY"          : 2400.0,
                    "YOUNG_MODULUS"    : 40E9,
                    "POISSON_RATIO"    : 0.3,
                    "YIELD_STRESS"     : 0.8e7,
                    "FRACTURE_ENERGY"  : 100000,
                    "SOFTENING_TYPE"   : 1
                },
                "Tables"           : {}
            }
        }]
    }]
```

```
33 }
```

Listing E.14: Example of an input data file for the Generic anisotropic CL. A simple example and the input data files can be found here.

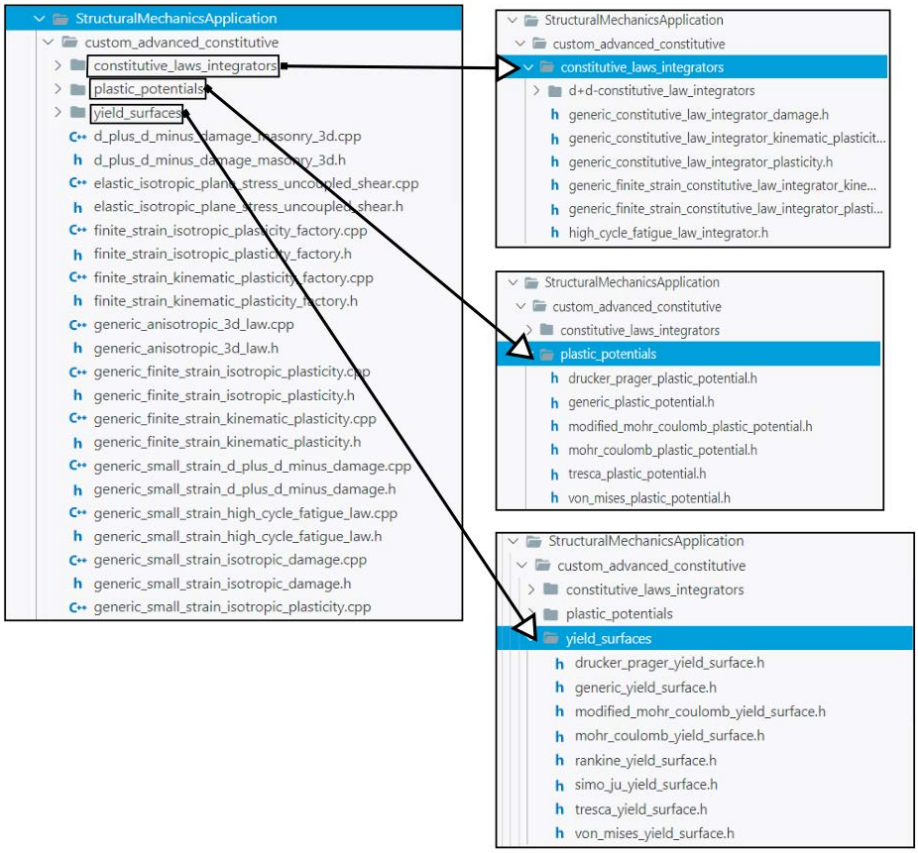

Figure E.3: Modular organization of the CL, yield surfaces, plastic potential and constitutive law integrators within the `StructuralMechanicsApp`.

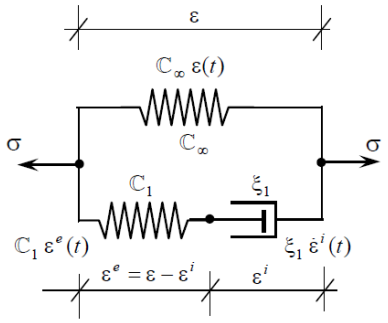

Figure E.4: Uniaxial spring-damper analogy of the Generalized Maxwell CL. Source: Oller [Oll02].

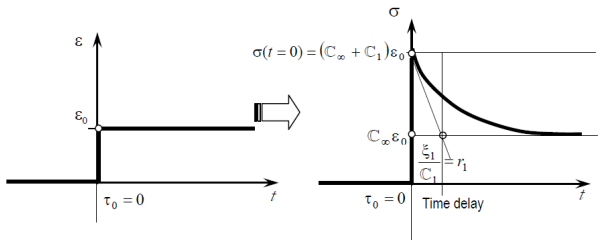

Figure E.5: Schematic behaviour of the Generalized Maxwell CL. Source: Oller [Oll02].

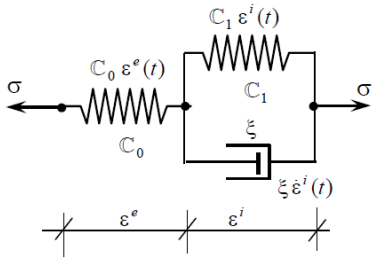

Figure E.6: Uniaxial spring-damper analogy of the Generalized Kelvin CL. Source: Oller [Oll02].

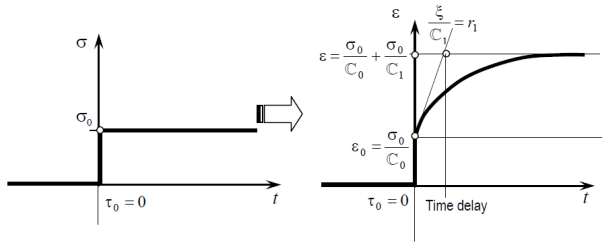

Figure E.7: Schematic behaviour of the Generalized Kelvin CL. Source: Oller [Oll02].

Appendices bibliography

[Bar+19] LG. Barbu et al. “Methodology for the analysis of post-tensioned structures using a constitutive serial-parallel rule of mixtures: large scale non-linear analysis”. *Composite Structures*. Vol. 216, pp. 315–330 , 2019.

[Bar+20] G. Barbat et al. “Structural size effect: Experimental, theoretical and accurate computational assessment”. *Engineering Structures*. Vol. 213, p. 110555 , 2020.

[Bar15] L.G. Barbu. *Numerical simulation of fatigue processes. Application to steel and composite structures.* Universitat Politècnica de Catalunya. 2015.

[Baz00] Z. Bazant. “Size effect”. *International Journal of Solids and Structures*. Vol. 37, pp. 69–80 , 2000.

[Baz99] Z. Bazant. “Size effect on structural strength: a review”. *Archive of Applied Mechanics volume*. Vol. 69, pp. 703–725 , 1999.

[BP98] Z. Bazant and J. Planas. *Fracture and size effect in concrete and other quasibrittle materials*. Boca Raton: CRC Press. 1998.

[CBC17] M. Cervera, G.B. Barbat, and M. Chiumenti. “Finite element modelling of quasi-brittle cracks in 2D and 3D with enhanced strain accuracy”. *Computational Mechanics*. Vol. 60, pp. 767–796 , 2017.

[CC06] M. Cervera and M. Chiumenti. “Mesh objective tensile cracking via a local continuum damage model and a crack tracking technique”. *Computer Methods in Applied Mechanics and Engineering*. Vol. 196(1), pp. 304–320 , 2006.

[CCC11] M. Cervera, M. Chiumenti, and R. Codina. “Mesh objective modeling of cracks using continuous linear strain and displacement interpolations”. *Int. J. Numer. Meth. Engng*. Vol. 87, pp. 962–987 , 2011.

[Cor+18] A. Cornejo et al. “Methodology for the analysis of post-tensioned structures using a constitutive serial-parallel rule of mixtures”. *Composite Structures*. Vol. 200, pp. 480–497 , 2018.

[Cor+19] A. Cornejo et al. “Combination of an adaptive remeshing technique with a coupled FEM-DEM approach for analysis of crack propagation problems”. *Computational Particle Mechanics*. Pp. 1–18 , 2019.

[CT17] M. Cervera and C. Tesei. “An Energy-Equivalent d+/d- Damage Model with Enhanced Microcrack Closure-Reopening Capabilities for Cohesive-Frictional Materials”. *Materials*. Vol. 10, p. 433 , 2017.

[DRO10] P. Dadvand, R. Rossi, and E. Oñate. “An Object-oriented Environment for Developing Finite Element Codes for Multi-disciplinary Applications”. *Computational Methods in Engineering*. Vol. 17, pp. 253–297 , 2010.

[GGC12] V. Garcia-Alvarez, R. Gettu, and I. Carol. “Analysis of mixed-mode fracture in concrete using interface elements and a cohesive crack model”. *Sadhana*. Vol. 37, pp. 187–205 , 2012.

[GRP13] D. Grégoire, L. Rojas-Solano, and G. Pijaudier-Cabot. “Failure and size effect for notched and unnotched concrete beams”. *International Journal for Numerical and Analytical Methods in Geomechanics*. Vol. 37, pp. 1434–1452 , 2013.

[Hil48] R. Hill. “A theory of the yielding and plastic flow for anisotropic metals”. *Proc. Roy. Soc. London*. Vol. 193, pp. 281–297 , 1948.

[Hil71] R. Hill. *The mathematical Theory of Plasticity*. Oxford University Press. 1971.

[JBO18] S. Jiménez, LG. Barbu, and S. Oller. *Analysis of post-tensioned structures by means of a constitutive serial-parallel rule of mixtures*. CIMNE. 2018.

[Joh87] K. L. Johnson. *Contact Mechanics*. Cambridge University Press. 1987.

[Kri89] M. Krizek. “Superconvergence results for linear triangular elements”. *Mathematical Institute, Czechoslovak Academy of Sciences*. , 1989.

[Kri94] M. Krizek. “Superconvergence phenomena in the finite element method”. *Comput. Methods Appl. Mech. Engrg*. Vol. 116, pp. 157–163 , 1994.

[Lev82] N. Levine. *Stress Sampling Points for Linear Triangles in the Finite Element Method*. University of Reading, Department of Mathematics. 1982.

[LP02] Y. Lee and K.C. Park. “Numerically generated tangent stiffness matrices for nonlinear structural analysis”. *Computer methods in applied mechanics engineering*. Vol. 191, pp. 5833–5846 , 2002.

[Mau92] G.A. Maugin. *The thermodynamics of plasticity and fracture*. Cambridge University Press. 1992.

[MOB11] X. Martinez, S. Oller, and E. Barbero. “Caracterización de la delaminación en materiales compuestos mediante la teoría de mezclas serie/paralelo”. *Revista Internacional de Métodos Numéricos para Cálculo y Diseño en Ingeniería*. Vol. 27, pp. 189–199 , 2011.

[Oll+93] S. Oller et al. “A finite element model for analysis of multiphase composite materials”. *Ninth International Conferences on Composite Materials. Zaragoza - Spain*. , 1993.

[Oll+95] S. Oller et al. “An anisotropic elastoplastic model based on an isotropic formulation”. *Engineering Computations*. Vol. 12, pp. 245–262 , 1995.

[Oll02] S. Oller. *Non-linear dynamics*. 2002.

[Oll03] S. Oller. *Simulación numérica del comportamiento mecánico de los materiales compuestos*. CIMNE - Barcelona. 2003.

[Oll88] S. Oller. *Un modelo de daño continuo para materiales friccionales*. 1988.

[San16] M. Santasusana. *Numerical tecniques for non-linear analysis of structures combining Discrete Element and Finite Element Methods*. 2016.

[SJ87] J.C. Simo and J.W. Ju. “Strain- and stress-based continuum damage modelsI. Formulation”. *International Journal of Solids and Structures*. No. 7, Vol. 23, pp. 821–840 , 1987. DOI: https://doi.org/10.1016/0020-7683(87)90083-7.

[SPO08] E. de Souza, D. Peric, and R.J. Owen. *Computational Methods for Plasticity: Theory and Applications*. Wiley. 2008.

List of Tables

List of Figures

Nomenclature

$^{f}\boldsymbol{\sigma}$	Fiber stress vector
$^{f}\boldsymbol{\varepsilon}$	Fiber strain vector
$^{f}\mathfrak{C}_{law}$	Fiber constitutive law
^{f}k	Fiber volumetric participation
$^{m}\boldsymbol{\sigma}$	Matrix stress vector
$^{m}\boldsymbol{\varepsilon}$	Matrix strain vector
$^{m}\mathfrak{C}_{law}$	Matrix constitutive law
^{m}k	Matrix volumetric participation
α, β	Rayleigh coefficients
$\bar{\boldsymbol{\sigma}}$	Effective Cauchy stress tensor
$\bar{\varepsilon}^{p}$	Acumulated plastic strain vector
$\boldsymbol{\eta}$	Weighting function or test function
$\boldsymbol{\Lambda}$	Rotation matrix
$\boldsymbol{\mathcal{C}}$	Tangent constitutive tensor
$\boldsymbol{\mathcal{C}}_0$	Elastic constitutive tensor
$\boldsymbol{\mathcal{C}}_s$	Secant constitutive tensor
$\boldsymbol{\mathcal{M}}$	Metric tensor
$\boldsymbol{\mathcal{M}}_1$	First metric tensor for metric intersection
$\boldsymbol{\mathcal{M}}_2$	Second metric tensor for metric intersection
$\boldsymbol{\mathcal{M}}_{aniso}$	Anisotropic metric tensor
$\boldsymbol{\mathcal{M}}_{iso}$	Isotropic metric tensor
$\boldsymbol{\sigma}$	Cauchy stress tensor
$\boldsymbol{\sigma}_p$	Parallel stress vector
$\boldsymbol{\sigma}_s$	Serial stress vector
ε^{p}	Plastic strain vector
ε_p	Parallel strain vector
ε_s	Serial strain vector
$\boldsymbol{\xi}$	Isoparametric coordinates
$\check{\mathbf{E}}$	Fictitious isotropic Green-Lagrange strain vector
$\check{\mathbf{S}}$	Fictitious isotropic second Piola-Kirchoff stress vector
$\ddot{\mathbf{d}}$	Discretized acceleration vector
$\delta\mathcal{W}_{ext}$	External virtual work
$\delta\mathcal{W}_{int}$	Internal virtual work
$\delta\mathcal{W}_{kin}$	Kinematic virtual work
δ_n	Ball to Ball indentation
$\dot{\gamma}$	Plastic multiplier increment
$\dot{\mathbf{d}}$	Discretized velocity vector

Γ_σ	Newmann boundary
Γ_u	Dirichlet boundary
$\hat{\mathbf{b}}_0$	Body force vector in the reference configuration
$\hat{\mathbf{t}}_0$	Traction vector in the reference configuration
$\hat{l}$	Characteristic length
κ	Uniaxial stress threshold
κ_f	Fluid bulk modulus
λ, μ	Lamé parameters
$\mathbb{A}$	Assembling operator
$\mathbb{C}$	Damping matrix
$\mathbb{P}_p$	Paralel direction projector
$\mathbb{P}_s$	Serial direction projector
$\mathcal{P}_{ext}$	External power
$\mathcal{P}_{int}$	Internal power
$\mathcal{P}_{kin}$	Kinematic energy
μ_f	Fluid dynamic viscosity
ν	Poisson ratio
ω	Aitken relaxation parameter
Ω_0	Computational body in its reference configuration
Ω_f	Computational fluid body in its current configuration
Ω_t	Computational body in its current configuration
$\partial\Omega$	Contour of the domain
ϕ	Friction angle
ϕ_t	Bijective non-linear deformation map
Ψ	Strain energy function
ρ	Spatial mass density
ρ_0	Reference spatial mass density
ρ_f	Fluid density
$\mathbf{A}^E$	Strain mapper operator
$\mathbf{A}^S$	Stress mapper operator
$\mathbf{d}$	Discretized displacement vector
$\mathbf{f}_{ext}$	External forces vector
$\mathbf{f}_{int}$	Internal forces vector
$\mathbf{H}$	Hessian matrix
$\mathbf{I}$	Contact impulse
$\mathbf{N}$	Plastic flow vector
$\mathbf{r}_{eff,dyn}$	Discrete momentum balance equation residual
$\mathbf{s}$	Stress deviator vector
$\mathbf{T}_\varepsilon$	Voigt size strain rotation operator
$\mathbf{u}_0$	Prescribed displacement vector
$\mathbf{v}_0$	Prescribed velocity vector
θ	Lode's angle

Υ	Hessian nodal indicator
d	Damage internal variable
d_{ex}	Blast hole diameter
E	Young modulus
f_t	Compressive strength
f_t	Tensile strength
G_f	Fracture energy
I_1	First invariant of the stress tensor
I_2	Second invariant of the stress tensor
I_3	Third invariant of the stress tensor
J_2	Second invariant of the stress deviator tensor
J_3	Third invariant of the stress deviator tensor
n_{elem}	Number of elements that share an edge
P	Blast pressure
S	Hole spacing
t	Thickness
t_{delay}	Blast detonation delay
W_{ex}	Weight of explosive
C	Right Cauchy-Green strain tensor
E	Green-Lagrange strain tensor
F	Deformation gradient tensor
K	Stiffness matrix
M	Mass matrix
P	First Piola-Kirchoff stress tensor
R	Rotation tensor
S	Second Piola-Kirchoff stress tensor
U	Right stretch tensor
u	Displacement vector
V	Left stretch tensor
X	Material point coordinates
x	Spatial point coordinates
G	Shear modulus
Grad(·)	Gradient with respect to reference coordinates
grad(·)	Gradient with respect to current coordinates
H	Hardening modulus
J	Deformation gradient tensor determinant or Jacobian, $J = det(\mathbf{F})$

Acronyms

ALE Arbitrary Lagrangian Eulerian.

ALM Augmented Lagrange Multipliers.

ANFO Ammonium Nitrate Fuel Oil.

BPM Bonded Particle Method.

CFD Computational Fluid Dynamics.

CFM Computational Failure Mechanics.

CIMNE International Centre for Numerical Methods in Engineering.

CL Constitutive Law.

CMOD Crack Mouth Opening Displacement.

CPT Closest Point Transfer.

CSM Computational Solid Mechanics.

DCA Discrete Crack Approach.

DE Discrete Element.

DEM Discrete Element Method.

DMM Distributed Memory Machines.

DoF Degrees of Freedom.

EASM Enhanced Assumed Strain Method.

EEM Element Erosion Method.

EFEM Embedded Finite Element Method.

FD Finite Differences.

FE Finite Element.

FEA Finite Element Analysis.

FEM Finite Element Method.

FEM-DEM Finite Element Method Discrete Element Method.

FIC Finite Calculus.

FSI Fluid Structure Interaction.

GFEM Generalized Finite Element Method.

IBM Inmersed Particle Method.

IBVP Initial Boundary Value Problem.

IP Integration Points.

JWL Jones Wilkins Lee.

LBM Lattice Boltzman Method.

LEFM Linear Elastic Fracture Mechanics.

LM Lagrange Multipliers.

LST Least Square projection Transfer.

MCCM Mesh Corrected Crack Model.

MPM Material Point Method.

ODE Ordinary Differential Equation.

PDE Partial Differential Equation.

PF Phase Field.

PFEM Particle Finite Element Method.

PUFEM Partition of Unit Finite Element Method.

PVW Principle of Virtual Work.

RBS Relative Bulk Strength.

RoM Rule of Mixtures.

SCA Smeared Crack Approach.

SFT Shape Function projection transfer.

SMM Shared Memory Machines.

SPH Smoothed Particle Hydrodynamics.

SPR Super convergent Patch Recovery.

SPRoM Serial Parallel Rule of Mixtures.

TL Total Lagrangian.

VOD Velocity Of Detonation.

XFEM eXtended Finite Element Method.